Atomic Force Microscopy in the Picometer Regime -
Resolving Spins and Non-Trivial Surface Terminations
Florian Pielmeier 2014

Atomic Force Microscopy in the Picometer Regime - Resolving Spins and Non-Trivial Surface Terminations

Dissertation zur Erlangung des Doktorgrades der Naturwissenschaften (Dr. rer. nat.) der Fakultät für Physik der Universität Regensburg

vorgelegt von

Florian Pielmeier

aus Regensburg

im Jahr 2014

Die Arbeit wurde von Prof. Dr. Franz J. Gießibl angeleitet.
Das Promotionsgesuch wurde am 16. April 2014 eingereicht.
Das Promotionskolloquium fand am 19. September 2014 statt.

Prüfungsausschuss:	Vorsitzender:	PD Dr. Falk Bruckmann
	1. Gutachter:	Prof. Dr. Franz J. Gießibl
	2. Gutachter:	Prof. Dr. Christian Back
	weiterer Prüfer:	Prof. Dr. Christian Schüller

Contents

1. Introduction

The discovery of the giant magnetoresistance effect in 1988 [1, 2] led to the first technologically relevant electronic devices utilizing not only the charge, but also the spin degree of freedom of an electron [3]. In the meantime, the field of spin-based electronics (spintronics) was growing rapidly, in particular in the area of data storage devices [4]. This also led to the development and investigation of a large number of materials from diluted magnetic semiconductors to topologically insulating materials [5]. With shrinking device size – Intel presented the first processor based on 14 nm technology last year [6] – the investigation of structural and magnetic properties at the atomic scale becomes more and more important.

The scanning tunneling microscope (STM) [7] as well as the atomic force microscope (AFM) [8] allow real-space imaging at the atomic scale [9, 10]. Spin-polarized STM (SP-STM) [11] and magnetic force microscopy (MFM) [12] enabled the investigation of magnetic structures at the nanoscale already around 1990. Ten years later antiferromagnetic structures were imaged at the atomic scale with SP-STM [13], and in 2007 the antiferromagnetic structure of a transition metal oxide was resolved by AFM utilizing iron coated silicon cantilevers [14]. In both experiments, the measured atomic corrugations were quite small, $3 - 4\,\mathrm{pm}$ and $0.5 - 1.5\,\mathrm{pm}$, respectively. The detection of such tiny signals necessitates experimental setups with very low noise, which is achieved by operating the microscopes at cryogenic temperatures.

The development of the qPlus sensor offered the possibility to perform STM and AFM simultaneously, which made it a versatile tool in the field of scanning probe microscopy [15, 16]. This sensor is based on standard quartz tuning forks used in clocks and wrist watches. Its larger stiffness compared to standard silicon cantilevers allows stable operation at sub-Angstrom oscillation amplitudes, leading to an increased sensitivity for short-range interaction forces [17]. Although excellent results were obtained with qPlus force sensors, like subatomic resolution [18–20], submolecular resolution [21], and the detection of single charges on individual atoms [22], the resolution of magnetic structures at the atomic scale still remains a challenge [23].

In this thesis, the relevant figures of merit determining the signal-to-noise ratio

(SNR) of quartz-based force sensors are analyzed, suggesting an improved SNR for miniaturized sensors. Modified qPlus force sensors are characterized at room and cryogenic temperatures and the expected improvement in SNR is confirmed.

These modified sensors are then used to resolve the antiferromagnetic structure of the nickel oxide (NiO) (001) surface. NiO is a prototypical antiferromagnetic insulator with planes of oppositely aligned Ni spins along the [111] direction. Apart from imaging the different spin states of the Ni ions at the surface, the spin state of sub-surface Ni ions was also detected due to a superexchange mechanism between tip and sample. The exchange interactions between tip and sample are also studied quantitatively where the magnitude of the measured exchange force is an order of magnitude smaller than predicted theoretically [24, 25]. The strength of the spin-related signal depends crucially on the tip material and best results were obtained with a tip made of a samarium cobalt alloy, a magnetically hard material.

A new class of materials, topological insulators (TI), have attracted a lot of attention in recent years due to their unique electrical properties [26]. Spin-orbit interaction leads to the formation of a helical surface state, where the propagation direction of electrons is coupled to their spin state. In absence of magnetic impurities which break time reversal symmetry the backscattering between different spin states is suppressed [27]. Usual TIs have bulk band gaps of a few tens to hundreds of meV and often the surface states mix with bulk states [5]. These materials are often layered ternary systems and for band structure determination with angle-resolved photoemission spectroscopy (ARPES) they are cleaved *in-situ*, though it is not a priori obvious where the cleaving occurs. Here, we study the surface of cleaved $TlBiSe_2$, a promising candidate for room temperature applications due to its relatively large band gap of around 250 meV. In STM mode, hexagonally ordered, nanometer sized patches could be identified. The AFM data additionally revealed a hexagonal atomic structure within these patches. From a detailed analysis of step heights and atomically resolved data, we deduce that the surface layer is formed by Tl islands. The disrupted surface layer explains the absence of trivial surface states in ARPES experiments [28].

This thesis is outlined as follows. In chapter 2 the basic theory and operating principle of STM and AFM is introduced. In particular, frequency modulation AFM (FM-AFM) [29] which is the operation mode used throughout this work.

The third chapter starts with a detailed introduction to quartz-based force sensors, followed by an experimental and theoretical comparison of the SNR of force sensors utilizing different quartz resonator geometries, namely tuning forks and length extensional resonators. As mentioned above, the relevant figures of merit are evaluated for

various types of sensors, clearly favoring miniaturized qPlus sensors in terms of SNR. Finally, the frequency change with temperature for a number of quartz resonators is determined at cryogenic temperatures.

The experimental setup, a combined STM/AFM ultrahigh vacuum system operated at liquid helium temperatures, is described in chapter 4. Furthermore, the tip preparation procedures used to fabricate magnetic tips are explained.

Chapter 5 deals with investigation of individual copper (Cu) adatoms on the (110) and (111) facets of a Cu single crystal with carbon monoxide (CO) functionalized tips. The measurements on Cu/Cu(110) revealed for the first time a non-trivial subatomic structure within a single atom on a flat surface. The comparison of the adatom data with complementary experiments, where a bulk Cu tip is probed by a CO molecule adsorbed on Cu(111), suggests a different interpretation of previously obtained "subatomically" resolved data [20, 30].

In chapter 6 spin-resolved measurements of the NiO(001) surface, as outlined above, are presented. Experiments with two different tip materials, bulk iron tips and SmCo tips, were conducted.

The surface termination of $TlBiSe_2$ is investigated in chapter 7, by a combination of STM and AFM imaging. The results suggest a disruption of the surface layer upon sample cleaving leading to a, at first glance, irregular surface structure.

2. Fundamentals of Scanning Probe Microscopy

This chapter briefly recaps the basic theory and operating principle of scanning tunneling microscopy in section 2.1. The focus of this work is mainly on atomic force microscopy, therefore this technique is described in more detail in section 2.2.

2.1. Scanning Tunneling Microscopy (STM)

Scanning tunneling microscopy was introduced by Binnig *et al.* in 1982 [7]. The capability of real-space atomic imaging and highly local spectroscopy was a major breakthrough in surface science [9, 31]. In STM piezoelectric elements (piezos) position a sharp metal tip laterally (x, y-direction) and vertically (z-direction) over a conductive sample. If a bias voltage V is applied between the two electrodes, a current flows between tip and sample already before an ohmic contact is formed. This current originates from quantum mechanical tunneling of electrons through the vacuum gap or more general the potential barrier between tip and sample [32, 33]. A simple model that reproduces the key observables is a rectangular potential barrier, where the barrier height is approximately given by the average value of tip (Φ_T) and sample (Φ_S) work functions $\Phi = (\Phi_T + \Phi_S)/2$ [33, 34]. From a quantum mechanical treatment of this one-dimensional potential wall the distance dependence of the tunneling current follows as [33]:

$$I(z) = I_0 \exp(-2\kappa z), \tag{2.1}$$

where $\kappa = \sqrt{2m_e\Phi}/\hbar$ with free electron mass m_e and reduced Planck constant $\hbar$. Common electrode materials are W and Cu with work function values of $\Phi \approx 4.6\,\mathrm{eV}$ [35] and a resulting value of $\kappa \approx 11\,\mathrm{nm}^{-1}$. Roughly, the tunneling current changes by an order of magnitude when the tip-sample distance changes by 100 pm. Furthermore, $I(z)$ is a monotonic function, enabling a straightforward implementation of a feedback circuit to control the tip-sample distance (*constant current mode*) by adjusting the z-position of the tip with the piezos. Another operation mode of the STM is the

constant height mode, where the feedback is switched off and the tip position in z-direction remains unchanged. In this mode a flat sample surface and a high stability of the microscope are mandatory.

In this work, the tunneling current is often used to determine the tip-sample distance with respect to a metal-metal point contact, whose conductance is given by the single-channel, spin-degenerate quantum of conductance $G_0 = 2e^2/h = (12906\,\Omega)^{-1}$, where e is the elementary charge and h is Planck's constant [34, 36]. The junction conductance $G(z) = I(z)/V = G_0 \exp(-2\kappa z)$ follows from Eq. (2.1). If the tip is oscillating with amplitude A at a frequency f like in a combined STM/AFM setup, the measured conductance is usually[1] a time average over one oscillation cycle and is given by

$$\langle G(z) \rangle = G_0 \exp(-2\kappa z) \mathrm{I}_0(2\kappa A) \exp(-2\kappa A), \tag{2.2}$$

where $\mathrm{I}_0(2\kappa A)$ is the modified Bessel function of the first kind [16, 34]. For typical values of $\kappa = 11\,\mathrm{nm}^{-1}$ and $A = 50\,\mathrm{pm}$, $\mathrm{I}_0(2\kappa A) = 1.33$ and $\mathrm{I}_0(2\kappa A)\exp(-2\kappa A) = 0.44$. Hence, the average conductance at $A = 50\,\mathrm{pm}$ is only about half the value of the stationary case. For an accurate determination of z it is therefore important to take the averaging into account. If κ is known from $\langle G(z) \rangle$ or rather $\langle I(z) \rangle$ curves Eq. (2.2) can be used to solve for z.

While equation Eq. (2.1) often leads to a correct description of current as a function of vertical tip height, it does not include a description of the electronic states or the influence of an applied bias voltage. Using Bardeen's method one obtains in the limit of small temperatures the following expression for the tunneling current [33, 37]:

$$I(V) = \frac{8\pi^2}{h} \int_0^{eV} \rho_T(E_F - eV + \epsilon)\rho_S(E_F + \epsilon)|M|^2 \mathrm{d}\epsilon. \tag{2.3}$$

Here, $\rho_{T,S}$ are the densities of states (DOS) of tip and sample, E_F is the Fermi energy, and $|M|^2$ is the tunneling matrix element which describes the probability of an electron tunneling from tip to sample or vice versa. In general, the STM measures a convolution of tip and sample DOS which makes a straightforward interpretation of STM data difficult. A common approximation is to assume spherical symmetric (s-wave) tip orbitals. Then the tunneling current is proportional to the local density of states of the sample at the Fermi energy, however, this holds only for small applied bias voltages ($V \ll \Phi$) [33, 38, 39]. The STM probes contours of constant local density of states in constant current mode and not the real topography of the sample.

[1] The bandwidth of the current preamplifier and of the input stage of the acquisition electronics is usually on the order of a few kHz whereas $f > 10\,\mathrm{kHz}$.

2.2. Atomic Force Microscopy (AFM)

The atomic force microscope (AFM) was developed, at least to some extent, to expand the STM capability of high resolution imaging to non-conductive samples [8]. A sharp tip is scanned again along a surface while the tip mounted to a cantilever, which gets deflected by tip-sample interaction forces. The key parameters of the cantilever are the spring constant k and, for dynamic operation modes, eigenfrequency f_0 and quality factor Q. In the static mode, the deflection of the cantilever is directly proportional to the tip-sample forces. Obviously, this is problematic because a high force sensitivity is accompanied with a small restoring force which can lead to tip-sample collisions. This problem is solved by oscillating the cantilever at an amplitude A in the so-called dynamic mode [16]. Either amplitude modulation (AM) [40] or frequency modulation (FM) [29] is used to detect tip-sample interactions. In AM-AFM, the cantilever is excited with a constant amplitude at a fixed frequency and changes in amplitude and phase of the oscillating cantilever upon tip-sample interactions are monitored. These changes occur on a time scale directly proportional to the Q value [16]. In ultra-high vacuum (UHV) and especially at low temperatures Q values exceeding 10^6 can be achieved, leading to a significant reduction in acquisition speed in AM mode. The FM-AFM mode, which is solely used throughout this work, overcomes this limitation and furthermore enables quantitative force measurements which is challenging with AM-AFM [41]. Before discussing FM-AFM and quantitative force measurements in more detail, the various types of long- and short-range forces acting between tip and sample are outlined in the following.

2.2.1. Long-Range Forces between Tip and Sample

In AFM, forces which do not vary on the atomic scale are called long-range forces. In UHV the main contributions come from van der Waals and electrostatic interactions. In general, the term van der Waals interaction describes dipole-dipole interactions where three cases can be distinguished. The interaction between permanent dipoles is referred to as orientation (Keesom) force, the interaction between a permanent and an induced dipole as induction (Debye) force, and the interaction between induced dipoles as dispersion (London) force [42, 43]. All these forces are attractive. For non-polar or weakly polar atoms and molecules the dispersion force constitutes the bulk part of the interaction between them [42]. In a semi-classical picture the dispersion force is caused by fluctuating charge distributions in an atom or molecule. They temporarily lead to an electric dipole inducing an oppositely oriented dipole which causes attraction between the two objects. In quantum mechanics the dispersion force follows from

second-order perturbation theory [42–44]. Throughout this thesis the term van der Waals (vdW) refers to the dispersion force, as these are the main contributions to the tip-sample interaction in AFM. The distance dependence of the vdW interaction potential between two atoms is given by

$$U_{\mathrm{vdW}} = -\frac{C}{z^6}, \tag{2.4}$$

where z is the distance between the atoms and C the London-van der Waals constant. Besides this short-range contribution to the tip-sample interaction, there is actually a much larger contribution due to the vdW interaction between macroscopic objects. This can be calculated by pairwise summation over all particles or integration over the geometric structure [43, 45]. For a parabolic tip with local radius R and a flat sample, the vdW force is given as follows [43]:

$$F_{\mathrm{vdW}} = -\frac{A_H R}{6z^2}. \tag{2.5}$$

Here, A_H is the Hamaker constant, which is around 1 eV for most solids [16]. The above equation describes no longer a short-range interaction, but a long-range force contribution which adds as an attractive background force to the tip-sample interaction. The distance dependence of the vdW force between tip and sample generally follows a z^{-n} power law, where n is usually between 1 and 2 [45]. In an AFM setup, given that the sample is flat, the resulting vdW forces depend on the tip geometry, and sharp tips reduce the influence of these long-range contributions. Electrostatic interactions arise between a conductive tip and sample due to differences in the contact potential, giving rise to a capacitance $C(z)$ between them. If a bias voltage V is applied, the force can be described as follows:

$$F_{\mathrm{el}} = \frac{1}{2}\frac{\partial C}{\partial z}(V - V_{\mathrm{CPD}})^2, \tag{2.6}$$

with V_{CPD} as contact potential difference (CPD). F_{el} is minimized when the applied bias voltage V compensates the CPD. Note, this picture still holds on insulating samples. In this case, the capacitor is filled with a dielectric media and the electric polarization on the sample surface is measured. One usually obtains again a parabolic dependence of the tip-sample interaction on the bias voltage V [46].

Another type of long-range force contribution is due to magnetic dipole-dipole interactions. These are used in Magnetic Force Microscopy (MFM) to study domain structured samples with a magnetized tip [12, 47]. The resolution is on the order of

10 nm [48, 49]. The magnetic force acting between tip and sample is given as

$$F_{\mathrm{mag}} = \mu_0(\mathbf{m}\nabla)\mathbf{H}, \tag{2.7}$$

$\mathbf{m}$ is the magnetic moment of the tip and $\mathbf{H}$ the sample magnetization. This interaction is quite weak and predominated by electrostatic and vdW forces. The contribution is negligible if either tip or sample is antiferromagnetic [39].

2.2.2. Short-Range Forces between Tip and Sample

Short-range forces are chemical bonding forces between the foremost atoms in tip and sample and give rise to atomic resolution imaging with AFM. Chemical bonds in solids include vdW bonds, ionic bonds, covalent bonds, and metallic bonds. These will be briefly discussed in the following. As mentioned above, the vdW interaction between single particles is short-range in nature (Eq. (2.4)), but usually negligible compared to other chemical bonding forces. Nevertheless, on inert samples like noble gas solids they allow atomic resolution imaging [50]. The total interaction is not solely attractive. To account for the repulsion of the electron clouds at close distances due to the Pauli exclusion principle [51] an empirical repulsive $1/z^n$ term is added to the vdW potential. For $n = 12$ one obtains the well-known form of the Lennard-Jones Potential [52]:

$$U_{LJ} = U_0 \left[\left(\frac{\sigma_0}{z} \right)^{12} - 2 \left(\frac{\sigma_0}{z} \right)^{6} \right], \tag{2.8}$$

where U_0 is the bonding energy at the equilibrium distance σ_0.

In ionic crystals the bonding is described by electrostatic attraction between positively charged cations and negatively charged anions. To obtain an equilibrium bonding length an empirical repulsion term is added to the Coulomb potential [53, 54]. If one sums the electric field from all cation and anion sites on the surface of an ionic crystal the resulting electric field decays exponentially with distance [55]. The decay constant κ is given as $\kappa = 2\pi/d$, where d is the lattice constant of the surface unit cell; e.g. $d = a_0/\sqrt{2}$ for an ionic crystal with bulk rock salt structure [56]. For NaCl with a bulk lattice constant of 0.56 nm the decay constant is $\kappa = 15.87\,\mathrm{nm}^{-1}$, which is even larger than typical values in STM. The strong exponential decay of the electric field is the reason why it is relatively easy to achieve atomic resolution imaging on ionic crystal surfaces with AFM [10, 57].

Ideally, vdW and ionic crystals can be described as closed shell systems, where no overlap between the wave functions of the particles occurs and the electrons are localized at the atomic sites. In metals electrons are delocalized and distributed

uniformly throughout the whole crystal leading to a reduction of their kinetic energy and the electrostatic repulsion between the ion cores is also reduced. This picture only holds for simple metals like Li, Na, or Ka. The remaining core electrons form again a closed shell system [53]. In between ionic and metallic bonding character is covalent bonding, where the individual atomic orbitals overlap and form new orbitals, bonding and anti bonding ones. The standard example is the H_2^+ molecule. The increased electron density between the H^+ ions reduces electrostatic repulsion. Such a simple system can be described to a good approximation by the semi-empirical Morse potential [58]

$$U_M = -U_0 \left[2 \exp\left(-\frac{z - \sigma_0}{\lambda} \right) - \exp\left(-2 \frac{z - \sigma_0}{\lambda} \right) \right], \tag{2.9}$$

where U_0 is the bonding energy and σ_0 the equilibrium distance. The decay lengths λ and $\lambda/2$ correspond to the attractive and repulsive part of the interaction. Similar to the Lennard-Jones potential the repulsive part is added empirically and originates from the Pauli repulsion at close distances.

The chemical bonding forces described above determine structural and electronic properties of solids and enable atomic resolution imaging and site-dependent spectroscopy with AFM. If one wants to study the magnetic structure of a sample on the atomic scale with AFM, the question arises which kind of short-range interaction between tip and sample can be employed to resolve the magnetic ordering. The classic dipole-dipole interaction between atomic magnetic moments is far too small to account for any magnetic ordering like ferro- or antiferromagnetism [53]. So far, there is no single model to explain all the various types of magnetic ordering in solids: For example, the Heisenberg model [59] describes the interaction between localized spins well, but fails to explain ferromagnetism in itinerant electron systems like iron or cobalt [60]. Irrespective of the different characteristics of magnetic ordering they have a common origin: the so-called *exchange interaction*. It is a consequence of the Pauli exclusion principle for indistinguishable particles and the Coulomb interaction [51]. In general, if the spins align parallel the kinetic energy is increased and Coulomb energy is decreasing, whereas for antiparallel alignment the situation is reversed. In the simple case of a He atom in the ground state the two electrons align antiparallel, or more precise, they form a singlet state [61]. As a general consequence, the spin states influence the spatial part of the wave functions. This can of course also affect covalent bonding in solids, where a larger number of electrons is involved.

In force microscopy the interaction of the spins which are localized at the foremost tip and sample atoms is crucial and therefore the Heisenberg model is used to describe

this situation [14, 39]. The Heisenberg model omits kinetic and Coulomb terms apart from the electron-electron interaction and solely considers the interaction between individual spins, leading to the following expression for the Hamiltonian:

$$H^{\text{spin}} = -\sum_{ij} J_{ij}\mathbf{S}_i \cdot \mathbf{S}_j, \tag{2.10}$$

the spin Hamiltonian H^{spin} depends on the relative alignment of the individual spins $\mathbf{S}_i$ and $\mathbf{S}_j$, and only nearest-neighbor interaction is taken into account. The factor J_{ij} is called *exchange integral* or *exchange coupling constant* and is given as:

$$J_{ij} = \int\int d\mathbf{r}_i d\mathbf{r}_j \Psi_i^*(\mathbf{r_i})\Psi_j^*(\mathbf{r_j}) H \Psi_i(\mathbf{r_j})\Psi_j(\mathbf{r_i}). \tag{2.11}$$

The Hamilton operator $H = e^2/|\mathbf{r_i} - \mathbf{r_j}|$ describes the pairwise Coulomb interaction and Ψ is the spatial part of the wave function of the particles. The name *exchange integral* is due to the exchange of coordinates between the corresponding Ψ and Ψ^*. If J_{ij} is positive, ferromagnetic order is favored if J_{ij} is negative, antiferromagnetic ordering is favored. AFM offers the unique ability to study exchange interaction between individual spins on the atomic scale. Therefore one has to combine the atomic resolution imaging capability of AFM with magnetic or rather spin-polarized tips [39]. The first experiment which unambiguously demonstrated the feasibility of this so-called Magnetic Exchange Force Microscopy (MExFM) was conducted in 2007 by Kaiser *et al.* [14]. Here, the antiferromagnetic order of the (001) surface of the insulator nickel oxide was resolved with atomic resolution. The term MExFM is somewhat misleading. Basically, the covalent bonds forming between tip and sample have different decay lengths depending on the extent of the wave functions which is determined by the different spin states.

2.2.3. Frequency Modulation Atomic Force Microscopy

In FM-AFM the force sensor, usually a single cantilever beam, is oscillated at constant amplitude A by an external drive signal [29]. The unperturbed cantilever can be described as a driven damped harmonic oscillator whose resonance frequency f_0 is given as

$$f_0 = \frac{1}{2\pi}\sqrt{\frac{k}{m^*}}, \tag{2.12}$$

where k is the stiffness and $m^* = 0.24\,m$ is the effective mass of the oscillating beam [33]. A perturbation k_{ts} which acts on the cantilever oscillation can be included by

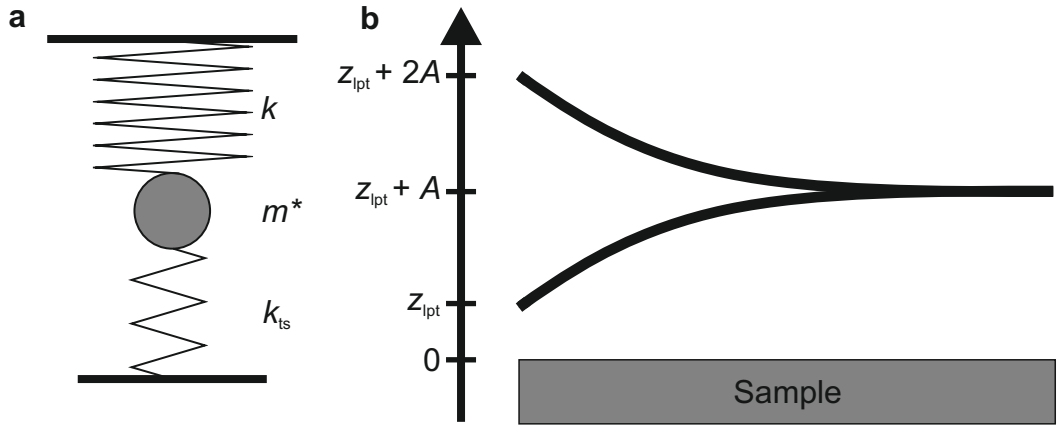

Figure 2.1.: Functional principle of AFM. **a**, equivalent mass and spring model for an oscillating beam with mass m^* and stiffness k. The tip-sample interaction is modeled as an additional spring with stiffness k_{ts}. **b**, beam oscillating with amplitude A and definition of z-axis. The lower turnaround point of the oscillating beam is indicated with z_{lpt} and the base of the beam is then located at $z_{\mathrm{lpt}} + A$.

replacing the stiffness k by an effective stiffness $k^* = k + k_{\mathrm{ts}}$ (Fig. 2.1a). If the force gradient $k_{\mathrm{ts}} = -\partial F_{\mathrm{ts}}/\partial z$ is constant during one oscillation cycle of the cantilever and $k \gg k_{\mathrm{ts}}$, the square root in Eq. (2.12) can be expanded in a Taylor series and the change in resonance frequency $\Delta f = f - f_0$ to first order is

$$\Delta f(z) = \frac{f_0}{2k} k_{\mathrm{ts}}(z). \tag{2.13}$$

The above gradient approximation is only justified if the oscillation amplitude A is significantly larger than the length scale of the interaction. For short-range forces one can assume an exponential force law with decay length λ and then, $A \ll \lambda$ must be fulfilled to apply Eq. (2.13) [16]. In most experiments this condition is not met and the oscillation of the beam in the varying, non-linear tip-sample interaction potential V_{ts} has to be taken into account.

The frequency shift Δf is measured as a function of the vertical base position of the cantilever. When z_{lpt} is the lower turnaround point of the oscillation then the base is at $z_{\mathrm{lpt}} + A$ (Fig. 2.1b). Giessibl derived the following expression for the frequency shift Δf [45]:

$$\Delta f(z_{\mathrm{lpt}}) = \frac{f_0}{2k} \frac{2}{\pi A^2} \int_{-A}^{A} F_{\mathrm{ts}}(z_{\mathrm{lpt}} + A + q') \frac{q'}{\sqrt{A^2 - q'^2}} dq'. \tag{2.14}$$

Here, V_{ts} was treated as a small perturbation to the harmonic potential $V = kA^2/2$ of the cantilever ($V_{\mathrm{ts}} \ll V$). Equation (2.14) is valid for arbitrary amplitudes and

describes a convolution of the force with an amplitude-dependent weight function. Integrating Eq. (2.14) by parts results in a more intuitive expression:

$$\Delta f(z_{\mathrm{lpt}}) = \frac{f_0}{2k}\frac{2}{\pi A^2}\int_{-A}^{A} k_{\mathrm{ts}}(z_{\mathrm{lpt}} + A + q')\sqrt{A^2 - q'^2}dq'. \tag{2.15}$$

Now, Δf is given as a convolution of the force gradient k_{ts} and a weight function $w(q') = 2/(\pi A^2)\sqrt{A^2 - q'^2}$ which describes a semicircle with radius A divided by its area $\pi A^2/2$ [62]. Hence, one can still use the neat form of Eq. (2.13) by substituting the force gradient k_{ts} by an averaged force gradient

$$\langle k_{\mathrm{ts}}(z)\rangle = \int_{-A}^{A} k_{\mathrm{ts}}(z + A + q')\frac{2\sqrt{A^2 - q'^2}}{\pi A^2}dq'. \tag{2.16}$$

In FM-AFM forces are not directly measured. To recover F_{ts} from measured $\Delta f(z)$ data Eq. (2.14) must be inverted. For this purpose several methods were proposed [63–66]. Most commonly used are the direct deconvolution methods by Giessibl [62] and Sader and Jarvis [67]. In this work, forces are recovered by the Sader-Jarvis method and the implementation is based on a MATLAB script supplied by Welker *et al.* [68].

FM-AFM detects an averaged force gradient which offers the possibility to adjust the sensitivity to short- or long-range forces by a proper choice of the amplitude of oscillation A. For example, large amplitudes ($\sim 10\,\mathrm{nm}$) are required if one wants to detect magnetic stray fields and small amplitudes ($\sim 0.1\,\mathrm{nm}$) if one is interested in chemical bonding forces. On the other hand, for a stable oscillation of the cantilever (no *jump-to-contact*) it must be ensured that the restoring force of the cantilever is higher than the tip-sample forces. This leads to the following stability criterion [69]:

$$kA > F_{\mathrm{ts}}^{\mathrm{max}}. \tag{2.17}$$

To detect large force gradients or respectively short-range forces it seems to be beneficial from Eq. (2.16) to use amplitudes as small as possible. On the other hand, noise also needs to be considered as it scales inversely with the amplitude A [16, 29]. For exponentially decaying tip-sample forces with a decay length λ the optimal ratio between amplitude and decay length is $A = 1.55\,\lambda$ [70]. In UHV the peak forces acting on the cantilever can be on the order of 100 nN [45]. This requires at least a stiffness of 1 kN when operating with amplitudes of $A = 100\,\mathrm{pm}$ [69]. Throughout this work qPlus sensors with stiffness values exceeding $k = 1800\,\mathrm{N/m}$ will be used

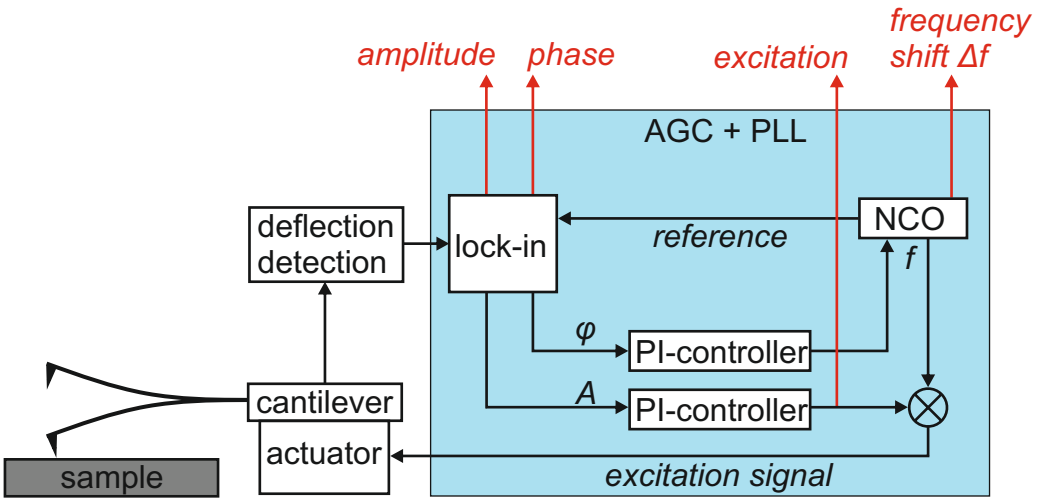

Figure 2.2.: Block diagram of FM-AFM electronics. The colored box shows the basic components and signal paths of the automatic gain control (AGC) and phase-locked loop (PLL) as realized in the Nanonis OC4. The deflection signal of the cantilever is fed into a lock-in – excitation signal and frequency shift are then determined by seperate feedback loops and the numerical controlled oscillator (NCO), see text for more details.

[71, 72]. Nevertheless, atomic resolution with FM-AFM on a reactive surface was first demonstrated with micro-fabricated Si-cantilevers with a stiffness of $k = 17\,\mathrm{N/m}$ and an amplitude of $A = 34\,\mathrm{nm}$ [73]. The signal-to-noise ratio needs to be analyzed in detail to judge which set of cantilever parameters (k, f_0, Q) is optimal for atomic resolution imaging. A comparison of different types of force sensors and a discussion about the set of cantilever parameters (k, f_0, Q) which is best suited for atomic resolution imaging based on a detailed analysis of the SNR in FM-AFM will be presented in chapter 3.

The basic operating principle of FM-AFM was introduced by Albrecht *et al.* [29]. The deflection signal from the cantilever is band-pass filtered and split up in two branches. One branch of the signal enters an amplitude controller consisting of an automatic gain controller (AGC) and a phase shift circuit to ensure positive feedback. The second branch enters a frequency demodulator, which determines the resonance frequency of the oscillating cantilever. In the early days of FM-AFM the required electronics was purely analog. Later, a common combination was to use an analog amplitude controller and a commercially available digital phase-locked loop (PLL) [16]. Nowadays, state-of-the-art electronic circuits are purely digital. In this work a commercial oscillation control unit (Nanonis OC4)[2] was used to keep A constant and to detect Δf.

[2]OC4 - Nanonis Oscillation Controller, Specs Zurich GmbH, 8005 Zurich, Switzerland

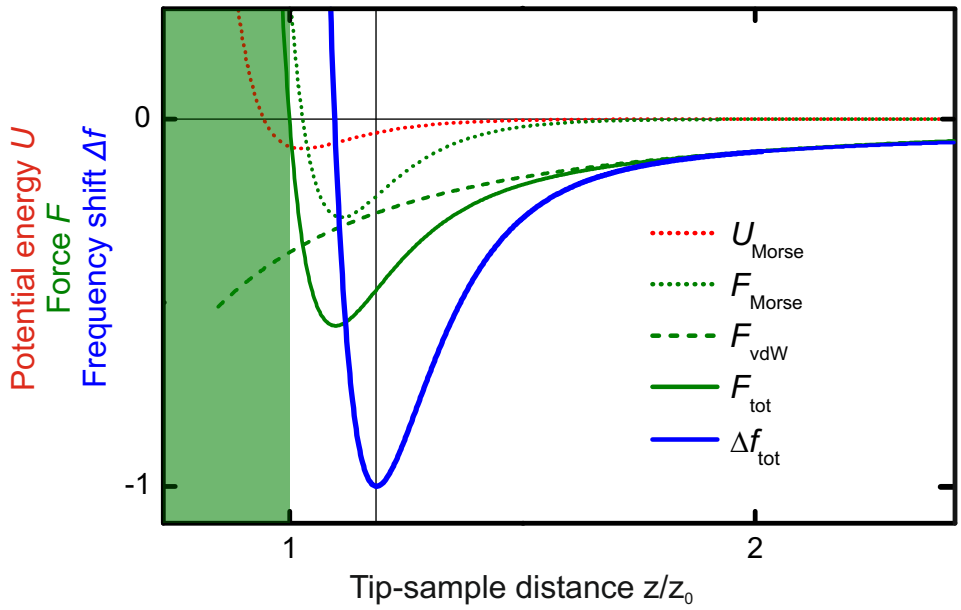

Figure 2.3.: Short- and long-range contributions to the tip-sample interaction in AFM. The short-range part is modeled by a Morse potential U_{Morse} (dotted red) and the corresponding force is F_{Morse} (dotted green). Adding a long-range vdW background force F_{vdW} (dashed green) to F_{Morse} results in the total force F_{tot} (solid green). The corresponding frequency shift Δf_{tot} in the gradient approximation is shown in blue. In the green shaded region F_{tot} is repulsive, but often the region past the minimum in Δf_{tot} (vertical line) is called the "repulsive" interaction regime.

A block diagram is shown in Fig. 2.2. The deflection signal enters a lock-in which acts as a band-pass filter and detects amplitude A and phase φ of the deflection signal. Both are adjusted to their set point value by separate proportional and integral (PI) controllers. The phase signal is sent to a numerical controlled oscillator (NCO), which is triggered by an oven-controlled quartz oscillator (OCXO) with a stability of 1 ppb/day. The output signal of the NCO is the momentary oscillation frequency f of the cantilever which is used again as a reference for the lock-in. After multiplication of the correction variable for the amplitude A with the momentary frequency f, the signal is routed to the actuator to excite the cantilever. The magnitude of this correction variable is a measure of the losses during an oscillation cycle. This is usually a combination of intrinsic losses of the excitation circuit including the sensor and dissipative processes between tip and sample [74]. The frequency shift $\Delta f = f - f_0$ is obtained by taking the difference between the momentary frequency f and the unperturbed resonance frequency f_0; f_0 must be determined in advance.

The frequency shift is caused by non-linear tip-sample interaction forces. Typical short- and long-range contributions are shown in Fig. 2.3. Short- and long-range forces are modeled as Morse and vdW forces (dotted and dashed green curves) and

their sum yields the total force F_{tot} (solid green curve) which determines the frequency shift Δf_{tot} (blue curve). Similar to the tunneling current in STM, Δf_{tot} can now be used as a feedback signal in an additional circuit to adjust the z-position of the cantilever. In contrast to the tunneling current, Δf is not monotonic. In principle both slopes can be used for the feedback, but stable operation is only found in the regime where Δf_{tot} decreases with decreasing tip-sample distance z. This is called the "attractive" or *non-contact* regime. The region past the Δf minimum is often called "repulsive" regime, although the total force is not yet repulsive there. The long-range attractive vdW background is not helpful to achieve atomic resolution imaging, but it is important for stable Δf feedback operation. The long-range vdW interaction enables the tip to stay further away from the sample, when large-scale overview topography scans are desired. To achieve atomic resolution the Δf setpoint is reduced to more negative values where the slope in $\Delta f(z)$ is larger. In the feedback or constant Δf mode one cannot approach closer than the minimum in $\Delta f(z)$. To go even closer the constant height mode can be used.

For quantitative force determination, Δf needs to be measured as a function of tip-sample distance z – a method called dynamic force spectroscopy [64]. By applying a bias voltage V to tip or sample, the local contact potential difference can be determined as at $V = V_{\mathrm{CPD}}$ the electrostatic force F_{el} is minimized (see Eq. (2.6)) [75].

3. Comparison of Quartz-Based Force Sensors

Most of the work presented in this section has been published in Physical Review B[1] [70] and Beilstein Journal of Nanotechnology[2] [76]. Parts of the text are identical to the publications, in particular to the later one.

A number of impressive results including atomic resolution imaging [10, 55, 73], site dependent force spectroscopy [77], and atom manipulation at room temperature [78] were obtained by FM-AFM with standard silicon cantilevers with oscillation amplitudes in the nanometer range and stiffness values on the order of 10 N/m. On the other hand, the sensitivity to a given interaction increases when the amplitude A matches the length scale of the interaction [17, 70]. To study short-range forces it is therefore desirable to operate the force sensor with amplitudes on the order of 0.1 nm. Soft Si cantilevers cannot be operated at such small amplitudes, because they suffer from *snap-to-contact* [45]. It was suggested that stiffness values in the range of $300 - 3000$ N/m are optimal for atomic resolution imaging [17]. Quartz tuning forks (TF) with a stiffness in the kN/m range were introduced by Güthner *et al.* in 1989 for distance control in scanning near field acoustic microscopy [79]. A major drawback of tuning forks is the coupled oscillation of the two prongs; any imbalance leads to a decrease in the quality factor Q [80]. Although the tip mass might be balanced by a counter weight [81], it is not possible to compensate the tip-sample interaction. For tuning forks this problem can be solved by immobilizing one of the two prongs to form a single harmonic oscillator where Q is not affected by the additional mass or tip-sample interactions. This configuration is called "qPlus" [71]. Another possibility is to use a coupled oscillator which has a significantly higher stiffness than

[1] F. J. Giessibl, F. Pielmeier, T. Eguchi, T. An and Y. Hasegawa, *Comparison of force sensors for atomic force microscopy based on quartz tuning forks and length-extensional resonators*, Physical Review B **84**, 125409 (2011).

[2] F. Pielmeier, D. Meuer, D. Schmid, C. Strunk, F. J. Giessibl, *Impact of thermal frequency drift on highest precision force microscopy using quartz-based force sensors at low temperatures*, Beilstein J. Nanotechnology **5**, 407 (2014).

a standard tuning fork, e.g. a length extensional resonator with a stiffness far beyond 100 kN/m. In this case, the tip-sample interaction does not affect the oscillation very much and a high Q value can be retained. This configuration is called "needle" sensor [82]. For obvious reasons it is challenging to detect the small influence of the tip-sample interaction on the oscillating prong. Nevertheless, atomic resolution in UHV on Si(111)-7×7 was obtained at room and low temperatures [83, 84]. In the following, the signal-to-noise ratio (SNR) of these two kinds of sensors is compared theoretically and experimentally.

3.1. Operating Principle and Theoretical Sensitivity

Before discussing the properties of quartz and the working principle of the sensors, an important difference between single and coupled oscillators needs to be pointed out. The standard formulas for FM-AFM (Eq. (2.13)-(2.16)) only hold for a single harmonic oscillator like the qPlus sensor and cannot be applied straightforward to coupled oscillators. The frequency shift Δf of qPlus sensors is given as:

$$\Delta f = \frac{f_0}{2k}\langle k_{\mathrm{ts}}\rangle. \tag{3.1}$$

For the LER the motion of both prongs relative to the support must be taken into account. The evaluation of a corresponding mechanical model showed that Eq. (3.1) still holds for coupled oscillators. Although, the effective stiffness k of a coupled oscillator is twice the value ($k_{coupled} = 2k'$) of a single oscillator ($k_{single} = k'$) [70]. In other words, at a given interaction strength a coupled oscillator yields only half the frequency shift as a single oscillator. For the following discussion it is distinguished between geometrical stiffness k' which is given by the beam dimensions and effective stiffness k which must be used in Eq. (3.1). The k' and k values for both sensors are summarized in Tab. 3.1.

Quartz resonators are used as frequency standards due to their small frequency variation with temperature [85]. Quartz is crystalline SiO_2 which appears in a lot of varieties in nature, whereas for device application synthetic α-quartz is commonly used [85]. For the following discussion quartz refers to α-quartz. This is the stable configuration of quartz at temperatures below 573° C with a trigonal-trapezohedral crystal structure [86]. The standard convention of the axis assignment for right-handed synthetic quartz is shown in Fig. 3.1a. The z-axis is parallel to the crystallographic c-direction and the x-axis is parallel to one of the a-directions [85, 86]. Quartz is an anisotropic material. Its

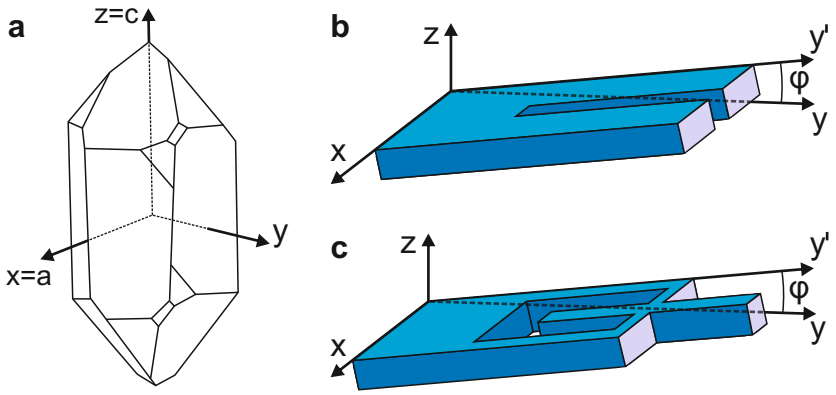

Figure 3.1.: Quartz crystal structure and orientation of crystal cuts. **a**, definition of rectangular x, y, z-axis system. The z-axis coincides with the crystallographic c-axis, x with one of the a-axis, and y is chosen to be perpendicular to x and z. **b**,**c**, tuning forks and length extensional resonators are cut along the x, y'-plane. The angle φ between y and y' is typically in the range of $0 - 5°$. Figure partly adapted from [87].

	L (µm)	L_e (µm)	t (µm)	w (µm)	k' (kN/m)	k (kN/m)	f_0 (kHz)
needle sensor	1340	1100	70	130	530	1 060	1 000
qPlus sensor	2400	1600	214	130	1.8	1.8	32.768

Table 3.1.: Geometrical parameters: length L, electrode length L_e, thickness t, and width w; geometrical stiffness k', effective stiffness k, and eigenfrequency f_0 of the quartz oscillators used.

properties, e.g. piezoelectric constants, elastic constants, and thermal expansion coefficients, depend on the orientation relative to the crystal axes. Therefore, the frequency variation with temperature of quartz resonators can be tuned by choice of the orientation of the crystal cut [85]. The standard crystal cut for TFs and LERs is depicted in Figs. 3.1b,c. The quartz crystal are cut almost along the orthogonal x, y, z-system, but there is a slight deviation along the y-axis and the angle φ is usually between $0-5°$ [87]. The x, y, z-axes are also called electrical, mechanical, and optical axes, respectively [87]. The prongs of the TF oscillate parallel to the x-axis in a bending mode, whereas the prongs of the LER oscillate perpendicular to the x-axis in a length extensional mode.

A qPlus sensor is built by fixing one of the prongs of a TF to an electrically non-conductive substrate (Al_2O_3) with non-conductive glue[3] (Fig. 3.2a). The LER is fixed to the substrate at its base without any modifications to form a needle sensor (Fig. 3.2b). Both resonators have two electrodes which are connected to the leads with conductive epoxy.[4] A tip is mounted on the freely oscillating prongs. The standard

[3]J-B Weld, J-B Weld Company, Sulphur Springs, TX, USA.
[4]EPO-TEK T4110, EPOXY Technology, Billerica, MA, USA.

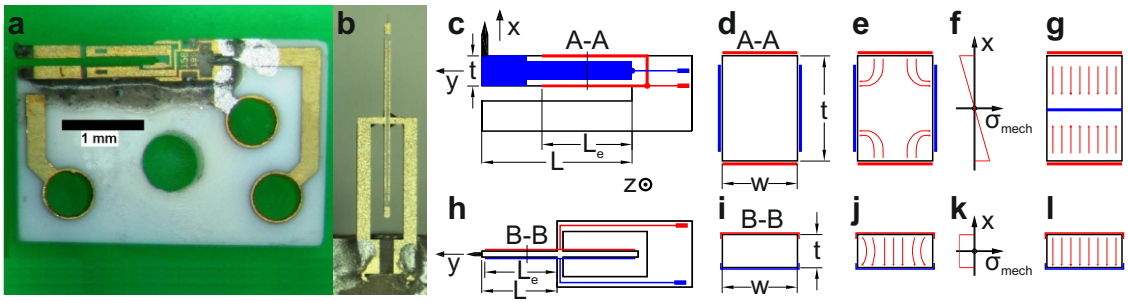

Figure 3.2.: Geometry of qPlus and needle sensors. **a**, one prong of a quartz tuning fork is fixed to an insulating substrate with electrically non-conductive epoxy and the tip is attached to the free prong. **b**, the base of the LER is also fixed to a support. A tiny tip is mounted on the non-encased prong. **c**,**d**,**h**,**i**, geometrical dimensions of qPlus and needle sensors as listed in Tab. 3.1. **e**,**j**, schematic view of the electrostatic field distribution in the cross section of each prong. **f**,**k**, mechanical stress profile along cross sections indicated in **c** and **h**. **g**,**l**, idealized field distribution within the quartz resonators. Figure adapted from [70].

geometries and electrode configurations of qPlus and needle sensors are outlined in Figs. 3.2c,d and Figs. 3.2h,i. The values for length L, thickness t, width w, and electrode length L_e are summarized in Tab. 3.1.

Two important parameters of a force sensor in FM-AFM are the resonance frequency and the geometrical stiffness k' of the oscillating beams. For the bending mode of the qPlus sensor the stiffness k' is given by [33]

$$k' = k = \frac{Ewt^3}{4L^3}, \tag{3.2}$$

where $E = 78.6\,\mathrm{GPa}$ is the Young modulus of quartz [88, 89]. The fundamental resonance frequency f_0 is given as [33]

$$f_0 = 0.162\frac{t}{L^2}v_s, \tag{3.3}$$

where $v_s = \sqrt{E/\rho}$ and $\rho = 2650\,\mathrm{kg/m^3}$ are the velocity of sound and the mass density of quartz [88]. For the extensional mode of the needle sensor the stiffness k' of each beam is given by

$$k' = \frac{k}{2} = \frac{Ewt}{L} \tag{3.4}$$

and the resonance frequency is [70]

$$f_0 = \frac{v_s}{4L}. \tag{3.5}$$

The charges generated by the quartz resonators are directly proportional to the

deflection of the prongs. When the prong is bent or elongated strain ϵ is generated which leads to a mechanical stress σ_{mech}. The piezoelectric effect then causes the emergence of a surface charge density σ_{el} given by

$$\sigma_{\mathrm{el}} = d_{12}\sigma_{\mathrm{mech}}, \tag{3.6}$$

where $d_{12} = 2.31\,\mathrm{pm/V}$ [88] is the transverse piezoelectric coupling coefficient of quartz which is equal to the longitudinal coupling coefficient d_{11}.[5] It is important to note that d_{12} is almost constant from 1.5 K up to room temperature [88]. Integrating the surface charge density over the electrode area gives the total charge q_{el} generated by a given deflection with amplitude A and the sensitivity is then defined as $S = q_{\mathrm{el}}/A$ [70]. The above discussion assumes a homogeneous distribution of the electric field within the quartz crystal as depicted in Figs. 3.2g,l. Actually, the field distribution looks more like that drawn in Figs. 3.2e,j. Especially for the qPlus sensor the deviation is expected to be quite large. The dissimilar operation modes and the resulting difference in the strain profiles (Figs. 3.2f,k) results in different formulas for the theoretical sensitivity of qPlus and needle sensors. For a qPlus sensor the following expression was derived [18]:

$$S^{\mathrm{theo}}_{\mathrm{qPlus}} = 12 d_{12} k' \frac{L_e(L - L_e/2)}{t^2}. \tag{3.7}$$

With the dimensions listed in Tab. 3.1 a standard qPlus sensor yields $S^{\mathrm{theo}}_{\mathrm{qPlus}} = 2.79\,\mu\mathrm{C/m}$. The experimental sensitivity is expected to deviate from that value due to the non-ideal electric field distribution [70]. The influence of the electrode configuration was studied by Welker *et al.* [90, 91]. Here, a geometry factor g was introduced to account for this deviation. It was determined to $g = 0.52$ by measuring the deflection of the beam with an optical microscope in a stroboscope setup. This gives an actual sensitivity of $S_{\mathrm{qPlus}} = 1.46\,\mu\mathrm{C/m}$. Note, the error in the stroboscope setup is mainly determined by the accuracy of the optical deflection measurement which is estimated to about $\pm 5\%$.[6]

For the needle sensor the sensitivity is given by [70]

$$S^{\mathrm{theo}}_{\mathrm{LER}} = 2 d_{12} k' \frac{L}{t} \sin\left(\frac{\pi L_e}{2L}\right). \tag{3.8}$$

With the values from Tab. 3.1 the theoretical sensitivity of a needle sensor is determined

[5] Actually, $d_{11} = -d_{12}$ is negative for right-handed quartz [86], but because the prongs oscillate the sign of the generated charge changes periodically and is neglected for the following discussion.

[6] The measured deflections are in the order of 10 µm and the optical resolution limit is around 0.5µm, resulting in a relative error of 5 %.

to $S_{\mathrm{LER}}^{\mathrm{theo}} = 45.0\,\mu\mathrm{C/m}$. The experimental sensitivity is expected to be quite similar to the theoretical one as the deviation from the ideal field distribution is small for the needle geometry (Figs. 3.2j,l).

3.2. Measurement of the Sensitivity of Quartz-Based Force Sensors

The theoretical sensitivity defined above is the intrinsic sensitivity of the self-sensing quartz resonator which refers to charge generated per deflection by the piezoelectric effect. In AFM the term sensitivity generally refers to the output signal per deflection of the cantilever. This is independent from the measurement method and is usually given in units of V/m. In this sense, the sensitivity is the calibration factor for the oscillation amplitude A. For the following discussion the intrinsic sensitivity is denoted as S_{C} and the calibration factor as S_{V}.

The oscillating beams generate a current which can be turned into a voltage output signal by a transimpedance amplifier or current-to-voltage converter (IVC, Fig. 3.3a). To obtain S_{V} the voltage output needs to be related to a given deflection. Therefore a reference amplitude is required. This can be achieved by measuring the output signal of the IVC without an external drive signal. Then the signal generated by the sensors due to random thermal excitation is measured. The equipartition theorem can then be employed to relate the voltage output signal to the thermally excited oscillation amplitude of the sensors. From there one can define the sensitivity S_{V} [18]. The validity of this method was confirmed in a temperature range from $140 - 300\,\mathrm{K}$ for quartz tuning forks and can be applied to qPlus and needle sensors in a similar way [90]. To justify the application of the equipartition theorem the excitation of the quartz sensors must be purely thermal. Therefore any spurious excitation of the sensors must be avoided. Mechanical vibrations from the environment can be an issue, in particular ultrasonic sound can easily excite the sensors. The qPlus design is generally more prone to unwanted excitations than coupled oscillators. Vibrations of the base cause a symmetric oscillation of the prongs, but coupled resonators oscillate in an anti-symmetric mode. Another issue is spurious electrical excitation. This can happen in the following way: An increased input capacitance C_{in} almost inevitably leads to an increase of the electrical noise floor at the output of an electronic amplifier. This is due to the input voltage noise density[7] of the operational amplifier which, together with C_{in}, leads to an increase in charge or, respectively, current noise density

[7]For low noise amplifiers this is typically in the order of $\mathrm{nV}/\sqrt{\mathrm{Hz}}$.

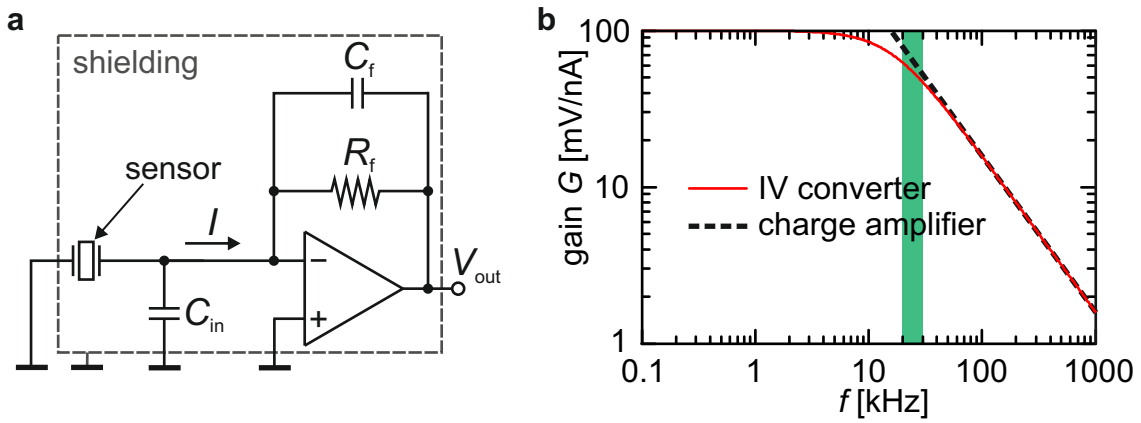

Figure 3.3.: Schematic setup to measure the thermal noise spectrum of a quartz sensor and transfer function of a current-to-voltage converter (IVC). **a**, the electrodes of the sensor are connected to ground and the IVC. Sensor and amplifier are placed in a grounded metal box for shielding. The output of the IVC is connected to a spectrum analyzer (not shown). **b**, ideal transfer function of an IVC with $R_f = 100\,\mathrm{M\Omega}$ and $C_f = 0.1\,\mathrm{pF}$ (solid red line), the input capacitance C_{in} is not taken into account. For frequencies $f \gg f_c$ (here, $f_c = 16\,\mathrm{kHz}$) the gain drops proportional to $1/f$. The green shaded region marks the typical operating range of qPlus sensors which is beyond f_c. The dashed black line corresponds to a constant charge gain of $10^{13}\,\mathrm{V/C}$ as realized by a commercial amplifier for a remarkably large frequency range from 250 Hz to 15 MHz.

at the input of the amplifier. The increased current noise density is transferred via the feedback resistance to a larger voltage noise at the output. If the amplifier is now connected to a self-sensing sensor there is another effect associated with this. The increased current noise at the input of the amplifier can serve as an electrical drive signal for the quartz resonator which might overwhelm the thermal white noise drive. This can be avoided by directly connecting the sensor to the amplifier. Then C_{in} is mainly determined by the static capacitance of the quartz sensor which is about 1 pF for both types.[8]

From the equipartion theorem the magnitude of the thermal oscillation amplitude of a qPlus sensor follows as [18]

$$\frac{1}{2}k\langle A_{th}^2\rangle = \frac{1}{2}k_B T \Longrightarrow A_{th}^{rms} = \sqrt{k_B T/k}. \tag{3.9}$$

With the definition of $k = 2k'$ for coupled oscillators Eq. (3.9) can also be used for tuning fork or needle sensors. At room temperature ($T = 296\,\mathrm{K}$) the thermal root mean square (rms) amplitude for a qPlus sensor is 1.5 pm and 62 fm for a needle

[8]Micro Crystal, DS-Series and CC4V-T1A data sheets for tuning forks and length extensional resonators, Micro Crystal, 2540 Grenchen, Switzerland.

sensor. The experimental sensitivity is then defined as

$$S_{\mathrm{V}} = \frac{V_{\mathrm{th}}^{\mathrm{rms}}}{A_{\mathrm{th}}^{\mathrm{rms}}}, \tag{3.10}$$

where $V_{\mathrm{th}}^{\mathrm{rms}}$ is the voltage output of the amplifier generated by thermal excitation of the quartz resonator. The thermal excitation signal is quite weak and it is not possible to measure $V_{\mathrm{th}}^{\mathrm{rms}}$ directly with a voltage meter. One can instead measure the power spectral density n_{V}^2 of the amplifier output with a spectrum analyzer. The total power spectral density n_{V}^2 contains the power spectral density n_{th}^2, which is due to thermal excitation of the quartz resonator, and n_{el}^2, which is the electrical noise density of the amplifier. The output voltage $V_{\mathrm{th}}^{\mathrm{rms}}$ is therefore given via the following relation [90]:

$$(V_{\mathrm{th}}^{\mathrm{rms}})^2 = \int_{f_0-B/2}^{f_0+B/2} n_{\mathrm{th}}^2(f)\mathrm{d}f = \int_{f_0-B/2}^{f_0+B/2} \left(n_{\mathrm{V}}^2(f) - n_{\mathrm{el}}^2\right)\mathrm{d}f. \tag{3.11}$$

Here, the electrical noise density n_{el} is assumed to be constant within the measurement bandwidth B. This is justified for bandwidths of $B \approx 400 - 800\,\mathrm{Hz}$ which are usually used for the thermal peak measurements. The combination of Eqs. (3.9)-(3.11) allows to determine the sensitivity S_{V}. This quantity depends on the amplifier and to relate S_{V} to S_{C} the charge gain in V/C needs to be determined from the transfer function of the amplifier.

The frequency response of an ideal IVC is given by

$$V_{\mathrm{out}} = -\frac{R_{\mathrm{f}} I}{1 + i2\pi f R_{\mathrm{f}} C_{\mathrm{f}}}, \tag{3.12}$$

where R_{f} is the feedback resistance and C_{f} its parasitic capacitance. The DC gain $G(f = 0) = |V_{\mathrm{out}}/I| = R_{\mathrm{f}}$ of the IVC is set by the feedback resistance. Its parasitic capacity C_{f} determines the frequency dependence of the gain to first order. The corner frequency f_{c} is given by $f_{\mathrm{c}} = 1/(2\pi R_{\mathrm{f}} C_{\mathrm{f}})$.[9] For frequencies f which are significantly smaller than the corner frequency f_c the gain is flat and it follows a low-pass behavior for higher frequencies. The output signal is given by $V_{\mathrm{out}} = -I/(i2\pi f C_{\mathrm{f}})$ for frequencies $f \gg f_{\mathrm{c}}$. The signal generated by the quartz is a sinusoidally varying charge $Q(t) = Q_0 \exp(i2\pi f t)$ corresponding to a current $I = \dot{Q} = Q_0 i2\pi f \exp(i2\pi f t)$. Thus, the gain can be expressed as $|V_{\mathrm{out}}/Q_0| = 1/C_{\mathrm{f}}$. Therefore such an amplifier is often called "charge amplifier" for frequencies significantly larger than f_{c}. Charges are not amplified but a voltage output proportional to the input charges is generated.

[9] At f_{c} the gain has dropped by $1/\sqrt{2}$ or $-3\,\mathrm{dB}$.

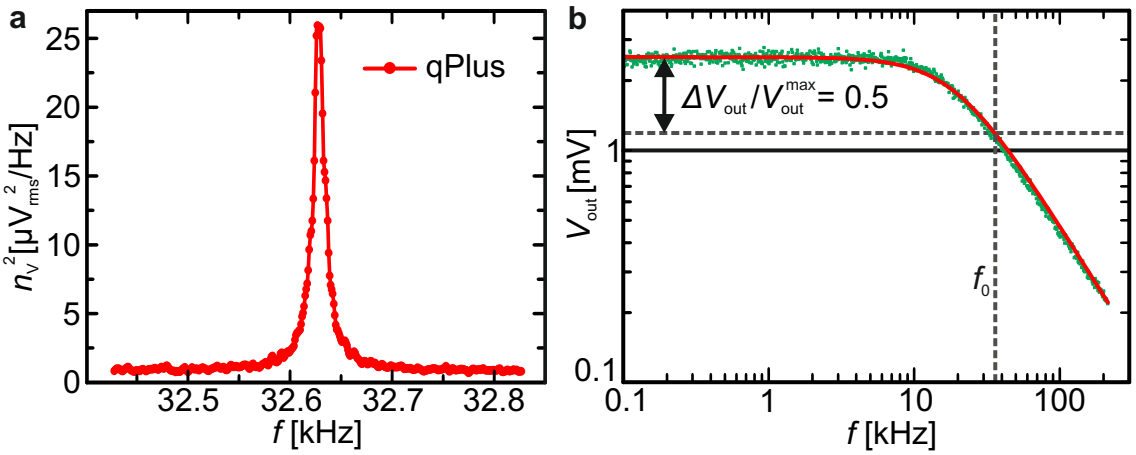

Figure 3.4.: Measurement of thermal excitation spectrum for a qPlus sensor and transfer function of the home-built IVC. **a**, squared voltage noise density of a standard qPlus sensor measured with the IVC at room temperature and ambient pressure. The bandwidth or measurement span of the spectrum analyzer is set to $B = 400\,\mathrm{Hz}$, the resolution is 1 Hz, the number of averages is 100, and n_V is measured in units of $\mathrm{V_{rms}}/\sqrt{\mathrm{Hz}}$. The electrical noise density is $n_{el} = 952\,\mathrm{nV_{rms}}/\sqrt{\mathrm{Hz}}$ and the sensitivity S_V is calculated to 15.0 μV/pm. **b**, transfer function of the OPA657 (green dots) measured with $R_{in} = 400\,\mathrm{k\Omega}$ and $R_f = 100\,\mathrm{M\Omega}$. The solid red line depicts a fit with a simple low-pass model. The parasitic capacitance $C_f = 84\,\mathrm{fF}$ and $f_c = 18.950\,\mathrm{kHz}$. The operating frequency of the qPlus sensor ($f_0 = 32.628\,\mathrm{kHz}$) is indicated by the vertical dashed line. From the intersection with the transfer function (horizontal dashed line) one can determine the effect of the finite gain. At f_0 the gain is reduced by a factor of 2.

Nevertheless, it is common to call an IVC in this regime a charge amplifier. If the parasitic capacitance C_f of the IVC is known the relation between input and output signal for $f \gg f_c$ could be determined straightforward. Figure 3.3b shows an ideal gain transfer function of an IVC with $R_f = 100\,\mathrm{M\Omega}$ and $C_f = 0.1\,\mathrm{pF}$. The dashed black line depicts the transfer function of a commercial charge amplifier with a constant charge gain of $10^{13}\,\mathrm{V/C}$ for the frequency range shown here.[10] In this example, the high frequency response of the IVC and the charge amplifier is similar. For frequencies between $5 - 50\,\mathrm{kHz}$ the gain of the IVC is neither determined by R_f or C_f solely, and for a proper determination of the gain the bandwidth reduction needs to be taken into account. In the following, two amplifiers are used to measure the output signal of the quartz sensors – a home-built IVC and the abovementioned commercial charge amplifier. The IVC is based on an OPA657[11] operational amplifier with a feedback resistance of $R_f = 100\,\mathrm{M\Omega}$ [92]. The amplifier is then mounted on an insulting ceramic

[10] HQA-15M-10T, High Frequency Charge Amplifier, Femto Messtechnik GmbH, 10179 Berlin, Germany.
[11] OPA657, 1.6GHz, Low-Noise, FET-Input Operational Amplifier, Texas Instruments, Dallas, Texas 75265, USA.

board[12] and $\pm 3\,\mathrm{V}$ batteries are used as supply voltage for the IVC. For additional filtering of the supply voltage 100 nF capacitors are connected parallel to the supply pins and ground as close as possible to the legs of the operational amplifier. The IVC is then placed close to the sensor to reduce C_{in}, and both are surrounded by a grounded metal box to avoid electromagnetic interference signals (Fig.3.3a). The output of the home-built IVC is connected to a spectrum analyzer[13] which has a frequency range from DC-102.4 kHz.

The result of such a measurement for a qPlus sensor with standard dimensions is shown in Fig. 3.4a. The sensitivity is determined from the area below the peak as $S_{\mathrm{V,qPlus}} = 15.0\,\mu\mathrm{V/pm}$. To related this to S_{C} the gain at the operating frequency of the sensor ($f_0 = 32.628\,\mathrm{kHz}$) must be figured out.

The transfer function of the IVC is measured by placing a SMD-type resistor ($R_{\mathrm{in}} = 400\,\mathrm{k\Omega}$) in series to the input of the IVC. The DC gain is then $R_{\mathrm{f}}/R_{\mathrm{in}} = 250$.[14] The thermally excited signal is very tiny, therefore the small signal transfer function of the IVC needs to be determined. The Nanonis OC4 was used to generate a small input signal with a constant amplitude of $10\,\mu\mathrm{V}$. The transfer function (Fig. 3.4b) is obtained by sweeping the input signal from $0.1 - 200\,\mathrm{kHz}$ and the output is also monitored with the OC4. At $f_0 = 32.628\,\mathrm{kHz}$, the gain is reduced by a factor of 2 ($G(f = f_0) = 0.50$). If one takes this into account, the sensitivity S_{C} is determined as

$$S^{\mathrm{OPA657}}_{\mathrm{C,qPlus}} = \frac{S_{\mathrm{V,qPlus}}}{2\pi f_0 R_{\mathrm{f}} G(f_0)} = \frac{15.0\,\mu\mathrm{V/pm}}{2\pi \cdot 32.628\,\mathrm{kHz} \cdot 100\,\mathrm{M\Omega} \cdot 0.50} = 1.46\,\mu\mathrm{C/m}.$$

The theoretical sensitivity from Eq. (3.7) is $S^{\mathrm{theo}}_{\mathrm{C,qPlus}} = 2.79\,\mu\mathrm{C/m}$ and when taking the independently determined geometry factor $g = 0.52$ into account one also obtains a value of $2.79\,\mu\mathrm{C/m} \cdot 0.52 = 1.46\,\mu\mathrm{C/m}$. This confirms that the above measured value for $S^{\mathrm{OPA657}}_{\mathrm{C,qPlus}}$ is indeed the intrinsic charge generated per deflection by a standard qPlus sensor.

The accuracy of the thermal peak method is determined by several factors. First of all, the uncertainty in the stiffness k of the sensor must be considered as it is used to determine the average thermally excited amplitude $A^{\mathrm{rms}}_{\mathrm{th}}$. The stiffness is usually determined from $k = (2\pi f_0)^2 \cdot m^*$ with $m^* = 0.24\,m = 0.24\,L\,w\,t\,\rho$. The main source of error is the determination of the dimensions of the beam which is estimated to be about $\pm 5\,\%$. The value of the feedback resistance $R_{\mathrm{f}} = 100\,\mathrm{M\Omega}$ was measured with a

[12] Al_2O_3 with a resistivity of $\rho \approx 10^{14}\,\Omega\mathrm{cm}$.
[13] Agilent 35670A, Dynamic Signal Analyzer, Agilent Technologies, Santa Clara, California, USA.
[14] The open loop gain of the OPA657 is 74 dB ≈ 5000. Therefore the gain has to be adjusted via the input resistance R, such that the DC gain is smaller than 5000.

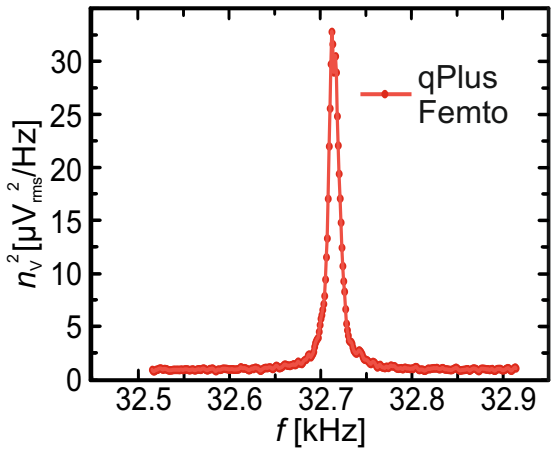

Figure 3.5.: Thermal spectrum measured with the commercial charge amplifier for another standard qPlus sensor ($f_0 = 32.715\,\mathrm{kHz}$). Here, only the sensor is placed in a grounded metal box and the charge amplifier is connected via a BNC feedthrough, see also Fig. 3.6a. The sensitivity $S_\mathrm{V} = 15.9\,\mu\mathrm{V/pm}$ is quite similar to the one obtained with the home-built IVC. With the specified gain of $10^{13}\,\mathrm{V/C}$ one can directly determine the intrinsic sensitivity $S^{\mathrm{HQA}}_{\mathrm{C,qPlus}} = 1.59\,\mu\mathrm{C/m}$.

digital multimeter[15] which has an accuracy of ±5%. Together with the uncertainty of the spectrum analyzer and the measurement of $G(f_0)$ this adds up to a relative error of around ±15 %.

The commercial charge amplifier (HQA) was also used to measure the thermal peak of another standard qPlus sensor. The result is shown in Fig. 3.5. The intrinsic sensitivity can be directly evaluated from the measured sensitivity via the given charge gain of the amplifier and one obtains $S^{\mathrm{HQA}}_{\mathrm{C,qPlus}} = 1.59\,\mu\mathrm{C/m}$. This is about 10 % higher than the value from above but within the experimental error. For this measurement the uncertainty of the stiffness k enters again plus the gain accuracy of the charge amplifier (±3%).

In principle, the measurement of the thermal excitation spectrum for needle sensors is now straightforward: Just replace the qPlus sensor by the needle sensor and use a spectrum analyzer with an appropriate frequency range. The latter was not available, therefore a lock-in amplifier with integrated Zoom FFT function was used.[16] The setup is depicted in Fig. 3.6a. The black curve in Fig. 3.6b shows the measured thermal excitation spectrum of a LER with resonance frequency $f_0 = 999.942\,\mathrm{kHz}$. For a quantitative analysis the downward bending of the curve and the sharp peak located at the center frequency ($f_\mathrm{center} = 1\,\mathrm{MHz}$) of the reference oscillator needs to be corrected. This was done in the following way: First, a reference spectrum was acquired at a

[15] MM47 digital multimeter, Martindale Electric Company Ltd., Watford, UK.
[16] Nanonis OC4 Oscillation Controller, Specs Zurich GmbH, 8005 Zurich, Switzerland.

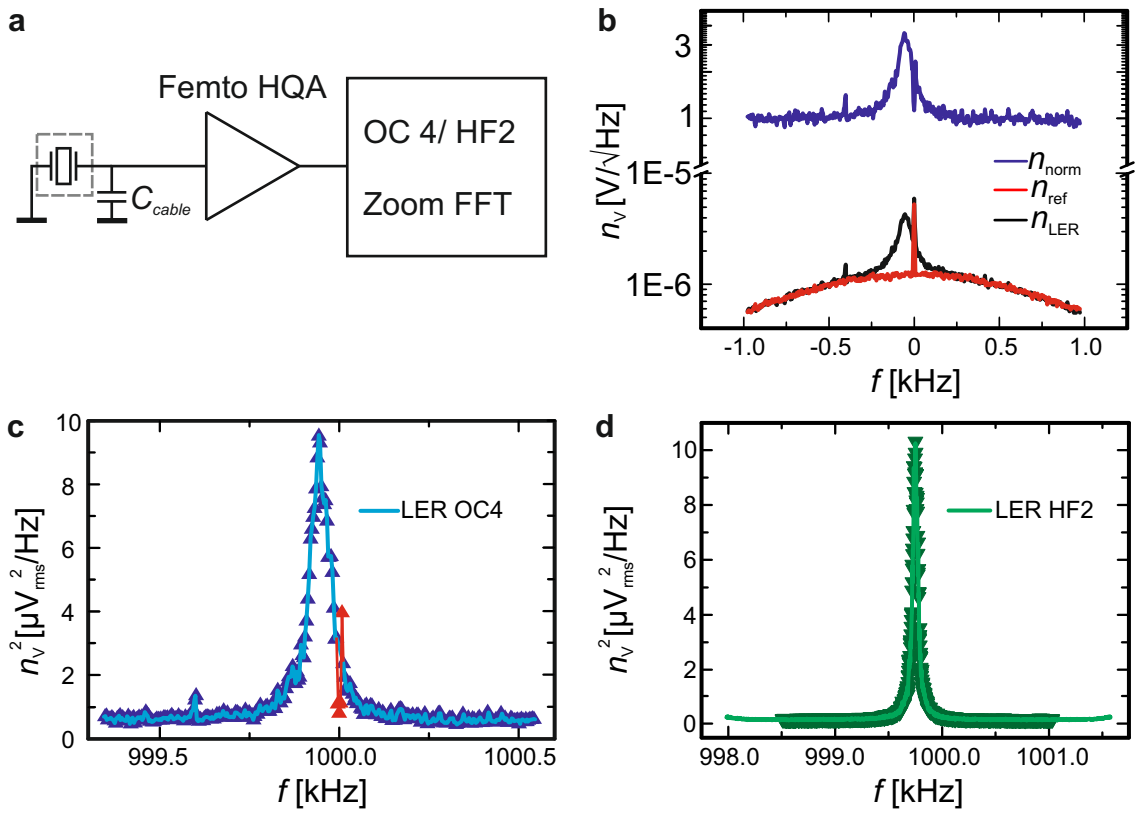

Figure 3.6.: Measurement of thermal excitation spectra for the needle sensor. **a**, the sensor is placed in a grounded metal box and connected via BNC plugs to the input of the Femto HQA amplifier. The power spectral density of the output signal is measured with the Zoom FFT feature of two commercial lock-ins. **b**, voltage noise density due to thermal excitation measured with the OC4 (black line); $B = 1950\,\mathrm{Hz}$ and $C_{\mathrm{in}} \approx 100\,\mathrm{pF}$ (1 m BNC cable). A reference spectrum (red line) 2 kHz aside from the resonance peak was acquired to correct for the artifacts due to digital filtering. The solid blue line indicates the normalized spectrum. **c**, squared voltage noise density for the needle sensor. The triangles marked in red are due to the imperfect compensation of the delta peak. The sensitivity is determined as $S_{\mathrm{V}}^{\mathrm{OC4}} = 455\,\mu\mathrm{V/pm}$. **d**, thermal peak of another needle sensor which was measured with the HF2 (solid green line); $B = 3.6\,\mathrm{kHz}$ and $C_{\mathrm{in}} \approx 10\,\mathrm{pF}$. The sensitivity is $S_{\mathrm{V}}^{\mathrm{HF2}} = 461\,\mu\mathrm{V/pm}$.

center frequency shifted by 2 kHz towards lower frequencies ($f_{\mathrm{center}}^{\mathrm{ref}} = 998.000\,\mathrm{kHz}$) (red curve in Fig. 3.6b). Assuming that the noise density of the amplifier is flat around 1 MHz one can create a normalized spectrum with a flat noise floor by dividing the thermal excitation spectrum through the reference spectrum ($n_{\mathrm{norm}} = n_{\mathrm{LER}}/n_{\mathrm{ref}}$). Now, the normalized spectrum n_{norm} must be multiplied with the average value of the noise density n_{V} aside form the delta peak in the reference curve in a region where the noise density is still flat.[17] For frequencies below 100 kHz the Zoom FFT shows the same values as the dedicated spectrum analyzer around the center frequency.

[17]Respectively, six data points left and right from the delta peak in the red curve were averaged.

Assuming the same consistency of the Zoom FFT at 1 MHz the value of the flat electrical noise density is $n_{\mathrm{el}} = 860\,\mathrm{nV_{rms}}/\sqrt{\mathrm{Hz}}$. Finally, the squared voltage noise density $n_{\mathrm{V}}^2 = (n_{\mathrm{norm}} n_{\mathrm{el}})^2$ is shown in Fig. 3.6c. The sensitivity $S_{\mathrm{V}}^{\mathrm{OC4}}$ is determined as described above and one obtains $S_{\mathrm{V}}^{\mathrm{OC4}} = 455\,\mu\mathrm{V/pm}$. With a charge gain of $10^{13}\,\mathrm{V/C}$ this corresponds to $S_{\mathrm{C,needle}}^{\mathrm{OC4}} = 45.5\,\mu\mathrm{C/m}$. The red marked triangles in Fig. 3.6c are not taken into account, because these data points are due to the insufficient cancellation of the delta peak. Note, even if one takes these points into account this would only change the end result by 1 %. This is far less than the overall error of the thermal excitation method of about ±15%. The value from above matches almost exactly the theoretical intrinsic sensitivity $S_{\mathrm{LER}}^{\mathrm{theo}} = 45.0\,\mu\mathrm{C/m}$ of a needle sensor as determined from Eq. (3.8).

To support these findings the same measurement was done after another commercial lock-in (HF2) became available.[18] Note, another needle sensor was used but it had the same dimensions as the one from above. The Zoom FFT function of the HF2 has an implemented filter correction and the output values were again compared with a dedicated spectrum analyzer at lower frequencies. The solid green curve in Fig. 3.6d shows the measured spectrum. The small upturn of the noise floor at the boundaries of the spectral range is only a minor artifact. It can be easily avoided by taking only the points which are marked by the green triangles into account. The sensitivity is determined as $S_{\mathrm{V}}^{\mathrm{HF2}} = 461\,\mu\mathrm{V/pm}$ and correspondingly, $S_{\mathrm{C,needle}}^{\mathrm{HF2}} = 46.1\,\mu\mathrm{C/m}$. The agreement with the calculated value within the experimental error is again very good. The electrical noise density is $n_{\mathrm{el}} = 322\,\mathrm{nV_{rms}}/\sqrt{\mathrm{Hz}}$. This is due to the smaller input capacitance compared to the measurement with the OC4. It is noteworthy that the commercial charge amplifier is quite insusceptible to input capacitance and the input charge noise density only increases from $40\,\mathrm{zC}/\sqrt{\mathrm{Hz}}$ with open input to $90\,\mathrm{zC}/\sqrt{\mathrm{Hz}}$ with 100 pF input capacitance.

In summary, we find a very good agreement for both sensors between calculated and measured sensitivity. For the thermal peak method it is crucial to characterize the electronic amplifiers precisely and to avoid any spurious excitations of the sensors. Although the needle sensor produces a larger signal than the qPlus at a given deflection, it is not necessarily better suited for high-resolution AFM. For a proper comparison noise needs to be taken into account. In the following, the noise sources which are inherent to FM-AFM will be introduced and their impact on the signal-to-noise ratio for quartz-based force sensors will be discussed.

[18] HF2LI Lock-in Amplifier, Zurich Instruments AG, 8005 Zurich, Switzerland.

3.3. Noise Contributions in FM-AFM

In FM-AFM an averaged force gradient is measured and the noise in this figure follows from Eq. (3.1) as

$$\delta k_{\mathrm{ts}} = 2k\frac{\delta\Delta f}{f_0}. \tag{3.13}$$

The accuracy of the measured force gradient depends on the relative error $\delta\Delta f/f_0$ in the frequency measurement. If the frequency could be measured with zero error one could measure infinitely small force gradients. In fact, there are four noise contributions limiting the accuracy of the frequency measurement. Other noise sources like mechanical vibrations from the environment, electrical noise from the piezo high voltages, or from the power lines (50 Hz hum) are also present. These noise sources are not unique to FM-AFM, but they exist in any scanning probe microscopy setup and are therefore not discussed in this context. The four noise contributions are: Deflection detector noise or also called noise in the displacement sensor, which scales with the measurement bandwidth B as $B^{3/2}$ [29]. Thermal noise and oscillator noise increase with the square root of B [29, 93]. The fourth contribution to the inaccuracy in the frequency measurement is the stability of the cantilever eigenfrequency f_0 with measurement time τ. It is mainly determined by the change of f_0 with temperature T. This effect is material dependent and we refer to this as thermal frequency drift.[19] In the following these noise contributions will be discussed in more detail.

3.3.1. Deflection Detector Noise

Frequency modulation refers to the modulation of a carrier frequency f_0 by a peak frequency deviation Δf at a rate or modulation frequency f_m [94]. In terms of FM-AFM the deviation Δf is the frequency shift and the acquisition time of the measurement is related to f_m – for high scan speeds the measured signal is modulated faster. To determine Δf, the cantilever deflection is measured. Independent from the measurement method (optical or electrical) which is used to read out the deflection, the output signal finally is a voltage output from an electronic amplifier like the IVC from the previous section. The noise density in the deflection measurement is then defined by the voltage noise density of the amplifier. To relate this voltage noise density to the uncertainty in the deflection measurement, one can use the sensitivity

[19] Note, this should not be confused with the usual thermal drift between tip and sample in scanning probe microscopes, which is caused by differences in the thermal expansion coefficients of the materials used to build the microscope.

S_V to define the so-called deflection noise density n_q as,

$$n_q = \frac{n_\mathrm{el}}{S_\mathrm{V}} = \frac{n_\mathrm{amp}}{S_\mathrm{C}}, \tag{3.14}$$

where n_el is the electrical or voltage noise density of the IVC. In terms of charge amplifiers, the charge noise density n_amp and the intrinsic charge sensitivity S_C can also be used to express n_q. The deflection noise density n_q $\left[\mathrm{m}/\sqrt{\mathrm{Hz}}\right]$ is a measure on how precise the cantilever deflection can be measured at a given bandwidth. Any uncertainty in the measurement of the deflection amplitude also involves an uncertainty in the phase, which translates into noise in the frequency measurement. The corresponding noise density is [29, 93–95]

$$n_{f_m} = \sqrt{2}\frac{n_q}{A} f_m. \tag{3.15}$$

The frequency error is obtained by integrating the squared noise density $n_{f_m}^2$ over the bandwidth B, similar to Eq. (3.11), leading to the following expression for the relative error in the frequency measurement:

$$\frac{\delta\Delta f^\mathrm{det}}{f_0} = \sqrt{\frac{2}{3}}\frac{n_q}{A f_0} B^{3/2} \tag{3.16}$$

and in terms of the force gradient one finds with Eq. (3.13):

$$\delta k_\mathrm{ts}^\mathrm{det} = \sqrt{\frac{8}{3}}\frac{k n_q}{f_0}\frac{B^{3/2}}{A} \propto \frac{k n_q}{f_0}. \tag{3.17}$$

One can now directly calculate explicit values for the contribution of the deflection detector noise to the force gradient noise. The values for k, f_0, and n_q of qPlus and needle sensors were determined in the previous section and are summarized in Tab. 3.2 for clarity. For the calculations the oscillation amplitude is always set to $A = 100\,\mathrm{pm}$. For the qPlus sensor the contribution of deflection detector noise is

$$\delta k_\mathrm{ts,qPlus}^\mathrm{det} = 57.2\,\mu\mathrm{N/m}\frac{B^{3/2}}{\mathrm{Hz}^{3/2}}, \tag{3.18}$$

and for the needle sensor it is

$$\delta k_\mathrm{ts,needle}^\mathrm{det} = 32.7\,\mu\mathrm{N/m}\frac{B^{3/2}}{\mathrm{Hz}^{3/2}}. \tag{3.19}$$

For a bandwidth $B = 100\,\mathrm{Hz}$ the uncertainty in the force gradient is thus 57.2 mN/m

	f_0 (kHz)	k (kN/m)	n_{el} ($\mathrm{V_{rms}}/\sqrt{\mathrm{Hz}}$)	S_{V} (μV/pm)	n_q ($\mathrm{fm_{rms}}/\sqrt{\mathrm{Hz}}$)
needle sensor	999.942	1 060	860	455	1.89
qPlus sensor	32.628	1.8	952	15.0	63.5

Table 3.2.: Parameters which are used to determine the influence of deflection detector noise on the force gradient noise for qPlus and needle sensor. For the needle sensor the n_q value obtained with 100 pF input capacitance is used to account for cable capacitance, because in a microscope setup the commercial amplifier cannot be placed close to the sensor like the home-built IVC.

for the qPlus sensor and 32.7 mN/m for the needle sensor. The needle sensor shows about a factor of 2 less deflection detector noise. This is due to the excellent adaption of the commercial charge amplifier to the needle sensor. At low temperatures the home-built IVC can be cooled and n_q reduces by about a factor of 2, resulting in a similar deflection detector noise as the needle sensor [96]. Deflection detector noise increases dramatically with bandwidth B. Therefore it can be reduced by bandwidth reduction. This is only possible if thermal drift and piezo creep of the microscope are sufficiently small to allow slow scanning speeds, e.g. at low temperatures.

3.3.2. Thermal Noise

Random thermal excitations from the environment affect the oscillation of the cantilever and lead to an uncertainty in the frequency measurement given by [29]:

$$\frac{\delta\Delta f^{\mathrm{thermal}}}{f_0} = \sqrt{\frac{k_B T B}{\pi k A^2 f_0 Q}}, \tag{3.20}$$

and in terms of the force gradient

$$\delta k_{\mathrm{ts}}^{\mathrm{thermal}} = \sqrt{\frac{4 k k_B T B}{\pi A^2 f_0 Q}} \propto \sqrt{\frac{k}{f_0 Q}}. \tag{3.21}$$

This contribution decreases with decreasing temperature T and increasing quality factor Q. For the needle sensor typical Q values at room temperature in UHV are about 50000 and 80000 at 4 K [83, 84]. For the qPlus sensor, $Q \approx 3000$ at room temperature and typical values at 4 K are about $200000 - 400000$ [20, 97]. Thus, the contribution of thermal noise to the force gradient noise at $T = 300\,\mathrm{K}$ is $\delta k_{\mathrm{ts,needle}}^{\mathrm{thermal}} = 3.3\,\mathrm{mN/m}$ per $\sqrt{\mathrm{Hz}}$ for the needle ($Q = 50000$) and $\delta k_{\mathrm{ts,qPlus}}^{\mathrm{thermal}} = 3.1\,\mathrm{mN/m}$ per $\sqrt{\mathrm{Hz}}$ for the qPlus sensor. At $T = 4\,\mathrm{K}$ the force gradient noise is $\delta k_{\mathrm{ts,needle}}^{\mathrm{thermal}} = 305\,\mu\mathrm{N/m}$ per $\sqrt{\mathrm{Hz}}$ for the

needle sensor and $\delta k_{\mathrm{ts,qPlus}}^{\mathrm{thermal}} = 44\,\mu\mathrm{N/m}$ per $\sqrt{\mathrm{Hz}}$ for a qPlus sensor with $Q = 200000$. The calculations refer again to $A = 100\,\mathrm{pm}$. In a UHV environment the contributions of both sensors are similar at room temperature, because the Q factor of the needle sensor is significantly larger in UHV than in ambient air (≈ 18000 vs. ≈ 50000). The qPlus sensor shows less thermal noise at low temperatures.

3.3.3. Oscillator Noise

The presence of noise in the oscillation controller which can affect the frequency detection was already recognized by Albrecht *et al.* in their early work [29]. Kobayashi *et al.* discussed the effect of a noisy drive signal (due to finite n_q) on the cantilever deflection. If the cantilever is excited slightly off resonance by a noisy drive signal, this leads to an uncertainty in the phase which translates into the frequency measurement [93]. Obviously, high Q cantilevers are less affected by such a process and this so-called oscillator noise is given as [93]

$$\frac{\delta\Delta f^{\mathrm{osc}}}{f_0} = \frac{n_q}{\sqrt{2}AQ}\sqrt{B}, \tag{3.22}$$

and in terms of the force gradient

$$\delta k_{\mathrm{ts}}^{\mathrm{osc}} = \sqrt{2}\frac{kn_q}{AQ}\sqrt{B} \propto \frac{kn_q}{Q}. \tag{3.23}$$

For the values given above and $A = 100\,\mathrm{pm}$ one finds room temperature values of $\delta k_{\mathrm{ts,needle}}^{\mathrm{osc}} = 0.57\,\mathrm{mN/m}$ per $\sqrt{\mathrm{Hz}}$ for the needle and $\delta k_{\mathrm{ts,qPlus}}^{\mathrm{osc}} = 0.54\,\mathrm{mN/m}$ per $\sqrt{\mathrm{Hz}}$ for the qPlus sensor. At $T = 4\,\mathrm{K}$, the contribution to the force gradient noise is $\delta k_{\mathrm{ts,needle}}^{\mathrm{osc}} = 354\,\mu\mathrm{N/m}$ per $\sqrt{\mathrm{Hz}}$ for the needle sensor and $\delta k_{\mathrm{ts,qPlus}}^{\mathrm{osc}} = 8.08\,\mu\mathrm{N/m}$ per $\sqrt{\mathrm{Hz}}$ for a qPlus sensor. Oscillator noise is usually already negligible at room temperature compared to thermal noise for quartz-based force sensors. At low temperatures Q increases and oscillator noise becomes even smaller. However, in a low Q environment like in liquids oscillator noise can become the dominating noise source [93].

3.3.4. Thermal Frequency Drift Noise

There are a lot of effects which influence the stability of the frequency of an oscillator, e.g. temperature fluctuations, acceleration due to mechanical shock or vibrations, ambient pressure, and long-term aging [98]. In FM-AFM, especially in a UHV environment, most of them can be neglected because an efficient vibration isolation system is anyway mandatory for an AFM setup. Long-term aging effects in quartz resonators are

also negligible, as they are on the order of a few ppm/year.[20] Temperature fluctuations or temperature drifts cause a change of the eigenfrequency of the resonators. This effect is material dependent. The relative frequency variation with temperature for silicon cantilevers is fairly linear around room temperature with a value of $-35\,\mathrm{ppm/K}$ (estimated from Fig. 2 in Ref. [99]). In contrast, quartz tuning forks and length extensional resonators show a quadratic frequency shift with temperature resembling an inverted parabola centered around the *turnover temperature* T_p [87]:

$$\frac{\delta\Delta f^{\mathrm{drift}}}{f_0} = -\chi(T - T_p)^2, \tag{3.24}$$

where $\chi = 35 \times 10^{-9}/\mathrm{K}^2$.[20] To obtain a frequency change of 35 ppm, like a silicon cantilever upon a temperature change of 1 K at room temperature, the temperature of a quartz resonator must change by about $\pm 32\,\mathrm{K}$ around T_p. The turnover temperature can be adjusted by the orientation of the crystal cut [85, 87]. Quartz tuning forks are often used in wrist watches and therefore T_p is usually set to $(25 \pm 5)\,^{\circ}\mathrm{C}$ and for LERs to $(39 \pm 5)\,^{\circ}\mathrm{C}$, because these are often used in printed circuit boards with higher operating temperatures. In this work, tuning forks, qPlus sensors, and needle sensors with a turnover temperature around 298 K were used to exclude any influence of the crystal cut. The thermal frequency drift leads to a noise contribution to the force gradient given by

$$\delta k_{\mathrm{ts}}^{\mathrm{drift}} = -2k\chi(T - T_p)^2. \tag{3.25}$$

This noise contribution solely scales with the effective stiffness k of the sensor and is therefore about a factor of 600 higher for the needle sensor than for a qPlus sensor.

A linear drift of the temperature T with time t results in a change of the frequency with time and the corresponding drift rate r is then

$$r = \frac{\partial(\delta\Delta f^{\mathrm{drift}})}{\partial t} = \frac{\partial(\delta\Delta f^{\mathrm{drift}})}{\partial T}\frac{\partial T}{\partial t} = -2f_0\chi(T - T_p)\frac{\partial T}{\partial t}, \tag{3.26}$$

and in terms of the force gradient

$$\frac{\partial(\delta k_{\mathrm{ts}}^{\mathrm{drift}})}{\partial t} = -4k\chi(T - T_p)\frac{\partial T}{\partial t}. \tag{3.27}$$

The time dependence of $\delta f(t) = r \times t$ can be expressed as a Fourier series. Interpreting the Fourier coefficients as the equivalent power components allows to derive the following expression for the power spectral density of a linear temperature, or

[20] MicroCrystal Product Brochure, MicroCrystal AG, 2540 Grenchen, Switzerland.

respectively frequency drift with time t [70]:

$$\left(n_{\Delta f}^{\text{drift}}(f_m)\right)^2 = \frac{r^2\tau}{\pi^2 f_m^2} \tag{3.28}$$

where r is the drift rate in Hz/s and τ the measurement time interval. Consequently, a linear frequency drift leads to a $1/f_m$ noise contribution in the frequency spectral density of the PLL output. The noise in the force gradient is obtained by multiplying Eq. (3.28) with $2k/f_0$. As the drift rate r is proportional to f_0 (Eq. 3.26), only the dependence on k is left.

So far, temperature variations were only discussed at room temperature where Eq. (3.24) is valid. The frequency variation for quartz tuning forks was measured by Hembacher *et al.* from room temperature down to liquid Helium temperatures where another minimum was observed. The overall frequency change was $-1620\,\text{ppm}$ [96]. For the needle sensor, An *et al.* found a similar frequency change of $-1755\,\text{ppm}$ for the same temperature range (estimated from Fig. 3 in Ref. [84]). This confirms that the relative frequency change is material dependent and mainly depends on the change in the velocity of sound of quartz with temperature [100]. From these measurements it is not possible to assess the influence of thermal frequency drift at low temperatures. Therefore precision measurements of the frequency variation with temperature from $4.8 - 48\,\text{K}$ were performed for various kinds of quartz sensors. The results of these will be presented and discussed in section 3.5.

3.3.5. Noise at the Frequency Demodulator Output

When the sensors are excited and oscillate at a constant amplitude one can observe the noise contributions discussed above at the output of the frequency demodulator. Actually, performing a fast Fourier transform (FFT) [101] of the frequency demodulator output signal (Δf) gives a frequency spectral density in units of $\text{Hz}/\sqrt{\text{Hz}}$. For comparison it is more instructive to look at the force gradient noise density where the scaling factor is again $2k/f_0$. The absolute force gradient noise terms from above are transformed into noise densities via

$$n_{k_{\text{ts}}}(f_m) = \sqrt{\left.\frac{\partial \delta k_{\text{ts}}^2}{\partial B}\right|_{B=f_m}}. \tag{3.29}$$

Then one finds for the detector noise contribution from Eq. (3.17):

$$n_{k_{\text{ts}}}^{\text{det}}(f_m) = \sqrt{2}\frac{2k}{f_0}\frac{n_q}{A} f_m. \tag{3.30}$$

For the thermal noise contribution from Eq. (3.21):

$$n_{k_{\mathrm{ts}}}^{\mathrm{thermal}} = \sqrt{\frac{4kk_BT}{\pi A^2 f_0 Q}}. \tag{3.31}$$

For the oscillator noise contribution from Eq. (3.23):

$$n_{k_{\mathrm{ts}}}^{\mathrm{osc}} = \sqrt{2}\frac{kn_q}{QA}. \tag{3.32}$$

The force gradient noise density including the above noise terms is then given by

$$n_{k_{\mathrm{ts}}}^{\mathrm{det}}(f_m) = \sqrt{\left(n_{k_{\mathrm{ts}}}^{\mathrm{det}}(f_m)\right)^2 + \left(n_{k_{\mathrm{ts}}}^{\mathrm{thermal}}\right)^2 + \left(n_{k_{\mathrm{ts}}}^{\mathrm{osc}}\right)^2}. \tag{3.33}$$

The parameters f_0 and Q for qPlus and needle sensors are determined from a frequency versus amplitude curve obtained by sweeping the frequency of the excitation signal at a constant drive amplitude. The values of k and n_q are already known from above. Table 3.3 summarizes the parameters and the force gradient noise contributions used to calculate the solid curves in Fig 3.7a,b. It is important to note that the parameters used for the calculated curves were determined independently and that no free parameters exist.

To compare these calculated noise densities to experimental ones, the qPlus and needle sensor from the previous section were excited electrically at room temperature and ambient pressure. The sensitivity S_{V} is used for both sensors as a calibration factor of the oscillation amplitude A. This allows then to operate each sensor at an amplitude of $A = 100\,\mathrm{pm}$ which enables a straightforward comparison of the force gradient spectral noise densities. Note, for the qPlus sensor the home-built IVC was used whereas for the needle sensor the commercial charge amplifier was employed.

	f_0 (kHz)	k $\left(\frac{\mathrm{kN}}{\mathrm{m}}\right)$	Q	n_q $\left(\frac{\mathrm{fm_{rms}}}{\sqrt{\mathrm{Hz}}}\right)$	$n_{k_{\mathrm{ts}}}^{\mathrm{det}}/f_m$ $\left(\frac{\mu\mathrm{N/m}}{\mathrm{Hz}^{3/2}}\right)$	$n_{k_{\mathrm{ts}}}^{\mathrm{thermal}}$ $\left(\frac{\mu\mathrm{N/m}}{\sqrt{\mathrm{Hz}}}\right)$	$n_{k_{\mathrm{ts}}}^{\mathrm{osc}}$ $\left(\frac{\mu\mathrm{N/m}}{\sqrt{\mathrm{Hz}}}\right)$
needle sensor	999.923	1,060	18470	1.89	56	5500	1530
qPlus sensor	32.628	1.8	2900	63.5	99	3170	560

Table 3.3.: Sensor parameters f_0, k, Q, and n_q at room temperature and ambient pressure used to calculate the contributions of deflection detector, thermal, and oscillator noise to the total force gradient noise density according to Eq. (3.33). The amplitude is fixed to $A = 100\,\mathrm{pm}$.

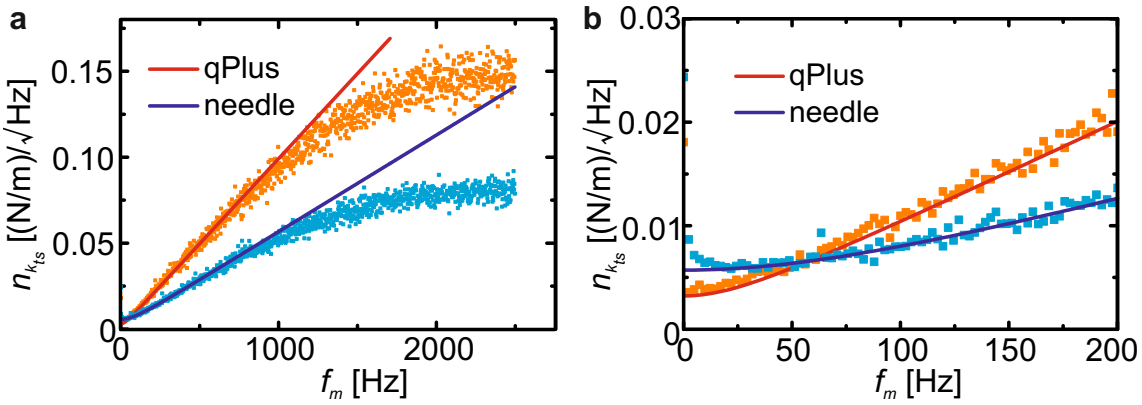

Figure 3.7.: Measured and calculated force gradient spectral densities. **a**, total experimental force gradient noise densities for qPlus (orange squares) and needle (light blue squares) sensor for $f_m = 0 - 2.5\,\text{kHz}$. **b**, frequency range from $0 - 200\,\text{Hz}$. For $f_m < 10\,\text{Hz}$ there is an upturn in the noise density for the needle sensor which might be attributed to a $1/f_m$ component caused by thermal frequency drift. PLL settings – phase and amplitude demodulation bandwidth: $B_\varphi = 1.3\,\text{kHz}$, $B_A = 50\,\text{Hz}$, lock-in cut off frequency $f_c = 6.22\,\text{kHz}$. FFT settings: sampling rate 5 kHz, span 2.5 kHz, bins 1024, resolution 2.44 Hz, averaging type: rms linear, number of averages: 100. The data in **b** is presented in Fig. 13 in Ref. [70].

As the commercial amplifier cannot be placed *in-situ*, a 1 m BNC cable ($C_{\text{in}} \approx 100\,\text{pF}$) was used to connect the needle sensor to mimic the additional cable capacitance of an AFM setup. Figure 3.7 shows the calculated (solid lines) and experimental (squares) force gradient spectral densities $n_{k_{\text{ts}}}(f_m)$. The spectral densities were measured with the spectrum analyzer feature of the Nanonis control electronics and cross checked with the spectrum analyzer from Agilent. In Fig. 3.7a the force gradient noise density as measured from the demodulator output of the Nanonis Oscillation Controller OC4 is shown from $0 - 2.5\,\text{kHz}$. The calculated noise densities are based on experimental values for f_0, k, Q, and n_q. The calculated curves start to deviate from the measured ones at around 1 kHz. This is due to the low-pass effect of the frequency or rather phase demodulator whose bandwidth was set to 1.3 kHz. Overall, the agreement between the calculated solid curves and the experimental data is very good. The solid curves include the contributions from deflection detector, thermal, and oscillator noise.

As expected, the needle sensor shows less deflection detector noise and the qPlus sensor shows less thermal, oscillator, and thermal frequency drift noise.

3.4. Optimization of Quartz-Based Force Sensors

The reduction of noise in measurements is always desirable and a fundamental goal of experimental physicists. In this section the noise contributions from above, Eqs. (3.17),(3.21),(3.23), and (3.25), are discussed for self-sensing sensors like qPlus and needle sensors. The main part of this section is devoted to the discussion about reducing deflection detector noise.

3.4.1. Decreasing Deflection Detector Noise

By combining Eq. (3.14) and Eq. (3.17) one can write,

$$\delta k_{\mathrm{ts}}^{\mathrm{det}} = \sqrt{\frac{8}{3}} \frac{n_{\mathrm{amp}}}{S_{\mathrm{C}}} \frac{k}{f_0} \frac{B^{3/2}}{A}. \tag{3.34}$$

This equation connects the noise to the physical parameters sensitivity S_{C}, stiffness k, and resonance frequency f_0. These three parameters all depend on the dimensions of the oscillating beams and it is therefore instructive to replace them by the corresponding equations. For the sensitivity the ideal situation of $L = L_e$ is assumed for simplicity. Then the theoretical sensitivity of a qPlus sensor from Eq. (3.7) is $S_{\mathrm{qPlus}} = 6 d_{12} k' L^2 / t^2$. With the equations for k (Eq. (3.2)), f_0 (Eq. (3.3)) and $k = k'$ one obtains for the detector noise contribution of a qPlus sensor:

$$\delta k_{\mathrm{ts}}^{\mathrm{det}} = 2.06 \sqrt{\frac{2}{3}} \frac{n_{\mathrm{amp}} t}{d_{12} v_s} \frac{B^{3/2}}{A}. \tag{3.35}$$

For the needle sensor one finds

$$\delta k_{\mathrm{ts}}^{\mathrm{det}} = 8 \sqrt{\frac{2}{3}} \frac{n_{\mathrm{amp}} t}{d_{12} v_s} \frac{B^{3/2}}{A}, \tag{3.36}$$

with $S_{\mathrm{needle}} = 2 d_{12} k' L / t$ and Eqs. ((3.4),(3.5)) and $k = 2k'$. As d_{12} and v_s are material constants the deflection detector noise depends only on the thickness t of the prongs for fixed n_{amp}. To compare the two equations the overestimate in the theoretical sensitivity of the qPlus sensor of about a factor of 2 needs to be taken into account. Then, a qPlus sensor with similar thickness as a needle sensor yields only about half the deflection detector noise than a needle sensor. This is due to the different operating modes and the resulting difference in the stress and strain profile. For the needle sensor it is uniform, but for the bending mode of the qPlus it is zero in the center and has its maximum value at the charge-collecting electrodes (Fig.

3.2f,k). Miniaturization is therefore a way to improve the performance of quartz-based sensors. The thickness of the needle sensor is already quite small and the electric field distribution is almost ideal. The difference in the thickness between the needle sensor (70 µm) and the standard qPlus sensor (214 µm) is the reason why the needle sensor showed less deflection detector noise in the previous section. There are two things which can be done to improve the standard qPlus sensor: First, the reduction of the beam thickness and second, the optimization of the electric field distribution by changing the electrode design. Thickness reduction results in a smaller stiffness and resonance frequency, which is not desirable. The road to success is therefore to reduce both L and t to keep k in the optimal range of a few kN/m and to increase f_0 at the same time.

Quartz tuning forks are commercially also available in miniature versions. Figure 3.8a shows a quartz tuning fork[21] with smaller dimensions and a standard quartz tuning fork[22] for direct comparison. This miniature tuning fork has the same geometry as a standard tuning fork apart from the etched grooves at the top and bottom (not visible) of the prongs. The electric field distribution is therefore closer to the ideal case. The stiffness can be calculated with Eq. (3.2) from the dimensions and $k \approx 740\,\mathrm{N/m}$. This is just a rough estimate of the stiffness as the grooves were not taken into account. The resonance frequency is $f_0 \approx 32.7\,\mathrm{kHz}$. In Fig. 3.8b another commercially available tuning fork[23] with different geometry is shown. At the end of the tapered beam is a larger mass to keep the resonance frequency around 33 kHz. The corresponding stiffness cannot be calculated straightforward, because the varying areal moment of inerta has to be taken into account. With an analytic approach the stiffness was determined to $k \approx 1280\,\mathrm{N/m}$ [102]. This was confirmed by finite element analysis methods [103]. The resonance frequency is $f_0 \approx 32.9\,\mathrm{kHz}$. With this type of sensor atomic resolution in ambient conditions was achieved [104]. A drawback of these two sensors is the smaller stiffness compared to the standard qPlus sensor. This can become a problem when the tip-sample interaction gets strong.

These commercial tuning forks still have the same operating frequency than standard qPlus sensors, but as pointed out above sensors with higher resonance frequencies are desirable. While one can easily shorten any tuning fork to increase the resonance frequency, this increases also the stiffness at the same time for rectangular beam cross sections. As f_0 scales with $1/L^2$ and k with $1/L^3$ the force gradient noise ($\sim k/f_0$) even increases if the beams of a tuning fork are simply shortened. Therefore custom-

[21] Statek Ultra-Miniature Crystal, CX9VSM, Statek Corporation, Orange, CA, USA.
[22] Micro Crystal, DS-26 series, Micro Crystal AG, 2540 Grenchen, Switzerland.
[23] Micro Crystal, CC7V-T1A, Micro Crystal AG, 2540 Grenchen, Switzerland.

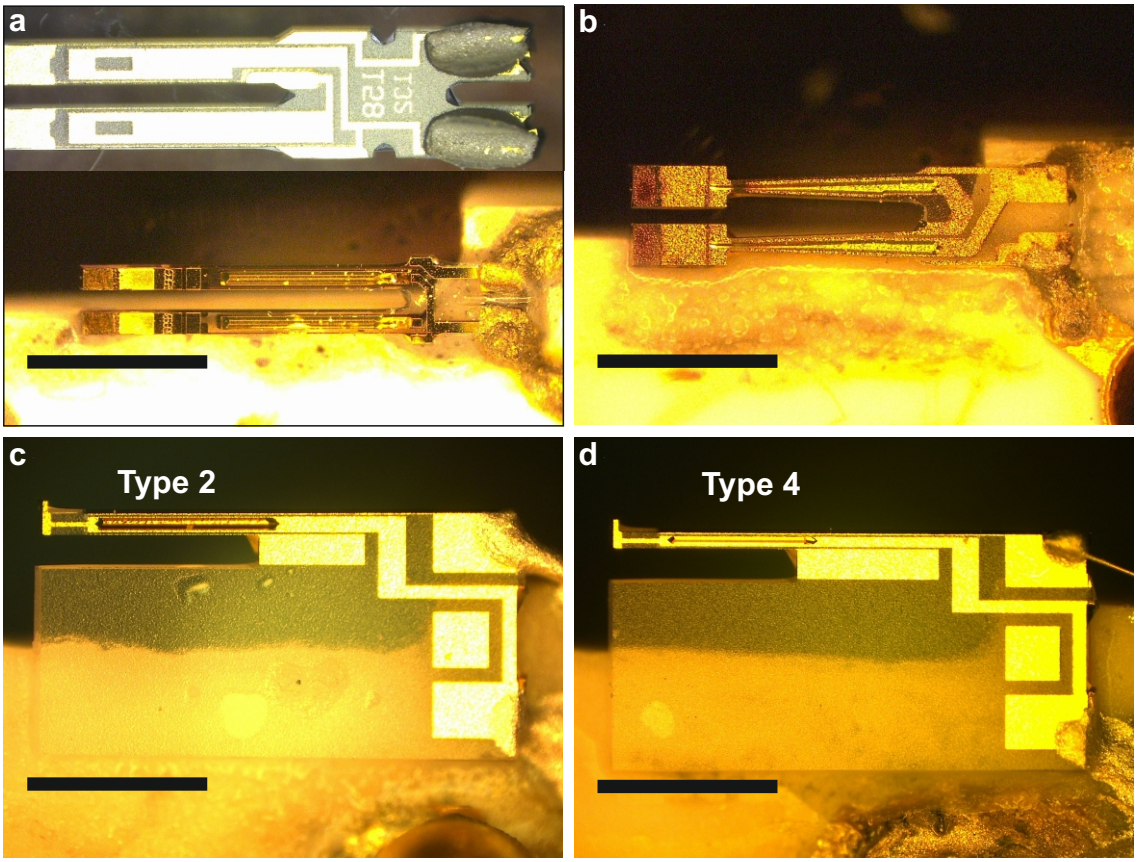

Figure 3.8.: **a**, standard quartz tuning fork (top) and a miniature version of a quartz tuning fork (bottom) with dimensions $L = 1750\,\mu\text{m}$, $t = 117\,\mu\text{m}$, and $w = 130\,\mu\text{m}$. **b**, quartz tuning fork with a different geometry. The length $L = 1500\,\mu\text{m}$ and the thickness at the free end of the prongs is $t = 214\,\mu\text{m}$. **c,d**, the customized quartz resonators consist only of a single prong and a larger base. The dimensions are $L = 1190\,\mu\text{m}$, $t = 116\,\mu\text{m}$, and $w = 145\,\mu\text{m}$ for **c**, and $L = 992\,\mu\text{m}$, $t = 85\,\mu\text{m}$, and $w = 145\,\mu\text{m}$ for **d**. All sensors have etched grooves on the upper and lower side of the prongs to optimize the electric field distribution. The scale bars in all images correspond to 1 mm.

designed quartz resonators were ordered.[24] Two of them are shown in Fig. 3.8c (type 2) and Fig. 3.8d (type 4). These sensors consist only of a single prong and a larger base. A small appendix at the end of the prongs serves for better accommodation of tips. The stiffness of these sensors was determined in two ways: First, by measuring the resonance frequencies f_0 of the sensors at room temperature and calculate k from $k = (2\pi f_0)^2(m^* + m_{\text{app}})$, where m^* is the effective mass of the beam and m_{app} the mass of the appendix at the end of the prong. The masses are calculated via $m = \rho V$, where ρ is the mass density of quartz. The volume V is determined by measuring the dimensions of the beams with an optical microscope.[25] By taking

[24]Micro Crystal AG, 2540 Grenchen, Switzerland.
[25]Keyence VHX-600 Digital Microscope, Keyence Deutschland GmbH, 63263 Neu-Isenburg, Germany.

	L (µm)	L_e (µm)	t (µm)	w (µm)	f_0 (kHz)	k $\left(\frac{\mathrm{N}}{\mathrm{m}}\right)$	S_V $\left(\frac{\mu\mathrm{V}}{\mathrm{pm}}\right)$	n_q $\left(\frac{\mathrm{fm_{rms}}}{\sqrt{\mathrm{Hz}}}\right)$	S_C $\left(\frac{\mu\mathrm{C}}{\mathrm{m}}\right)$	$S_\mathrm{C}^\mathrm{theory}$ $\left(\frac{\mu\mathrm{C}}{\mathrm{m}}\right)$
type 2	1190	975	116	145	67.134	2410	20.4	32.3	2.04	3.40
type 4	992	750	85	145	73.351	1870	14.7	44.9	1.47	3.32

Table 3.4.: Parameters for custom sensors of type 2 and 4. The sensor dimensions L, L_e, t, and w are determined from optical microscope images (Figs. A.1 and A.2). The sensor parameters f_0, k, S_V, n_q, and S_C are obtained from thermal excitation spectra. The sensitivity $S_\mathrm{C}^\mathrm{theory}$ for the custom sensors is calculated from Eq. (3.11). For images and thermal peak data see A.1.1.

the additional mass m_app at the end into account one obtains $k^\mathrm{type2} = 2410\,\mathrm{N/m}$ and $k^\mathrm{type4} = 1830\,\mathrm{N/m}$. The grooves were not considered and for further details on the stiffness determination see A.1.1. Another way is to simulate the stiffness utilizing finite element analysis (FEA) methods. From the FEA simulations with a realistic 3D-model where the grooves were also taken into account we obtain values of $k_\mathrm{FEA}^\mathrm{type2} = 2408\,\mathrm{N/m}$ and $k_\mathrm{FEA}^\mathrm{type4} = 1870\,\mathrm{N/m}$.[26] The experimentally observed resonance frequencies are $\approx 67.1\,\mathrm{kHz}$ and $\approx 73.4\,\mathrm{kHz}$, respectively. The simulated resonance frequencies are 67.3 kHz and 73.4kHz and they match the experimental values very well. Therefore the stiffness determined via FEA is assumed to be quite reasonable and for the following discussion the values $k^\mathrm{type2} = 2410\,\mathrm{N/m}$ and $k^\mathrm{type4} = 1870\,\mathrm{N/m}$ will be used for the custom sensors. All relevant sensor parameters including also sensitivities S_V, S_C, and deflection noise densities n_q for the custom sensors are summarized in Tab. 3.4.

After Eqs. (3.34) and (3.35) detector noise is proportional to

$$\delta k_\mathrm{ts}^\mathrm{det} \sim \frac{k n_q}{f_0 A} \sim \frac{k n_\mathrm{amp}}{f_0 S_\mathrm{C} A} \sim \frac{n_\mathrm{amp} t}{A}. \tag{3.37}$$

So far, n_amp was considered to be independent from the operating frequency of the sensor. This is in general not the case and depends on the amplifier which is used to measure the deflection signal. For a proper comparison of the custom and standard qPlus sensors the noise levels of the commercial charge amplifier at the operating frequencies of the sensors were measured. This was done without a sensor connected to the amplifier and at 32 kHz the voltage noise density was determined to $860\,\mathrm{nV_{rms}}/\sqrt{\mathrm{Hz}}$ and at $\approx 70\,\mathrm{kHz}$ to $620\,\mathrm{nV_{rms}}/\sqrt{\mathrm{Hz}}$.[27] The signal-to-noise ratio increases with the ratio

[26] See A.1.1 for further details on FEA simulations and size determination of the sensors.

[27] The voltage noise density at the resonance frequencies of the custom sensors (67 kHz and 73 kHz) should be determined, but there is only a small variation in this frequency range.

of the noise levels giving $\xi = 860/620 = 1.39$. This factor needs to be considered in Eq. (3.37) for sensors type 2 and 4. For a fixed value of A one expects an improvement in detector noise relative to a standard qPlus sensor by a factor of

$$\gamma^{\text{type2}} = \xi \cdot t^{\text{qPlus}}/t^{\text{type2}} = 1.39 \cdot 214\,\mu\text{m}/116\,\mu\text{m} = 2.56 \tag{3.38}$$

and

$$\gamma^{\text{type4}} = \xi \cdot t^{\text{qPlus}}/t^{\text{type4}} = 1.39 \cdot 214\,\mu\text{m}/85\,\mu\text{m} = 3.50. \tag{3.39}$$

This can be checked experimentally by determining n_q, f_0, and k. This is again done by the thermal excitation method at room temperature in ambient conditions. The Femto charge amplifier was used to measure the thermal excitation spectra. The measured values of n_q for a standard qPlus sensor (from Fig. 3.5) and for the custom sensor type 2 (4)[28] are $n_q^{\text{qPlus}} = 60.0\,\text{fm}/\sqrt{\text{Hz}}$ and $n_q^{\text{type2}} = 32.3\,\text{fm}/\sqrt{\text{Hz}}$ ($n_q^{\text{type4}} = 44.9\,\text{fm}/\sqrt{\text{Hz}}$). With the values for k and f_0 one obtains an improvement in SNR for the custom sensor type 2 of

$$\frac{\delta k^{\text{det}}_{\text{ts,qPlus}}}{\delta k^{\text{det}}_{\text{ts,type2}}} = \frac{1800\,\text{N/m} \cdot 67.134\,\text{kHz} \cdot 60.0\,\text{fm}/\sqrt{\text{Hz}}}{2410\,\text{N/m} \cdot 32.715\,\text{kHz} \cdot 32.3\,\text{fm}/\sqrt{\text{Hz}}} = 2.85, \tag{3.40}$$

and for the sensor type 4 of

$$\frac{\delta k^{\text{det}}_{\text{ts,qPlus}}}{\delta k^{\text{det}}_{\text{ts,type4}}} = \frac{1800\,\text{N/m} \cdot 73.351\,\text{kHz} \cdot 60.0\,\text{fm}/\sqrt{\text{Hz}}}{1870\,\text{N/m} \cdot 32.715\,\text{kHz} \cdot 44.9\,\text{fm}/\sqrt{\text{Hz}}} = 2.88. \tag{3.41}$$

The decrease in deflection detector noise is almost equal for both sensors. The reduction for sensor type 2 is $\approx 10\%$ more than theoretically expected, whereas for sensor type 4 the reduction is almost 20% *less* than expected. This discrepancy cannot be attributed to the amplifier because there is only a little difference in the voltage noise density from 67 kHz to 73 kHz. To understand this deviation one should compare the theoretical sensitivities $S_{\text{C}}^{\text{theory}}$ which are calculated after Eq. (3.7) with the experimental values of S_{C}. These values are given in Tab. 3.4. For sensor type 2 the ratio between the measured and calculated value is $g^{\text{type2}} = 2.04/3.40 = 0.60$ and for type 4 $g^{\text{type4}} = 1.47/3.32 = 0.44$. Remember, for a standard qPlus sensor this ratio was $g = 0.52$. The experimental sensitivity for the sensor type 2 is closer to the theoretical value which is expected for the optimized electrode geometry. On the other hand, the experimental sensitivity of sensor type 4 is even further off from the calculated value

[28] These are not the same sensors as shown in Figs. 3.8c,d but similar ones. The quartz resonators used to build the custom qPlus sensors are all from the same wafer. The only differences are slightly varying resonance frequencies (less than 0.5 %). For thermal peak spectra see A.1.2.

than a standard qPlus sensor which explains the $\approx 20\%$ deviation. This is unexpected and indicates that there might be problems with further miniaturization.

Summing up these findings, the recipe for decreasing deflection detector noise for quartz-based force sensors is to decrease the thickness t and length L of the prongs at the same time. A thickness reduction from $\approx 210\,\mu\text{m}$ to $\approx 120\,\mu\text{m}$ resulted in the expected improvement in SNR of a factor of about 3. Surprisingly, a reduction of t to $\approx 90\,\mu\text{m}$ only led to a similar reduction in deflection detector noise which indicates that below a certain thickness the SNR does not increase any more. The above discussion still relies on the simple formula for the sensitivity which assumes a homogeneous electric field distribution within the quartz crystal. To find the ideal thickness value and beam cross shape for further optimization of the SNR of custom designed sensors, FEA simulations might be helpful. It was shown that the needle sensor has about a factor of 2 less deflection detector noise than a standard qPlus sensor. For custom sensors of type 2 and 4 this noise source is therefore decreased by factor of about 1.5 compared to a needle sensor.

3.4.2. Decreasing Thermal, Oscillator, and Thermal Frequency Drift Noise

The reduction of the other three noise contributions is discussed briefly. For clarity, Eq. (3.21) is repeated:

$$\delta k_{\text{ts}}^{\text{thermal}} = \sqrt{\frac{4kk_BTB}{\pi A^2 f_0 Q}} \propto \sqrt{\frac{k}{f_0 Q}}. \tag{3.42}$$

Thermal noise is reduced when going to lower temperatures and by using a stiffness as small as possible, but compatible with the stability requirements for small amplitude operation. Furthermore high resonance frequencies f_0 and quality factors Q are desirable. All these criteria are fulfilled by the custom sensors type 2 and 4. Typical Q values of standard qPlus sensors are between $20,000 - 400,000$ at $T = 4\,\text{K}$. With sensors of type 4 Q values exceeding $1,000,000$ were achieved [105].

Oscillator noise is reduced by combining the recipes for decreasing deflection detector and thermal noise, because oscillator noise decreases with decreasing k and n_q, and increasing Q.

Frequency drift noise scales with the stiffness of the cantilever and a stiffness as small as possible should therefore be chosen. Quartz resonators are usually tailored for room temperature applications. If another operating temperature is desired the

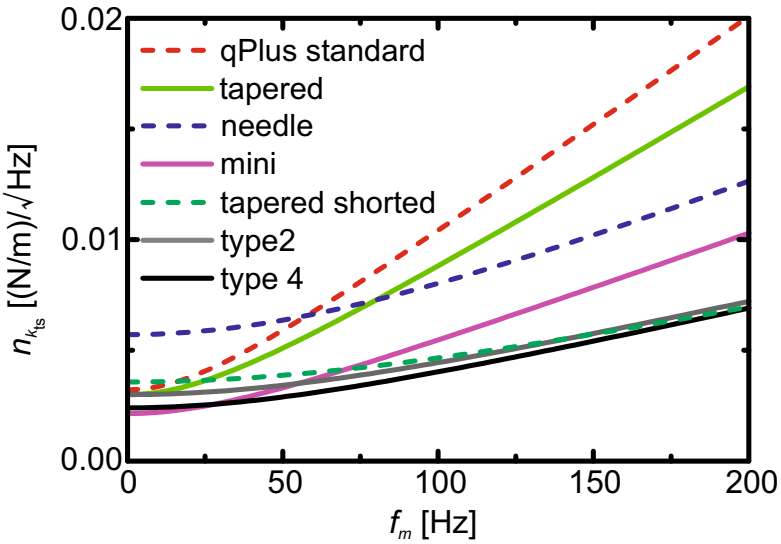

Figure 3.9.: Calculated force gradient spectral noise densities based on the parameters summarized in Tab. 3.5 and Eq. (3.33). The curves for the standard qPlus and needle sensor are the same as in Fig 3.7. The miniature quartz tuning fork (Fig. 3.8a) is denoted as "mini". Two versions of the tapered tuning fork (Fig. 3.8b) were used. The standard one ("tapered") and another one ("tapered shorted") where the large mass at the end was removed. Finally, the force gradient noise densities of the custom sensors type 2 and 4 (Figs. 3.8c,d) are also shown. Note, the dashed curves are the ones published in Fig. 14 in Ref. [70].

turnover temperature can be shifted within certain boundaries by changing the crystal cut [85].

3.4.3. Comparison of Noise Contributions for Optimized Sensors

It was shown before that the experimental force gradient spectral noise densities match the calculated noise densities very well (Fig. 3.7). The noise densities for the non-standard sensors presented in Fig. 3.8 were therefore calculated with the help of Eq. (3.33) and plotted in Fig. 3.9. The relevant parameters of the sensors are summarized in Tab. 3.5. Up to a modulation frequency of $f_m = 50\,\mathrm{Hz}$, the needle sensor has the largest noise density $n_{k_{\mathrm{ts}}}$. The standard qPlus sensor shows the largest contribution to the deflection detector noise. The "mini" tuning fork (Fig. 3.8a) and the standard version of the tapered tuning fork (Fig. 3.8b) also show higher deflection detector noise than the needle sensor. For the shorted version of the tapered tuning fork and the custom sensors type 2 and 4, deflection detector noise is similar and it is even less than for the needle sensor. Hence, these types of sensors show a better performance at high measurement bandwidths, e.g. faster scanning speeds. Although the needle sensor with its high resonance frequency of 1 MHz can reach measurement bandwidths

	f_0 (kHz)	k (kN/m)	Q	n_q $\left(\mathrm{fm_{rms}}/\sqrt{\mathrm{Hz}}\right)$
qPlus standard	32.628	1.80	2900	63.5
needle sensor	999.923	1,060	18470	1.89
Statek mini	32.700	0.74	2650	78.6
Tapered standard	32.880	1.28	2365	71.3
Tapered shorted	92.785	3.50	1650	28.0
Custom Type 2	67.134	2.41	2160	32.3
Custom Type 4	73.351	1.87	2430	44.9

Table 3.5.: Summary of sensor parameters f_0, k, Q, and n_q used to calculate the total force gradient noise density according to Eq. (3.33). The amplitude is fixed to $A = 100\,\mathrm{pm}$ and $T = 300\,\mathrm{K}$. The parameters f_0, Q, and n_q were determined from thermal excitation spectra at room temperature and ambient conditions. The stiffness values were discussed in the text above. The commercial charge amplifier was used to measure the thermal excitation spectra, except for the standard qPlus sensor. Thermal excitation spectrum data for the tapered sensors, Statek mini, and custom sensors type 2 and 4 can be found in appendix A.1.

of around 100 kHz, which are achieved in nowadays state-of-the-art high-speed AFM setups [106]. The spectral noise densities in Fig. 3.9 clearly show that by proper tailoring the geometry of qPlus sensors, a better performance in terms of SNR can be obtained than for needle sensors.

Another important point, though not related to noise, is the attachment of tips onto the sensor. For the needle sensor the additional mass of the tip must be kept small, because otherwise the oscillation of the prongs becomes asymmetric and the Q factor decreases. To keep the tip mass small, very thin wires ($\approx 5 - 10\,\mu\mathrm{m}$) were used for the first needle sensors reaching atomic resolution [83]. If the tip is too long, this can lead to a considerable loss of lateral stiffness and prevent high resolution imaging. Furthermore, the attachment of such a thin piece of wire onto the small prong of a needle sensor is quite tedious. Keeping the mass of the tip small is of course also important for qPlus sensors to maintain a high resonance frequency f_0, but it is not as critical than for a needle sensor. On a qPlus sensor more massive tips can be mounted which are laterally more stiff and easier to handle.

3.5. Characterization of Quartz Resonators at Cryogenic Temperatures

The main focus of this section is to assess the influence of thermal frequency drift on the measured force gradient at cryogenic temperatures. Due to the higher stability of the tip-sample junction at low temperatures the measurement bandwidth B can be significantly reduced. This results in a suppression of all noise contributions which scale directly with B like deflection detector noise, thermal, and oscillator noise. In turn, when B is small the stability of the eigenfrequency f_0 is particularly important. The main cause of frequency drift are changes in f_0 with temperature T. These can even occur in a stable cryogenic environment like for experiments conducted at liquid helium temperature. The boiling temperature of helium can be affected by changes in ambient pressure – the vapor pressure of He^4 at 4.4 K changes at a rate of $\approx 10^5$ Pa/K [107]. Typical changes in ambient pressure are between $100 - 500$ Pa/day [108] leading to temperature changes in the range of $1 - 5$ mK/day.

Quartz-based force sensors are often used at low temperatures, but little is known about the frequency variation with temperature in this regime. Hembacher *et al.* evaluated the relative frequency change $\varepsilon = \delta f / f_0$ of an encapsulated quartz tuning fork over a large temperature range from 300 K down to 4.2 K, where ε decreased monotonically with T [96]. At 300 K and 4.2 K ε reached extreme values and the influence of temperature variations is therefore reduced at these temperatures. In a more detailed measurement, Rychen *et al.* measured the frequency change of a quartz tuning fork from 1.5 K to 50 K at a constant pressure of 10 mbar. The eigenfrequency f_0 was not increasing monotonically with increasing T, but ε showed a local minimum around 20 K [109]. This resembles qualitatively the temperature dependence of the Grüneisen parameter γ which relates thermal expansion to vibrational properties [110]. The values for γ show a maximum around 30 K decreasing sharply to lower temperatures and gradually to higher ones [110, 111]. Additionally the anisotropic thermal expansion coefficients of quartz, $\alpha_\parallel$ and $\alpha_\perp$, parallel and perpendicular to the optical axis also show a non-linear behavior with temperature [112]. From $6 - 283$ K $\alpha_\perp$ is positive and increases monotonically with T, whereas $\alpha_\parallel$ is negative below ≈ 12 K [111].

The eigenfrequencies f_0 of qPlus (Eq. (3.3)) and needle (Eq. (3.5)) sensors depend on the dimensions of the oscillating beams and v_s. Hence, f_0 changes when the dimensions or v_s change due to thermal expansion. The orientation of the oscillating beams deviates slightly from a perpendicular orientation to the optical axis (z-axis,

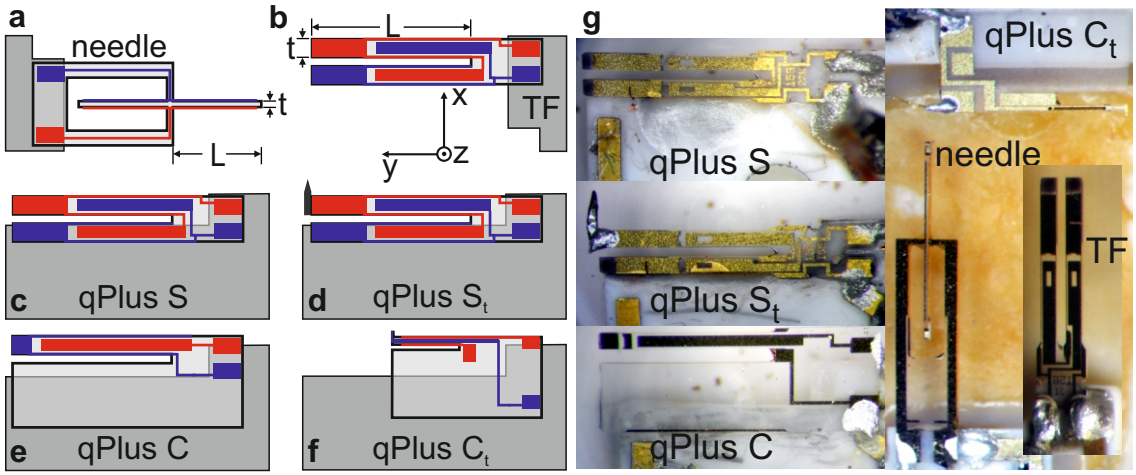

Figure 3.10.: Geometry of needle sensor **a**, tuning fork **b**, standard qPlus sensors **c**,**d**, and custom qPlus sensors **e**,**f**. Coupled oscillators are fixed to the substrate at their base. Both prongs oscillate with no additional mass or tip attached to the prongs. Standard qPlus sensors (S and S_t) are made up of quartz tuning forks. In **d** a tip is added to the free prong. Custom-designed qPlus sensors consist only of a single prong with a larger base, which is fixed to the substrate. Unnecessary electrodes are removed to reduce capacity. **e**, the beam dimensions of sensor C are the same as for sensors S and S_t. **f**, sensor C_t is the sensor type 4 from the previous section. Figure adapted from [76].

Fig. 3.1). This is due to the crystal cut which is not exactly along the optical axis, but off by about 2° (+2°X-cut). For this type of cut the direction of t (x-axis) is perpendicular to the z-axis and L is off by 2° from the y-axis (Fig. 3.10a,b). The thermal expansion along x,y-directions is determined by $\alpha_\perp$ [111]. By neglecting the small deviation of L from the y-axis the frequency change with temperature T for tuning forks and qPlus sensors follows from Eq. (3.3) as

$$\frac{\partial f_0}{\partial T} = f_0 \left(\frac{1}{t}\frac{\partial t}{\partial T} - \frac{2}{L}\frac{\partial L}{\partial T} + \frac{1}{v_s}\frac{\partial v_s}{\partial T} \right) =$$
$$f_0 \left(\alpha_\perp - 2\alpha_\perp + \frac{1}{v_s}\frac{\partial v_s}{\partial T} \right) = f_0 \left(-\alpha_\perp + \frac{1}{v_s}\frac{\partial v_s}{\partial T} \right). \tag{3.43}$$

The same result is obtained for the needle sensor geometry. For X-cut crystalline quartz no change in v_s with T within a precision of 0.1 ppm was observed below 10 K [113–115]. The measured values of $\alpha_\perp$ below 10 K are in the order of 0.01 ppm/K [111]. According to Eq. (3.43) the variation of ε with T below 10 K is expected to reach about 0.1 ppm/K. Furthermore, no difference between tuning forks, qPlus sensors, and needle sensors is expected.

Therefore, the frequency change with temperature from 4.8 K to 48 K for quartz-based force sensors is measured. Six different quartz resonators were investigated to

	$L\,(\mu\mathrm{m})$	$t\,(\mu\mathrm{m})$	$w\,(\mu\mathrm{m})$	$f_0\,(\mathrm{Hz})$	$k\,(\mathrm{N/m})$
qPlus S	2400	214	130	32680	1800
qPlus $\mathrm{S_t}$	2400	214	130	19658	1800
qPlus C	2400	214	130	32884	1800
qPlus $\mathrm{C_t}$	992	85	145	73303	1830
TF	2400	214	130	32742	1800
needle	1340	70	130	998148	530000

Table 3.6.: Dimensions (length L, thickness t, and width w), resonance frequency f_0, and stiffness k of the different types of sensors investigated. Table adapted from [76].

directly evaluate and compare the influence of thermal frequency drift on the force gradient noise. Figure 3.10 shows schematics (a-f) and photographs (g) of the quartz sensors. Two coupled oscillators without a tip are investigated: A needle sensor (needle, Fig. 3.10a) and a tuning fork (TF, Fig. 3.10b). Two standard qPlus sensors made from quartz tuning forks one without tip (S, Fig. 3.10c) and one with a tip ($\mathrm{S_t}$, Fig. 3.10d) are also studied. Finally, custom-designed quartz cantilevers are used to build qPlus sensors with standard[29] and smaller beam dimensions (C and $\mathrm{C_t}$, Figs. 3.10e,f). Sensor $\mathrm{C_t}$ is the sensor type 4 as introduced in the previous section, due to the additional mass at the end it is labeled with $\mathrm{C_t}$. In Tab. 3.6 the relevant parameters L, t, w, f_0, and k of the sensors are summarized.

All quartz resonators were glued with electrically non-conductive but thermally conductive epoxy[30] onto an aluminum oxide substrate which is commonly used for the qPlus sensors. The electrodes are then contacted with conductive epoxy[31] to the leads. For the low temperature measurements the substrates where glued again with non-conductive epoxy onto a piece of copper. This serves as a thermal anchor and can be mounted on a $\mathrm{He^4}$ stick usually used for transport measurements. The stick is equipped with a heater resistor and a Si diode to measure the temperature T. For measurements at low temperatures the stick is immersed in a liquid helium vessel. The sensors were excited electrically with a constant drive signal and the deflection signal was measured with the Femto charge amplifier. The frequency shift was determined by a digital phase-locked loop which is stabilized by an OCXO with a precision of 1 ppb/day.[32]The temperature setpoint was increased at a rate

[29]Statek Corporation, USA.
[30]EPO-TEK T7110, EPOXY Technology, Billerica, MA, USA.
[31]EPO-TEK T4110, EPOXY Technology, Billerica, MA, USA.
[32]OC4 - Nanonis Oscillation Controller, Specs Zurich GmbH, 8005 Zurich, Switzerland

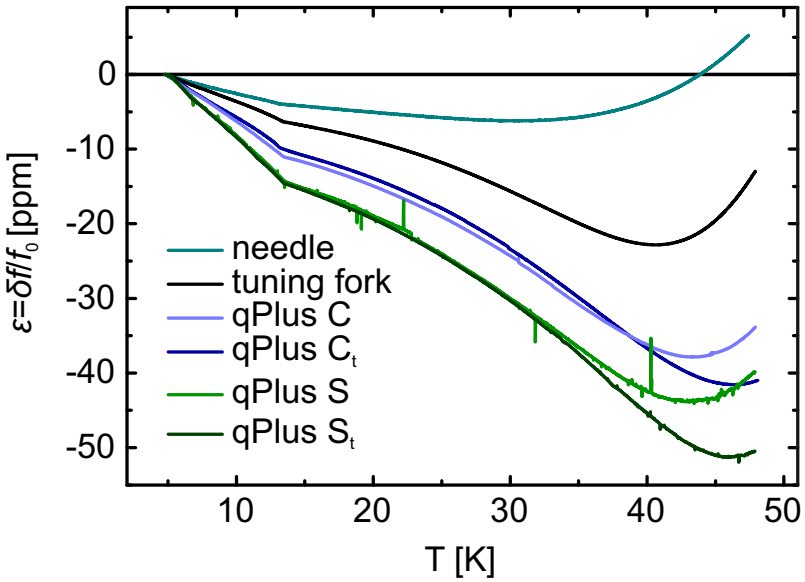

Figure 3.11.: Relative frequency change of quartz-based AFM sensors from $4.8 - 48\,\mathrm{K}$. The coupled oscillators show less relative frequency change with temperature as the qPlus sensors. For custom-made qPlus sensors ε is smaller as for the standard ones. The spikes in the curves of the qPlus sensors arise from mechanical excitations of the sensors due to external vibrations or sound. Figure adapted from [76].

of $0.5\,\mathrm{K/min}$ and the change in eigenfrequency was monitored. At this rate the maximum deviation of the actual temperature from the setpoint temperature was below $0.1\,\mathrm{K}$.

The results of the low temperature measurements are shown in Fig. 3.11, where the relative frequency change ε is plotted against T. As the He^4 stick is not equipped with a vibration isolation system there are some sharp peaks in the curves for the qPlus sensors caused by mechanical excitations of the sensors. This is not an issue for the coupled oscillators, and also for the sensor C_t which has a higher resonance frequency and is therefore less affected by external vibrations. Obviously, there is a difference in ε for the various types of sensors used. The relative change is smallest for the needle sensor followed by the TF and the custom qPlus sensors (C, C_t). The standard qPlus sensors (S, S_t) show the strongest change of f_0 with T. The curves for S and S_t lie exactly on top of each other and start to split up at around $33\,\mathrm{K}$. For the two custom sensors ε is also quite similar and they split up at around $40\,\mathrm{K}$. For sensors S and C, without an additional mass at the end of the prong, ε changes its sign earlier than in case of S_t and C_t. All curves show a fairly linear decrease of ε up to $13\,\mathrm{K}$ where a distinct kink appears, which might be due to the sign change in $\alpha_{\parallel}$. After this kink, ε still decreases for all types of sensors. In the case of the needle sensor the sign

	$\eta\left(\frac{\text{ppm}}{\text{K}}\right)$	$\frac{\partial k_{\text{ts}}}{\partial T}\left(10^{-3}\frac{\text{N}}{\text{mK}}\right)$
qPlus S	-1.69	6.1
qPlus S_t	-1.63	5.9
qPlus C	-1.25	4.5
qPlus C_t	-1.11	4.3
TF	-0.70	5.0
needle	-0.46	960

Table 3.7.: Slopes η from linear fits to the data in a temperature range from $5-12\,\text{K}$ and corresponding variation of the force gradient with respect to temperature $\partial k_{\text{ts}}/\partial T$. Table adapted from [76].

of $\partial\varepsilon/\partial T$ changes from negative to positive at around 30 K. This agrees qualitatively with the temperature dependence of the Grüneisen parameter γ. For TF and qPlus sensors ε still decreases, and $\partial\varepsilon/\partial T$ changes its sign at temperatures between $40-47\,\text{K}$.

In the temperature range from $5-12\,\text{K}$ the slopes η of the curves can be obtained from a linear fit to the data in Fig. 3.11. The values are summarized in Tab. 3.7. They are all in the order of 1 ppm/K, which is an order of magnitude larger than expected from the change in v_s or $\alpha_\perp$ as discussed above. From neutron irradiation it is known that $\partial v_s/\partial T$ depends on the quality of the crystal. The relative change of v_s with T increases linearly with the defect density [114–116]. Because the quartz resonators studied here are from different wafers and manufacturers, one might argue that the differences in $\partial\epsilon/\partial T$ can be caused by different crystal quality and material processing. On the other hand, there are two important observations from the measurements presented in Fig. 3.11 which are contradictory to that: First, the difference between the standard qPlus sensors (S, S_t) and the tuning fork is somewhat unexpected, because these are all made from the same type of quartz tuning forks.[33] Second, sensors C and C_t have different beam dimensions and are not even from the same manufacturer. Nevertheless, $\partial\epsilon/\partial T$ is strikingly similar (blue curves in Fig. 3.11). If there is an influence of different crystal quality or material processing on the frequency variation with temperature, it should actually lead to a larger difference between the custom sensors than between the tuning fork and the standard qPlus sensors. This is not the case and the origin of the difference

[33] Micro Crystal DS26 series

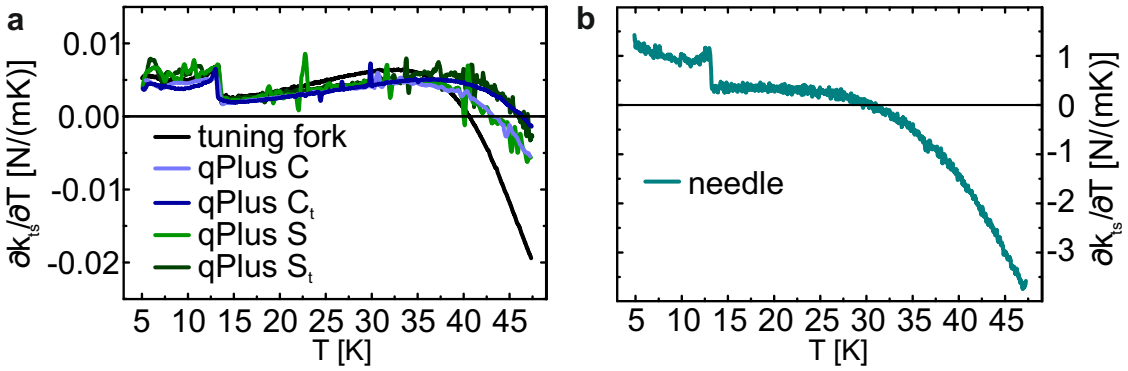

Figure 3.12.: **a**, numerical derivative $\partial k_{ts}/\partial T$ for all tuning fork and qPlus sensors from $5-47\,\mathrm{K}$. **b**, $\partial k_{ts}/\partial T$ for the needle sensor. Note, the y scale for **a** and **b** is different. Figure adapted from [76].

between the tuning fork and the standard qPlus sensors is very likely caused by a different mechanism. One possibility could be the different geometry and the resulting difference in the mechanical coupling of the beam to the support. As coupled sensors are less influenced by movements of their base this could explain the smaller values of η.

The resonance frequency of qPlus sensors follows the relation $f_0 \sim \sqrt{k/m^*}$. Hence, $\partial\varepsilon/\partial T$ can be interpreted as a variation of the stiffness with temperature implying m^* remains unchanged. The similarity of $\partial\varepsilon/\partial T$ for sensors S and $\mathrm{S_t}$ up to a temperature of around 33 K leads to the conclusion that there is no significant influence of the additional mass of the tip on the effective stiffness of sensor $\mathrm{S_t}$ compared to sensor S.

So far, the relative frequency change with temperature was discussed. To obtain the influence on the measurement of the force gradient $\partial k_{\mathrm{ts}}/\partial T$ the slopes η need to be multiplied with the according value of $2 \times k$ [70]. The values for $\partial k_{\mathrm{ts}}/\partial T$ are given in Tab. 3.7. Force gradient drift noise scales with k, therefore it is $160-240$ times higher for needle sensors than for standard and custom-designed qPlus sensors. This is illustrated in Fig. 3.12, where $\partial k_{\mathrm{ts}}/\partial T$ is displayed for the tuning fork and the qPlus sensors (Fig. 3.12a) and the needle sensor (Fig. 3.12b). The wiggles in the curves for the qPlus sensors are caused by external excitations due to a lacking damping system. The kink around 13 K (Fig. 3.11) shows up as a clear step. In temperature dependent measurements it might therefore be beneficial for a stable operation of the force sensor to avoid temperatures around $13\,\mathrm{K} \pm 0.5\,\mathrm{K}$. For temperature changes in the order of 1 mK the minimum detectable force gradient is about 1 mN/m for the LER and about 5 µN/m for qPlus sensors.

Finally, a few words on the Q factor. Table 3.8 summarizes the Q values of the sensors investigated above, which were measured at liquid helium (vacuum, $p \approx 10^{-6}\,\mathrm{mbar}$) and room temperature (ambient air pressure, $p \approx 1\,\mathrm{bar}$). Admittedly, the values might be different for other sensors of the same type, especially at low temperatures, because the Q value depends on hardly accessible details of the gluing process. On the other hand, there is a general trend towards higher Q values for the custom sensors compared to standard ones. At least from the experience of the author with a number (≈ 100) of other standard and custom qPlus sensors. This is most likely due to the larger base of these sensors, which allows to position the sensor such that the clamping point of the beam is further away from the glued part. As the mechanical stress and strain is highest at the clamping point the glue can effectively soften this section which can lead to a decrease in Q. The Q values of the custom sensors are therefore higher and more reproducible than for the standard ones. Apart from that, the larger base is also advantageous for handling. As a general rule of thumb Q values at room temperature in air of "good" standard qPlus sensors are usually in the range of $2000 - 3000$ and for "good" custom qPlus sensors between $3500 - 6000$. Cooling such a good sensor to liquid helium temperatures usually, but not necessarily, leads to Q values around $100,000$ and for custom sensors even Q values exceeding $1,000,000$ were achieved [105].

	Q ($T = 4.2\mathrm{K}$)	Q ($T = 296\mathrm{K}$)
qPlus S	264,000	2,900
qPlus S_t	179,000	2,900
qPlus C	397,000	3,600
qPlus C_t	312,000	2,200
TF	140,000	—
needle	202,000	17,300

Table 3.8.: The Q values at 4.2 K are obtained from resonance curves, where the sensors were excited with a constant amplitude. The room temperature values were determined by fitting a simple damped harmonic oscillator transfer function to the thermal excitation spectra, except for the needle sensor which was excited electrically.

4. Experimental Tools and Setup

The following chapter briefly describes the experimental setup and the measurement instrumentation. The qPlus sensor itself was introduced in detail in the previous chapter. Here, the low temperature scanning probe system used throughout this work and the *in-situ* tip and sample preparation methods are described. To study magnetic interactions magnetically sensitive tips are necessary. For this purpose, the fabrication of bulk iron (Fe) and samarium-cobalt (SmCo) tips is also explained.

4.1. Low Temperature STM/AFM Setup

The low temperature (LT) STM/AFM setup is a commercial system from Omicron NanoTechnology[1] and consists of two UHV chambers, an analysis chamber and a preparation chamber. The system was already described in detail by Welker [91] and Hofmann [117], therefore this is kept short in the following.

The analysis chamber is unmodified and hosts a cryostat onto which the microscope is attached. The cryostat has an inner and an outer tank. For operation at a base temperature of around 4.4 K the inner one is filled with liquid helium and the outer one with liquid nitrogen. The hold time of the cryostat was usually around 60-65 hours. The microscope stage hangs on three springs and eddy current damping is used for vibration isolation. On the stage are the piezo motors for coarse positioning, the tube scanner, and the sample inventory.

The preparation chamber is equipped with standard sputtering and annealing systems for sample preparation. Either resistive heating for metallic samples or direct current heating for semiconducting samples can be employed. In this work all samples were annealed with the resistive boron nitride heater which reaches a maximum temperature of around 1200 K. To analyze the cleanliness of the sample surface an Auger electron spectrometer is available. A gas handling system with two leak valves is installed. Additionally, the tips can be prepared by electron beam heating and by field emission or more important field evaporation. The latter is possible, because the system is

[1] Low Temperature UHV STM in the qPlus configuration, Omicron NanoTechnology GmbH, 65232 Taunusstein, Germany.

equipped with a field ion microscope (FIM)[118]. This requires positive voltages in the range of $10 - 15\,\mathrm{kV}$ to be applied to the tip. At such high voltages the electric field at the tip apex is large enough to ionize tip atoms and remove them. This turned out to be very powerful in cleaning off oxide layers from the tips. After field evaporation the tip was introduced into the microscope and usually stable tunneling conditions were observed without further tip treatment which indicated a complete removal of contaminating oxide layers. The operation of the FIM itself is also described in [91]. A commercial scanning probe microscopy (SPM) acquisition electronics system is used for operating the microscope.[2]

4.1.1. Omicron qPlus Sensor

The system is a modified LT STM, where instead of a bare tip a qPlus sensor is now fixed to the tube piezo scanner. A custom-designed qPlus sensor on an Omicron sensor holder is shown in Fig. 4.1. The quartz resonator is glued with non-conductive epoxy onto an insulating ceramic plate and the two contacts (STM and AFM) are connected to the corresponding legs of the sensor holder with conductive epoxy. The sensor is held magnetically on the scanner and the electrical and mechanical connections are made by the three legs. The AFM channel is directly connected to an *in-situ* preamplifier stage on the microscope head. The STM contact on the sensor is grounded in this setup and the third contact is also grounded for shielding. The tunneling current is measured from the sample which is biased via a floating STM preamplifier. If the bias voltage V is applied to the tip the electric field between the STM and AFM electrodes leads to a bending of the prong, which makes it challenging to acquire $I(V)$ or $\Delta f(V)$ curves. After a sensor was built, the Q factor and the sensitivity S_V were checked by the thermal excitation method at room temperature. Only sensors with reasonable good values should be introduced into the LT system. Furthermore, the connection of the tip to the STM electrode needs to be checked. When a sensor is broken another issue can occur: The quartz itself can be easily removed with a soldering iron to soften the glue, but this can sometimes also lead to a damage of other glue connections from the ceramic to the bent legs and the plate itself.
Once introduced into the microscope the Q value is determined by sweeping the excitation signal for the sensor. Usually, Q values in the order of $100,000$ are achieved. The sensors are excited mechanically via a separate ring electrode of the tube scanner.

[2]Nanonis SPM Control System Base Package including signal conditioning (SC4), high voltage supply (HV4) and oscillation controller (OC4), Specs Zurich GmbH, 8005 Zurich, Switzerland

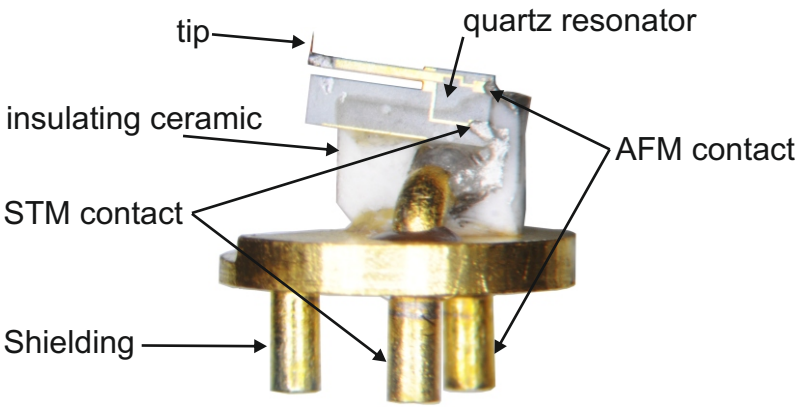

Figure 4.1.: Image of a home-built Omicron qPlus sensor. The bare holder without the quartz is supplied by Omicron. It consists of a cylindric metal plate with three legs towards the scanner and two legs bent towards the insulating ceramic to contact the quartz resonator electrically. The ceramic is fixed to the cylindrical plate with non-conductive epoxy and the two bent legs are connected with conductive epoxy to the contacts on the ceramic. The third leg is isolated from the two others and is used for shielding.

The next step is the calibration of the oscillation amplitude A, which is usually performed in STM or AFM feedback as described in [119].

4.2. Fabrication of Magnetic Tips

Magnetically sensitive tips are widely used in magnetic force microscopy (MFM) and spin-polarized STM (SP-STM) [39, 120]. In MFM, tips with a well defined domain structure are desirable. This is achieved by using non-magnetic tips coated with a thin magnetic layer, e.g. cobalt on silicon. Nevertheless, a qPlus sensor with bulk Fe tips also revealed the bit structure of a hard disc in MFM mode [121]. The configuration of the foremost tip apex atoms is not so crucial for MFM. In contrast, for SP-STM only the magnetic properties of the front atom matters. Attaching a single magnetic atom to the apex of a non-magnetic tip allows to perform SP-STM experiments in the presence of an external magnetic field [122, 123]. Depending on the application and the experimental setup either non-magnetic tips coated with magnetic material or bulk magnetic tips are used [39]. Antiferromagnetic tip materials are generally favored because their magnetic stray field is negligible [39]. On antiferromagnetic surfaces like nickel oxide (001) also materials with high saturation magnetization like Fe can be used.

The qPlus sensor offers the possibility to attach any kind of bulk tip material to the free prong and even *in-situ* cleaving of crystallographically oriented tips is possible [124]. On the other hand, using *in-situ* coated tips could be problematic, because the electrodes might be shorted by the evaporated material. Therefore, bulk magnetic tips were used in this work.

4.2.1. Electrochemically Etched Iron Tips

Sharp bulk metal tips with a high aspect ratio are usually made from a high purity wire by electrochemical etching [125]. The wire is immersed in the etching solution

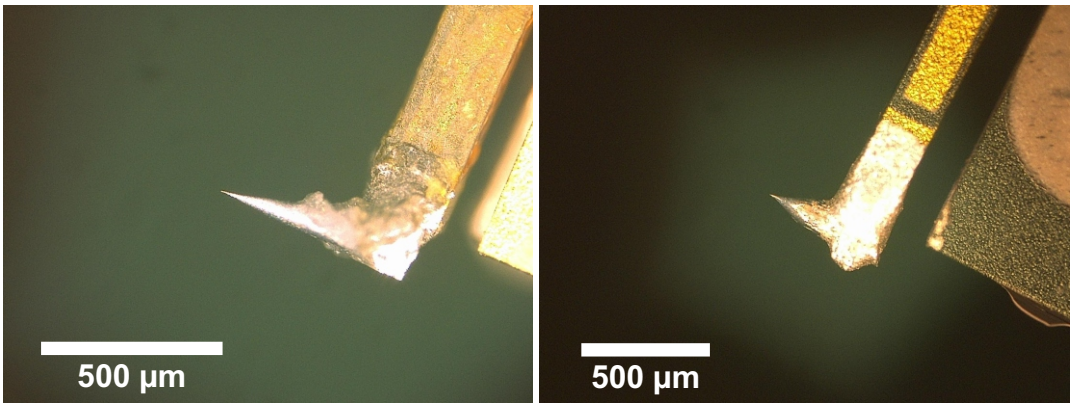

Figure 4.2.: Optical microscopy images of two electrochemically etched Fe tips, which were attached to the prong after the etching process.

and a voltage is applied between the wire and the anode which is also immersed in the solution. Positive voltages on the order of a few volts are usually applied to the wire. Utilizing an electronic cut off circuit leads to sharper and more reliable tip apices [126]. The ferromagnetic elements (Fe, Co and Ni) can be etched by several solutions, e.g. KCl, NaCl, or HCl – as long as chlorine is contained etching usually works. The chemical reaction between the solution and the wire leads to the formation of chlorine-metal compounds which are soluble in H_2O or ethanol and aceton [127].

The first magnetic tips were etched from 125 µm wires[3] with a solution of nitric and hydrochloric acid (HNO_3(1)+ HCl(1) + H_2O(2))[4] and a DC voltage of +5 V was applied to the wire [128]. After the etching process the wire was cut with pliers or a scalpel such that only a small piece (about 0.5 mm in length) including the tip was left. This small piece was then attached to the prong of a qPlus sensor with conductive glue. Figure 4.2 shows two examples of Fe tips fabricated in this way. Reasonably sharp tips could be produced, but the yield of this procedure is rather small. The main problem is the transfer of the small tip to the prong which often failed or led to a damaged tip apex.

Therefore, a procedure where the tip is directly etched from the sensor is desirable. Such a method is used for tungsten (W) and copper (Cu) tips and gives reproducible results. It is based on the recipe described in [129] and explained in more detail in [117]. Throughout this work some measurements were also performed with W tips which were also prepared by this method. With the above solution and also with concentrated HCl or 2-4 molar NaCl the tip etching for Fe did not yield satisfactory results: Either the tips were blunt or the surface was quite rough. A less aggressive solution, which is used for electrochemical polishing [130] was tested by A. Härtl during his bachelor thesis on the optimization of the etching process for Fe and Co tips [131]. This solution consists of a 20:1 mixture of acetic acid (concentration: 100%) and perchloric acid (concentration: 70%).

For the second batch of magnetic tips a piece of wire[5] with a length of about 1 cm was glued to the prong of a qPlus sensor. Then the wire was immersed in the above solution and the cut off electronics was switched on. After a few tens of seconds the lower part of the wire felt off and the etching stopped automatically. The result of this method is shown in Fig. 4.3 for a Fe tip. In the optical microscope image (Fig. 4.3a) the surface looks shiny indicating a good surface quality with low roughness. The

[3]Fe wire purity: 99.99+, Goodfellow Corporation
[4]Volume fraction is given in brackets
[5]Here, the wire was pre-etched to reduce the diameter of the wire from 125 µm to about 60 µm.

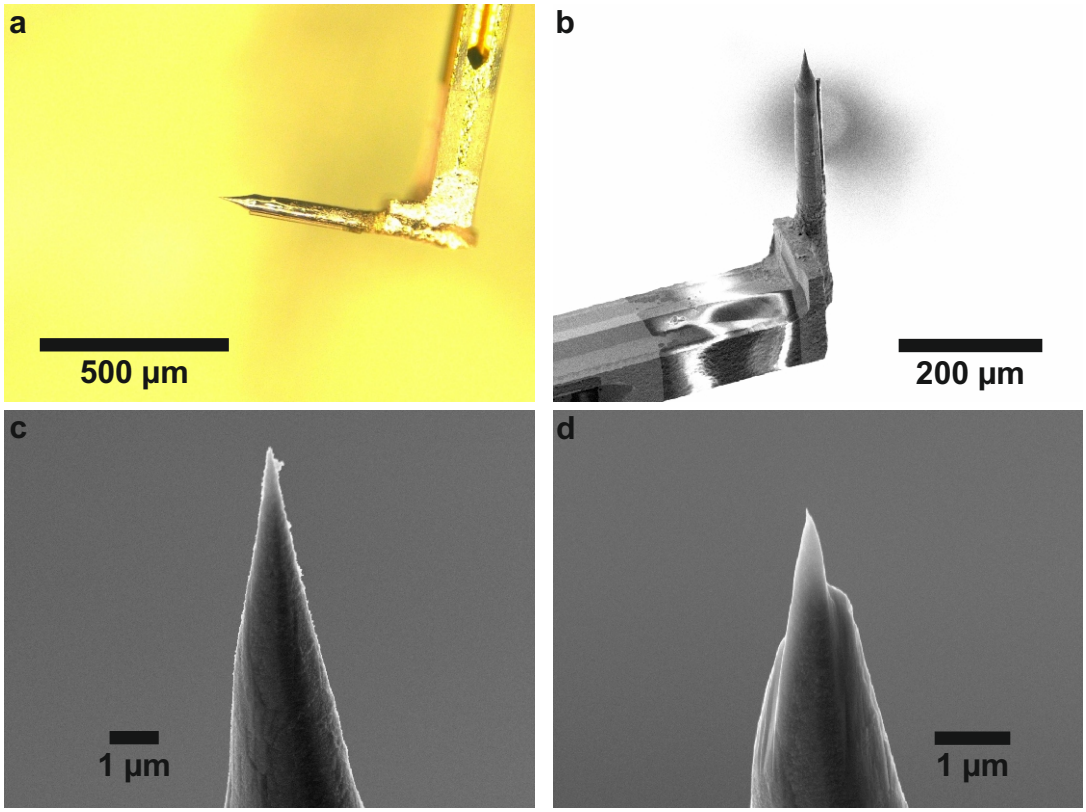

Figure 4.3.: **a**, optical microscopy image of an electrochemically etched Fe tip, where the tip was directly etched from the prong. **b**, electron microscopy image of the same tip as in **a**. **c**, zoomed view of the tip apex showing the roughness of the surface at the apex. **d**, same tip apex after ion milling, the surface at the apex is now smoother.

scanning electron microscopy[6] (SEM) images (Figs. 4.3b,c) show some contamination at the apex which is probably residual Fe_2Cl or some iron oxides. Sometimes these contaminants could not be removed by *in-situ* tip preparation methods like heating or field evaporation, probably because the contaminant layer was too thick. Therefore an additional step was introduced in the tip preparation procedure. Focused ion beam (FIB) with Ga^+ ions was used to remove the contaminants. The outcome of such a FIB treatment is shown in Fig. 4.3d. The tip is now even sharper with a tip radius of about 10 nm and additionally the surface at the apex is smoother indicating less contamination. Of course, the tip is oxidized when exposed to air during the transfer from the SEM to the STM/AFM system. These thinner oxide layers are easily removed by field evaporation, especially when the tip apex has a small radius of curvature [132].

[6]Zeiss Auriga FIB-SEM system, Carl Zeiss Microscopy GmbH, 73447 Oberkochen, Germany

4.2.2. Bulk Samarium-Cobalt Tips

The idea behind using a SmCo tip is that its large magnetocrystalline anisotropy energy (MAE)[7] may help to stabilize the magnetic moments at the tip apex similar to an external magnetic field. For instance, the MAE of SmCo is about 500 times larger than for bulk Fe [105]. A lot of magnetic materials, especially the ones with high MAE like SmCo, NdFeB, or FePt are alloyed materials [133]. These are usually not commercially available in wire form. If such a tip material is desired one can glue a sharp piece of this material onto the free prong of a qPlus sensor [134]. This is shown in Fig. 4.4a for SmCo. A SmCo permanent magnet was smashed with a hammer and a sharp splinter was selected and glued to the qPlus prong. From the SEM images it is obvious that in terms of aspect ratio and sharpness such a tip is far from ideal. To improve the tip geometry, at least a bit, focused ion beam was used again (Figs. 4.4b,c). Finally, the tip only showed a single protrusion pointing towards the sample (Fig. 4.4d). In the AFM system the tip can be cleaned *in-situ* by field evaporation though it is not a priori clear whether this is sufficient to remove oxide layers.

[7]This is the energy required to switch the magnetization from the magnetic easy to the hard axis.

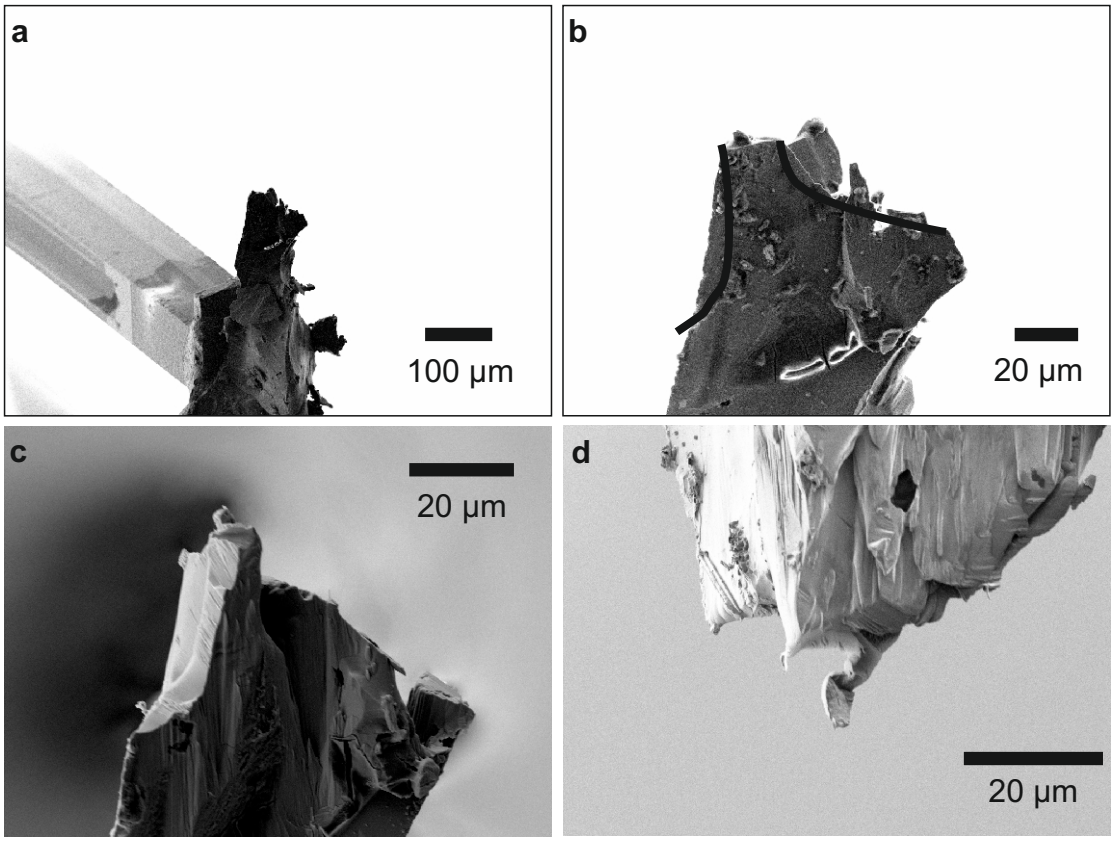

Figure 4.4.: a, SEM image of a splinter from a SmCo permanent magnet attached to a qPlus sensor. **b**, tip with multiple protrusions before ion milling, the black lines indicate the area where material was removed. **c**, tip after ion milling where only one large protrusion is left. **d**, SEM image of the tip apex from another perspective confirming that there is a single protrusion at the apex, though it is not very sharp.

5. Angular Dependent Short-Range Forces

The main focus of this chapter is on the investigation of copper (Cu) adatoms on the (110) and (111) surfaces of Cu single crystals by combined STM/AFM. To enhance the AFM resolution, a carbon monoxide (CO) molecule is attached to the metallic tip of the STM/AFM [21, 135]. The so-called carbon monoxide front atom identification (COFI) is a complimentary technique where a metal tip is scanned over a CO molecule adsorbed on Cu(111) [20]. The CO serves then as a sharp probe for the tip apex. The angular dependent short-range interactions observed in COFI measurements with bulk W, Fe, or Cu tips were interpreted in terms of the non-spherical charge density of a single metal atom terminating the tip [20, 30, 97]. Otherwise, the measurements on Cu adatoms on Cu(110) and Cu(111) suggest another interpretation of the COFI data. It seems very likely that clusters of several (2-4) atoms lead to the observed angular dependency and not the charge distribution within a single atom. Nevertheless, the measurements on Cu(110) provide a clear evidence for the observation of non-trivial *subatomic* features. However these are much more subtle than in the previously reported COFI experiments [20, 30, 97]. Before discussing the results, an introduction to angular dependent short-range interactions is given followed by a description of the experimental details and the data analysis.

In the last part of this chapter the characterization of bulk Fe tips via the COFI method is discussed. The distinction between Cu and Fe terminated tips is of major importance for the detection of spin-dependent interactions.

5.1. Introduction to AFM with Subatomic Resolution

Multiple features within the diameter of a single atom were already reported back in 2000 on Si adatoms on the Si(111) $-$ 7×7 surface utilizing a qPlus sensor with small oscillation amplitudes [136]. This is referred to as *subatomic* resolution and was interpreted in terms of the dangling bonds of a silicon atom terminating the tip. In

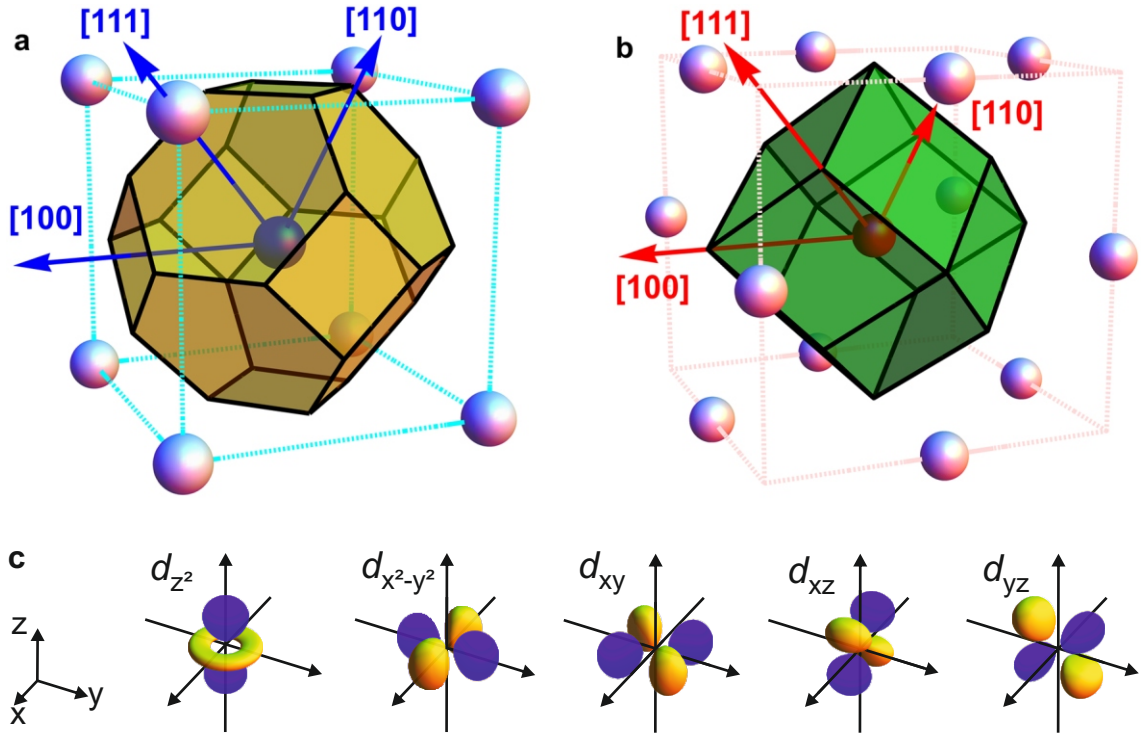

Figure 5.1.: a, Wigner-Seitz cell for bcc crystal structures like W or Fe, the center atom has 8 nearest neighbors along ⟨111⟩ directions. **b**, Wigner-Seitz cell for fcc structures like Cu, the center atom has 12 nearest neighbors along ⟨110⟩ directions. **c**, schematic illustration of atomic d orbitals [137]; blue and yellow color indicates different signs of the wave function.

2004, Hembacher *et al.* performed simultaneous STM and AFM measurements on graphite with a tungsten tip [19]. The tunneling current only showed a single feature whereas multiple features could be identified in the higher harmonics of the cantilever oscillation. The different appearances of these features were related to the bulk bcc symmetry of the tungsten (W) tip (Fig. 5.1a), which is probed by the significantly smaller carbon atoms of the graphite surface. Another step in this direction was the observation of multiple features in the frequency shift data when scanning a Cu terminated iridium tip over a CO molecule adsorbed on a Cu(111) single crystal [138]. Based on these experiments, Welker and Giessibl performed a well controlled study, where a W tip was scanned along a single CO molecule adsorbed on Cu(111) and constant height slices at various tip-sample distances were obtained to generate a $\Delta f(x, y, z)$ data set for force recovery [20]. Using tip-sample interactions, the tip apex was repeatedly changed to probe structurally different tips. Three high-symmetry short-range force fields were observed and related to the increased charge density of W towards their nearest neighbor directions [139–141]. The interaction of the W tip atom with the CO was quantitatively explained with a model potential based on short-range

electrostatic interactions [20]. The CO bonds with its carbon atom on top of a Cu atom [142]. Therefore the oxygen atom points towards the tip and it is assumed to be negatively charged [143, 144]. This leads then to an attractive electrostatic interaction with the W tip atom along next nearest neighbor ⟨100⟩ directions, where the electron density is reduced. Repulsive interaction occurs along the nearest neighbor ⟨111⟩ directions, where the electron density is increased. Hence, a ⟨100⟩ oriented tip shows a single attractive minimum, whereas the ⟨110⟩ and ⟨111⟩ oriented tips show two and three minima, respectively. It was also possible to identify the symmetry of the tip in the tunneling current data via Laplace filtering or differential current analysis [20, 91]. Though a lot of experimental evidence supported the interpretation from above, the larger spatial extent of the ⟨110⟩ and ⟨111⟩ oriented tips compared to a ⟨100⟩ tip was always a bit stunning and attributed to the bending of the CO molecule on the Cu(111) surface [20].

In a more recent experiment, we utilized the same technique to study bulk Cu and Fe tips [30]. Three high-symmetry orientations were again observed for both materials. For Cu, two were circular symmetric and one was twofold symmetric. In contrast to W, Cu has completely filled d orbitals (Fig. 5.1c) resulting in a spherical charge density in the bulk [145–147]. Therefore the observation of angular-dependent force fields in COFI images were somewhat unexpected. The Smoluchowski effect [148] can lead to a reduced electron density of surface atoms or adatoms resulting in partially filled d shells [147, 149–152]. Based on that, a model potential was developed by Giessibl, which takes into account the angular overlap of the d orbitals to the nearest neighbor atoms [153]. As the partial occupation of the d shell was underestimated by the model (≈ 6 electrons instead of ≈ 10) the positive core charge was adjusted to give realistic values for the total charge of the tip atom. The model allowed then an assignment of the observed symmetries in the COFI images to the ⟨100⟩, ⟨110⟩, and ⟨111⟩ fcc crystal directions of bulk Cu (Fig. 5.1b). The ⟨100⟩ and ⟨111⟩ tips showed a circular symmetric COFI image and the main difference was the magnitude of the attractive forces ($\approx -150\,\mathrm{pN}$ vs. $\approx -30\,\mathrm{pN}$). The reduced electrostatic attraction for the ⟨111⟩ tip was explained by a higher populated d_{z^2} orbital in contrast to the ⟨100⟩ direction. The twofold symmetric image was explained by an asymmetric occupation of the d_{xz} and d_{yz} orbitals.

An important aspect in this work was the discrimination of tips which were terminated by different materials. For instance, a bulk W tip coated with Cu showed a similar force versus distance behavior as a bulk Cu tip, but a different one than clean bulk W or Fe tips. Hence, it is possible to identify if a bulk W or Fe tip is covered by sample material, which can happen after poking the tip into the Cu surface.

The reverse situation of the COFI measurements with bulk Cu tips is a Cu adatom on the (100), (110), and (111) facets of a Cu single crystal. Therefore, Cu adatoms were studied on Cu(111) and Cu(110). The (110) surface adatom is especially interesting, because the corresponding COFI image showed a twofold symmetry, which could be expected for the adatom as well.

5.2. Experimental Methods and Data Analysis

To perform abovementioned COFI and also to investigate adatoms with CO terminated tips, a Cu single crystal with low CO coverage is required. The Cu surface, either Cu(110) or Cu(111), is cleaned by repeated sputtering and annealing cycles.[1] Surface contamination with e.g. carbon, nitrogen, or sulphur was absent after this preparation as verified by Auger electron spectroscopy (AES). Afterwards the sample is introduced into the microscope and CO is leaked into the preparation chamber up to a pressure of $\approx 2 \cdot 10^{-6}$ mbar. The ion getter pump in the preparation chamber is switched off and the valve to the analysis chamber and the shields of the cryostat are opened before. The sample temperature usually increases to about 10 K when the shields are opened. After about 10 min, the shields are closed and the qPlus sensor is approached to the sample. The sensor is equipped with a bulk metal tip which was cleaned by field evaporation and the tunneling junction is usually stable upon approach. Applying bias pulses ($|1 - 5|$ V) or gentle poking[2] is often sufficient to obtain a tip which provides high resolution.

Figure 5.2a shows an example of a large scale topography image of the Cu(111) surface with various step heights, corresponding to single, double, and triple steps, see line profile in Fig. 5.2b. The STM topography image in Fig. 5.2c reveals the standing wave pattern of the Cu(111) surface state electrons scattered at defects [154]. Two types of defects are present in the image which appear as small and large spots. The smaller ones also appear slightly darker. They are identified as CO molecules, as their number increases when CO is leaked into the chamber. The shallower defect type is unknown. After a bias pulse was applied to the tip, the same area is imaged again. Figure 5.2d shows the result of the bias pulse: A protrusion of about 1 nm in height, indicating material transfer from the tip to the sample. The CO molecules can now be clearly identified as smaller and darker spots than the other defects.

[1] Annealing: $T_{\text{anneal}} \approx 700 - 800$ K, Sputtering: $p_{\text{Ar}} \approx 5 \cdot 10^{-5}$ mbar, $V_{\text{sputter}} = 1$ kV, Cycles: 3-8.
[2] The tip is approached a few hundreds of pm towards the surface from the STM set point and a bias voltage of 1-5 V is applied.

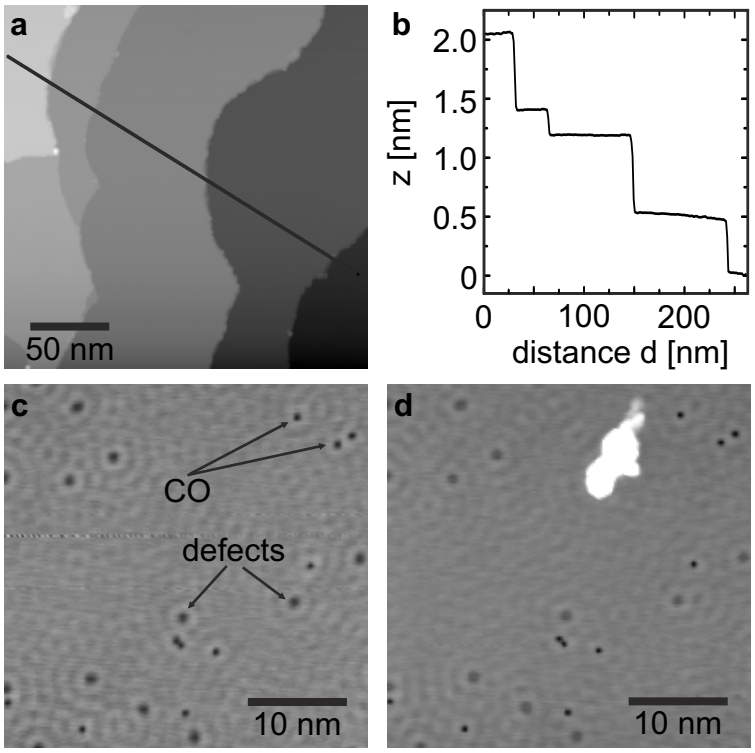

Figure 5.2.: **a**, large scale ($230 \times 230\,\mathrm{nm}^2$) STM topography image of the Cu(111) surface. **b**, line profile revealing single, double, and triple steps. The nearest neighbor distance of Cu is 255 pm and the distance between (111) planes is 208 pm. **c**, $36 \times 36\,\mathrm{nm}^2$ sized image showing a number of defects. The smaller dark spots are CO molecules. **d**, same area as in **c**. After applying a bias pulse to the tip, a protrusion appears on the surface. The COs can now be clearly distinguished from the other defects indicating that the tip got sharper. Note, the contrast in **d** is adjusted to highlight the COs. All images show raw data. Imaging conditions: **a**, $V = 1\,\mathrm{V}$, $I = 100\,\mathrm{pA}$, $A = 50\,\mathrm{pm}$; **c**,**d**, $V = -10\,\mathrm{mV}$, $I = 1\,\mathrm{nA}$, $A = 50\,\mathrm{pm}$.

Figure 5.3 shows the two basic experiments performed in this chapter where the CO always serves as a probe for the metal atom or atoms. In Fig. 5.3a the metal tip is scanned along a CO molecule on Cu(111). The shaded planes indicate constant height $\Delta f(x, y)$ maps at various tip-sample distances z to recover the interaction forces between tip and CO molecule. This kind of measurement is called COFI. The reversed situation is depicted in Fig. 5.3b where a CO molecule is attached to the tip and a single adatom on e.g. Cu(111) is investigated. The starting point of a $\Delta f(x, y, z)$ measurement is just before the CO, adsorbed either on the sample or the tip, is laterally manipulated by the tip-sample interaction forces. Between two constant height images the distance z from the sample is increased by Δz which is usually 5 or 10 pm. A typical data set consists of 50 to 100 constant height slices spanning a z range of 500 pm. Each slice contains frequency shift, excitation, amplitude, phase, and current data. For the following discussion, only the frequency shift and current data

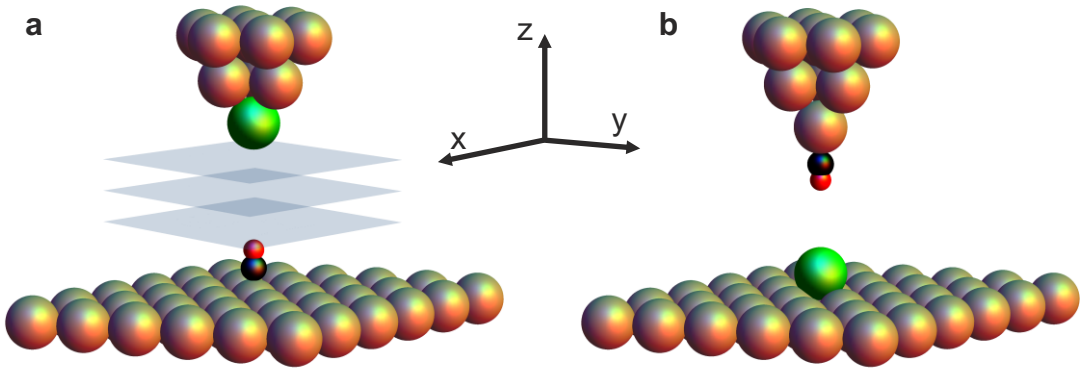

Figure 5.3.: **a**, principle of COFI and $\Delta f(x, y, z)$ data acquisition. The tip is repeatedly scanned in constant height mode above a CO (carbon = black ball, oxygen = red ball) molecule adsorbed on Cu(111) with varying tip-sample distances. **b**, CO terminated metal tip scanning across an individual adatom on the surface.

is relevant. Common parameters for image acquisition are a scan size of 2 by 2 nm^2 and an image resolution of 128×128 pixels. With a scan time of 2 s/line, the total acquisition time for 50 slices is around 7 h. When the feedback is off, the tip-sample junction is subject to lateral and vertical drift even at low temperatures.[3] The vertical drift can be corrected after the data acquisition if an $I(z)$ curve on the bare Cu surface is available. The $I(z)$ curve must be acquired fast enough to avoid any drift effects. The correction is then performed by matching the average tunneling current value above the bare Cu surface for each constant height slice with the $I(z)$ curve. Lateral drift can be either corrected by cross correlation of subsequent current images or, in case of a constant drift rate, by linear correction. Further details to these correction methods can be found in [20, 30, 91, 117]. Another possibility to account for the drift is to compensate it already during data acquisition. This is done in the following way:

1. A fast STM feedback image (e.g. 0.1 s/line, $|U| = 10$ mV, $I = 100$ pA) of a CO or adatom is acquired. Then the tip is positioned above the bare Cu surface and the change in tip-sample distance z is monitored. After a certain time (e.g. $5 - 20$ min) another STM feedback image is acquired. The lateral drift velocities are determined from cross correlation with the first feedback image. A higher number of pixels for the feedback image than for the constant height slices results in a better correction. The vertical drift is obtained from a linear fit to the monitored z data, of course, the drift needs to be linear within the time interval. Afterwards, the values of the drift velocities v_x, v_y, and v_z are set

[3] Typical values for the vertical drift rate of the commercial LT STM/AFM are around $5 - 10$fm/s, corresponding to a substantial vertical drift of $130 - 260$ pm within an acquistion time of 7 h.

into the linear drift correction feature of the control electronics. Step 1 is only executed once to find the initial drift velocities.

2. A constant height image is now acquired while the drift correction is active. Afterwards a STM feedback image is recorded again to determine the new values of the lateral drift velocities v_x and v_y from cross correlation with the previous feedback image. The new value for v_z is again determined from the change in z during the acquisition time of the constant height image. The updated set of v_x, v_y, and v_z is then used for the linear correction during the next constant height image, which is offset by Δz from the previous one. Step 2 is repeated until the desired number of constant height slices is obtained.

This method only works reliably when there is no significant change of the drift velocities within the acquisition time of a single constant height image. If the drift velocity is linearly reduced from 10 fm/s to 9 fm/s within 10 min the z position is over corrected by 300 fm. For $\Delta z = 10$ pm this corresponds to a tolerable error of 3%. In contrast, a change from 10 fm/s to 1 fm/s within the same time results in 3 pm overcorrection which is definitely too high. In principle, one could also perform the correction after each scan line or even after each pixel, but due to the overall high stability of the microscope this was not necessary. The above steps are automatically implemented via a LabVIEW[4] routine[5] into the SPM control software.

The drift corrected $\Delta f(x, y, z)$ data set is then used to evaluate the short-range force F_{sr} and potential E_{sr} of the interaction between CO and the metal tip atom or adatom. In the Δf images there is no atomic scale contrast visible above the bare Cu surface (Fig. 5.4a), therefore the Δf values at the edges are averaged. This average value is then subtracted from the constant height map leaving only the short-range contribution to the tip-sample interaction Δf_{sr}. From Δf_{sr}, the force F_{sr} can be obtained via deconvolution as described in section 2.2.3. The Sader-Jarvis method includes a derivation which leads to an enhancement of any noise present in the raw data. Therefore the Δf data is filtered before the deconvolution. Two filters are applied to reduce the noise. First, a Fourier filter is used to remove random vibrations which are always present in our system regardless of tip and sample conditions. They are attributed to intrinsic mechanical resonances of the cryostat which are insufficiently damped by the vibration isolation system of the microscope. This leads to certain peaks in a frequency range from $7 - 9$ Hz. These peaks are removed from the Fourier

[4]LabVIEW 2009, National Instruments, Austin, USA.

[5]Programmed by Johannes Licha during his Bachelor thesis on "Implementierung einer Driftkorrektur für subatomar aufgelöste 3D-Rastersondenspektroskopie" [155], advised by T. Hofmann.

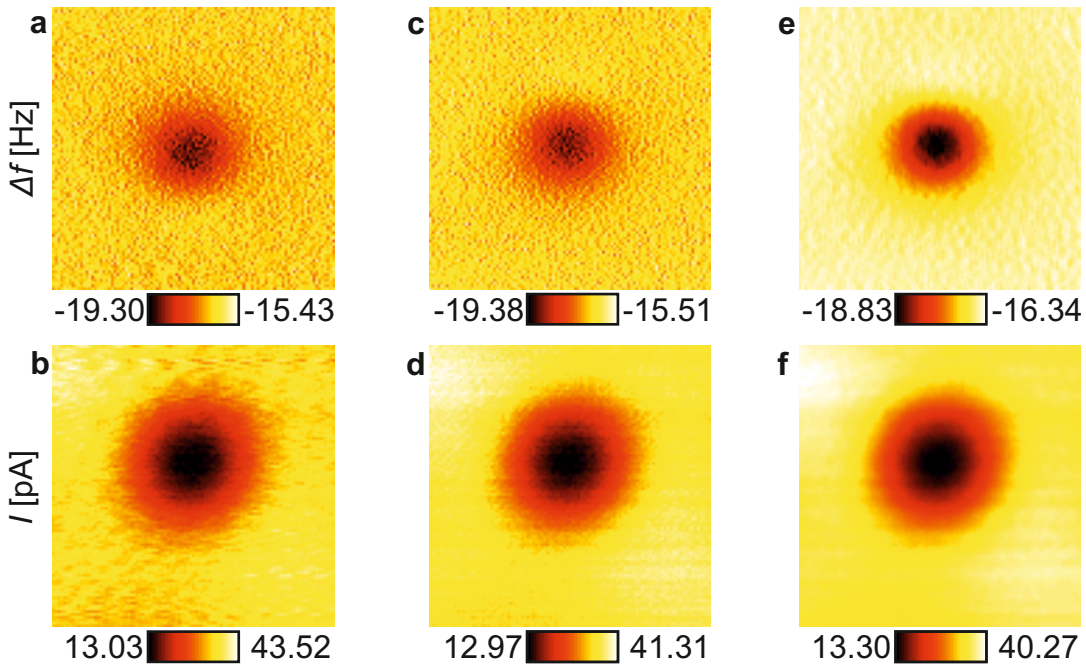

Figure 5.4.: Effect of Fourier and low-pass filtering on raw image data representing a circular symmetric COFI image of a bulk Fe tip. **a**,**b** Δf and I raw data. The uncorrelated oscillations are more apparent in the I data in **b**. **c**,**d**, Δf and I data after applying the Fourier filter. **e**,**f**, same data after additional low-pass filtering with a two dimensional Gaussian function with a width of 31 pm. The images are cutouts with a size of $1.56 \times 1.56\,\mathrm{nm}^2$ of the original images ($2 \times 2\,\mathrm{nm}^2$). The clipping of the images is necessary because both filters introduce artifacts at the edges which can falsify the force deconvolution and the average tunneling current values. Note, there is no vertical offset between the Δf and I data, but the tunneling current minimum does actually not coincide with the Δf minimum. Imaging parameters of the original image: frame size $= 2 \times 2\,\mathrm{nm}^2$, pixels $= 128 \times 128$, scan speed $= 3\,\mathrm{s/line}$, $V = -1\,\mathrm{mV}$, $k = 1800\,\mathrm{N/m}$, $f_0 = 59.369\,\mathrm{kHz}$, $A = 50\,\mathrm{pm}$.

spectrum of each constant height image by replacing them with an average of the values which embed the $7 - 9\,\mathrm{Hz}$ band. The inverse Fourier transform is applied to obtain a filtered real-space image.[6] The Fourier filter can of course only be applied if the signal frequency differs significantly from the mechanical resonances. This is the case when a single CO or adatom is scanned at a rate of 2s/line which corresponds to a signal frequency of 0.5 Hz. Second, a two-dimensional Gaussian low-pass filter is applied with a width of $\sigma = 31\,\mathrm{pm}$. For an image with 128×128 pixels and a size of $2 \times 2\,\mathrm{nm}^2$ this corresponds to a standard deviation of 2 in terms of pixels.[7] The influence of the filtering on the frequency shift and tunneling current raw data is shown

[6]The script used to implement this routine into MATLAB was supplied by Dr. Jay A. Weymouth. MATLAB, The MathWorks, Inc., Natick, USA.

[7]More information on Gaussian filtering with MATLAB can be found at `http://www.mathworks.de/de/help/images/ref/fspecial.html?searchHighlight=fspecial`

in Fig. 5.4 for a COFI image representing a circular symmetric tip. The mechanical oscillations are more apparent in the I raw data (Fig. 5.4b) than in Δf (Fig. 5.4a). In Figs. 5.4c,d the oscillations are removed without changing the appearance of the constant height images. Furthermore, the contrast[8] in the Δf image (Fig. 5.4c) is not changed. The additional low-pass filter (Figs. 5.4e,f) reduces the roughness of the images in particular for the Δf data.

5.3. Adatoms Studied with CO Functionalized Tips

The COFI method probes the tip apex with a CO molecule which is bonded to the surface. Another common application of the CO molecule is to terminate a metallic tip by picking up a CO from the sample. This was first demonstrated in STM by Bartels *et al.* [135] and can be used for adsorption site determination due to the enhanced structural resolution [156]. Another possibility is to make use of the p wave character of the CO orbital structure to achieve higher resolution in molecular orbital imaging [157]. The combination of CO terminated tips and AFM with small oscillation amplitudes led to a breakthrough in the study of molecules adsorbed on surfaces, namely, the imaging of the chemical structure of a pentacene molecule on Cu(111) and NaCl/Cu(111) [21]. This is possible because the lone pair electrons of the oxygen atom terminating the CO tip are unable to form covalent bonds [142]. The submolecular resolution stems from Pauli repulsive forces when regions with high electron density overlap [21, 158]. Although CO terminated tips offer very high resolution, they also create some artifacts. Especially when imaging at close tip-sample distances, CO bending and amplification of apparent bond lengths occurs [21, 159]. In the following, Cu adatoms are studied on Cu(111) and Cu(110) with CO terminated tips.

5.3.1. Cu Adatoms on Cu(111)

Cu adatoms on Cu(111) are created by strong pokes (poke depth is tens of nanometers) of a bulk W tip into the Cu surface. This results usually in a large indention in the surface (Fig. 5.5a). Small protrusions can often be found in the vicinity of such a poke site (inset Fig. 5.5a). These are almost certainly Cu atoms from the surface which are sprayed around the poke site. Before picking up a CO molecule from the surface the tip is gently poked until a highly attractive, circular symmetric Δf profile shows up in the COFI image (Fig. 5.5b). It turned out that the CO pickup only

[8] In Fig. 5.4a the contrast is $|-15.43+19.30| = 3.87$ which equals $|-15.51+19.38| = 3.87$ from Fig. 5.4b.

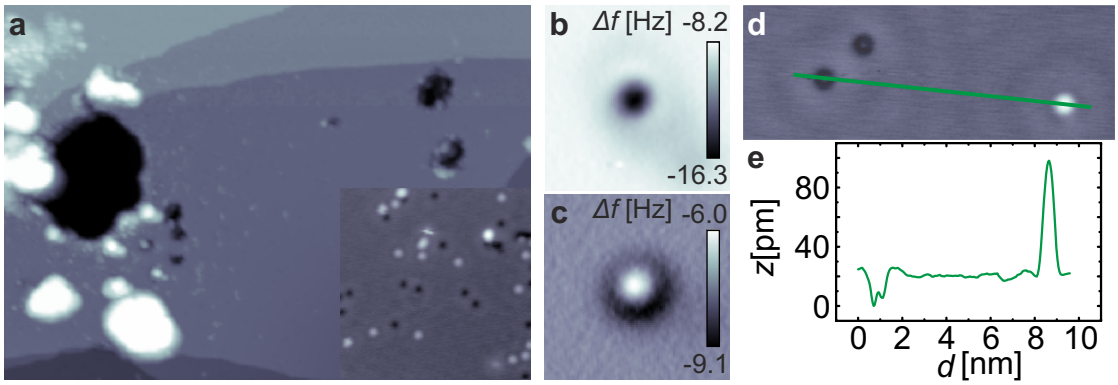

Figure 5.5.: **a**, large scale ($173 \times 104\,\mathrm{nm}^2$) topographic image of Cu(111), showing smaller and larger indentations which were created by heavily poking a W tip. The poke sites are surrounded by many small protrusions, which are most likely individual Cu atoms and Cu clusters. The inset ($21.1 \times 21.1\,\mathrm{nm}^2$) shows several adatoms and clusters (protrusions) and CO molecules (depressions). **b**,**c**, constant height Δf maps ($1.5 \times 1.5\,\mathrm{nm}^2$) of the interaction of a metallic tip and a CO tip with a CO molecule on Cu(111). **d**, topography image with a CO terminated tip. Two CO molecules and a single Cu adatom with a height of about 80 pm, see line profile in **e**, can be identified. Imaging parameters: **a**, $V = -1\,\mathrm{V}$, $I = 100\,\mathrm{pA}$; inset in **a**, $V = -1\,\mathrm{V}$, $I = 50\,\mathrm{pA}$; **b**, $V = -10\,\mathrm{mV}$, $A = 50\,\mathrm{pm}$; **c**, $V = -100\,\mathrm{mV}$, $A = 50\,\mathrm{pm}$; **d**, $V = 100\,\mathrm{mV}$, $I = 50\,\mathrm{pA}$.

works reliable with such tips. As a next step the tip is positioned on top of a CO and the tunneling parameters are set to $V = 1\,\mathrm{V}$ and $I = 1\,\mathrm{nA}$. Then the feedback is switched off and the bias voltage V is increased in 0.1 V intervals. Usually, nothing happens below $V = 2.0 - 2.3\,\mathrm{V}$. Somewhere in the range between $V = 2.5 - 3.0\,\mathrm{V}$ the CO either jumps to a neighboring lattice site, disappears, or is adsorbed to the tip front atom. A successful pick up can be identified via COFI (Fig. 5.5c). The CO-CO interaction is repulsive in the center, surrounded by an attractive ring [160, 161]. Furthermore, one can already identify a slight deviation from a perpendicular alignment between the two CO molecules. This can be seen from the asymmetry of the CO-CO interaction where the ring around the repulsive center is more attractive (darker) on the lower side. In the STM topography the CO tip can also be identified by the characteristic "donut-like" appearance of CO molecules on the surface [135]. Figure 5.5d shows two CO molecules and an adatom imaged with a CO terminated tip. The apparent height of the Cu adatom is $\approx 80\,\mathrm{pm}$ (Fig. 5.5e).

The interaction between the Cu adatom and a CO tip can now be investigated and compared to the COFI data for bulk Cu tips obtained by Hofmann [30, 117]. Figures 5.6a,b show Δf images of a so-called $\langle 111 \rangle$ oriented bulk Cu tip probed by a CO on the surface and a Cu adatom on Cu(111) imaged with a CO terminated tip. Both images were acquired in constant height mode. The appearance of the tip atom

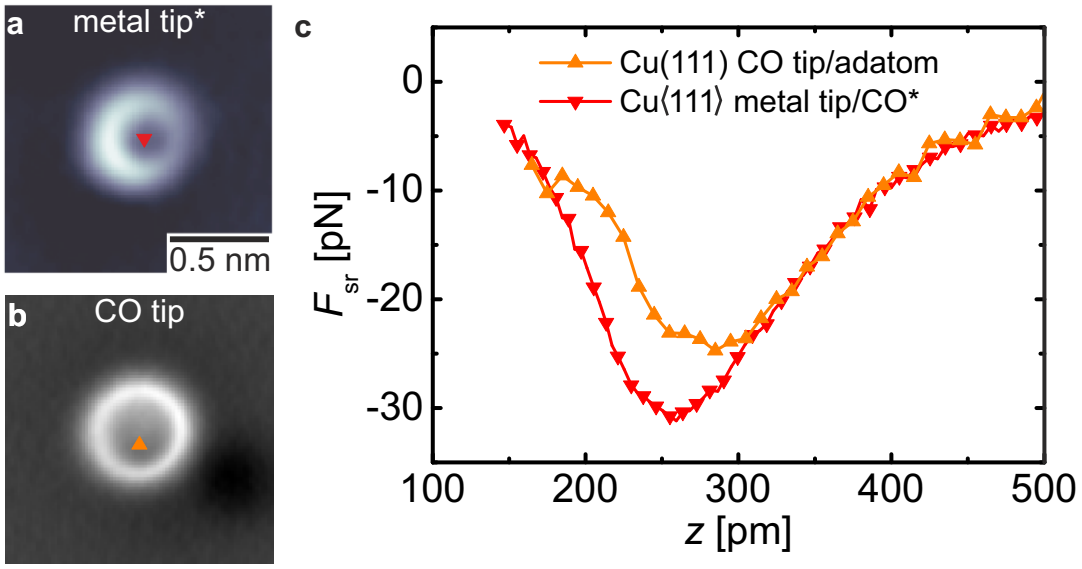

Figure 5.6.: Comparison of constant height Δf images. **a**, COFI with a $\langle 111 \rangle$ oriented Cu tip. **b**, low-pass filtered ($\sigma = 47\,\mathrm{pm}$) image of a Cu adatom on Cu(111) surface, acquired with the CO terminated tip from Fig. 5.5b. **c**, deconvoluted $F_{\mathrm{sr}}(z)$ curves. The triangles in **a** and **b** mark the positions where the corresponding $\Delta f_{\mathrm{sr}}(z)$ curves were acquired. These are the positions of the minimum attractive interaction in the $\Delta f_{\mathrm{sr}}(x, y, z)$ data set. This is not exactly at the center which is probably due to the tilted CO tip. Sensor parameters: $\langle 111 \rangle$ tip, $k = 1800\,\mathrm{N/m}$, $f_0 = 26.969\,\mathrm{kHz}$, $A = 50\,\mathrm{pm}$; $\langle 111 \rangle$ adatom, $k = 1800\,\mathrm{N/m}$, $f_0 = 27.851\,\mathrm{kHz}$, $A = 50\,\mathrm{pm}$. Data marked with an asterisk (*) was acquired by T. Hofmann and is adapted from [30]. The scale bar is valid for both images.

and the adatom is quite similar both are circular symmetric and have a toroidal or ring-like shape. For the adatom (Fig. 5.6b) the ring is a bit sharper which is probably due to the stronger bending of the CO when adsorbed on the tip [161]. Figure 5.6c shows $F_{\mathrm{sr}}(z)$ curves for quantitative comparison. The curves are extracted from a $F_{\mathrm{sr}}(x, y, z)$ data set[9] and the position of the curve corresponds to the minimum in the attractive force. The z distance for the Cu tip (red triangles) was referenced to the metal-metal point contact [30]. The curve for the Cu adatom (orange triangles) was shifted such that the attractive branch overlaps. This is based on the assumption that at larger separations the electrostatic and van-der-Waals interactions for both systems are similar. The good agreement in this region shows that the two cases, CO/tip-atom versus adatom/CO-tip, are quantitatively comparable. For the Cu tip, the force reaches a minimum of about $-31\,\mathrm{pN}$ whereas for the Cu adatom it is $-25\,\mathrm{pN}$. The deviation at closer distances ($z < 300\,\mathrm{pm}$) is probably caused by the different stiffness of the CO when it is adsorbed on the tip or on the plain surface [161].

[9] For the COFI data set the drift was corrected after image acquisition [117], whereas for the adatom data set the drift was already compensated during data acquisition.

It should be mentioned that the interaction between a CO terminated tip and a Cu adatom was already studied by Welker and a minimum attractive force of −28 pN was observed [91].

5.3.2. Cu Adatoms on Cu(110)

The experimental procedure for Cu(110) is the same as for Cu(111): A poked W tip is used, however the CO pickup turned out to be more difficult than on Cu(111) but finally it worked (Figs. 5.7a,b). Figure 5.7c shows CO molecules and an adatom on Cu(110) imaged with the CO terminated tip. The apparent height of the adatom is about 70 pm. The fcc crystal structure and its (110) surface is depicted in Figs. 5.8a,b. The surface unit cell is rectangular and the natural adsorption site of a Cu adatom is the hollow site (∘ in Fig. 5.8b). In Figs. 5.8c,d STM topography z raw and filtered data is shown. The low-pass and Laplace[10] filtered image in Fig. 5.8d reveals the atomic lattice below the Cu adatom which is indicated by the superimposed grid (dashed lines). The center of the adatom (black cross) is very close to the position of the hollow site which is indicated by the intersection of the two solid lines in Fig. 5.8d. One can therefore deduce that the adatom is adsorbed on a hollow site. The simultaneously collected Δf image (Fig. 5.8e) also resolves the atomic lattice, but there is a systematic shift along the [001] direction with respect to the STM data (the grid in Figs. 5.8d,e is the same). Note, this shift is not an artifact of the phase

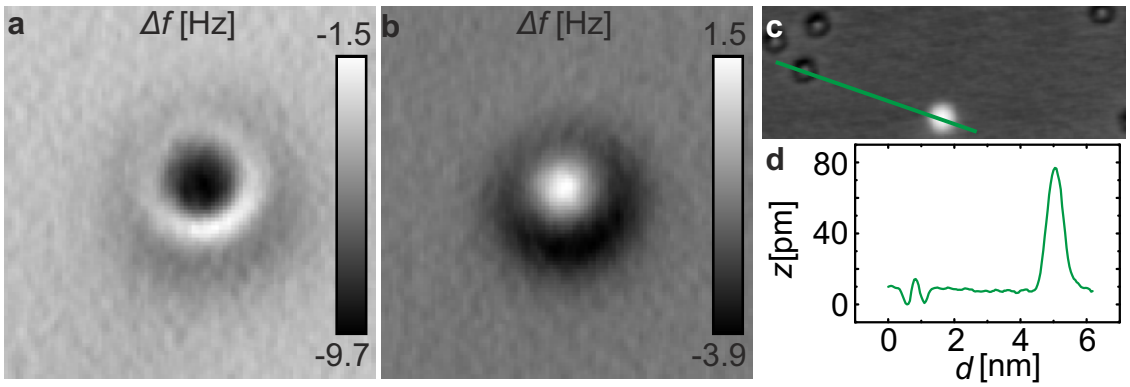

Figure 5.7.: **a**,**b**, COFI images ($1.5 \times 1.5\,\mathrm{nm}^2$) before and after CO pickup on Cu(110). **c**, STM image with a CO terminated tip ($V = 500\,\mathrm{mV}$, $I = 50\,\mathrm{pA}$). Several CO molecules and a single adatom can be identified. The apparent height of the adatom is about 70 pm, see line profile in **d**.

[10]Laplace filter refers to the second derivative with respect to x and y ($\Delta z(x,y) = \frac{\partial^2 z}{\partial x^2} + \frac{\partial^2 z}{\partial y^2}$). The mathematical symbol for the Laplace operator is Δ, but to avoid confusion with other expressions like Δf the Laplace filter is indicated with Lap(Δf) or Lap(z). Data processed with WSxM 5.0 Develop 5.1, Nanotec Electronica S.L., Madrid, Spain, [162].

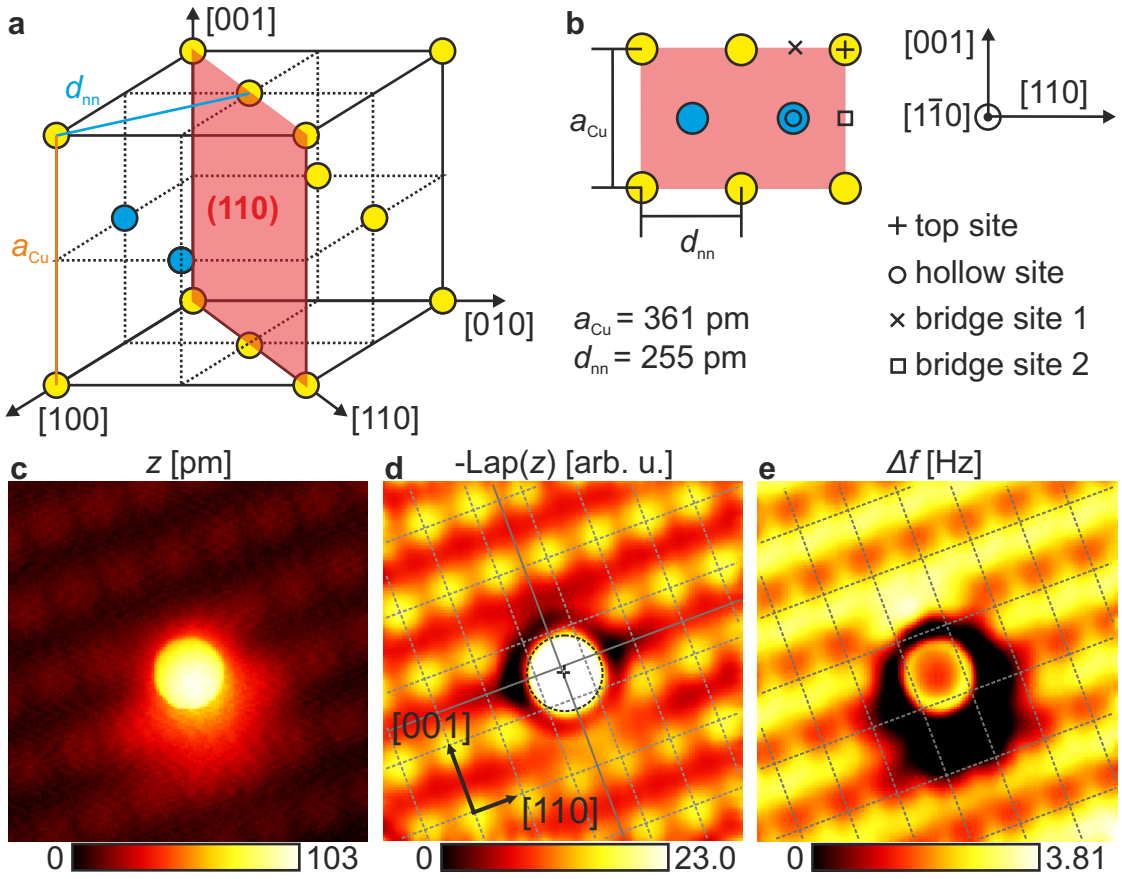

Figure 5.8.: **a**, (110) plane indicated in fcc unit cell. **b**, top view onto (110) plane. The balls in yellow indicate the surface layer atoms, whereas the cyan blue balls indicate the expected position of adatoms or a subsequent layer of Cu atoms. The rectangular surface unit cell has four high symmetry positions – hollow site (○), top site (+), bridge site 1 (×), and bridge site 2 (□). **c**, STM topography image of Cu adatom acquired with the CO tip from Figs. 5.7c,d. **d**, inverted Laplace filtered version from **c**. The contrast is increased for the Cu surface atoms and the image was low-pass ($\sigma = 140\,\mathrm{pm}$) filtered before and after the Laplace filter was applied. **e**, simultaneously acquired Δf data ($\sigma = 70\,\mathrm{pm}$). The solid grid lines correspond to the surface layer and the dashed ones to the adatom layer. Imaging parameters: $1.8 \times 1.8\,\mathrm{nm}^2$, $V = -10\,\mathrm{mV}$, $I = 3\,\mathrm{nA}$, $A = 50\,\mathrm{pm}$.

demodulator. The scan time per line is 2.57 s and the scan direction is from left to right. Assuming that 7 atoms are scanned within one line[11], this corresponds to a modulation frequency of $\approx 2.7\,\mathrm{Hz}$ whereas the phase demodulator bandwidth was set to 30 Hz. If the phase demodulator bandwidth would be too small, there would also be a lag between the STM and Δf data acquisition which results in a lateral shift of the observed features. Such a lateral shift is not present in Figs. 5.8d,e. Instead the shift is along the [100] direction which is rotated with respect to the lateral scan

[11] This is an overestimate, because 7 atoms would be scanned within one line if the scan direction would be along the [110] crystal direction.

direction. The frequency shift is a non-monotonic function of the distance z, therefore the contrast regime (attractive or repulsive) on top of the surface atoms needs to be known if one would like to compare Figs. 5.8d,e properly. In the following, distance dependent Δf data will be analyzed and discussed.

Figure 5.9 shows Δf data of the Cu adatom for three distances z. The corresponding $\Delta f(x, y, z)$ data set was acquired with the automated drift correction routine ($\Delta z = 5\,\mathrm{pm}$) similar as for the adatom on Cu(111). The adatom first shows more negative frequency shift than the surrounding Cu surface and therefore the interaction between the CO tip and the adatom is attractive (Fig. 5.9a). When approaching the tip closer by 110 pm (Fig. 5.9b) the adatom appears more repulsive than the background Cu surface. At the distance of closest approach $\Delta z = 0$ (Fig. 5.9c) the adatom has a ring-like shape, similar to the adatom on Cu(111) (Fig. 5.6b). The rectangular unit cell of the Cu(110) surface can again be identified from the atomically resolved surface layer besides the adatom. In the [110] direction the adatom is in between two atomic rows, but along the [001] direction a clear assignment cannot be made. It almost seems that the adatom sits directly on a Cu atom of the underlying layer, however the actual adsorption site is the hollow site (Fig. 5.8).

The Δf images in Figs. 5.9a-c are just an example for a general problem which occurs when imaging with CO functionalized tips in constant height mode [163]. When the underlying Cu lattice is resolved at close tip-sample distances (Fig. 5.9c) there is already a strong repulsive interaction present between the CO tip and the adatom. On top of the adatom lateral forces act on the CO tip and lead to a bending of the CO. This can create artifacts as mentioned above. Therefore, a straightforward relation between the position of the adatom relative to the underlying Cu lattice is problematic, e.g. from Fig. 5.9c it seems that the adsorption site of the Cu adatom is rather a bridge site instead of a hollow site. The possible adsorption sites of an adatom on the Cu(110) surface are indicated in the schematic of the fcc (110) surface unit cell in Fig. 5.8b.

To analyze this discrepancy in more detail, the experimental images are low-pass filtered and the contrast is adapted to highlight the corrugation of the underlying Cu lattice (Figs. 5.9d-f). At further tip-sample distances (Fig. 5.9d) only the rows along the [110] direction are faintly detectable. As the adatom appears attractive in this regime the surface layer atoms also appear attractive. The rows which appear darker in the Δf image are indicated by dashed red lines. This is where the surface layer atoms are located along the [110] direction. The center (green cross) of the green ellipse marks the position of the adatom. It is very close to the solid red line in Fig.

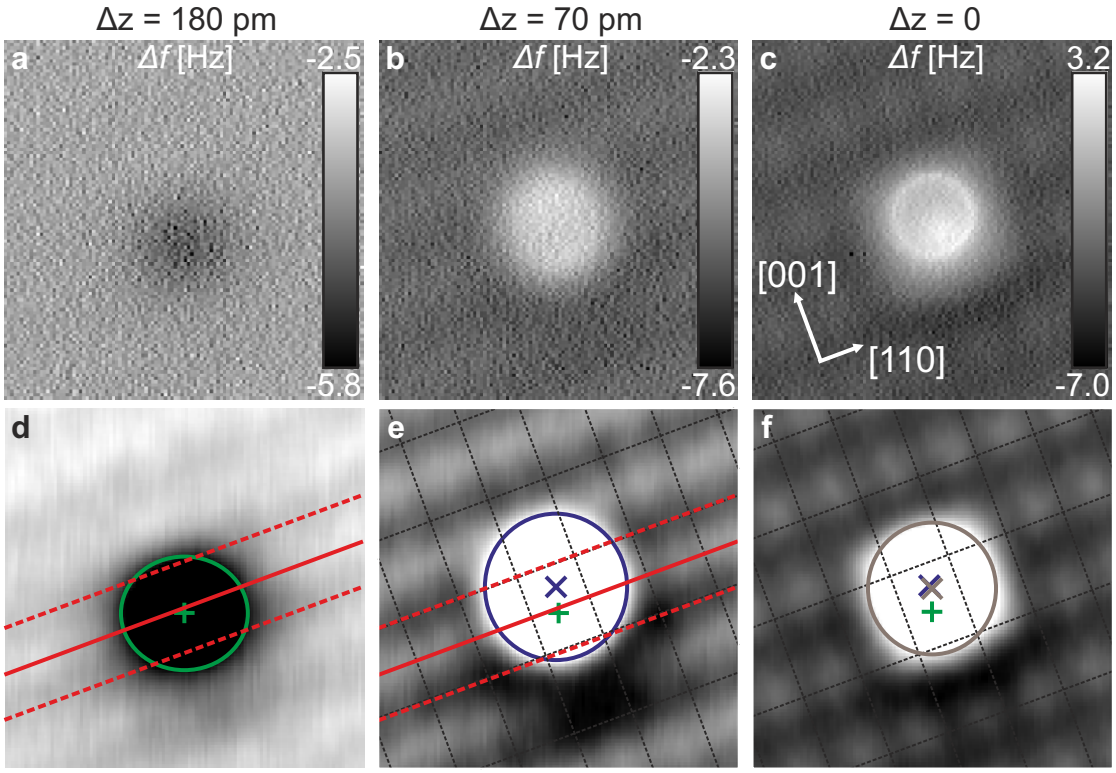

Figure 5.9.: Distance dependent constant height Δf images of a Cu adatom on Cu(110) for three distance regimes. The images were acquired with a CO terminated tip. The first row shows raw data. The second row shows same data, but low-pass filtered (**d**, $\sigma = 155\,\mathrm{pm}$; **e**,**f**, $\sigma = 113\,\mathrm{pm}$.) and with adjusted z scales to increase the contrast on the underlying Cu lattice. **a**,**d**, at a relative z position of 180 pm from the closest approach the adatom appears as a depression in Δf. **b**,**e**, tip is approached closer by 110 pm and the adatom now shows up as a protrusion. **c**,**f**, at closest approach ($\Delta z = 0$) the adatom still remains overall repulsive, but a dip appears in the center resulting in a toroidal shape of the adatom. Imaging parameters: $1.55 \times 1.55\,\mathrm{nm}^2$, 110×110 pixels, 1.5 s/line, $V = -10\,\mathrm{mV}$, $k = 1800\,\mathrm{N/m}$, $f_0 = 27.846\,\mathrm{kHz}$, $A = 50\,\mathrm{pm}$.

5.9d which indicates the position in between two rows of atoms from the surface layer. In Fig. 5.9e one can also identify the position of the atoms along the [001] direction. The surface unit cells are indicated by the overlaid grid (dashed lines). A comparison of the red lines from Fig. 5.9d with the grid in Fig. 5.9e shows that the surface layer atoms still appear more attractive in Δf. Therefore, the contrast inversion from attractive to repulsive which happened for the adatom from Figs. 5.9a,d to Figs. 5.9b,e did not yet occur for the surface layer atoms. As a consequence one cannot relate the center position of the adatom (blue cross) in Fig. 5.9e to the position of the Cu atoms indicated by the grid. The repulsive adatom in Fig. 5.9e is marked by the blue circle and its center (blue cross) is shifted upwards by about 100 pm with respect to the adatom center in Fig.5.9d (green cross). The position of the blue cross relative to the overlaid grid does not fit to any of the high symmetry positions of the

underlying lattice. This can be inferred from a comparison with the structural model (Fig. 5.8b). In contrast, the original position of the adatom (green cross) is close to the center of one of the dashed rectangles from the grid. This position corresponds to the hollow site.

At the closest imaging distance (Fig. 5.9f), the adatom position relative to Fig. 5.9e changed only slightly (compare brown and blue cross). But now, there is a shift of the atomically resolved surface atoms with respect to the position of the dashed grid which is the same as in Fig. 5.9e. If the shift is just due to a contrast inversion of the surface layer atoms from attractive to repulsive, one would expect that the intersection points of the grid in Fig. 5.9f coincide with the local repulsive maxima (brighter spots). This is not the case, but the intersection points of the grid are located somewhere in between and again do not match to any of the high symmetry sites of the unit cell. Therefore it is unlikely that a pure contrast inversion is responsible for this systematic shift which has no clear relation to the lattice vectors of the surface. Instead, it is most likely that the shift is caused by the bending of the asymmetric CO tip [160, 161]. First, this affects the imaging of the adatom which gets apparently shifted and after approaching closer to the surface the imaging of the underlying Cu lattice is also affected. Note, creep or thermal drift as a source of these shifts can be excluded, because the drift correction was performed after each constant height slice during data acquisition.

Finally, the above presented analysis also leads to the conclusion that the adsorption site of the investigated adatom on Cu(110) is a hollow site. Although, it is very important for a proper adsorption site assignment to compare Δf images (Fig. 5.9d,e) at different relative tip sample distances Δz to avoid misinterpretation of the constant height data for this system.

Similar as for the measurements on Cu(111), the adatom data is compared with the corresponding tip data. Figure 5.10a shows the twofold symmetric COFI image of a Cu tip which was assigned to a $\langle 110 \rangle$ oriented tip [30]. Obviously, the adatom in Fig. 5.10b does not show such a twofold symmetry, but shows a similar ring structure as the adatom on Cu(111). Although the appearance in the Δf images is quite different the force versus distance behavior is also compared (Fig. 5.10c). The adatom data was shifted again to match the attractive branch of the COFI data. Surprisingly, they match very well and also the position ($\approx 270\,\mathrm{pm}$) and the magnitude ($\approx -23\,\mathrm{pN}$) of the attractive force minimum is equal. The higher slope in the repulsive regime for the $\langle 110 \rangle$ tip is probably due to the higher stiffness of the CO on the surface [161].

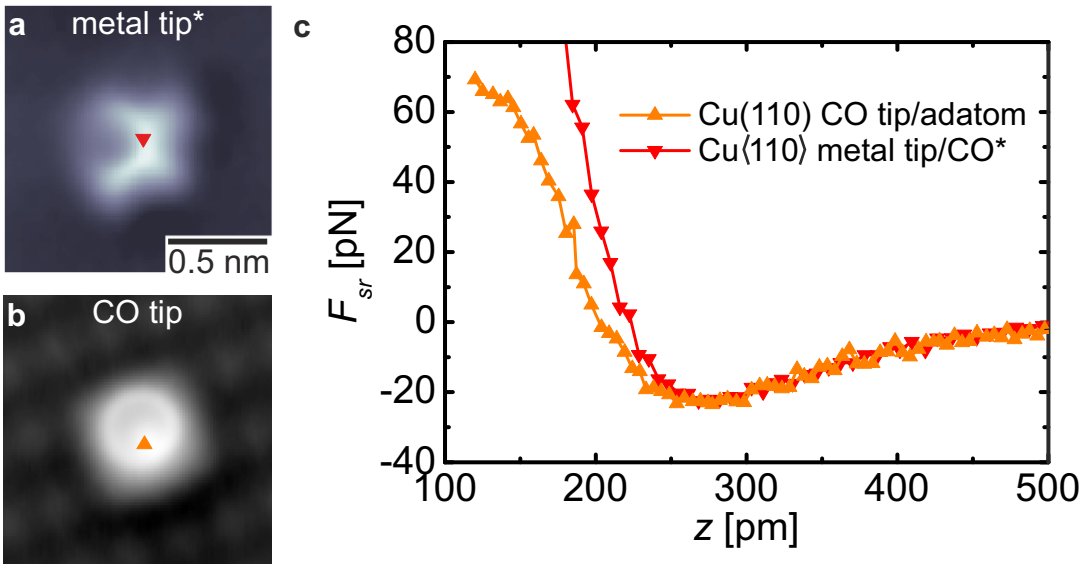

Figure 5.10.: Comparison of constant height Δf images. **a**, low-pass filtered COFI image of a $\langle 110 \rangle$ oriented Cu tip. **b**, low-pass filtered ($\sigma = 70\,\mathrm{pm}$) adatom image from Fig. 5.9c. **c**, deconvoluted $F_{\mathrm{sr}}(z)$ curves. In **b** the curve was taken at the position of the attractive minimum, which is not exactly at the center, due to the tilted CO tip. Sensor parameters: $\langle 110 \rangle$ tip, $k = 1800\,\mathrm{N/m}$, $f_0 = 26.969\,\mathrm{kHz}$, $A = 50\,\mathrm{pm}$; $\langle 110 \rangle$ adatom, $k = 1800\,\mathrm{N/m}$, $f_0 = 27.851\,\mathrm{kHz}$, $A = 50\,\mathrm{pm}$. Data marked with (*) was acquired by T. Hofmann and is adapted from [30]. The scale bar is valid for both images.

The absence of a clearly apparent twofold symmetry in Fig. 5.10b is to some extent astonishing. Therefore Δf images at $\Delta z = 25\,\mathrm{pm}$[12] and $\Delta z = 70\,\mathrm{pm}$ are analyzed in more detail (Fig. 5.11). In the raw image data (Figs. 5.11a,e) the adatom has a ring-like shape at $\Delta z = 25\,\mathrm{pm}$ whereas at $\Delta z = 70\mathrm{pm}$ it appears as a single protrusion. This still seems to be the case after applying a low-pass filter to the raw data (Figs. 5.11b,f). Additional Laplace[13] filtering confirms the ring-like shape of the adatom at $\Delta z = 25\,\mathrm{pm}$ (Fig. 5.11c). In contrast, at $\Delta z = 70\,\mathrm{pm}$ the Laplace filtered image clearly reveals a twofold symmetry in the Δf data. The twofold symmetric feature lines up with the rows along the [110] direction. Figures 5.11d,h display enlarged Laplace filtered images in a different color code to pronounce the local minima and maxima. One can now also identify a slight asymmetry at $\Delta z = 25\,\mathrm{pm}$ (Fig. 5.11d). None of these twofold symmetric images resembles the COFI image of a presumably $\langle 110 \rangle$ oriented bulk Cu tip (Fig. 5.10a).

To reveal the twofold symmetry, heavy low-pass and Laplace filtering of the raw data is required. This demonstrates already that the effect is rather subtle. Fig-

[12] At this distance the asymmetry in the image is not pronounced as strongly as at closest approach.
[13] Data processed with WSxM 5.0 Develop 5.1, Nanotec Electronica S.L., Madrid, Spain, [162].

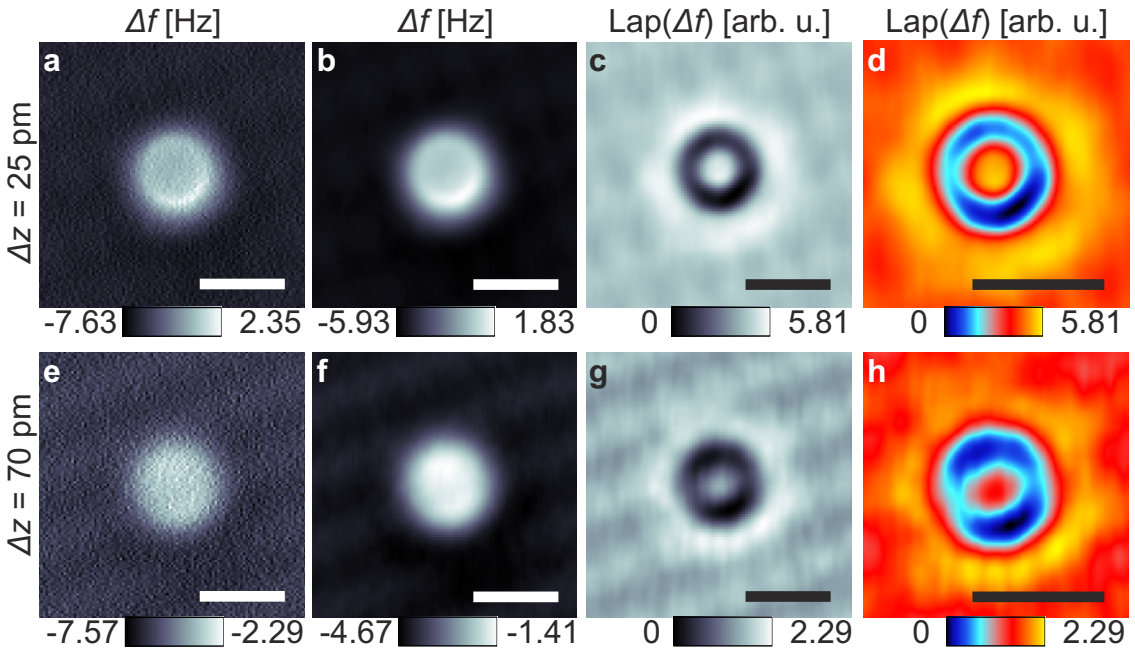

Figure 5.11.: Comparison of Δf images at $\Delta z = 25\,\mathrm{pm}$ (**a**-**d**) and $\Delta z = 70\,\mathrm{pm}$ (**e**-**h**). **a**,**e**, show raw data; **b**,**f**, low-pass filtered data ($\sigma = 70\,\mathrm{pm}$); **c**,**g**, Laplace and low-pass filtered data ($\sigma = 210\,\mathrm{pm}$); **d**,**h**, zoomed and interpolated versions from **c** and **g** which are plotted in a different color code to highlight the deviation from circular symmetry. In **h** a twofold symmetric structure which aligns with the rows along the [110] direction can be clearly identified. All scale bars are 0.5 nm. Frame size: $1.55 \times 1.55\mathrm{nm}^2$ except for (**d**,**g**) which are $1.0 \times 1.0\mathrm{nm}^2$. Imaging parameters: see Fig. 5.9.

ure 5.12 shows cross sections of the low-pass filtered adatom images from Figs. 5.11b,f.[14] At $\Delta z = 25\,\mathrm{pm}$ (Fig. 5.12b) the shape of the cross sections is qualitatively similar for the [110] and [00$\bar{1}$] direction. Both curves have two local maxima and a minimum in between. The Δf values of the two local maxima along the [110] direction (green curve) are $r_1^{25\,\mathrm{pm}} = 5.94\,\mathrm{Hz}$ and $r_3^{25\,\mathrm{pm}} = 6.22\,\mathrm{Hz}$ whereas the value of the local minimum is $r_2^{25\,\mathrm{pm}} = 5.63\,\mathrm{Hz}$. This gives an average difference between minimum (2) and maxima (1,3) for the green curve of 0.45 Hz. This is only about 7.5% of the overall Δf signal of $\approx 6\,\mathrm{Hz}$ which is caused by the adatom. A similar analysis for the [00$\bar{1}$] direction (blue curve) in Fig. 5.11b gives values of $b_1^{25\,\mathrm{pm}} = 5.97\,\mathrm{Hz}$, $b_3^{25\,\mathrm{pm}} = 7.58\,\mathrm{Hz}$, and $b_2^{25\,\mathrm{pm}} = 5.73\,\mathrm{Hz}$. The resulting average distance between minimum and maxima is 1.05 Hz which reaches about 15% of the overall contrast ($\approx 6.8\,\mathrm{Hz}$). This is about twice as much than for the green curve and is due to the asymmetry in the adatom image which is caused by the CO tip. The distance between the two local maxima is

[14] Figures 5.12a,c are interpolated (×8) versions from Figs. 5.11b,f for better visualization of the contours, whereas the line profiles (Figs. 5.12b,d) correspond to the non-interpolated data.

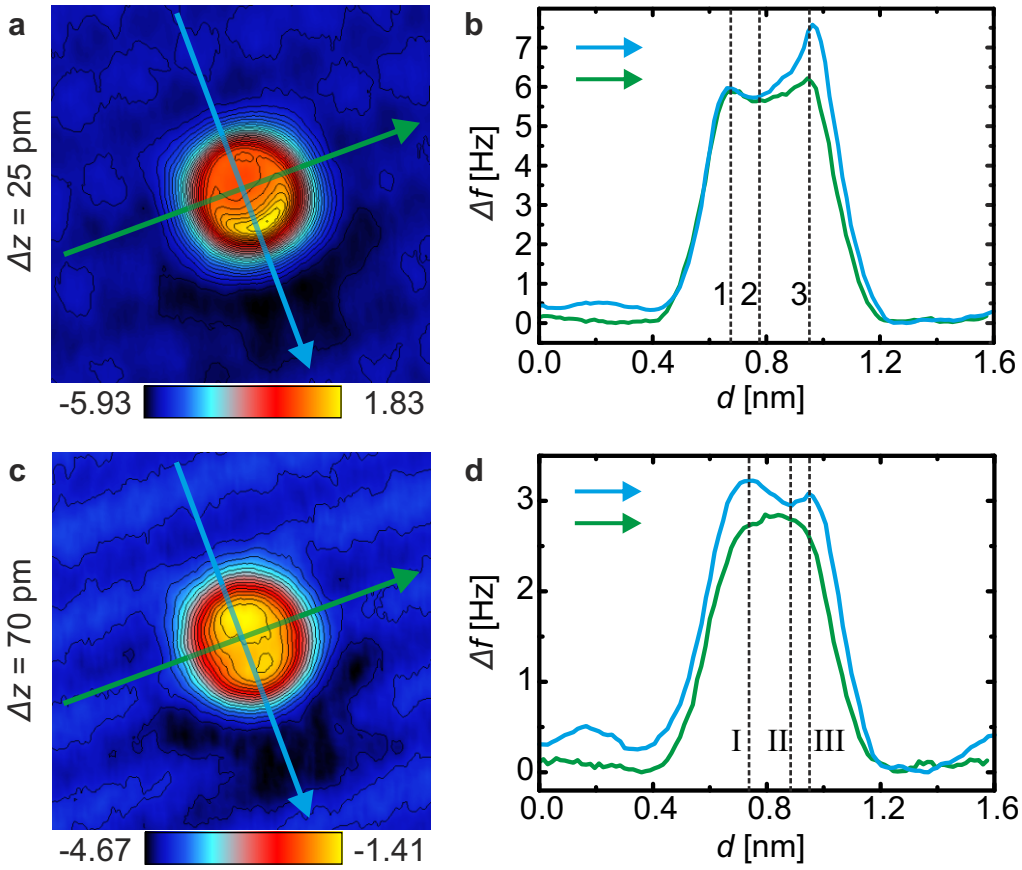

Figure 5.12.: **a**,**c** interpolated data as in Figs. 5.11b,f with contour lines (spacing: 0.28 Hz and 0.19 Hz) and line profiles across the adatom at $\Delta z = 25\,\mathrm{pm}$ (**b**) and $\Delta z = 70\,\mathrm{pm}$ (**d**). The line profiles are taken along two high symmetry directions (green = [110], blue = $[00\bar{1}]$). The dashed lines in **b** and **d** indicate the position of the local maxima and minima. Imaging parameters: see Fig. 5.9.

$\Delta d_{1,3} \approx 300\,\mathrm{pm}$.

At $\Delta z = 70\,\mathrm{pm}$ the shape of the two line profiles is distinctly different. The blue curve shows again two local maxima and a minimum whereas the green curve shows a single protrusion. Performing the same analysis as above for the blue curve yields $b_{\mathrm{I}}^{70\,\mathrm{pm}} = 3.22\,\mathrm{Hz}$, $b_{\mathrm{III}}^{70\,\mathrm{pm}} = 3.08\,\mathrm{Hz}$, and $b_{\mathrm{II}}^{70\,\mathrm{pm}} = 2.95\,\mathrm{Hz}$. The average difference between positions I,III and II is about 0.2 Hz which amounts to 6.3% of the overall Δf signal of 3.15 Hz. The distance between the two local maxima is $\Delta d_{\mathrm{I,III}} \approx 210\,\mathrm{pm}$. The analysis of the line profiles from the low-pass filtered images confirms that the twofold symmetries revealed by Laplace filtering (Figs. 5.11c,d,g,h) are real and not just over-interpretations of the filtered data. Furthermore one can roughly state that these *subatomic* features contribute less than 10% to the overall signal caused by the adatom.

Another interesting fact can be deduced from the simultaneously collected tun-

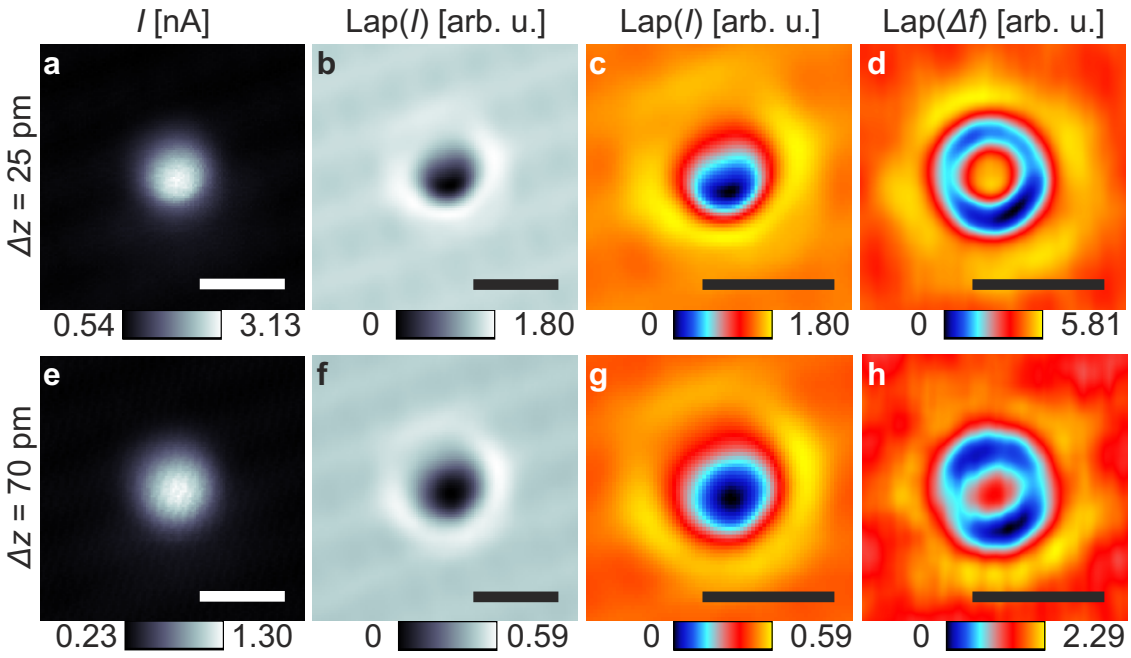

Figure 5.13.: Tunneling current I raw data (**a**,**e**) and low-pass ($\sigma = 210\,\mathrm{pm}$) and Laplace filtered data (**b**,**f**). **c**,**d** and **g**,**h** show a comparison between Laplace filtered I and Δf data at $\Delta z = 25\,\mathrm{pm}$ and $\Delta z = 70\,\mathrm{pm}$. Frame size for **a**,**b** and **e**,**f** is $1.55 \times 1.55\,\mathrm{nm}^2$; for **c**,**d** and **g**,**h** it is $1.0 \times 1.0\,\mathrm{nm}^2$. All scale bars are 0.5 nm. Imaging parameters: see Fig. 5.9.

neling current I. Figures 5.13a,e show the I data which corresponds to the Δf images from Figs. 5.11a,e. The tunneling current is increased above the adatom. In contrast to the Δf images, there are no twofold symmetric features revealed by applying low-pass and Laplace filters (Figs. 5.13b,f). In Figs. 5.13c,d and 5.13g,h enlarged Laplace filtered images of the tunneling current and frequency shift are shown for better comparison. The I data is qualitatively quite similar at both distances. At the same time it is obviously different from the Δf images as no twofold symmetry can be identified. The absence of a twofold symmetry in the tunneling current suggests that the small variation in the Δf signal is caused by electrons or orbitals which do not contribute to the tunneling current or at least not very much. The charge distribution of the more localized $3d$ orbitals is therefore a possible origin for the observed features. It should be noted that in COFI measurements the configuration of the tip apex can be identified in the tunneling current data via Laplace filtering [20, 91, 117]. This suggests that there is a distinct difference between the twofold symmetry observed on the adatom and the twofold symmetry observed for the Cu tip (Fig. 5.10a).

5.3.3. Model for the Charge Density of a Cu Adatom on Cu(110)

In order to understand the distance dependence of the Δf data for the Cu(110) adatom a simple model to determine the charge density of the Cu $3d$ orbitals is used [164]. To calculate the total interaction potential one should also consider e.g. the $4s$ orbital of the Cu adatom as this extends furthest into the vacuum [164]. On the other hand, the model presented in the following does not strive to obtain a quantitative agreement with the experimental data, but it should qualitatively explain the origin of the subtle twofold symmetric features from above. When going from a surface layer atom to an atom at a step edge charge redistribution occurs [165, 166]. The redistribution is more pronounced for s and p electrons than for d electrons. Nonetheless, there is an effect on the d orbital occupation which will be important for the following discussion. Slater-Type-Orbitals (STO) are used to describe the wave functions of the d electrons, their radial part has the following form [164]:

$$\phi(r) = N r^{n-1} \exp(-\zeta r), \tag{5.1}$$

where ζ is an effective screening constant which can be derived from the Slater rules [164, 167]. The normalization factor N is given by [168]

$$N = (2\zeta)^n \sqrt{\frac{2\zeta}{(2n)!}}, \tag{5.2}$$

for $3d$ orbitals $n = 3$ and $N = \sqrt{8/45}\,\zeta^{7/2}$. To account for the angular dependence of the d orbitals we use the corresponding real spherical harmonics d_i ($i \in z^2, x^2-y^2, xy, xz, yz$) which are summarized in (Tab. 5.1) [169]. Together with the radial part, the STOs are then given as

$$\Psi_{\mathrm{STO}}^{d_i} = \phi(r) d_i = \sqrt{\frac{8}{45}} \left(\frac{\chi}{a_{\mathrm{B}}}\right)^{7/2} r^2 \exp\left(-\frac{\chi r}{a_{\mathrm{B}}}\right) d_i, \tag{5.3}$$

where $\zeta = \chi / a_{\mathrm{B}}$ is expressed in units of the Bohr radius $a_{\mathrm{B}} = 52.9\,\mathrm{pm}$. We use a value of $\chi = 2/3$ for the adatom on Cu(110). This corresponds to a screening constant $\zeta = 1.26 \cdot 10^{10}\,\mathrm{m}^{-1}$ which was derived from the experimental $F_{\mathrm{sr}}(z)$ curve in Fig. 5.10c; more details can be found in A.2.

The electron density of the Cu adatom is then calculated via:

$$\rho = \sum_i q_{d_i} \cdot |\Psi_{\mathrm{STO}}^{d_i}|^2, \tag{5.4}$$

	d_{z^2}	$d_{x^2-y^2}$	d_{xy}	d_{xz}	d_{yz}
d_i	$\sqrt{\frac{5}{16\pi}}\frac{2z^2-x^2-y^2}{r^2}$	$\sqrt{\frac{15}{16\pi}}\frac{x^2-y^2}{r^2}$	$\sqrt{\frac{15}{4\pi}}\frac{xy}{r^2}$	$\sqrt{\frac{15}{4\pi}}\frac{xz}{r^2}$	$\sqrt{\frac{15}{4\pi}}\frac{yz}{r^2}$

Table 5.1.: Real part of spherical harmonics in cartesian coordinates which correspond to the d orbitals with $r^2 = x^2 + y^2 + z^2$.

where q_{d_i} is the charge per d orbital. Reference [30] gives the occupation of each d orbital which was calculated by taking the angular overlap of the tip atom with its nearest neighbor atoms (five for a Cu⟨110⟩ tip) into account. First, a relative energy splitting was determined which was then normalized to give a maximum occupation of $2e$ for the energetically lowest orbitals. The higher lying orbitals were then filled with the according fractions of the angular overlap, for details see Refs. [30, 117]. The occupations obtained from the angular overlap model were around 6 electrons per d shell for the three main symmetries, whereas a free Cu atom has 10 electrons in the d shell. The large deviation is attributed to the increased Smoluchowski effect at the tip apex.

For Cu(100), Cu(110), and Cu(111) surfaces *ab-initio* calculations found values of the d orbital occupation around $9.4 - 9.8e$ [147, 149, 152]. Interestingly, the calculated number of electrons in the d shell of an adatom on Cu(111) is $9.9e$ [150]. This is in agreement with calculations of the electronic structure of stepped surfaces where an increase in d orbital occupation for lower coordinated surface atoms is predicted [165, 166]. For the magnitude of the occupation of the d shell we therefore use a value of $9.7e$ which is somewhere in between the values given above. The distribution of this $9.7e$ among the individual d orbitals is such that all d orbitals, except the d_{yz} orbital, are filled with $2e$ (Fig. 5.14a). This occupation is based on the following arguments: If the CO tip approaches from $z = +\infty$ (Fig. 5.14a) towards the adatom or respectively the d orbitals it first interacts with electrons which are localized in orbitals with larger contributions in the $+z$ direction. Among the d orbitals these are the d_{z^2}, d_{xz}, and d_{yz} orbitals. As d_{z^2} is symmetric around the z axis it cannot give rise for a twofold symmetry and therefore its occupation is left untouched. The $d_{x^2-y^2}$ and d_{xy} orbitals are also not considered to contribute to the asymmetry in the charge distribution detected by AFM as they are more confined to the (x, y) plane at $z = 0$. The surface unit cell of Cu(110) is rectangular, therefore the overlap of the d_{xz} and d_{yz} orbitals with the nearest neighbor atoms is not equal and one can expect a difference in the occupation. Now, one of these two orbitals, d_{xz}, is still occupied by $2e$ whereas the other one, d_{yz}, is only partially filled with $1.7e$.

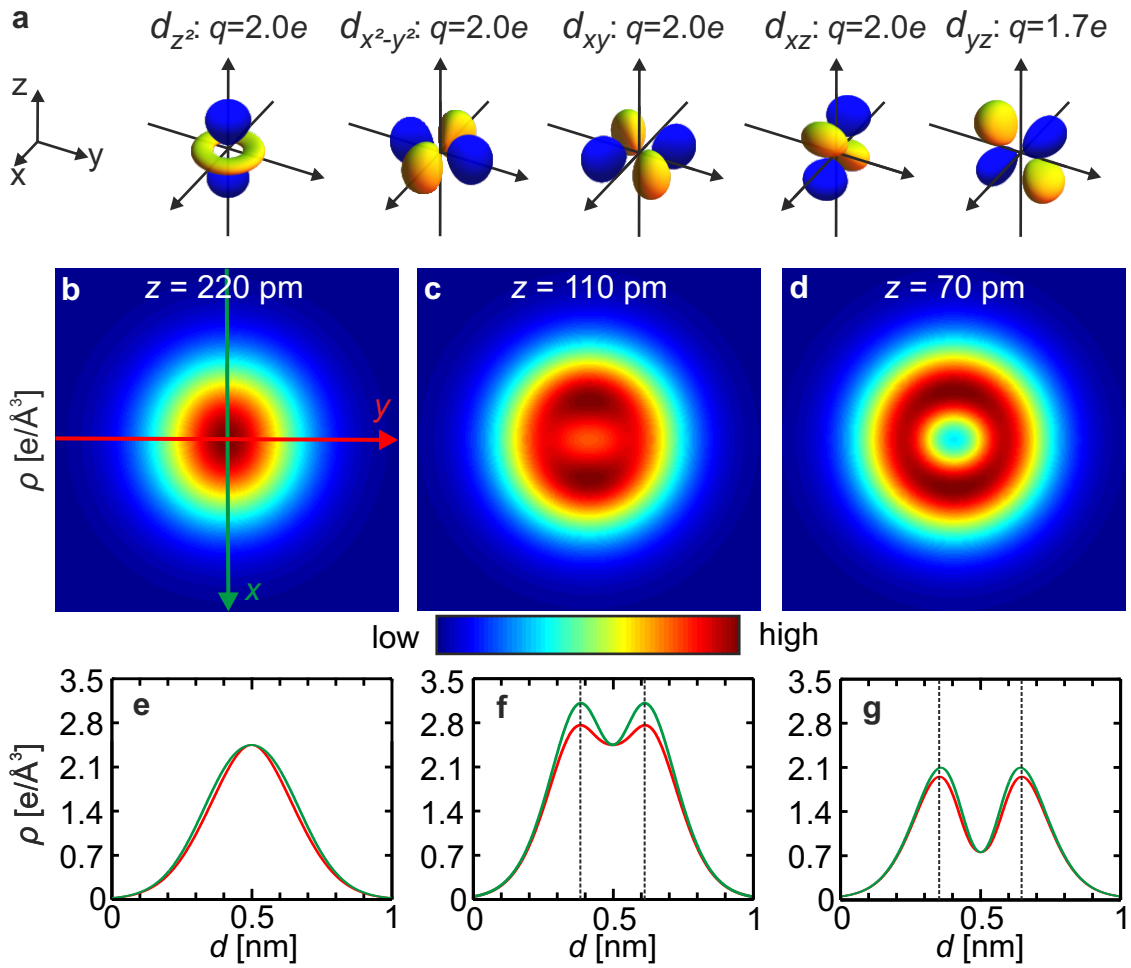

Figure 5.14.: **a**, representation of d orbitals and their occupation which is assumed for the determination of the charge density. **b**,**c**,**d**, calculated charge density for three distances. **e**,**f**,**g**, line profiles along the two high symmetry directions of the charge density plots. The dashed lines indicate the position of the maxima.

Figures 5.14b-d show the calculated charge densities for three distance regimes. The charge densities cannot be directly compared to the experimental data. The experimental data reflects the force gradient acting between CO tip and Cu adatom and not the charge density. Furthermore, the absolute tip-sample distance in the experiment is unknown, but the relative distances between the charge density plots and the Δf data presented above is similar (e.g. model Figs. 5.14c,d: 110 pm − 70 pm = 40 pm; experiment Figs. 5.12a,c: 70 pm − 25 pm = 45 pm). In Fig. 5.14b the charge density is plotted at a distance of $z = 220$ pm and it is almost circular symmetric. At closer distance ($z = 110$ pm) two maxima in the charge density along the x direction can be identified (Fig. 5.14c). For even closer distances the maxima are still present but less pronounced (Fig. 5.14d). This trend is also clearly resolved in the line profiles of the modeled charge densities (Figs. 5.14e,f,g). At $z = 110$ pm the difference between

the local maxima in x and y direction is $0.35\,e/\text{Å}^3$ and the average magnitude of the charge density at the position of the maxima is $2.92\,e/\text{Å}^3$ (dashed lines in Fig. 5.14f). The relative contribution of the asymmetry between the red and green line profile to the total charge density at this distance is therefore $0.35/2.92 = 12\%$. The same analysis for $z = 70\,\text{pm}$ (Fig. 5.14g) gives values of $0.13\,e/\text{Å}^3$ for the difference along x, y directions and $2.03\,e/\text{Å}^3$ for the average value of the charge density. This results in a reduced contribution of the unequal occupation to the total charge density at closer distances of only $0.13/2.03 = 6\%$. The position of the local maxima also changes laterally and the distance between the dashed lines in Figs. 5.14f,g changes from $\Delta d^{110\,\text{pm}} = 230\,\text{pm}$ to $\Delta d^{70\,\text{pm}} = 290\,\text{pm}$.

The simple model reproduces some of the key observations from the experimental data which is the stronger manifestation of the twofold symmetry at further tip-sample distances (Fig. 5.11h) than at closer distances (Fig. 5.11d). Additionally, the evolution of the spatial extent in x, y directions is also similar to the experimental observation. In the experiment the local maxima were separated by 300 pm at a closer distance ($\Delta z = 25\,\text{pm}$, Fig. 5.12a) and by 210 pm at a distance of 45 pm further away ($\Delta z = 70\,\text{pm}$, Fig. 5.12c).

It is noteworthy that a twofold symmetry can in principle also be created from p orbitals by an unequal occupation of p_x and p_y orbitals. But it is not possible to obtain a similar distance behavior of the charge density than in the above case for d orbitals.

Although the simple picture of atomic d orbitals is illustrative and qualitatively explains the experimental data it is definitely limited, e.g. one could argue that also the degeneracy between the $d_{x^2-y^2}$ and d_{xy} orbitals should be lifted due to the different local environment. This would lead to an unequal occupation of these orbitals as well. For a more quantitative comparison *ab-inito* calculations of the electronic structure of the Cu adatom including the CO tip are desirable.

5.3.4. Discussion

The measurements on Cu adatoms on Cu(111) and Cu(110) demonstrated that it is possible to detect the contribution of the d orbitals to the total charge density of adatoms on Cu(110) and Cu(111). On Cu(111) the *subatomic* resolution manifests itself in the observation of a ring-like structure whereas on Cu(110) a non-trivial subatomic feature could be clearly resolved. It originates most likely from an unequal occupation of the d_{xz} and d_{yz} orbitals. The possibility that these subatomic features on Cu(111) and Cu(110) adatoms are artifacts of the CO tip is quite unlikely. In

particular for the adatom on Cu(110) the twofold symmetry is more pronounced at further tip-sample distances than at closer imaging distances. If the CO tip is responsible for the observed features the most likely cause for artifacts is CO bending, but this effect is more severe at closer imaging distances [21]. Indeed, the CO bending probably causes the sharpening of the ring at closer imaging distances, but not the ring itself. This is similar to the imaging of organic molecules by AFM with CO tips where the carbon-carbon bonds are artificially sharpened by the bending of the CO [21]. Furthermore, if CO bending causes the twofold symmetric features one would expect that they also show up in the tunneling current data like in COFI experiments [20]. CO bending as a source of the observed subatomic structures could be finally ruled out by imaging the same systems with xenon terminated tips, because these do not create bending artifacts [163].

A minor deficiency of the measurements on the adatoms is the uncontrolled generation of the adatoms by poking the tip into the surface. Though it is quite unlikely that something else than Cu adatoms were studied there is a little chance that W atoms from the tip were deposited on the surface.[15] The interpretation from above would of course also apply to W atoms which have partially filled d shells as well.

The comparison of the adatom data with the corresponding tip data is ambivalent. For Cu(111) they match very well, but the discrepancy for the adatom on Cu(110) is unexpected (Fig. 5.10a,b). A twofold symmetric feature can be clearly identified at further distances in the Δf data for the adatom on Cu(110), but it does not resemble the COFI image of the supposedly Cu$\langle 110 \rangle$ tip from Fig. 5.10a [30]. One might argue that an adatom on a surface plane is still different from an atom at the tip apex. As the Smoluchowski effect [148] is more pronounced at the tip apex it should affect the orbital occupation of tip apex atoms even more. While this is true for *s,p* electrons, the situation is actually reversed for d electrons which are less depopulated with decreasing coordination number [165, 166]. Overall, there is only a small variation on the order of a few percent in the occupation of the d orbitals when going from a surface atom to an adatom and it is quite unlikely that this small difference causes such a distinct disparity in the appearance of the adatom on Cu(110) and the Cu$\langle 110 \rangle$ oriented tip. Furthermore, the fairly good agreement for the Cu(111) case already shows that a Cu adatom and a tip terminated with a threefold coordinated Cu atom is quite similar.

Therefore one should consider another possibility for this discrepancy: The $\langle 110 \rangle$ oriented tip does not reflect a single atom tip, but is indeed a cluster consisting of four atoms. This is further supported by the larger size of the tip image compared

[15] The purity of the Cu single crystal and the W wire is better than 99.99 %.

to the adatom (Fig. 5.10). The distance between the twofold symmetric features on Cu/Cu(110) is about $200 - 300\,\mathrm{pm}$ depending on the distance Δz from the sample (Fig. 5.12). This is significantly smaller than the distance between the attractive minima in COFI images of bulk W tips ($\approx 500 - 600\,\mathrm{pm}$, [20]). Of course, this raises the question if the two- and threefold symmetric appearances of W and Fe tips are due to clusters of two or three atoms. Recent, yet unpublished experiments[16] from our group on Fe adatoms and clusters on Cu(111) also support the cluster interpretation of the COFI data [170]. Consequently, the interpretation of COFI images for Cu, Fe, and W tips with non-circular symmetric appearances in Δf data as presented in [20, 30] is questionable. An electric dipole located at each atom of the cluster can also explain the experimental data. A model based on the interaction of two electric dipoles with a CO molecule adsorbed on NiO(001) was used to explain twofold symmetric images in AFM data [171].

Finally, one can deduce a general recipe to observe subatomic features on metal adatoms from the above experiments. We suggest to deposit metal adatoms on a surface which lifts the degeneracy of the d orbitals in a non-trivial way, e.g. on higher indexed Cu surfaces. Another interesting experiment would be the investigation of adatoms on bcc crystal surfaces like Fe(110). This experiment was actually intended during this thesis, but the large amount of impurities in the bulk of the Fe single crystal prevented a successful preparation of a clean Fe(110) surface.[17] A less time consuming and even more interesting experiment might be to study Fe adatoms on Fe islands which are grown on Cu(111). It is known that these islands exhibit fcc as well as bcc stacking which would allow to study different adsorption sites within one experiment [172].

[16] Performed by M. Emmrich and F. Huber.

[17] After 2 weeks of sputtering and annealing there was still a significant amount of impurities detected by AES.

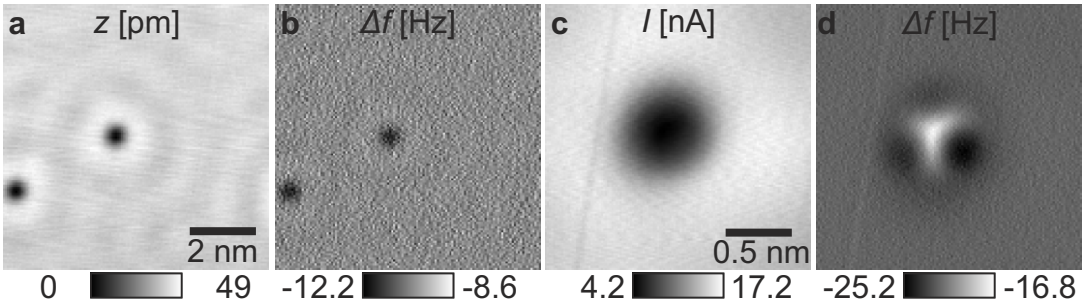

Figure 5.15.: **a**, constant current ($V = 100\,\mathrm{mV}$, $I = 1\,\mathrm{nA}$) image obtained with a bulk Fe tip, resolving two circularly symmetric COs with an apparent depth of about 40 pm. **b**, simultaneously acquired Δf data. At this distance only a circular attractive feature is visible on the COs. **c**,**d**, constant height I and Δf data recorded with the same tip at a distance of about 250 pm closer to the surface than in **a**. The current channel shows a slightly distorted circular dip, whereas in Δf the threefold symmetry is clearly apparent. All images show unfiltered raw data. Imaging parameters for **c**,**d**: $V = 10\,\mathrm{mV}$, $A = 50\,\mathrm{pm}$, $k = 1800\,\mathrm{N/m}$, $f_0 = 28.031\,\mathrm{kHz}$.

5.4. Characterization of Bulk Iron Tips

The idea to apply the COFI method to bulk Fe tips came up because it was not clear how the tip is terminated after field evaporation and if field evaporation is sufficient to clean of the native oxide layers of Fe. The detection of a tunneling current upon approach of the Fe tip to the Cu(111) sample is already a good indicator for a well conductive tip and it suggests a successful removal of the oxide layer. As a next step a tip which provides atomic resolution is desired. This can be achieved by applying bias pulses to the tip or poking it into the surface. As there is the constraint that the tip should still be terminated with Fe after the tip treatment on Cu(111), strong poking into the surface should be avoided. The appearance of CO molecules in constant current imaging was used as a measure of the sharpness of the tip like in plain STM.

An example is shown in Fig. 5.15a, where the COs appear as single, circularly symmetric dips. The simultaneously collected Δf signal (Fig. 5.15b) shows attractive interaction of the tip with each CO. To perform COFI, the tip is approached closer to the surface by about 250 pm from the STM setpoint. A single, though slightly distorted dip is visible in I (Fig. 5.15c) whereas three attractive minima are observed in Δf (Fig. 5.15d). Different bulk Fe tips with various tip conditions were investigated by the COFI method. This resulted in a number of Δf images and the corresponding $\langle k_{\mathrm{ts}} \rangle$ data is presented in Fig. 5.16 for better comparability with previously published

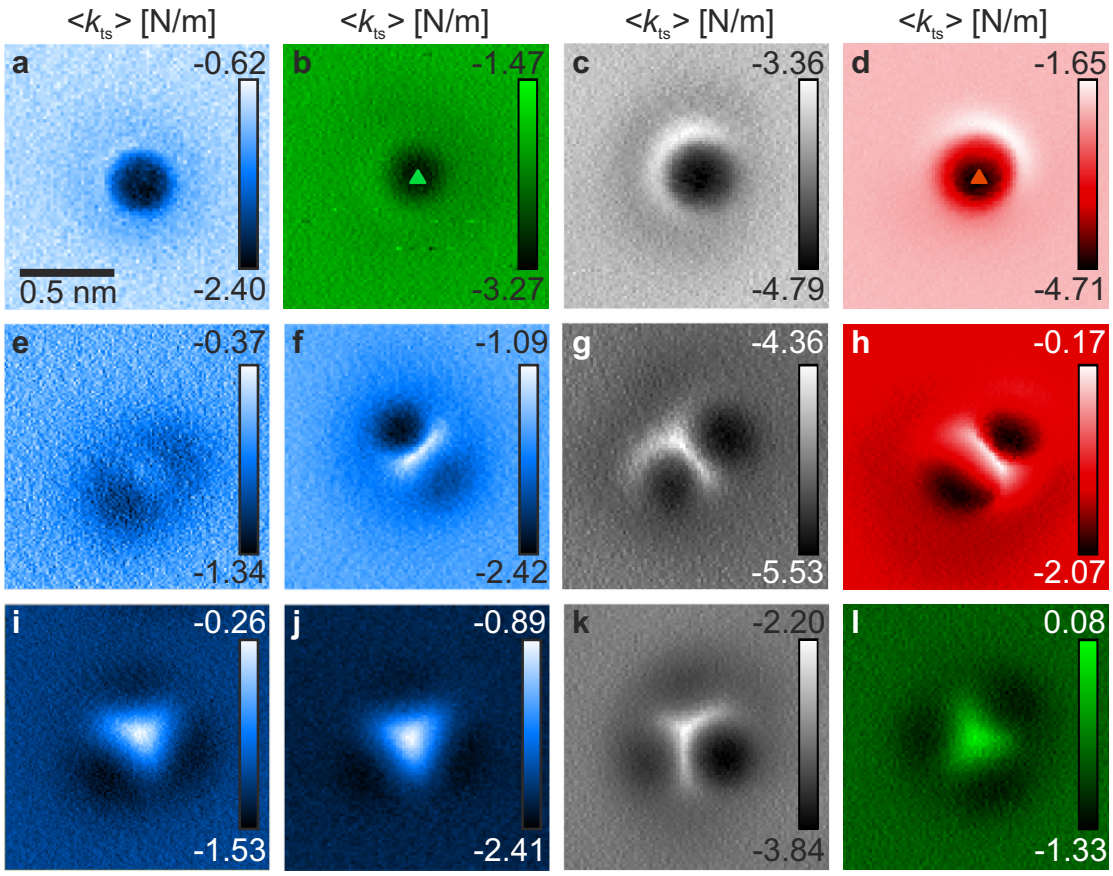

Figure 5.16.: Selection of $\langle k_{\mathrm{ts}} \rangle$ maps. Different bulk tips are indicated by different color codes. Modifications of the tip apices leads to the appearance of three main COFI images. **a-d**, circular symmetry with solely attractive interaction in the center. **e-h**, twofold symmetry with two attractive minima. **i-l**, threefold symmetry with three attractive minima. Note, tips **i** and **j** look quite similar, but there was a number of pokes in between which completely altered the tip apex. The triangles in **b** and **d** mark the position, where the $F_{\mathrm{sr}}(z)$ curves from Fig. 5.17 were recorded. All images show unfiltered raw data and the scale bar in **a** is valid for all of them. Imaging parameters: $A = 50\,\mathrm{pm}$ and $k = 1800\,\mathrm{N/m}$ for all images; **a**,**e**,**f**,**i**,**j**, $f_0 = 27.975\,\mathrm{kHz}$; **b**,**l**, $f_0 = 23.940\,\mathrm{kHz}$; **c**,**g**,**k**, $f_0 = 28.030\,\mathrm{kHz}$; **d**,**h**, $f_0 = 59.369\,\mathrm{kHz}$.

results [30]. Images obtained with the same tip, but altered tip apex, are plotted in the same color code.

Three main configurations were found for the $\langle k_{\mathrm{ts}} \rangle$ maps: Circular (Figs. 5.16a-d), twofold (Figs. 5.16e-h), and threefold (Figs. 5.16i-l) symmetric tip apices. Similar images were observed with bulk W tips and interpreted as monoatomic tips where the observed features are due to the increased charge density towards nearest neighbors [20, 91]. In the previous section it has been indicated that this interpretation might not be correct and instead the two- and threefold tips represent a tip terminated by two or three atoms. In all the raw data images in Fig. 5.16 the contrast is dominated

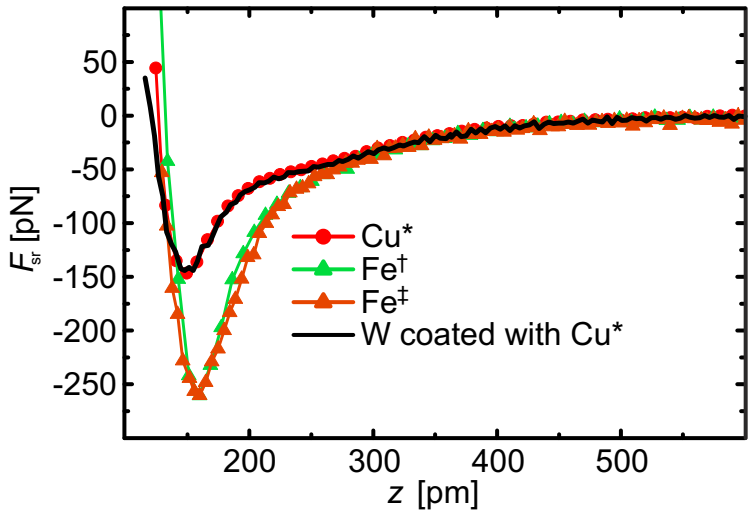

Figure 5.17.: $F_{sr}(z)$ curves recovered from $\Delta f(z)$ data. All curves were obtained with tips exhibiting a circularly symmetric COFI image. The interaction between CO and the two Fe tips († = Fig. 5.16b, ‡ = Fig. 5.16d) is about 75% larger than between Cu terminated tips. Sensor parameters: $A = 50\,\text{pm}$ for all curves. Cu*: $k = 1800\,\text{N/m}$, $f_0 = 26.969\,\text{kHz}$; Fe†: $k = 1800\,\text{N/m}$, $f_0 = 23.900\,\text{kHz}$; Fe‡: $k = 1800\,\text{N/m}$, $f_0 = 59.369\,\text{kHz}$; W/Cu*: $k = 1800\,\text{N/m}$, $f_0 = 27.846\,\text{kHz}$. Figure adapted from [30], the curves marked with (*) were acquired by T. Hofmann.

by the attractive and repulsive angular-dependent features. In contrast, the subatomic features on Cu/Cu(110) give only rise for a subtle difference in the Δf data which can hardly be identified in the raw image data. This further supports the interpretation of the COFI images in Figs. 5.16e-l as a tip apex which consists of more than one atom.

Nevertheless, for the following discussion this aspect is not crucial, but instead it is more important that the tip termination can be determined via COFI. For circular symmetric tips this can be done by analyzing $F_{sr}(z)$ curves, because these allow a distinction between Cu terminated tips and Fe or W terminated tips [30]. For this purpose site dependent $\Delta f(z)$ spectroscopy was performed. The difference between spectra on CO and on Cu yields the short-range contribution Δf_{sr}. Figure 5.17 shows deconvolved $F_{sr}(z)$ curves for the tips from Figs. 5.16b,d. The minima of the force curves for the Fe tips are at about $-260\,\text{pN}$, whereas a Cu tip only leads to an attractive force of about $-150\,\text{pN}$ as measured by T. Hofmann for bulk Cu and Cu coated W tips [30]. The strength of the attractive interaction between CO and Fe is similar to the one between CO and clean bulk W tips [20, 30]. Hence, it is expected that a Cu covered Fe tip is similar to a Cu covered W tip. This allows a clear distinction between these two situations via $\Delta f(z)$ spectroscopy.

For a couple of tips presented in Fig. 5.16, $\Delta f(x, y, z)$ data sets were also acquired. Three of them which are representative for each tip orientation are depicted in Fig.

5.18. Here, I, Δf_{sr}, and F_{sr} are presented for a circular symmetric tip (Figs. 5.18a-c), for a twofold tip (Figs. 5.18d-f), and for a threefold tip (Figs. 5.18g-i). Characteristic for the circular tip is the strong attractive interaction with the CO molecule. The attractive force reaches a value of $-305\,\mathrm{pN}$ which is larger than the values from $\Delta f(z)$ curves. Most likely this is because it is difficult to hit the exact position of the minimum with single $\Delta f(z)$ curves, while constant height slices provide an immediate map of the complete $\Delta f(x, y, z = \mathrm{const.})$ manifold. In contrast, the attractive forces for the two other tips are significantly smaller (about -80 and $-130\,\mathrm{pN}$). The repulsive force for all three tips is in the range of $30 - 40\,\mathrm{pN}$. The lateral extent of the dip in the tunneling current I is similar for all three tip configurations (Fig. 5.18a,d,g). In the case of the two- and threefold symmetric tips, some additional features can already be identified without Laplace filtering (Fig. 5.18d,g). These features are due to the bending of the CO which causes a modulation of the tunneling gap [20].

The distinction between Cu terminated tips and Fe tips is very important if spin-sensitive measurements are desired. Although it should be mentioned that this is only possible for circular symmetric tips whereas for two- and threefold tips one cannot state if it is a Fe or Cu cluster which is at the tip apex [30]. In the following chapter Fe tips will be used to investigate the spin orientation of an antiferromagnet at the atomic scale.

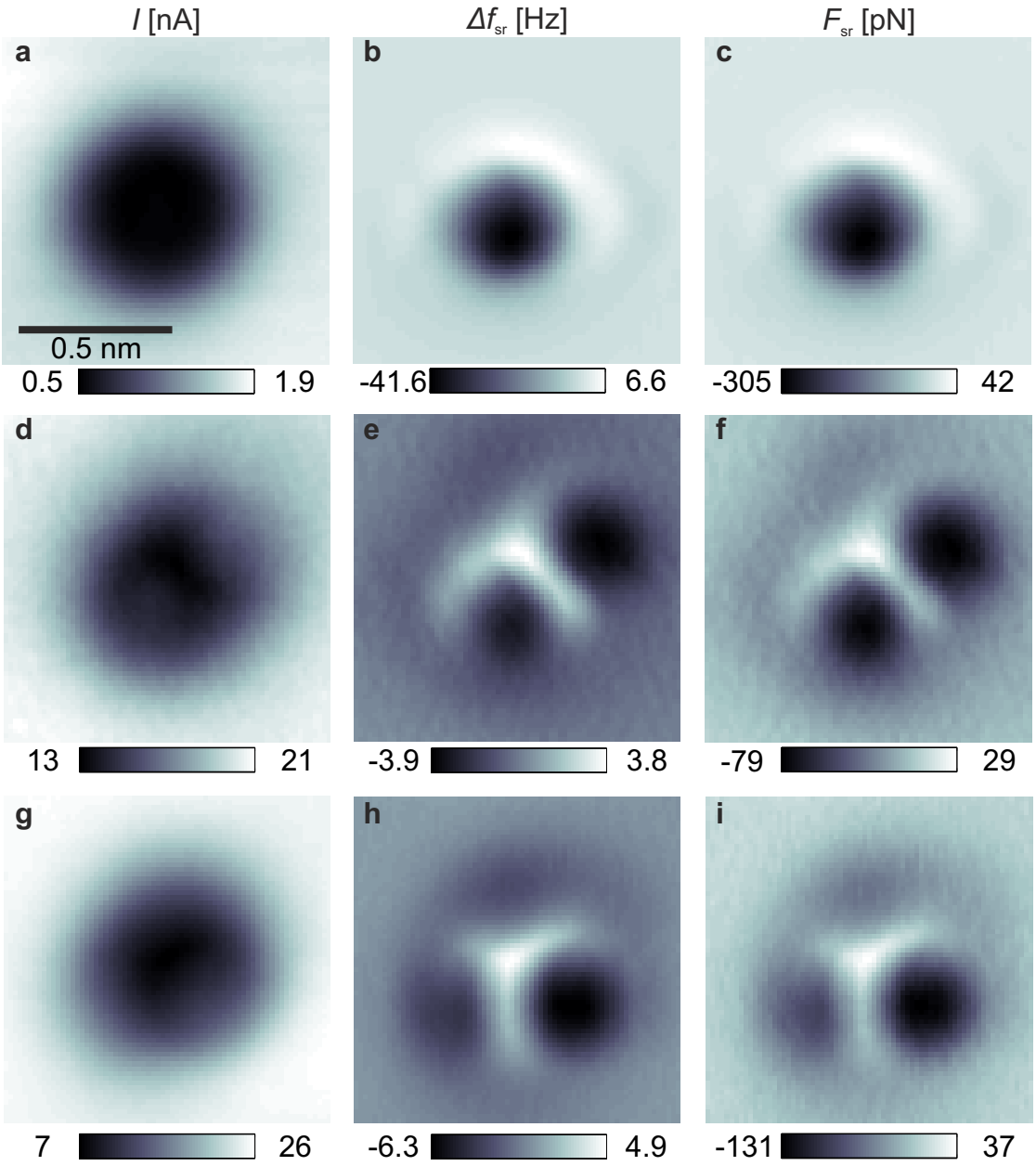

Figure 5.18.: Tunneling current I, short-range frequency shift Δf_{sr}, and force F_{sr} data for Fe tips which represent the three high symmetry configurations. **a-c**, circular symmetric tip, $z = 163\,\mathrm{pm}$. **d-f**, twofold symmetric tip, $z = 163\,\mathrm{pm}$. **g-i**, threefold symmetric tip, $z = 144\,\mathrm{pm}$. The maps for the two- and threefold tips were acquired with positive bias voltages, therefore the scale bar in **d** and **g** was inverted to match **a**, dark corresponds to low current. The scale bar is valid for all images. Imaging and sensor parameters: circular, $V_{\mathrm{a-c}} = -1\,\mathrm{mV}$, $k = 1800\,\mathrm{N/m}$, $f_0 = 59.369\,\mathrm{kHz}$, $A = 50\,\mathrm{pm}$; two- and threefold, $V_{\mathrm{d-i}} = 10\,\mathrm{mV}$, $k = 1800\,\mathrm{N/m}$, $f_0 = 28.031\,\mathrm{kHz}$, $A = 50\,\mathrm{pm}$. **b**, **e** and **h** are adapted from [30].

6. Spin Resolution and Evidence for Superexchange on NiO(001) Observed by Force Microscopy

Most of the work presented in this chapter has been published in Physical Review Letters[1] [105]. Parts of the text are identical to the publication.

This chapter is divided into four sections. First an introduction to the sample system and an overview of the existing literature and previous experiments on spin resolution by AFM is given. In the second and third section, the results obtained with bulk Fe and SmCo tips will be presented. Finally, the results are discussed and measured exchange forces are compared to theoretical predictions.

6.1. Introduction to Spin-Resolved Force Microscopy

Wiesendanger *et al.* estimated in 1990 that magnetic exchange interactions that occur in spin-polarized scanning tunneling microscopy can amount to about one pN per Å^2 of tip area [11]. Several calculations predicted even larger magnitudes of exchange forces [24, 173–176]. Once atomic resolution by FM-AFM in UHV became feasible [73], extended efforts to detect exchange interactions by AFM on the antiferromagnetic insulator nickel oxide (NiO) at $T = 4\,\mathrm{K}$ and $300\,\mathrm{K}$ were conducted [23, 177–179], initially without success.

In 2007, Kaiser *et al.* imaged the (2×1) spin pattern of the (001) surface of NiO [14]. The experiment was conducted at liquid helium temperatures using an iron coated silicon cantilever with $f_0 = 159\,\mathrm{kHz}$ and $k = 34\,\mathrm{N/m}$ operated at $A = 6.65\,\mathrm{nm}$. The magnetization of the tip was stabilized by applying a $5\,\mathrm{T}$ magnetic field out-of-plane [14, 180, 181]. The observed periodic height variation in topographic imaging mode

[1] F. Pielmeier, F. J. Giessibl, *Spin Resolution and Evidence for Superexchange on NiO(001) Observed by Force Microscopy*, Physical Review Letters **110**, 266101 (2013)

was only 1.5 pm, on top of an also rather small atomic or chemical contrast of 4.5 pm. The signal-to-noise ratio in these experiments was quite small and unit cell averaging was applied to allow for a quantitative measure of the height variations which were barely visible in the raw image data.

The exchange interaction between tip and sample was qualitatively described with a Heisenberg Hamiltonian, $H = -J_{12}\vec{S_1} \cdot \vec{S_2}$, where J_{12} is the exchange coupling constant and $\vec{S_1}$, $\vec{S_2}$ are the spins in tip and sample. Hence, for a large signal the alignment of the spins should be either parallel or antiparallel and J_{12} should be large. A tip material dependent study showed that Fe coated tips reveal the spin structure of NiO whereas nickel and gadolinium coated tips do not [181]. To achieve a high signal-to-noise-ratio a high magnetic moment of the foremost tip atom is therefore desirable, but also the spatial extent of the orbitals where the spins are localized is important. Gadolinium (Gd) has a high magnetic moment of $\mu_{Gd} = 7.1\,\mu_B$ compared to Fe ($\mu_{Fe} = 2.2\,\mu_B$), but the unpaired electrons are localized in deeper lying $4f$ shells and therefore the overlap with the spin-carrying d orbitals of the sample is small [181].

Up to now the detection of exchange forces only worked out with Fe coated tips [14, 180–183]. On the other hand, it is also known that these coated Fe tips can form superparamagnetic clusters, where the magnetization becomes unstable upon decreasing tip-sample distance [184]. Additionally, complex spin-dependent hysteretic effects can occur at closer tip-sample distances, manifesting themselves in the dissipation signal of the cantilever motion [185]. Although it is interesting to study such effects from a basic physics point of view, they complicate the measurement of exchange interactions itself. Therefore, part of this work is to find other tip materials which are more suitable for high-resolution measurements of exchange interactions.

In previous work, the spin-dependent contrast on NiO was only detected qualitatively, but a quantitative measure of the exchange interaction is still lacking [14, 180, 181]. Quantitative measurements of exchange interactions were performed on an antiferromagnetically ordered Fe monolayer on W(001), which provides a stronger signal due to a hybridization of the Fe $3d$ and W $6s$ orbitals [182, 183]. Here, corrugations due to the exchange interaction of up to 10 pm where observed, which sometimes even exceeded the atomic corrugation.

The structure of NiO is shown in Fig. 6.1a. NiO exhibits a rock salt structure with a lattice constant of $a = 417$ pm [186]. The Néel temperature is 523 K [187–189]. In the simplest picture, NiO is an ionic crystal with Ni^{2+} and O^{2-} ions and partially filled Ni $3d^8$ orbitals. Strong on-site d-d coulomb repulsion makes NiO insulating with a band gap of 4.3 eV [190]. The valence band is formed by hybridized

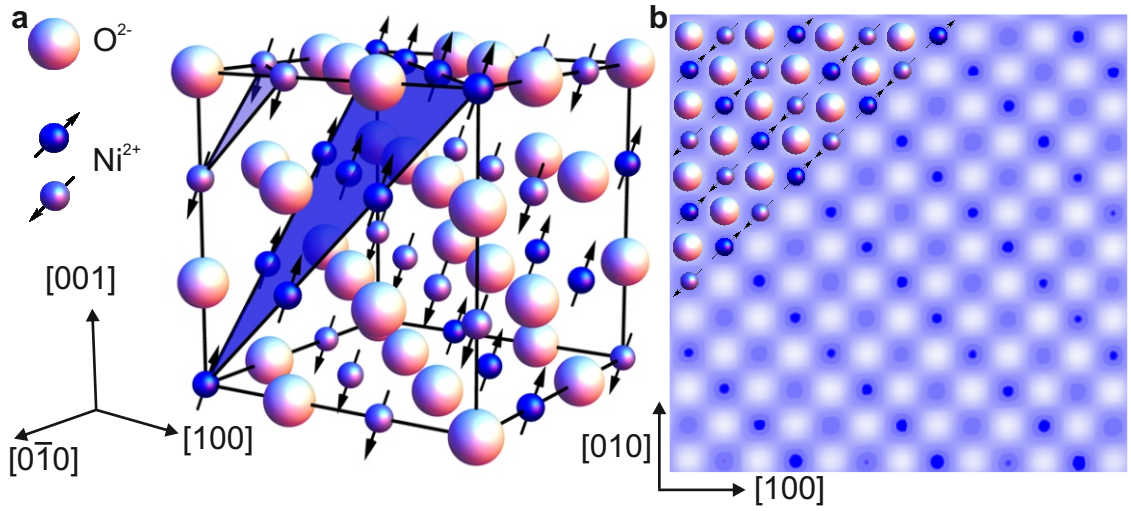

Figure 6.1.: a, bulk crystal structure of NiO. Ni ions couple ferromagnetically within {111} planes and neighboring {111} planes couple antiferromagnetically. This leads to a 2×1 magnetic unit cell at the {100} surfaces. **b**, structure of (001) surface superimposed onto an experimental image showing the row-wise variation of the apparent height of the oppositely aligned Ni spins. For details about the experimental data see section 6.3. Figure adapted from [105].

Ni $3d$ and O $2p$ states, whereas the conduction band is mainly constituted by Ni $3d$ states [190–192]. It is a type 2 antiferromagnet consisting of two fcc sublattices, each hosting spin-up and spin-down Ni ions, respectively. Within one sublattice Ni ions are coupled ferromagnetically via a direct exchange mechanism between the Ni d orbitals within {111} planes. Neighboring Ni planes are coupled antiferromagnetically via superexchange mediated by the O atoms [193, 194]. This leads to an antiferromagnetic structure at the (001) surface with alternating spin orientations of nickel atoms along the [110] direction (Fig. 6.1b).

Cleaved NiO surfaces exhibit a bulk-terminated orientation of magnetic moments [195]. Furthermore, there is no reconstruction at the surface and only a tiny relaxation of 1.5% of the surface layer towards the bulk occurs [196]. The four $\langle 111 \rangle$ directions are equivalent resulting in four so-called twin (T) domains. Within each T-domain there are three possible orientations of the spins which point along the $\langle 211 \rangle$ directions [195]. Overall, this results in 12 possible domains which are randomly distributed and have a lateral size of less than 1 µm [197]. In AFM experiments, it is usually not possible to determine the domain structure and to position the tip accordingly. Furthermore, the exact alignment of the spin magnetic moment at the tip apex cannot be controlled very well, even with an external B-field [180]. This leads to some arbitrariness in the AFM experiments, but usually there is an in- as well as an out-of-plane component of the magnetic moment of the Ni ions in the surface. It is therefore unlikely that,

within the Heisenberg picture, tip and sample spins are exactly perpendicular to each other and do not provide any spin-dependent signal at all.

When imaging an ionic crystal with a metallic tip the anion usually appears attractive, because the metal tip is partially positively charged due to the Smoluchowski effect [46, 148]. This was explicitly calculated for NiO [176], where the O atoms appear then as maxima in constant Δf mode and the minima refer to Ni sites (Fig. 6.1b). The detection of the spin-dependent contrast in topographic imaging of the NiO(001) surface manifests itself as a difference in apparent height between two neighboring nickel sites along $\langle 100 \rangle$ directions. The spin alignment of the surface Ni atoms relative to the tip moment causes differences in the exchange interaction which leads to varying chemical interaction forces. A direct exchange mechanism was predicted for an Fe atom probing the NiO surface [24]. The magnitudes of the exchange forces between an Fe tip atom and the Ni surface atoms is predicted to be on the order of 0.1 nN. Furthermore, a sign change of the exchange force is expected to occur at close tip-sample distances [24, 25].

NiO was also studied with STM at elevated temperatures of $T \approx 470\,\mathrm{K}$, where the conductivity is high enough to allow for stable tunneling operation [191, 198, 199]. Depending on the bias polarity, either the Ni or O sites are imaged. These studies confirmed the current picture of NiO being a charge-transfer insulator with strongly correlated electrons, where the valence band mainly consists of O p states and the conduction band of Ni d states.

The aim of the following work is to resolve the spin structure of NiO with atomic resolution without an external magnetic field. Furthermore, a quantitative measure of the exchange interaction is desired.

6.2. Measurements with Iron Tips

So far, Fe is the material of choice for spin-dependent measurements by AFM. Therefore Fe tips were also used in the initial experiments presented in the following. In contrast to the previous studies [14, 180, 181], bulk Fe tips were used and no external magnetic field is applied. The first set of experiments was performed with electrochemically etched Fe tips without further characterization of the tip apex by COFI. Second, bulk Fe tips which were treated with FIB and characterized by COFI were used to detect the exchange interaction.

6.2.1. Results with Uncharacterized Iron Tips

The NiO single crystals[2] with a typical size of $3 \times 1 \times 8\,\mathrm{mm}^3$ were either clamped mechanically, or just fixed with non-conductive glue onto Omicron sample plates. The samples were cleaved in the analysis chamber with the help of the wobble stick at a pressure $p < 10^{-10}\,\mathrm{mbar}$. Clean and flat terraces were obtained with a width of $5 - 100\,\mathrm{nm}$. Although no systematic study of the cleaving behavior was performed, thinner samples usually resulted in better cleavage quality. After cleaning the bulk tips by field evaporation they were approached to the NiO surface. Sometimes atomic resolution was obtained right after the approach, but often the tip was scanned along step edges or poked into the sample until a tip change occurred.

The topographic image in Fig. 6.2a was acquired with a bulk Fe tip which made already contact to the NiO surface. The Δf setpoint was decreased from $-23.0\,\mathrm{Hz}$ (bottom) to $-37.9\,\mathrm{Hz}$ (top). This corresponds to a decrease in tip-sample distance of $\Delta z = 90\,\mathrm{pm}$. Atomic resolution is visible in the upper third of the image plus an additional modulation of the contrast in the regions indicated by the white arrows. The smoothed and flattened version in Fig. 6.2b illustrates this further. In the bottom part of the image no atomic or spin contrast is present. Atomic contrast starts to emerge at around one half of the image (dotted line) after the tip was approached by around 75 pm closer to the surface. An additional decrease in tip-sample distance of around 20 pm (dashed line) leads to the appearance of the expected modulation of the atomic contrast due to exchange forces between magnetic moments in the surface and the tip.

The exchange contrast is presented and analyzed in more detail in Fig. 6.3 where a zoom into the upper region of Fig. 6.2a is shown. To increase the SNR unit cell

[2]SurfaceNet GmbH, 48432 Rheine, Germany

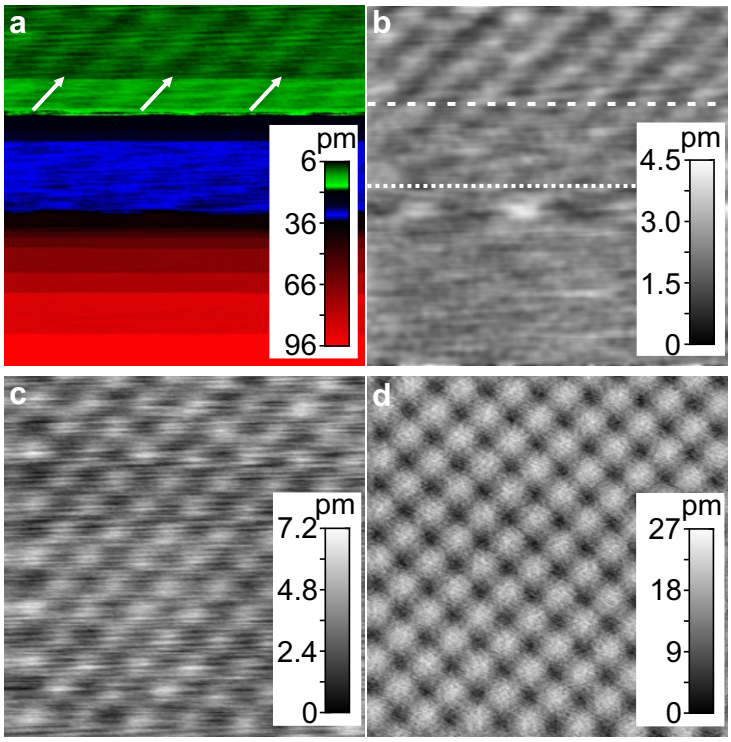

Figure 6.2.: **a**, topography raw data and **b**, filtered and flattened data while the tip is approached (bottom to top) to the sample in constant Δf mode. Atomic (dotted line) and spin resolution (dashed line) show up at about one half and two thirds of the image in **b**. **c**, tip is approached only 10 pm closer, now only atomic contrast is visible again. **d**, typical atomic resolution image on NiO, with a presumably Ni or O covered tip. Imaging Parameters: $3 \times 3\,\mathrm{nm}^2$, $k = 1800\,\mathrm{N/m}$, $f_0 = 24.467\,\mathrm{kHz}$, $A = 100\,\mathrm{pm}$, $Q = 99,850$ and $V = 0\,\mathrm{V}$. Figure adapted from [105].

averaging was performed [14, 162]. A 2×2 unit cell was used, like depicted in Fig. 6.3b, to avoid superimposing the data with the expected 2×1 unit cell. The filtered image on the right in Fig. 6.3b is generated by multiple patching of the averaged unit cell. The difference between the neighboring rows of minima can now be identified more easily. The overall atomic corrugation is about 1.6 pm and the difference due to the exchange interaction is only 0.4 pm (Fig. 6.3c). The calculated unit cell averaging error is about 0.3 pm.

The error bar is determined as follows: In constant Δf mode, frequency noise translates into an uncertainty in the z-position of the tip relative to the sample. This is reflected as an uncertainty of the z-value of each pixel in the images of the NiO surface. The z-noise of each pixel can be estimated from the z-position noise density of about $n_z = 100\,\mathrm{fm}/\sqrt{\mathrm{Hz}}$. This number is experimentally determined by closing the feedback loop at scan size zero and taking a Fourier transformation of the z-position versus time. The square of the absolute noise is then determined by integrating the square

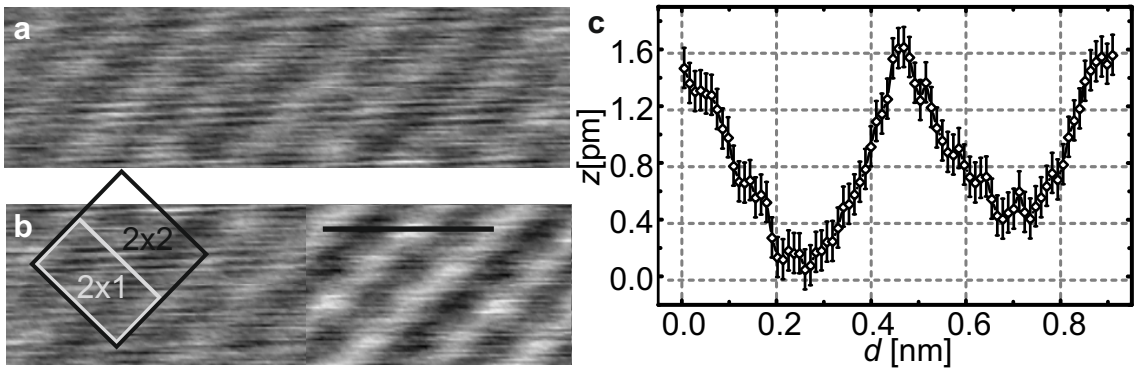

Figure 6.3.: Topographic image and profile of NiO. **a**, upper section of Fig. 6.2a, where the modulation of the atomic contrast with twice the periodicity of the atomic lattice shows up. **b**, overlay of raw (left) and unit cell averaged (right) data. **c**, line profile along the [100] direction, the measured difference between magnetically nonequivalent Ni sites is 0.4 pm with an error bar of 0.3 pm. Figure adapted from [105].

of n_z from zero up to the measurement bandwidth B, where in our experiment, B corresponds to the PLL bandwidth of 40 Hz. Thus, the vertical noise for each pixel amounts to $z_{\text{noise}} = 632\,\text{fm}$ – corresponding to $n_z \times B^{0.5}$. In Fig. 6.3b unit cell averaging was performed to allow the determination of a more precise value of the spin-dependent contribution to the z-position of a given pixel. The number of pixels of the analyzed section in Fig. 6.3a is $256 \times 72 = 18432$ pixels and the number of pixels per 2×2 unit cell is $53 \times 53 = 2809$. Therefore the error after unit cell averaging reduces by a factor of $(18432/2809)^{0.5} = 2.57$. Thus, the z-error of the unit cell averaged image is about $632\,\text{fm}/2.57 = 250\,\text{fm}$ per pixel.

An important observation of these measurements is that the spin-dependent signal disappears when the tip is approached closer to the surface. In Fig. 6.2c the same area as in Fig. 6.2a is imaged with a reduced Δf set point of -41.9 Hz which corresponds to a decrease in tip-sample distance of only 10 pm. The modulation due to the magnetic 2×1 unit cell of NiO(001) is no longer visible, but atomic contrast is still present. Hence, the distance regime where magnetic exchange forces can be detected is only about $15 - 20$ pm. The overall corrugation of 2.3 pm is still quite small compared to usually measured corrugations of about $16 - 20$ pm (Fig. 6.2d).

Figure 6.4 summarizes the three distance regimes observed in the experiment. On the left, the distance regime is indicated and in the middle schematic line profiles along the [100] direction are drawn. The insets on the right show the corresponding experimental data obtained in this regime. In regime I (Fig. 6.4a) there is no overlap yet between the spin-carrying d orbitals in tip and sample and only faint atomic contrast is detectable. When the tip approaches by about 20 pm closer to the surface

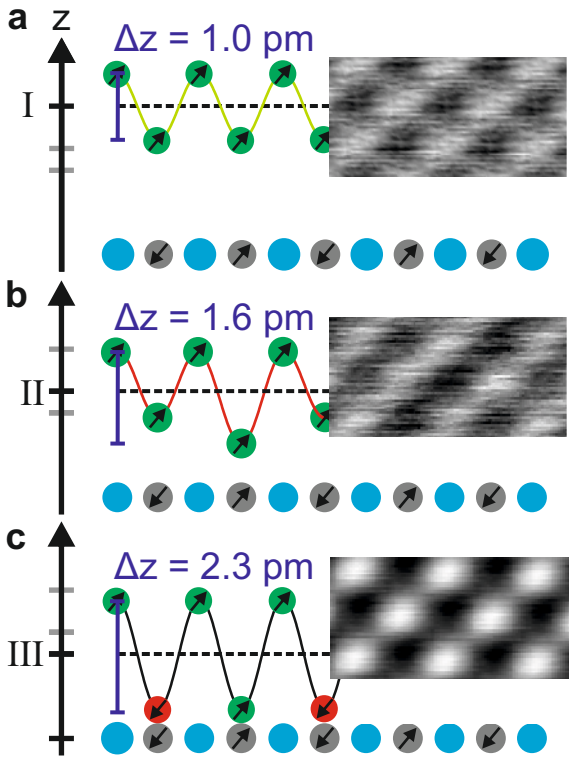

Figure 6.4.: Tip trajectories for the three distance regimes: **a**, in regime I ($z \approx 30\,\mathrm{pm}$) the tip is further away from the sample and some small atomic corrugation is already present. **b**, tip is approached some tens of picometers and region II ($z \approx 10\,\mathrm{pm}$) where spin-dependent signals can be detected is reached. **c**, after an additional decrease in tip-sample distance (regime III, $z = 0$) the spin alignment is apparently altered by the tip-sample interaction which impeds the detection of short range exchange interactions. The insets show unit cell averaged images of the middle and upper region of Fig. 6.2a and of Fig. 6.2c. Figure adapted from [105].

regime II is reached (Fig. 6.4b). The exchange interaction now influences the chemical interaction between tip and sample atoms on top of the Ni sites leading to the detection of the 2×1 magnetic structure. In region III (Fig. 6.4c) the spin-dependent signal vanishes. A possible mechanism to explain this observation could be that the spin alignment at the apex is not stable enough and aligns with the sample spins at closer tip-sample distances. This could also be vice versa or a combination of both. On the other hand, it seems more likely that the spin of the apex atom is more easily altered due to the lower coordination.

Regardless of the exact mechanism which underlies this contrast change, the small width of the distance range where exchange forces are detectable indicates that the stability of the spin orientation of the tip apex atom is easily changed by increasing tip-sample interaction forces. Locally, the stability of the spin orientation is governed by the directional dependent magnetocrystalline anisotropy (MA), which is a consequence of the spin-orbit coupling in solids [200]. Hence, the tip cluster orientation may

affect the signal strength in spin-resolved experiments. Therefore, tips with known orientations which were determined via the COFI method are used for the following measurements.

6.2.2. Results with Characterized Iron Tips

In the above experiments, a bulk Fe tip was used but the tip termination itself is unknown. The tip cleaning by field evaporation might not be sufficient to completely remove an oxide layer or other contaminants and also the contamination of the tip apex during transfer between the preparation and analysis chamber cannot be fully excluded. Therefore the Fe tips were characterized prior to the measurements on NiO by imaging CO molecules adsorbed on a Cu(111). As described in chapter 5, this method enables the distinction between Fe and Cu which is of major importance here. Another improvement is the use of the custom qPlus sensor of type 4 which was introduced in chapter 3.

Figures 6.5a,d,g present the three characteristic configurations of bulk Fe tips observed via the COFI method. After characterization of the Fe tips by COFI, the Cu(111) sample was removed and a cleaved NiO sample was introduced into the microscope. The tip was then approached carefully to the NiO(001) surface to avoid tip-sample collisions, and the metallic nature of the tip apex was confirmed by $\Delta f(V)$ curves (Figs. 6.5c,f,i). The similarity of the forward and backward voltage sweep direction is an indication for a metallic tip apex, because no charging effects or tunnel events to localized states are observed [46]. Once the surface was reached, only small scale ($< 5\,\mathrm{nm}$) images were acquired until a decent, flat spot was found and atomic contrast could be obtained without further manipulation of the tip apex. Figures 6.5b,e,h show atomically resolved constant height Δf images of the NiO(001) surface, which were acquired with the COFI characterized tips. Electrostatic forces were minimized by applying a bias voltage to the sample. In none of these three images the 2×1 magnetic unit cell is revealed. On the other hand, it is already known from the previous section that the distance regime of interest is only $10 - 20\mathrm{pm}$. Therefore distance dependent constant height slices with each tip were acquired, especially in the region where atomic corrugation is small.

Figure 6.6a shows unfiltered Δf data measured with the Fe tip from Fig. 6.5a. Only very faint atomic corrugation can be recognized by eye. The 2D FFT (Fig.6.6b) reveals four peaks with higher intensity which correspond to the atomic lattice. Additionally, there is a slightly increased intensity (white boxes) along the diagonal from the lower

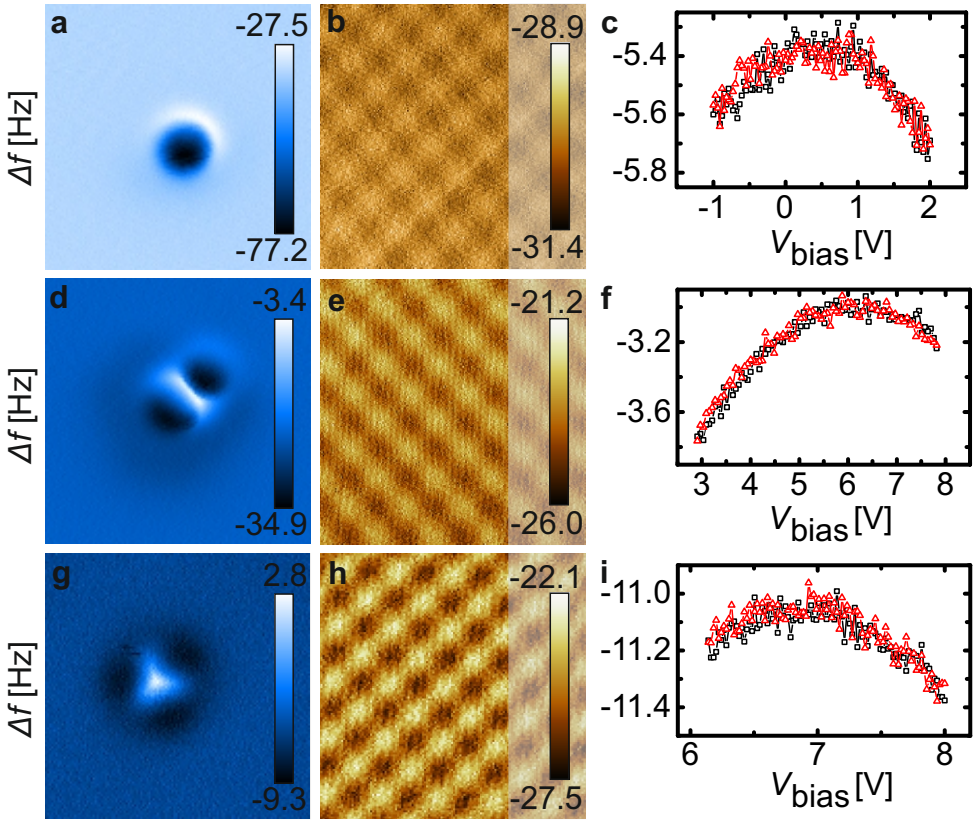

Figure 6.5.: COFI images (**a**, circular, **d**, twofold, **g**, threefold) for Fe tips, which were used to acquire atomically resolved constant height images on NiO (**b**,**e**,**h**). $\Delta f(V)$ curves (**c**,**f**,**i**), no difference between forward (black squares) and backward (red triangles) voltage sweep direction can be observed, confirming a well conductive tip apex. COFI (NiO) imaging parameters: **a**,(**b**) $k = 1800\,\mathrm{N/m}$, $f_0 = 59.369\,\mathrm{kHz}$, $A = 50\,\mathrm{pm}$, $Q = 355,500$ $(1,360,000)$ and $V = -1\,\mathrm{mV}$ $(0.5\,\mathrm{V})$; **d**,(**e**), k, f_0, A as in **a**, $Q = 1,120,000$ $(1,100,000)$ and $V = -1\,\mathrm{mV}$ $(6.0\,\mathrm{V})$; **g**,(**h**), $k = 1800\,\mathrm{N/m}$, $f_0 = 23.939\,\mathrm{kHz}$, $A = 50\,\mathrm{pm}$, $Q = 55,800$ $(27,200)$ and $V = -10\,\mathrm{mV}$ $(6.8\,\mathrm{V})$. Size of all images: $2 \times 2\,\mathrm{nm}^2$. Figure adapted from [105].

left to the upper right peak of the atomic lattice. The distance between these two faint peaks is just half the distance between the peaks originating from the atomic lattice. In the FFT on the right in Fig. 6.6b the contrast was adjusted to highlight the additional peaks. The presence of these two peaks in the FFT of the raw image data indicates that there is indeed a signal component related to the 2×1 magnetic unit cell. Figure 6.6c shows a low-pass filtered and unit cell averaged version of Fig. 6.6a where a 2×2 unit cell was used again for averaging. The additional modulation of the atomic contrast can now be identified as a row-wise changing apparent height of the minima, see also corresponding line profile in Fig. 6.6d. For better comparison with the measurements from the previous section the Δf line profile (Fig. 6.6d) can be converted into topography. For this purpose a conversion factor is required. It

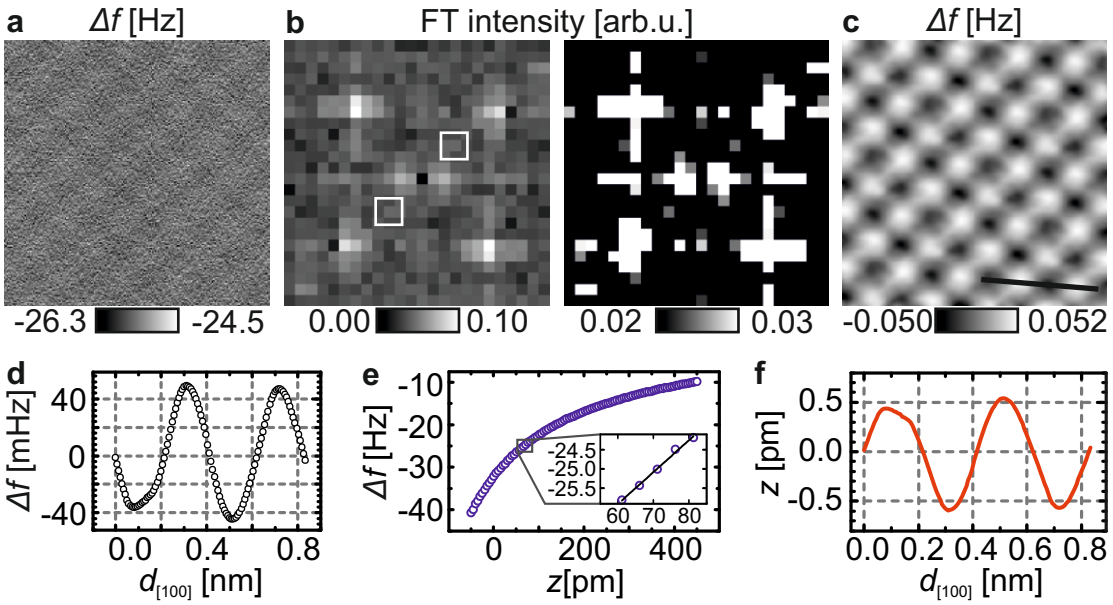

Figure 6.6.: **a**, Δf raw data, acquired with the circular symmetric Fe tip. **b**, Fourier spectra of the raw data with normal (left) and high (right) contrast. **c**, low-pass filtered and 2×2 unit cell averaged Δf data. **d**, line profile from **c**, showing the row-wise contrast. **e**, $\Delta f(z)$ curve used to translate Δf to topography z. **f**, the topography line profile shows a height difference between the local maxima of 0.1 pm, the average atomic corrugation is 1.1 pm. Imaging parameters: $2 \times 2\,\mathrm{nm}^2$, $k = 1800\,\mathrm{N/m}$, $f_0 = 59.369\,\mathrm{kHz}$, $A = 50\,\mathrm{pm}$, $Q = 1,360,000$, $V = 6.8\,\mathrm{V}$. Figure adapted from [105].

can be obtained by evaluating the slope of a $\Delta f(z)$ curve at the imaging distance. This is depicted in Fig. 6.6e. The average Δf value of the image in Fig. 6.6a is $\Delta f \approx 25.4\,\mathrm{Hz}$. The inset in Fig. 6.6e shows a linear fit to the data points around this average value and the slope is $0.0826\,\mathrm{Hz/pm}$. With this value the Δf line profile in Fig. 6.6d is converted to the topography profile in Fig. 6.6f. Note, there is also a sign change involved, because more negative Δf corresponds to a protrusion in Δf feedback mode.

The height variation now shows up on the *maxima* and the difference between two local maxima is only 0.1 pm. The average atomic corrugation is 1.1 pm. The larger height variation on the maxima is unexpected, because usually oxygen is imaged as protrusion. Possible reasons for the appearance of larger spin-dependent signal on top of the maxima could be that either the Ni sites are imaged as maxima or due to superexchange on O sites which might be stronger in this distance regime [24].
With the two other tips (Fig. 6.5d,g) no additional modulation of the atomic contrast was observed which indicates that these tips might not have been Fe terminated. On the other hand it is interesting that one can obtain atomic resolution at all with these two tips, because they are very likely terminated by more than one atom.

The overall magnitude and the small distance regime where the spin contrast is observed are in line with the experiments with uncharacterized Fe tips. Here, a value of 0.4 pm on top of a small chemical interaction of 1.6 pm was found (Fig. 6.3c). Apparently, Fe tips only yield weak spin-dependent signals over a small distance range where chemical forces are weak. The spin resolution gets lost when the tip height deviates from the ideal height by more than ±15 pm. The observation of low or no spin contrast can be due to an unfavorable alignment of tip and sample spins, but Fe tips systematically yield low spin contrast as several experiments with different Fe tips and on different spots of a given NiO sample were performed.

The spin orientation of the Fe apex atoms becomes unstable upon increased chemical bonding forces between tip and sample. This indicates that the MAE in Fe is not high enough to stabilize the magnetic moment of the front atom. Indeed, the MAE for bcc Fe is only 2.4 μeV/atom whereas hcp Co already has a MAE of 45 μeV/atom [200]. Materials with even higher MAEs are rare-earth alloys like samarium-cobalt (SmCo) which are used for permanent magnets. Their MAE is about 20-40 times larger than hcp Co and hence about a factor of 500 higher than the MAE of bulk bcc Fe [133, 201]. Using such high MAE materials as tips in MExFM experiments should lead to a higher stability of the spin orientation of the tip apex. To test this hypothesis, the measurements on NiO were repeated with bulk SmCo tips.

6.3. Measurements and Results with Samarium-Cobalt Tips

The preparation of bulk SmCo tips was described in chapter 4. A splinter of a SmCo permanent magnet was glued onto one of the new types of qPlus sensors, namely sensor type 2 as introduced in chapter 3. The SmCo tip was cleaned by field evaporation and then approached to the NiO sample without prior COFI characterization. It should be mentioned that the SmCo tip did not yield spin resolution directly upon approach, but after a spontaneous tip change images with very good SNR of the 2×1 unit cell could be obtained. Figure 6.7a shows unfiltered topography data z. The additional modulation is hardly perceptible due the superimposed higher frequency fluctuations. In the low-pass filtered image (Fig. 6.7e) the difference in apparent height of the lines indicated by the arrows and the neighboring rows can be clearly identified. Figures 6.7b,f show the corresponding Fourier transformed images. The low-pass filter removes the frequency bands outside of the central features (box in Fig. 6.7b) of the Fourier

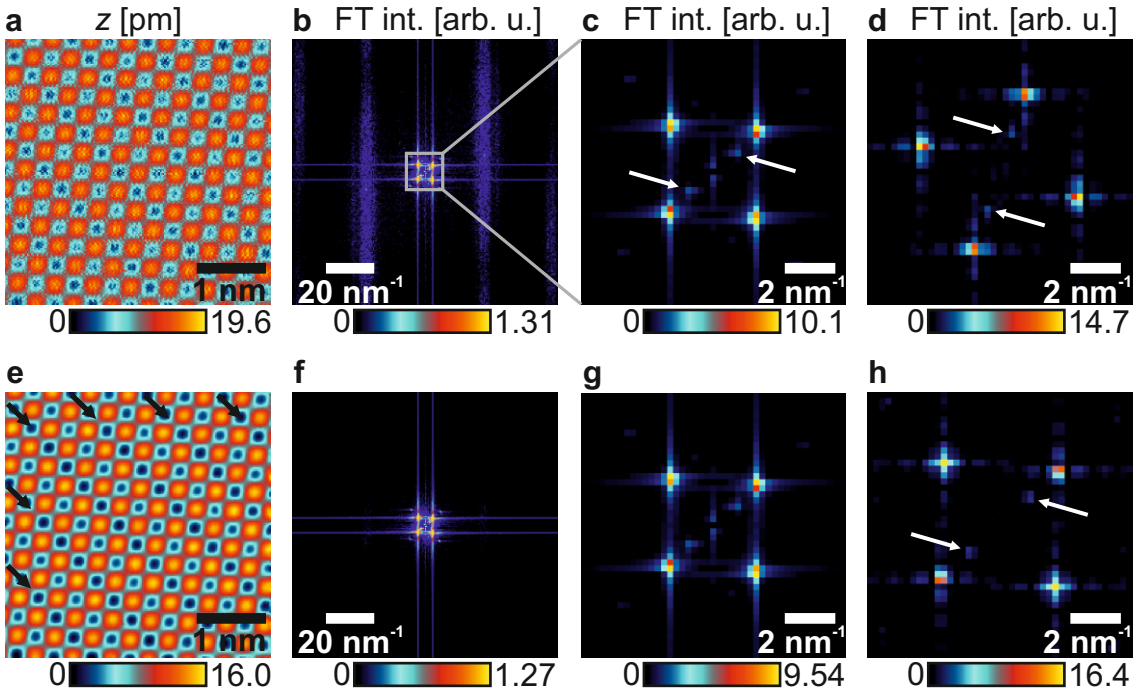

Figure 6.7.: **a**,**e**, topography raw data and low-pass filtered version ($\sigma = 50$pm). The arrows in **e** indicate the rows which appear darker in constant Δf feedback mode. **b**,**f**, Fourier transformated images corresponding to **a** and **e**. The z-scale is adjusted to increase the contrast on the vertical noise bands. **c**,**g**, zoom into the Fourier transformated images from **b** and **f** as indicated by the rectangle in **b**. The z-scale was not adjusted this time. The two additional peaks can be clearly identified (arrows). The low-pass filtering has no impact on the position and magnitude of the peaks. **d**, Fourier transform of an image where the scan direction was rotated by 30° with respect to **a**. All peaks including the spin related ones (arrows) are rotated accordingly. **h**, Fourier transform of an image where the scan speed was increased by a factor of 4 with respect to **a**. The distance in the Fourier images is reciprocal to the distance in the real space images. Imaging parameters for **a**: $3 \times 3\,\mathrm{nm}^2$, 192×192 pixels, 8 s/line, $\Delta f_{\mathrm{set}} = -35\,\mathrm{Hz}$, $k = 2425\,\mathrm{N/m}$, $f_0 = 39.761\,\mathrm{kHz}$, $A = 36\,\mathrm{pm}$, $Q = 31,000$, $V = 0.06\,\mathrm{V}$.

spectrum. Note, the images were interpolated from 192×192 pixels to 256×256 pixels to avoid numerical artifacts from the discrete Fourier transform as $192 \notin 2^n$ for $n \in \mathbb{N}$. Zooms into the full ranged Fourier transformed images in Figs. 6.7b,f are shown in Figs. 6.7c,g. The four peaks which originate from the atomic lattice and the two additional peaks due to the spin contrast (arrows in Fig. 6.7c) are not affected by the low-pass filtering. Figure 6.7d presents the Fourier transform of a topography image where the scan frame was rotated by 30° with respect to Fig. 6.7a and the peaks are rotated accordingly. This time the topography image was not interpolated to 256×256 pixels which leads to horizontal and vertical bars and dots originating from each of the main peaks. Another Fourier transformed image is shown in Fig. 6.7h where the scan speed was increased by a factor of 4 compared to Fig. 6.7a. The

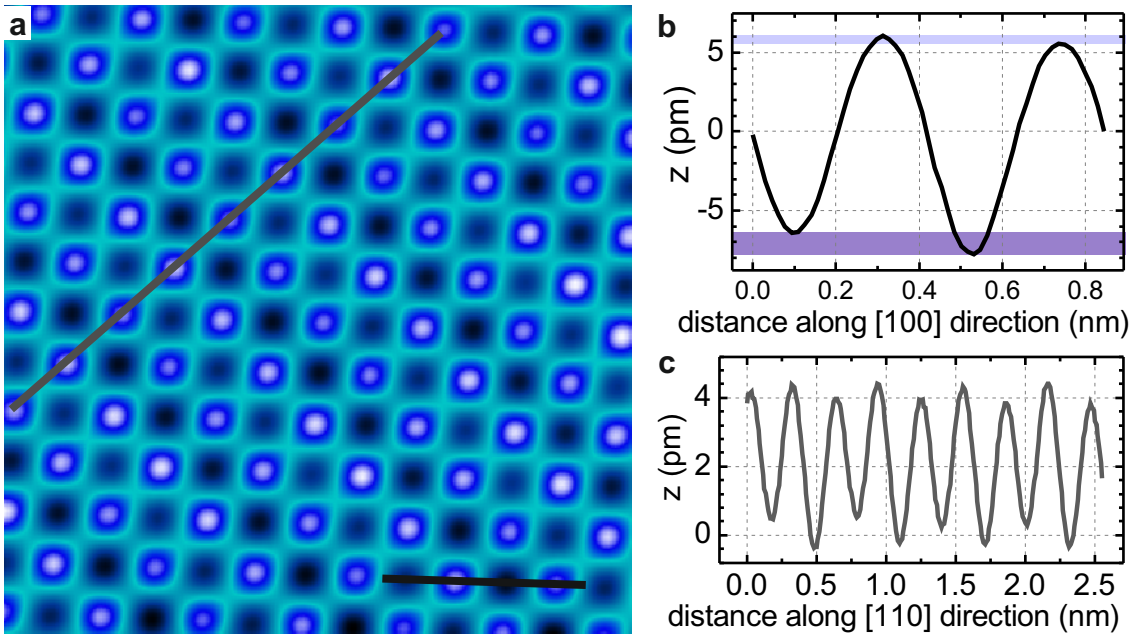

Figure 6.8.: **a**, low-pass (σ = 156 pm) filtered topography image ($2.7 \times 2.7\,\mathrm{nm}^2$), displayed such that the contrast on minima and maxima is enhanced. **b**, line profile along [100] direction, the difference between local minima (maxima) is indicated by the dark (light) blue shaded bars. **c**, line profile along [110] direction confirming the periodicity of the height variation on the maxima. Imaging parameters: see caption Fig. 6.7. Figure adapted from [105].

two additional peaks are still located at the same position relative to the four main peaks. The presence of the two additional peaks in Figs. 6.7d,h excludes an oscillatory noise signal whose phase matches by change the periodicity of the atomic lattice [14, 202]. Note, there is no unit cell averaging performed as in case of the Fe data from the last section and the previously reported results on NiO [14].

Figure 6.8a shows the same data as in Fig. 6.7a with a heavier low-pass filter and in a color code which highlights minima and maxima. An analysis of line profiles (Fig. 6.8b,c) allows to determine the height variation on minima to 1.35 pm as indicated by the dark blue shaded bar in Fig. 6.8. The average atomic corrugation is 12.9 pm. There is not only an additional modulation on the minima but also on the maxima. The height difference between the local maxima is only 0.50 pm (light blue shaded bar). These height variations show the same periodicity as the height variation on the local minima (Fig. 6.8c) – each second maximum has a similar apparent height. A modulation of the atomic contrast on top of both atomic sites was already discussed by Kaiser *et al.* in [180]. They attributed this to a magnetic double tip, mainly because the line profile showed an asymmetric, wedge-like shape of the atoms. As the line profile in Fig. 6.8c

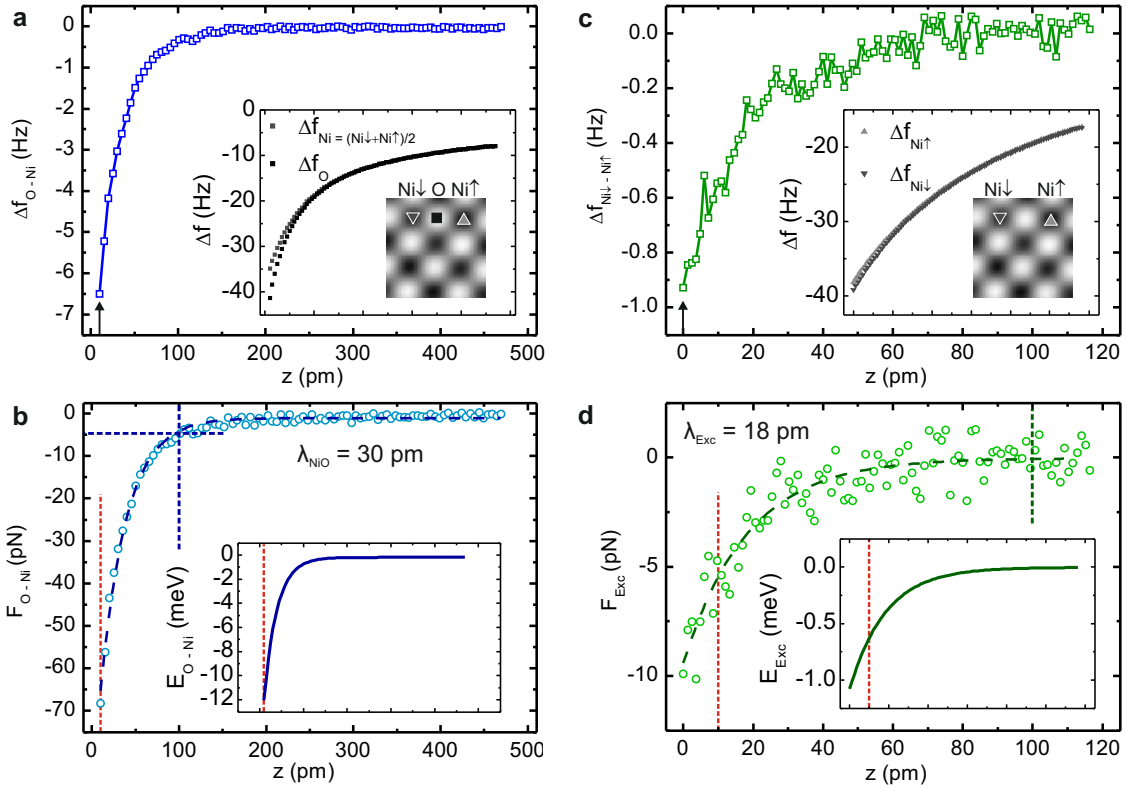

Figure 6.9.: **a**, $\Delta f(z)$ spectra on Ni($\downarrow,\uparrow$) and O sites (see inset) and difference between these curves (blue □). Starting positions of spectra are indicated by arrows in **a** and **c**, while the dashed red lines in **b** and **d** indicate the distance $z = 10\,\mathrm{pm}$ where Fig. 6.8a was imaged. **b**, deconvolved force between Ni and O site including an exponential fit ($\propto \exp(-z/\lambda)$) with $\lambda = 30\,\mathrm{pm}$ (dashed blue line). Integration of the force yields the energy difference (inset, solid blue line). **c**, $\Delta f(z)$ curves on Ni $\downarrow$ and Ni $\uparrow$ sites (inset) and difference between both sites (green □). **d**, resulting exchange force F_{Exc} with an even smaller decay length of $\lambda_{\mathrm{Exc}} = 18\,\mathrm{pm}$. Imaging parameters: see caption Fig. 6.7. Figure adapted from [105].

has an overall sinusoidal shape, the height difference on top of the minima is not due to a magnetic double tip but rather caused by an indirect or superexchange exchange mechanism between the tip moment and the second layer atoms. A direct exchange mechanism is unlikely because the magnetic moment of the oxygen atoms is about an order of magnitude smaller than the moment on the nickel sites [24, 192]. Therefore, we conclude that the minima correspond to Ni sites and a direct exchange mechanism leads to the observed difference in apparent height of 1.35 pm. The maxima are then O sites, where superexchange interaction between the tip and sub-surface Ni ions leads to the observed difference in apparent height of 0.50 pm.

The distance dependence of the atomic and exchange interactions is evaluated with the help of site dependent $\Delta f(z)$ curves (Fig. 6.9). These curves were acquired

on the oxygen and the two different nickel sites. For the following discussion these are denoted as O, Ni ↓, and Ni ↑ as indicated in the insets of Figs. 6.9a,c. The O sites are also not equivalent, but unfortunately this was not recognized during data acquisition and therefore no data on the distance dependence of the superexchange interaction is available. The value of $z = 0$ indicates the position of closest approach in the $\Delta f(z)$ curves in Fig. 6.9c, whereas the curves in Fig. 6.9a start at $z = 10\,\mathrm{pm}$. The image in Fig. 6.8a was also acquired at $z = 10\,\mathrm{pm}$, marked by the dashed red lines in Figs. 6.9b,d. The difference in frequency shift between the O and the average of the Ni sites at $z = 10\,\mathrm{pm}$ is $\Delta f_{\mathrm{O-Ni}} = \Delta f_{\mathrm{O}} - \Delta f_{\mathrm{Ni=(Ni\downarrow - Ni\uparrow)/2}} = 6.5\,\mathrm{Hz}$ (Fig. 6.9a). Open circles in Fig. 6.9b depict the corresponding force values which were obtained by deconvolution with the Sader-Jarvis method. Fitting an exponentially decaying function yields a value of $F_{\mathrm{O-Ni}} = -65\,\mathrm{pN}$ at the imaging distance and a decay length of $\lambda_{\mathrm{NiO}} = 30\,\mathrm{pm}$. The difference between Ni ↓ and Ni ↑ at $z = 10\,\mathrm{pm}$ is $\Delta f_{\mathrm{Ni\downarrow - Ni\uparrow}} = \Delta f_{\mathrm{Ni\downarrow}} - \Delta f_{\mathrm{Ni\uparrow}} = 0.93\,\mathrm{Hz}$ (Fig. 6.9c). This is caused by the difference in the exchange interaction between tip and sample leading to a variation of the decay constant of the covalent bonds forming between tip and sample. The exchange force is shown in Fig. 6.9d and at $z = 10\,\mathrm{pm}$ one obtains $F_{\mathrm{Ni\downarrow - Ni\uparrow}} = -5.4\,\mathrm{pN}$ and a decay length of $\lambda_{\mathrm{Exc}} = 18\,\mathrm{pm}$.

At a distance of $z = 100\,\mathrm{pm}$, there is still a detectable difference in the chemical interactions on Ni and O sites of about 5 pN, see intersection of dashed blue lines in Fig. 6.9b. In contrast, one cannot discriminate F_{Exc} from zero within the experimental error at this position ($z = 100\,\mathrm{pm}$, indicated by the dashed green line in Fig. 6.9d). A measurable difference in F_{Exc} of around $1 - 2\,\mathrm{pN}$ arises at a relative distance of about $40 - 50\,\mathrm{pm}$ from the closest approach. This indicates that there is a difference in the spatial extent of the involved orbitals. First, s or p orbitals with no net magnetic moment start to interact and give rise to atomic resolution. Next, at a distance of about 50 pm closer the spin carrying d orbitals overlap and lead to a formation of different spin configurations between tip and sample. This influences the spatial part of the wave functions and leads to the observed difference in forces or apparent heights in the images.

6.4. Discussion

One of the main challenges in obtaining spin resolution on NiO is to detect the tiny influence of the exchange interaction on the covalent bonding between tip and sample atoms. Theoretical predictions, where an Fe atom probes the NiO surface, find values of the chemical forces in the range of nN and exchange forces on the order of 0.1 nN

[24, 25]. The experimental exchange force on NiO(001) is about 10 pN. Although the SmCo results are not directly comparable to these calculations, it is still instructive to discuss them here. The height difference on Ni sites observed by Kaiser *et al.* with Fe coated tips was 1.5 pm which is in the same range as observed above with the SmCo tips. Hence, the strength of the exchange interaction is likely to be similar in both experiments. One obvious reason for a deviation between experimental and theoretical exchange forces is that the calculations assume a collinear alignment of the spins whereas this is unknown in the above experiments. On the other hand, the magnitude of about 1.5 pm was now measured by two completely different experimental setups and it is unlikely that this is just a coincidence.

The experiments with bulk Fe tips suggest that at close tip-sample distances tip and sample spins align such that no net difference in exchange interactions is detectable, see regime III in Fig. 6.4c. Although SmCo tips yield a better contrast this does not necessarily mean that such a process does not occur, but it might instead be just less pronounced. A comparison of the chemical forces, which are also calculated in Refs. [24, 25] is difficult as these can depend strongly on the involved atomic species [78, 203, 204].

The exchange force and energy decrease monotonically with decreasing tip-sample distance. The predicted change in the magnetic coupling was not observed within the resolution of our measurements [24, 25]. The presence of a difference in exchange forces on the O sites, as measured with the SmCo tip, was predicted for a Fe tip and is probably due to a superexchange mechanism between tip atom and second-layer Ni atom [24].

The difference between the decay lengths for the atomic and spin resolution, indicates that different orbitals are involved in the imaging process. For the spin-dependent part the electron wave functions which are localized in d or f shells must overlap. These extend less into the vaccum gap than s type orbitals which give rise for atomic resolution [164].

In hindsight, the FIB treatment of the magnetic tips is not a good idea, because it is known that the implanted ions can destroy or reduce the magnetization [205]. This is probably the reason why the FIB treated bulk Fe tip yielded an even smaller contrast of 100 fm versus 400 fm than the untreated tips. On the other hand, this did not have a significant influence on the SmCo tip. Nevertheless, the detection of a spin-dependent signal with the COFI characterized tip from Fig. 6.5a indicates that the tip is indeed Fe terminated. With the other two tips from Figs. 6.5d,g, no exchange interaction was detected, which might be due to a Cu contaminated bulk Fe tip.

With the SmCo tip similar contrast (1.35 pm) was observed than in previous experiments where an external B-field of 5 T was applied [14, 180, 181]. This suggests that the increased MAE of SmCo helps to stabilize the spin at the tip apex and that the magnetic moment itself is not the only crucial parameter. The MAE of SmCo is approximately 1 meV per atom which is even higher than the Zeeman energy $E_\mathrm{Z} = g\mu_B B = 0.6\,\mathrm{meV}$ for a g-factor of 2.2 for Fe and $B = 5\,\mathrm{T}$ [14]. Based on the above findings, materials with high MAE should be best suited for resolving the spin structure of a surface by AFM. Of course, SmCo is not a standard tip material and difficult to handle because it is rather brittle. There are other materials like PtFe, PtCo, or CoFe which might be better suited to utilize common electrochemical etching processes for tip fabrication.

The increased MAE of SmCo is most likely responsible for the increased spin-dependent signal on NiO compared to bulk Fe tips. Though, this cannot account for the significantly higher signal-to-noise ratio compared to the previous work by Kaiser *et al.* We attribute this to the increased sensitivity to short-range interactions due to the small amplitude operation (35 pm vs. 6.65 nm) and the improved SNR of the custom-designed sensors.

For future experiments it would be very interesting to study the exchange interaction at defects or step edges of the NiO(001) surface. Moreover, one could investigate individual adatoms (e.g. Fe or Co) on NiO(001) and depending on their adsorption site different spin-dependent signals could be expected. Differences in the spin state would also be related to different occupations of the d orbitals. Such differences where resolved on the Cu adatom on Cu(110) in the previous chapter and it might therefore be possible to observe these different spin states also with non-magnetic CO tips.

7. Determination of $TlBiSe_2$ Surface Termination by Force Microscopy

This chapter consists of three sections, the first gives a brief introduction to the field of topological insulators. In the second section, the properties of the material under study, $TlBiSe_2$ and the experimental results will be presented. Finally, the extraordinary surface morphology of $TlBiSe_2$ is discussed.

7.1. Introduction to Topological Insulators

The material class of so-called topological insulators has attracted a lot of attention in the past ten years due to its unique electronic structure and it is considered as a new phase of matter [26, 206]. In the following, the basic principle of topologically insulating materials will be presented. A complete description of the field of topological insulators is beyond the scope of this work and also not necessary for the following discussion of the experimental observations. For further details the reader is referred to a number of review articles [26, 27, 206, 207].

First of all, topological insulators are not classical insulators with band gaps in the order of a few eV like NiO from the previous chapter. They are usually semiconducting or semimetallic materials with band gaps in the range of a few tens to hundreds of meV [5]. What makes them special is the band structure topology. In a conventional insulator or semiconductor valence and conduction band are separated by an energy gap E_g. The top of the valence band is usually formed by bonding p-type states and the bottom of the conduction band by antibonding s-type states [207]. In some materials, the order of the bands is swapped which leads to a inverted band structure or a so-called "negative-band-gap" [208–210]. The origin of the band inversion is the spin-orbit interaction. If a material with inverted band structure is in contact with a normal band structure material, the band gap must become zero at the interface, because of the transition from a "positive" to a "negative" gap [26, 211]. This leads to the evolution of gapless or conductive states at the interface with a linear dispersion

relation around the crossing or respectively Dirac point [211–214].

The presence of conducting edge channels itself is not so peculiar as this is already known for decades from the integer quantum hall effect (IQHE) [215]. What makes topological insulators very interesting is the presence of these channels in the absence of an external magnetic field. This is due to the spin-momentum locking [26]. The strong spin-orbit interaction effectively acts as an intrinsic magnetic field and forces electrons to move in a certain direction depending on their spin orientation [213, 216]. In a simple picture, a 2D topological insulator can be viewed as two copies of the IQHE which consists of a spin-up and a spin-down channel of counterpropagating electrons [206]. This is also called quantum spin hall effect (QSHE) [212]. These channels are spin-polarized and as long as spin-dependent scattering on magnetic impurities can be excluded the transport is expected to be dissipationless [26]. The first realistic system which was predicted to host a quantum spin hall state was a HgTe/CdTe quantum well [211]. Shortly afterwards, the QSHE was observed in such a system experimentally [217]. Other material systems which are well known for their inverted band structure are also investigated in terms of the QSHE, e.g. the QSHE is also predicted for inverted InAs/GaSb quantum wells [218].
For obvious reasons, the prospect of having quantized, spin-polarized conductive channels which do not require high magnetic fields or even low temperatures is very attractive for the field of spintronics, especially in terms of spin injection and spin transport [4].

For a so-called 3D topological insulator, there is not such a "classical" analogy like the IQHE. In a 3D topological insulator the transition from inverted to normal band structure occurs for example at the interface between the bulk of the material and the vacuum[1], hence at the surface [5, 26, 27, 214]. This in itself is again not new. Surface states, even spin-polarized ones, are well known in surface science [154, 219–223]. The interesting physics lies again in the existence of surface states where spin-momentum locking is present. This leads to a helical Dirac cone at the surface [214]. Such unique electronic properties were first predicted for $Bi_{1-x}Sn_x$ compounds [224] and shortly later confirmed by angle resolved photoemission spectroscopy (ARPES) and its spin-sensitive version (SARPES) [225, 226]. Another class of materials exhibiting such properties is the Bi_2Se_3, Bi_2Te_3, and Sb_2Te_3 family [5, 227–229].

In the above systems the surface states are not well isolated from bulk states leading to scattering between them and reduced electron or hole mobility [28]. This is were $TlBiSe_2$ comes into play: Here, an isolated Dirac cone within the bulk band gap was predicted at the surface [230–233] and confirmed by ARPES measurements [28,

[1]In this context, vacuum is considered as a normal band structure "material".

234–237]. The band gap of $200 - 350\,\mathrm{mV}$ is among the highest for known TI materials [5]. This makes $TlBiSe_2$ also a promising candidate for room temperature spintronics applications.
There are still a few open questions, e.g. discrepancies between theoretical predicted and experimentally observed surface states. This is independent from the surface termination considered in the calculations [232, 233]. Therefore it is interesting to clarify the actual surface termination of this material which will be the scope of the next section.

7.2. Properties of $TlBiSe_2$ and Results of STM/AFM Measurements

Topological insulators like the Bi_2Se_3 family are layered materials consisting of quintuple layers, which are weakly bound by vdW interactions. For ARPES or STM/AFM experiments in UHV they are cleaved where the weakly bonded layers constitute the natural cleaving planes [238, 239]. A $TlBiSe_2$ crystal consists of (-Tl-Se-Bi-Se-) layers which are stacked along the c axis of the hexagonal unit cell [240]. The bonding between the layers is covalent. The crystal structure with its primitive rhombohedral unit cell is depicted in Fig. 7.1a and the rhombohedral [111] direction coincides with the hexagonal [001] direction. The experimental hexagonal unit cell parameters of bulk $TlBiSe_2$ crystals are $a = 425\,\mathrm{pm}$ and $c = 2.205\,\mathrm{nm}$ [240]. Similar values were obtained on thin films with $a = 424\,\mathrm{pm}$ and $c = 2.233\,\mathrm{nm}$ [241]. The theoretical values given in Fig. 7.1a from Ref. [233] match the experimental ones within a few percent. If the crystal cleaves between, e.g. Tl and Se layers, a (111) surface is exposed to vacuum, but due to the covalent bonding it is not a priori obvious where the cleaving occurs.

In a recent study by Kuroda *et al.* the surface termination was investigated by STM and x-ray core-level spectroscopy [239]. The STM topography showed regular steps with heights of about $0.8\,\mathrm{nm}$ corresponding to the height of a (-Tl-Se-Bi-Se-Tl-) stack (Fig.7.1a). Furthermore, small and disordered islands were observed on all terraces and within the islands a hexagonal closed packed atomic structure could be identified. Overall, about half of the surface was covered with these islands. Therefore, the authors concluded that during the cleaving one of the layers is ripped apart, with one half remaining on each side of the junction. The x-ray analysis revealed a core-level shift of the Tl binding energy. This led them to the conclusion that a Tl layer is

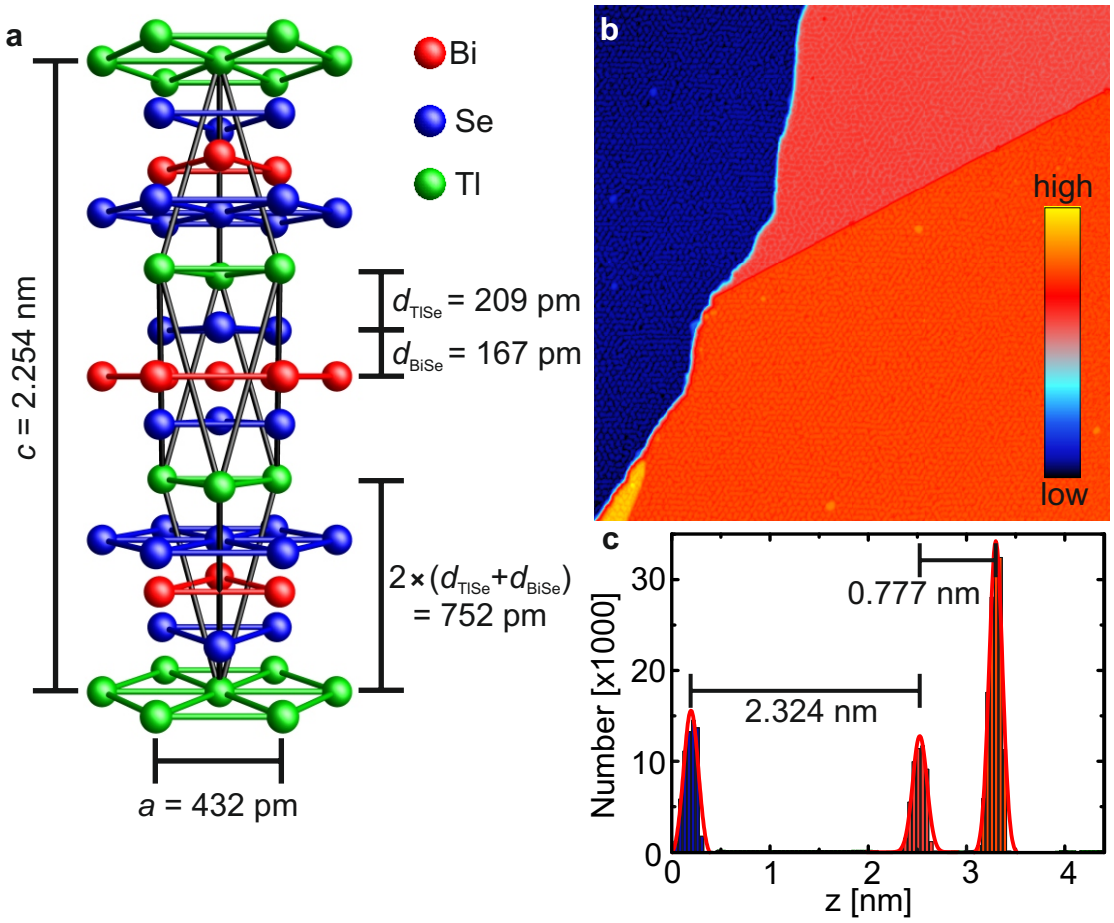

Figure 7.1.: **a**, crystal structure of $TlBiSe_2$, each Tl and Bi layer is sandwiched by two Se layers. The rhombohedral unit cell (black lines) is also depicted. The values for the lattice constants a, c and the layer spacings d_{TlSe}, d_{BiSe} are theoretical values from Ref. [233]. **b**, $200 \times 200\,nm^2$ STM topography image of the (111) surface. On each of the three large scale terraces an amorpheous structure can be identified. **c**, histogram of step heights from **b**. Two different heights are present which correspond to the lattice constant c and $c/3$. Imaging parameters: $V = 0.8\,V$, $I = 130\,pA$, $A = 50\,pm$.

disrupted and the surface is terminated by Tl islands sitting on a Se layer.

Figure 7.1b shows an overview image of the (111) surface of a cleaved $TlBiSe_2$ single crystal[2] acquired in constant current mode with a bulk W tip mounted on a qPlus sensor. Two step edges are clearly apparent, the straight one separates two terraces with a height difference of 777 pm (Fig. 7.1c). This corresponds to the height of one (-Tl-Se-Bi-Se-Tl-) stack. The step between the left terrace and the upper right is about 2.32 nm which fits to the hexagonal unit cell parameter c. Each peak is fitted

[2]The oriented single crystals were glued on an Omicron sample holder and cleaved *in-situ* by knocking off a top-post.

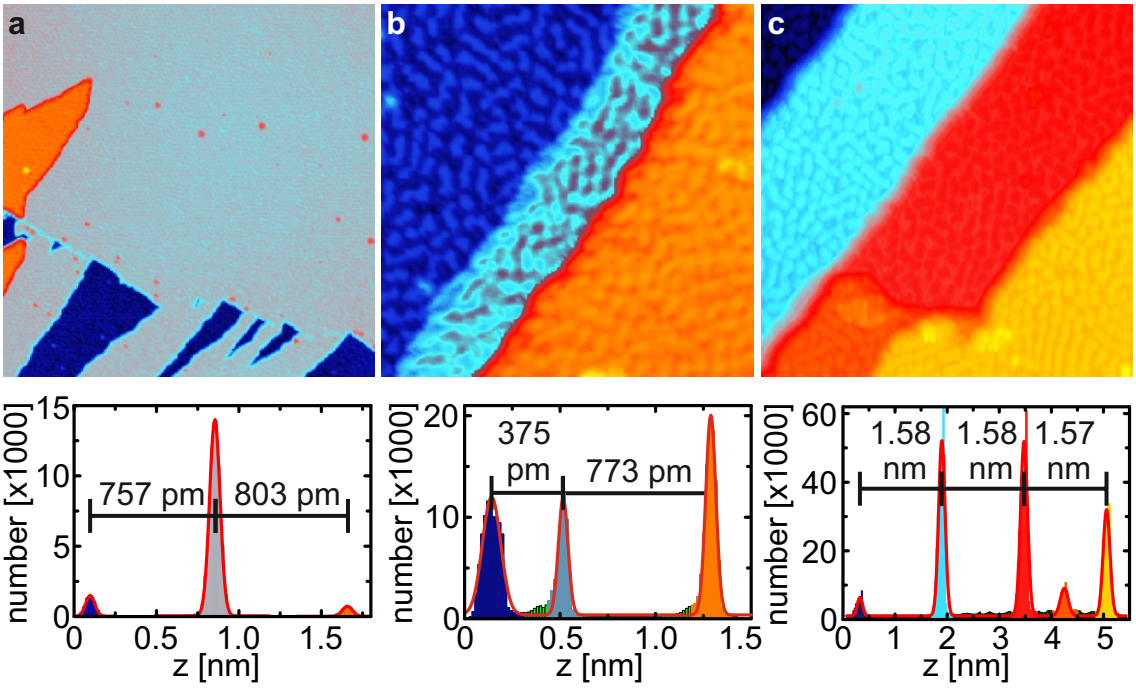

Figure 7.2.: STM topography images and histogram height analysis. The area below the Gaussian envelope is shaded in the color of the corresponding terrace. **a**, $200 \times 200\,\mathrm{nm}^2$ sized image where three terraces seperated approximately by the (-Tl-Se-Bi-Se-Tl-) stack distance of $c/3$ are found. For all peaks $\sigma = 28 - 32\,\mathrm{pm}$. **b**, slighlty low-pass filtered $44 \times 44\,\mathrm{nm}^2$ image. One step with a height of $\approx c/3$ is observed. Interestingly, the step between the two lower lying terraces is only 375 pm. The standard deviation is not similar for all peaks, see text for further details. **c**, $61 \times 61\,\mathrm{nm}^2$ image where three steps with a height of $\approx 1.58\,\mathrm{nm}$ can be identified plus a smaller step with about half of this height. For the three larger peaks $\sigma_{2,3,5} \approx 65\,\mathrm{pm}$, for the two smaller ones $\sigma_1 = 50\,\mathrm{pm}$ and $\sigma_4 = 75\,\mathrm{pm}$. Imaging parameters: **a**, $V = 0.8\,\mathrm{V}$, $I = 100\,\mathrm{pA}$, $A = 500\,\mathrm{pm}$. **b**, $V = 0.5\,\mathrm{V}$, $I = 50\,\mathrm{pA}$, $A = 50\,\mathrm{pm}$. **c**, $V = 0.5\,\mathrm{V}$, $I = 10\,\mathrm{pA}$, $A = 50\,\mathrm{pm}$.

with a Gaussian function and the standard deviation[3] σ for all peaks in the histogram of Fig. 7.1c is about 70 pm. The histogram bars under the Gaussian envelope of each peak are shaded in the color of the corresponding terrace in the image.

More step height data is shown in Fig. 7.2.[4] Mainly steps with a height of $\approx 0.75 - 0.8\,\mathrm{nm}$ and $\approx 1.55 - 1.58\,\mathrm{nm}$ are observed. These step heights are unit fractions of the lattice parameter c. Therefore complete (-Tl-Se-Bi-Se-Tl-) stacks are removed from the bulk crystal. The question is: Is it a Tl-Se bond or Bi-Se bond which is broken and which part remains on the surface?

The possibility of a Bi-Se bond breaking is unlikely, because the covalent bonding is

[3]For a Gaussian function the standard deviation σ is related to the full width at half maximum (FWHM) via: $\mathrm{FWHM} = 2\sqrt{2\ln 2}\sigma \approx 2.35\sigma$.

[4]The data in Fig. 7.2b,c was acquired by Julian Berwanger during his Bachelor thesis on "Oberflächencharakterisierung Topologischer Isolatoren mittels Rastersondenmikroskopie im Ultrahochvakuum" [242], advised by F. Pielmeier.

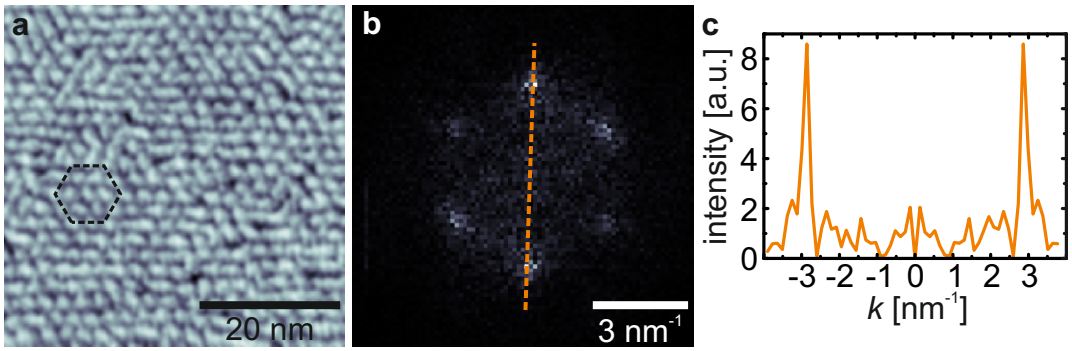

Figure 7.3.: a, STM image showing hexagonally ordered patches as indicated by the dashed hexagon. **b**, FFT from **a** where six peaks can be identified. **c**, line profile along the dashed line in the FFT. The distance between the peaks and the center is 2.86 nm^{-1}. Imaging parameters: $48.4 \times 48.4\,\mathrm{nm}^2$, $V = 0.8\,\mathrm{V}$, $I = 100\,\mathrm{pA}$, $A = 500\,\mathrm{pm}$.

stronger there – 167 pm bond length versus 209 pm for Tl-Se. In Fig. 7.2b there is a step with a height of only 375 pm, which corresponds very well to $d_{\mathrm{TlSe}} + d_{\mathrm{BiSe}} = 209\,\mathrm{pm} + 167\,\mathrm{pm} = 376\,\mathrm{pm}$. Two scenarios could give such a step height. First, if a Se-Bi stack would be removed from a remaining Tl layer or if a Se-Tl stack would be removed from a remaining Bi layer. The presence of a step height smaller than $c/3$ leads inevitably to the presence of two different surface terminations. This is clarified with the following example: Assuming that the lowest lying layer in Fig. 7.2b is Tl terminated then the step height of 375 pm corresponds to an additional layer of Se and Bi, leading to a Bi terminated surface on the middle terrace. The next step is 773 pm which is the height of a complete stack, but now with sequence (Bi-Se-Tl-Se-Bi). This results again in a Bi terminated upper terrace. Of course, Bi and Tl can be swapped, but anyway there are two different surface terminations present in Fig. 7.2b. Additionally, the appearance of the disordered structures is different between the lower and the two upper terraces, because the height variation within the islands is larger on the lower one. This shows also up in the standard deviation σ of the histogram peaks where $\sigma_1 = 48\,\mathrm{pm}$ for the lower terrace is significantly larger than $\sigma_{2,3} = 25 - 27\,\mathrm{pm}$ for the two upper terraces. It is not possible to obtain such a step height with a Se terminated surface layer, because on Se layers there would either follow a Bi-Se or a Tl-Se stack. These two scenarios would correspond to step heights of $2 \times d_{\mathrm{BiSe}} = 334\,\mathrm{pm}$ or $2 \times d_{\mathrm{TlSe}} = 418\,\mathrm{pm}$. Note, the smaller step height in Fig. 7.2b was rarely observed, indicating that the surface is usually equally terminated.
In Fig. 7.2c there are again only steps with unit fractions of the lattice parameter c. The difference in the standard deviations for the two smaller peaks, here σ varies from $\sigma_1 = 50\,\mathrm{pm}$ to $\sigma_4 = 75\,\mathrm{pm}$, is most likely caused by the small number of points available for these two terraces and not due to different surface terminations.

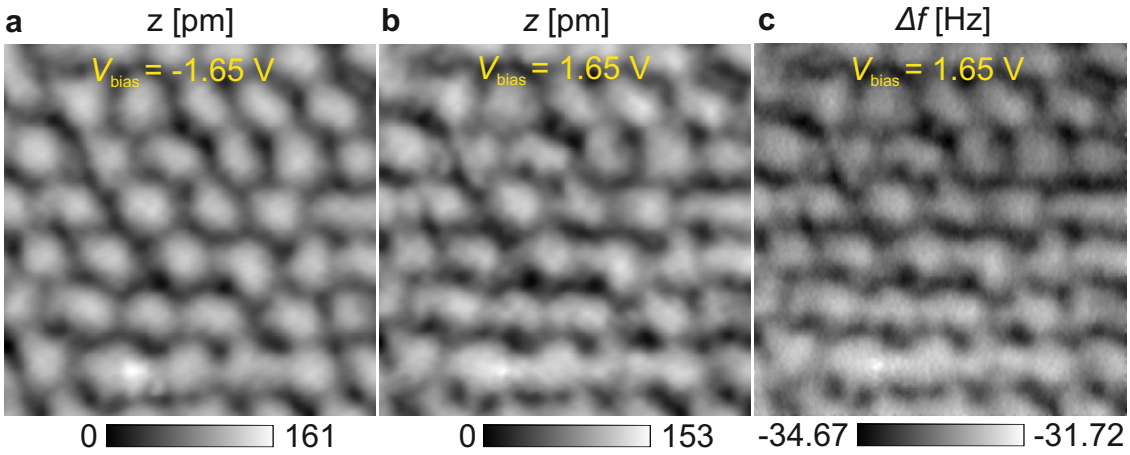

Figure 7.4.: **a**, **b** STM images with opposite bias polarities, $V = -1.65\,\mathrm{V}$ and $V = 1.65\,\mathrm{V}$. **c**, Δf acquired simultaneously with topography data in **b**. All images are low-pass filtered with $\sigma = 180\,\mathrm{pm}$. Imaging parameters: $15.45 \times 15.45\,\mathrm{nm}^2$, $I = 100\,\mathrm{pA}$, $A = 500\,\mathrm{pm}$.

Figure 7.3a shows a zoom onto the large terrace in Fig. 7.2a, apparently there is some hexagonal order present within the patches. The Fourier transform (Fig. 7.3b) clearly resolves this and the distance of the peaks from the center is $k_{0-p} = 2.86\,\mathrm{nm}^{-1}$ (Fig. 7.3c). With the definition of $k = 2\pi/\lambda$ and taking into account that the reciprocal lattice is rotated by 30° with respect to the direct lattice [53], the average distance of the patches equals $\lambda = 2\pi/(\cos(30°) \cdot 2.86\,\mathrm{nm}^{-1}) = 2.54\,\mathrm{nm}$. This is about 5 times larger than the interatomic distance of $a = 425\,\mathrm{pm}$.

The influence of the bias polarity on the appearance of the patches was also investigated, but apart from slightly varying apparent heights there is no significant difference between imaging with $V = \pm 1.65\,\mathrm{V}$ (Fig. 7.4a,b). The Δf data corresponding to Fig. 7.4b is shown in Fig. 7.4c and looks like an almost exact copy of the topography or respectively, the tunneling current. This is probably caused by the so-called phantom force which is an apparent short-range electrostatic repulsive force caused by a reduction of the gap voltage. The effect was first studied on semiconducting Si samples and increases with reduced sample conductance [243].

In contrast to the previous STM work [239], it was not possible to resolve any structure within the patches in constant current mode, neither in topography nor Δf channel. Figure 7.5a shows a $11.9 \times 11.9\,\mathrm{nm}^2$ topography image acquired at a gap resistance of $1.54\,\mathrm{G}\Omega$[5], the apparent height of the patches is about 250 pm (Fig. 7.5b). A reduction of the current setpoint lead to unstable imaging conditions, therefore the constant height mode was used to approach the tip closer to the sample. Figure 7.5c

[5]Kuroda *et al.* obtained atomic resolution in STM already at a gap resistance of $12\,\mathrm{G}\Omega$ [239].

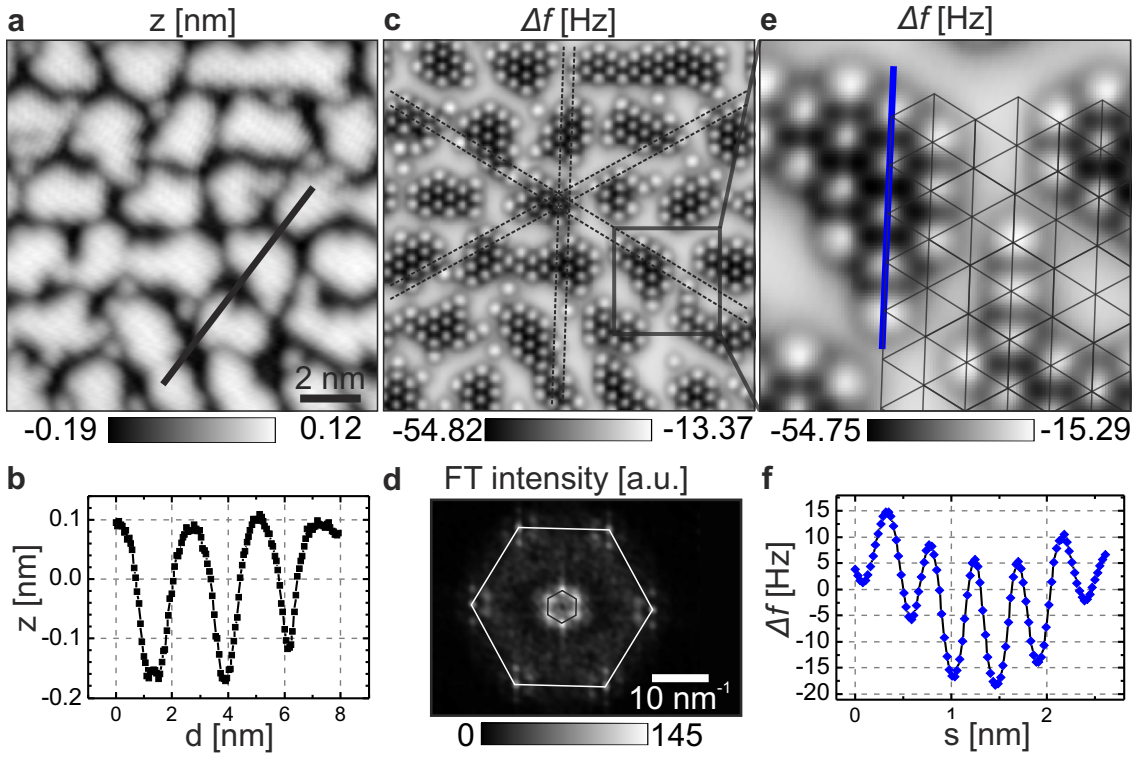

Figure 7.5.: **a**, $11.9 \times 11.9\,\mathrm{nm}^2$ low-pass filtered ($\sigma = 140\,\mathrm{pm}$) STM image. **b**, line profile along solid line in **a**. **c**, low-pass filtered ($\sigma = 140\,\mathrm{pm}$) constant height Δf data showing the same area as **a**. **d**, low-pass filtered ($\sigma = 0.17\,\mathrm{nm}^{-1}$) Fourier spectrum of **c**. **e**, $3.4 \times 3.4\,\mathrm{nm}^2$ Δf image of the area indicated in **c**. The overlaid hexagonal lattice has a nearest neighbor distance of 445 pm. **f**, line profile along 5 atoms in **e**. Imaging parameters: **a**, $V = 0.2\,\mathrm{V}$, $I = 130\,\mathrm{pA}$. **c**,**e**, $V = 10\,\mathrm{mV}$, $A = 50\,\mathrm{pm}$.

shows Δf data of the same area as in Fig. 7.5a. The relative distance between tip and sample was reduced by about 230 pm. Within the patches a hexagonal arrangement of the atoms is clearly resolved. The dashed lines indicate that there is no registry shift between the islands. This demonstrates that only the surface layer is distorted and the islands sit on the well ordered hexagonal grid of the underlying layer. Additionally, there is also a number of atoms which are not bound to one of the islands.

The Fourier spectrum (Fig. 7.5d) of this Δf image is quite interesting: Two hexagonal structures can be observed. The inner hexagon (black) shows the same orientation and dimensions as the one in Fig. 7.3b and corresponds to the superstructure of the patches, whereas the outer hexagon (white) resembles the atomic lattice. It is rotated by 30° with respect to the superstructure. Two subsequent layers of the $TlBiSe_2$ crystal are also rotated by 30° with respect to each other. This indicates that the superstructure is indeed caused by the underlying layer. Each of the six outer peaks shows satellites which originate from to the superstructure. Note, the Fourier spectrum is low-pass filtered, because in the raw image data the satellites are difficult

to identify. Figure 7.5e shows another constant height Δf image of the area indicated by the square in Fig. 7.5c. The overlaid grid has a lattice constant of $a_{nn} = 445\,\text{pm}$, which is about 5% larger than the literature value of 425 pm from above. On Cu(111), the lattice spacing was determined within an accuracy of 2% – 260 pm were measured instead of $d_{\text{nn}} = 255\,\text{pm}$. This implies that there is at least a +3 % relaxation of the atomic spacing at the distorted surface layer. A variation of the piezo calibration within the scan range can also be ruled out for this measurement.[6] The line profile (Fig. 7.5f) along the solid blue line in Fig. 7.5e shows the atomic contrast in Δf. At this imaging distance the atoms show less negative frequency shift, hence they appear repulsive. In the middle of the patches the contrast in Δf is quite large reaching values of about 25 Hz.

A count of the occupied lattice positions in Fig. 7.5c yielded a number of 420, see section A.3 for further details. The total number of primitive units cells of area $A = \sqrt{3}a_{nn}^2/2$ which fits within the $11.9 \times 11.9\,\text{nm}^2$ scan area is 826. This results in a ratio of $420/826 = 0.51$ and demonstrates that indeed one half of the surface layer is removed upon cleaving.

To study the distance dependence of the contrast a constant height data set was acquired with each constant height map spaced by 20 pm. In addition to the Δf channel the excitation signal V_{exc} and the tunneling current I were also monitored. Figures 7.6a-g show the first seven Δf slices and Figs. 7.6h-n show the corresponding ΔE data. This is the dissipated energy per oscillation cycle calculated from V_{exc} by using [185, 244]

$$\Delta E = \frac{\pi k A^2}{Q}\left(\frac{V_{\text{exc}}}{V_{\text{exc},0}} - 1\right), \tag{7.1}$$

where $V_{\text{exc},0}$ is the excitation amplitude required to compensate intrinsic losses of the cantilever.

When the tip is further away from the sample at a relative distance of 120 pm from the closest approach the islands appear attractive in Δf (Fig. 7.6a). Upon approach of the tip towards the sample atomic resolution can be identified within the islands. The atoms show up as protrusions in Δf (Figs. 7.6c-g). More interesting is the ΔE channel, where far from the surface an increased dissipation can be observed on the islands (Figs. 7.6h,i). When the tip approaches closer to the surface the dissipation

[6] The distance between the tip positions on Cu(111) and $TlBiSe_2$ within the scan range ($2.37\,\mu\text{m}^2$) is about 500 nm. On Cu(111) there was no difference in the piezo calibration between scan positions spaced by 300 nm.

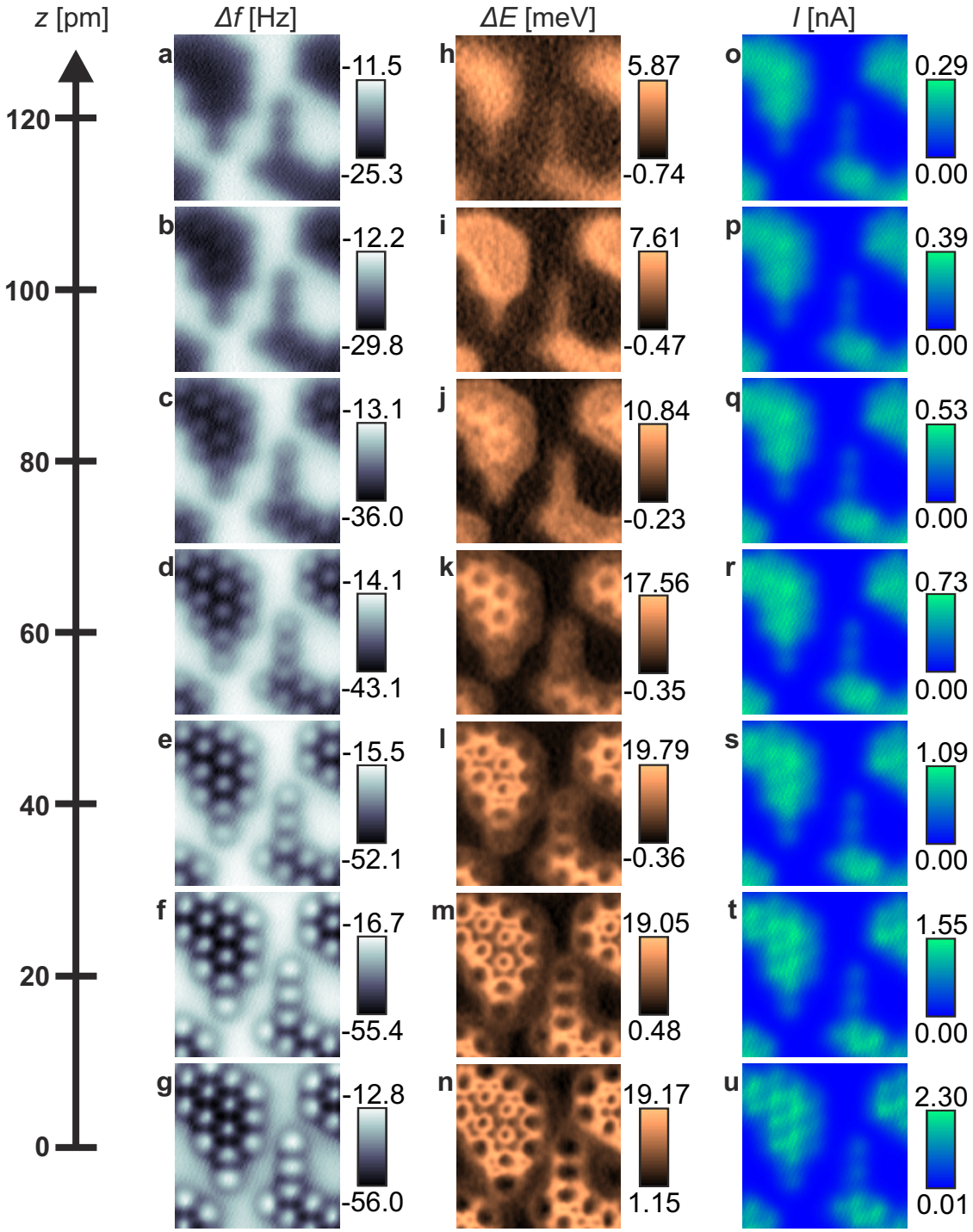

Figure 7.6.: frequency shift Δf (**a**-**g**), dissipation per cycle ΔE (**h**-**n**), and tunneling current I (**o**-**u**) for varying tip-sample distances. The Δf and I data is low-pass filtered with $\sigma = 7\,\mathrm{pm}$, for ΔE data $\sigma = 190\,\mathrm{pm}$. Imaging parameters: $3 \times 3\,\mathrm{nm}^2$, $V = 10\,\mathrm{mV}$, $f_0 = 26.666\,\mathrm{kHz}$, $A = 50\,\mathrm{pm}$, $Q = 28140$, $k = 1800\,\mathrm{N/m}$, $V_{\mathrm{exc},0} = 86\,\mu\mathrm{V}$.

decreases at the atomic sites. At the same time the repulsive contrast in the Δf data shows up (compare Figs. 7.6c,j or 7.6d,k). In Figs. 7.6l,m,n the contrast changed again, while the dissipation is still reduced at the atomic sites it now also reduced in

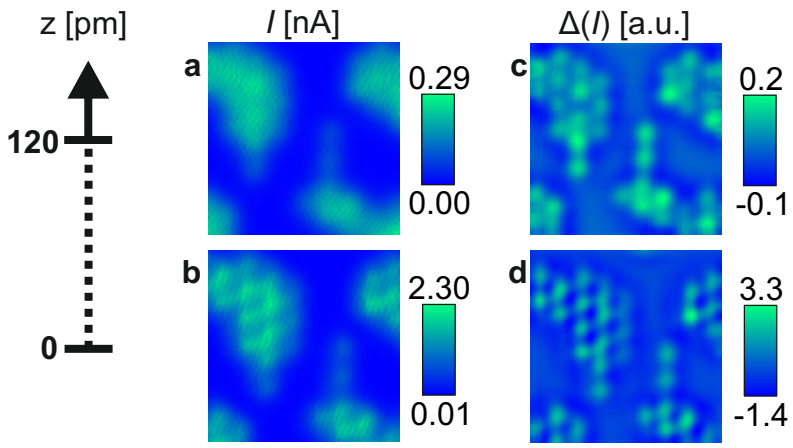

Figure 7.7.: **a**,**b**, tunneling current I data from Fig. 7.6o,u, corresponding to closest and furthest tip-sample distance. **c**,**d** low-pass ($\sigma = 170\,\mathrm{pm}$) and Laplace filtered I data. One can clearly identify the hexagonal arrangement of the atoms at both distances. Imaging parameters: see Fig. 7.6.

between the atoms. This leads to a ring of increased dissipation around the atoms in the center of the islands. Note, the negative values for the minimum in ΔE (Figs. 7.6h-l) are not due to a "real" negative excitation, but rather due to noise. It could be filtered by applying a stronger low-pass filter, but this would lead to a loss of lateral resolution.

Before discussing the ΔE data in more detail, the simultaneously acquired tunneling current I is mentioned briefly. Figures 7.7o-u show low-pass filtered I data. At closest approach the tunneling current reaches values of 2.3 nA at a bias voltage of 10 mV. In the first two or three current images one can also identify some atomic scale resolution, but it is not as pronounced as in the Δf data. Figure 7.7 shows I data at $z = 0$ and at $z = 120\,\mathrm{pm}$. After applying a Laplace filter (Figs. 7.7c,d) the hexagonal lattice is nicely resolved even at larger tip-sample distances. In the image at $z = 0$ some distortions are already present.

Figures 7.8a,c show five ΔE and Δf line profiles. The lateral position is indicated in the atomically resolved images to the right of the line profiles. The horizontal y axis in Figs. 7.8a,c corresponds to the vertical y axis in the images where $y = 0$ is located at the bottom of the images. The dashed gray lines indicate the position of the maxima in Δf which are assumed to correspond to the atomic positions. At these sites the dissipation is reduced. For the three closest distances ($\Delta z = 0, 20, 40\,\mathrm{pm}$) an additional minimum appears between two atomic sites in ΔE. The emergence of these additional minima coincides with a leveling off of the contrast in the ΔE data (Fig. 7.8b). Although not as pronounced, there is also a reduction in the Δf contrast at closer tip-sample distances (Fig. 7.8d). Hence, in this distance regime significant

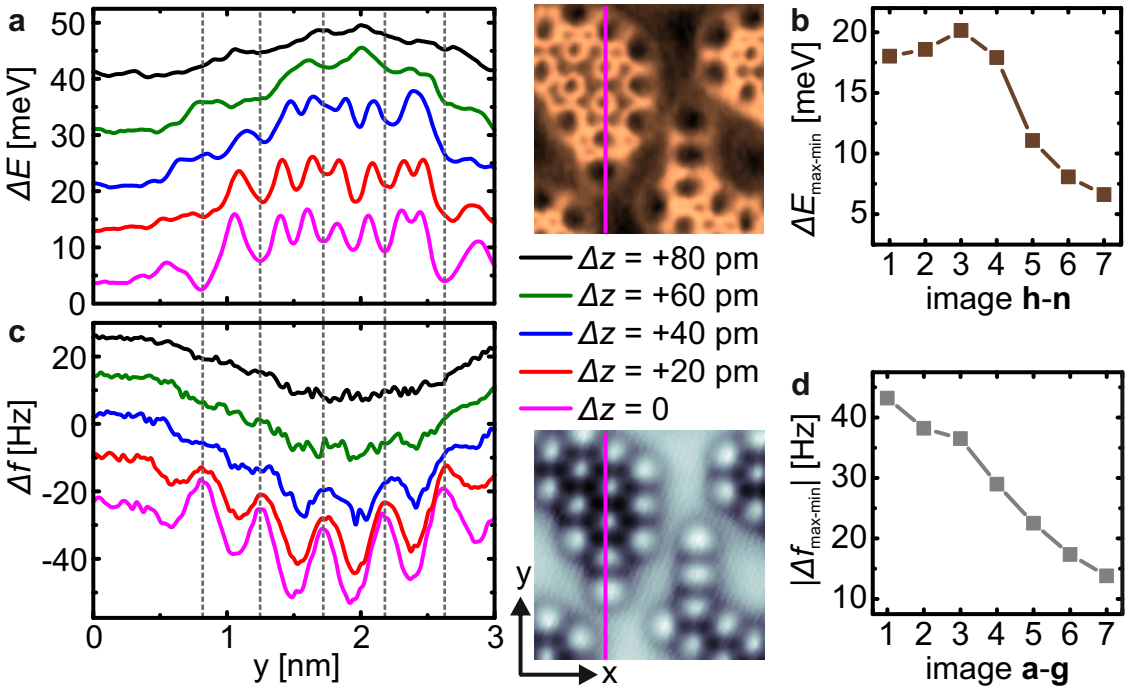

Figure 7.8.: **a**,**c**, profiles of ΔE and Δf along the line indicated in the atomically resolved images. For each channel the first five line profiles are shown, the curves are offset to each other by 10 meV or respectively, 10 Hz for clarity. In the line profiles $y = 0$ corresponds to the bottom and $y = 3$ nm to the top of the images. The dashed gray lines indicate the position of the local maxima in Δf. **b**,**d**, distance dependence of the contrast in ΔE (Fig. 7.6i-p) and Δf (Fig. 7.6a-h) data, where the labeling 1-7 of the horizontal axis corresponds to $\Delta z = 0 - 120$ pm.

relaxations are present between tip and sample. The increased dissipation signal on top of the islands at further tip-sample distances, where the interaction is attractive, could be due to a vertical displacement of the islands as a whole. If the islands are displaced from the surface layer by more than the equilibrium bonding length between the Tl and Se atoms a hysteresis can occur which leads to an increased dissipation signal. When the tip approaches closer the island the dissipation is decreased at the atomic sites. This might be caused by the tip, which is now closer to the atoms and therefore prevents them from being displaced by more than their equilibrium bonding length. Above the atomic sites the excitation signal is therefore reduced (Fig. 7.6j,k). At even closer distances ($\Delta z = 0 - 40$ pm) a lateral displacement of the atoms could explain the decreased dissipation, because on top and in between the atoms lateral forces are equal.

7.3. Discussion

The surface morphology of $TlBiSe_2$ was studied with STM and AFM. The step height analysis showed that mainly steps with a height corresponding to integer multiples of the (-Tl-Se-Bi-Se-Tl-) stack height are present on cleaved samples. This is in line with the results obtained by Kuroda *et al.* [239]. Furthermore, steps with a smaller height were rarely observed, but they led to the conclusion that the surface is either Tl or Bi terminated. Because the Tl-Se (209 pm) bond is softer than the Bi-Se (167 pm) bond, one could expect that a Tl-Se bond breaking is more likely to occur upon sample cleavage. The presence of a number of individual atoms which are not integrated into one of the islands is indicative for metallic atoms like Tl and not for a chalcogen like Se. Hence, it is most likely that a removal of half a Tl layer occurs upon cleaving. This leads to Tl islands which sit on an intact Se layer. Again, this is in agreement with the x-ray analysis of Kuroda *et al.*

The disrupted surface of $TlBiSe_2$ is probably the reason for the absence of surface states predicted by theory, because the disordered surface layer does not allow any extended bloch type states and therefore has a trivial topology. The transition to a non-trivial topology occurs one layer below the surface layer.

8. Summary

In this work, I presented results obtained with high resolution atomic force microscopy where sub-picometer vertical resolution was reached when detecting exchange interactions. To obtain this extraordinary resolution, it is important to optimize all parameters of the force sensors which are relevant to increase the signal-to-noise ratio.

In chapter 3 the signal-to-noise ratio of a standard qPlus sensor and a needle sensor was compared theoretically and experimentally. First, the calculated sensitivity for both sensors was compared to measured values from thermal excitation spectra. For both sensors the agreement between theoretical and experimental sensitivity is very good, if one takes the geometry factor for qPlus sensors into account. Second, it was shown that the measured force gradient noise density at the frequency demodulator output matches the calculated noise densities very well. The needle sensor shows less deflection detector noise than the qPlus sensor in its original dimensions, whereas the qPlus sensor exhibits less thermal, oscillator, and thermal frequency drift noise.
Identifying the geometrical parameters which define the magnitude of deflection detector noise revealed that deflection detector noise scales linearly with the thickness of the oscillating prong. This led then to the development of qPlus sensors with smaller beam thickness and length to keep the stiffness k and the resonance frequency f_0 in an optimal range. The expected improvement of about a factor of three in deflection detector noise was again confirmed experimentally. The custom sensors exhibit even less deflection detector noise than a needle sensor. The stiffness values of these sensors were determined with finite element analysis methods taking their precise geometry into account and they are in good agreement with experimental estimates. Several other non-standard types of quartz tuning forks were also analyzed, but these did not reach the performance of the custom miniaturized qPlus sensors.
Furthermore, the influence of thermal frequency drift at cryogenic temperatures from $4.8 - 48\,\mathrm{K}$ was determined. It turned out that the change of f_0 with temperature T varies on the order of ppm/K. Coupled oscillators show less frequency variation with T than qPlus sensors. Custom qPlus sensor also showed less frequency change with T than standard qPlus sensors, suggesting that the mechanical coupling of the beam to

the support has an influence on $\partial f/\partial T$. This is further reassured by the increased quality factor Q of the custom sensors.

In chapter 4 the experimental setup, a low temperature STM/AFM UHV system, and a method for reliable fabrication of electrochemically etched tips made from Fe wires was presented. The possibility to etch tips directly from a piece of wire which is attached to the prong of the qPlus sensor is very convenient for sensor handling. A SmCo tip made from a piece of permanent magnet was also presented.

In chapter 5 Cu adatoms were investigated on different facets, (110) and (111), of a Cu single crystal with CO functionalized tips. At close tip-sample distances a ring-like structure was observed on both adatoms, whereas the adatom on Cu(110) additionally showed a twofold symmetric feature at further tip-sample distances. The hardly perceptible twofold symmetry in case of the adatom on Cu(110) is most likely caused by an unequal occupation of the d_{xz} and d_{yz} orbitals. A simple model for the charge density based on Slater-Type-Orbitals qualitatively reproduces the distance dependence of the experimental data.
The comparison of the adatom data with complementary COFI measurements obtained with bulk Cu tips is also twofold. For the Cu/Cu(111) system the agreement between both experiments is quite good, whereas the COFI image of a presumably $\langle 110 \rangle$ oriented Cu tip does not resemble at all the Cu adatom data on Cu(110), neither close nor far from the sample. A likely explanation for this discrepancy is that the Cu$\langle 110 \rangle$ tip does not reflect a single atom tip but rather consists of a cluster of four atoms. If this is the case also the current interpretation of COFI data for bulk Fe and W tips is questionable.
In the last part of chapter 5, COFI measurements on the characterization of bulk Fe tips were presented. Similar as reported for W tips, three high-symmetry orientations of the tip apex could be identified. Namely tips with one, two, or three attractive minima. Fe tips with a single attractive minimum exhibited a similar magnitude of the attractive force than W tips and can therefore be distinguished from Cu coated tips.

The spin-resolved measurements on NiO were presented in chapter 6. Measurements with bulk Fe tips revealed only a very small ($\approx 400\,\mathrm{fm}$) spin-dependent signal which could only be observed in a thin ($10 - 20\,\mathrm{pm}$) distance range relative to the surface. The expected improvement in signal strength by performing these experiments with COFI characterized Fe tips and optimized qPlus sensors was not observed. Only one Fe tip resolved a tiny magnetic signal of only 100 fm.
A SmCo tip nicely resolved the 2×1 spin pattern not only on Ni but also on O sites.

This is due to the detection of direct and superexchange interaction between surface and sub-surface Ni spin magnetic moments with the tip moment. The height variation on Ni sites was 1.35 pm and on O sites it was 0.50 pm. Additionally, the difference in exchange force on Ni sites was measured. It is in the range of $5 - 10$pN which is about an order of magnitude smaller than predicted by theory. The SmCo tip provided a much more stable magnetic configuration than bulk Fe tips, which turned out to be of major importance to achieve a large signal-to-noise ratio. For future measurements on exchange interactions with AFM, tips should be made of materials with high magnetocrystalline anisotropy energy.

In chapter 7 the surface termination of $TlBiSe_2$, a bulk topological insulator, was investigated. In standard STM mode, only hexagonally ordered patches with an average distance of about 2.5 nm were observed. Constant height AFM data revealed the hexagonal atomic structure within the patches. This particular surface structure is caused by the cleaving of the samples to prepare a clean surface in UHV. One half of a Tl layer is removed and the other half of the atoms remains on the surface. The unusual surface termination is also the origin for the absence of surface states predicted by theory, finally leading to a band structure with a well isolated Dirac cone located at the interface between bulk and vacuum. This also has some practical implications, because by deliberately destroying the surface of this material one could tailor the band structure.

A. Appendix

A.1. Non-Standard qPlus Sensors

In section 3.4 the signal-to-noise ratio of custom qPlus sensors and a few other quartz resonators was compared. The deflection noise density n_q was determined from thermal excitation spectra shown in the following. The required stiffness k for the custom sensors from Fig. 3.8c,d was determined with the help of COMSOL Multiphysics[1] which is a modeling tool for physical properties based on finite element methods.

A.1.1. Stiffness of Optimized qPlus Sensors

For beams with a rectangular cross section which are clamped on one side the stiffness is given as

$$k_{\text{beam}} = \frac{Ewt^3}{4L^3}. \tag{A.1}$$

As there is always an error in the determination of the dimensions (width w, thickness t, and length L) the resulting error in the stiffness is about 7 times larger. A better way to determine the stiffness is therefore to measure the resonance frequency and the dimensions of a given sensor and then calculate k from

$$k_{\text{m}} = (2\pi f_0)^2 \times m^*, \tag{A.2}$$

where $m^* = 0.24m = 0.24V\rho$ is the effective mass of the beam, V volume, and ρ mass density of quartz. If a mass m' is added to the end of the prong, m^* has to be replaced by $(m^* + m')$ in the above equation.

The cross sections of the custom sensors introduced in chapter 3 (Figs. A.1 and A.2) deviate from a rectangular shape which complicates the calculation of their stiffnesses. Both have etched grooves at the top and bottom which do not run along the whole beam. Hence, the areal moment of inertia is not constant over the beam length. To

[1] COMSOL Inc., 744 Cowper Street, 94301 Palo Alto, California, USA

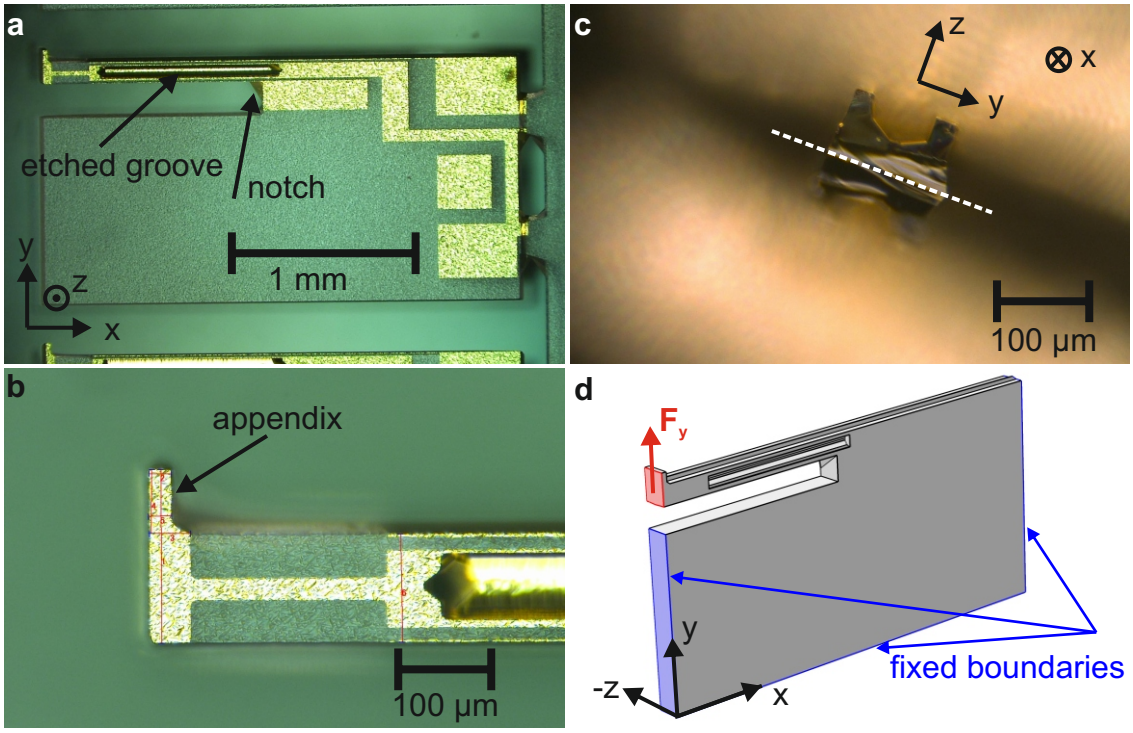

Figure A.1.: a,b, optical microscope images of the custom sensor of type 2. **c**, cross section of the beam, only the upper half is in the focus, because the beam is not cleaved perfectly perpendicular to the x direction. The profile is symmetric with respect to the dashed line. The coordinate system in **c** is not exact, but just serves as an orientation guide. **d**, 3D model and boundary conditions as used for the simulations with COMSOL.

analyze the shape of the beam cross sections of the two custom sensors some of them were cleaved with a scalpel. Images of the cross sections are shown in Figs. A.1c and A.2c, clearly, these are not rectangular in shape. The thicker end of the beams, which simplifies the attachment of tips, should also be considered. In the following, the stiffness values obtained with the simple formulas and finite element analysis (FEA) will be compared.

For an estimate of the stiffness a rectangular beam with dimensions as given in Tab. A.1 is assumed to calculate the stiffness k_{beam} via Eq. (A.1) and k_{m} via Eq.

	L (µm)	t (µm)	w (µm)	k_{beam} (N/m)	k_{m} (N/m)	$k_{\mathrm{m}'}$ (N/m)	f_0^{exp} (Hz)
type 2	1190	116	145	2640	2270	2410	67134
type 4	992	85	145	1790	1650	1830	73303

Table A.1.: Geometrical parameters, length L, thickness t and width w and stiffness values of custom qPlus sensors. k_{beam} values are calculated from Eq. (A.1), k_{m} and k'_{m} values are calculated from Eq. (A.2), without (k_{m}) and with (k'_{m}) taking the additional mass into account.

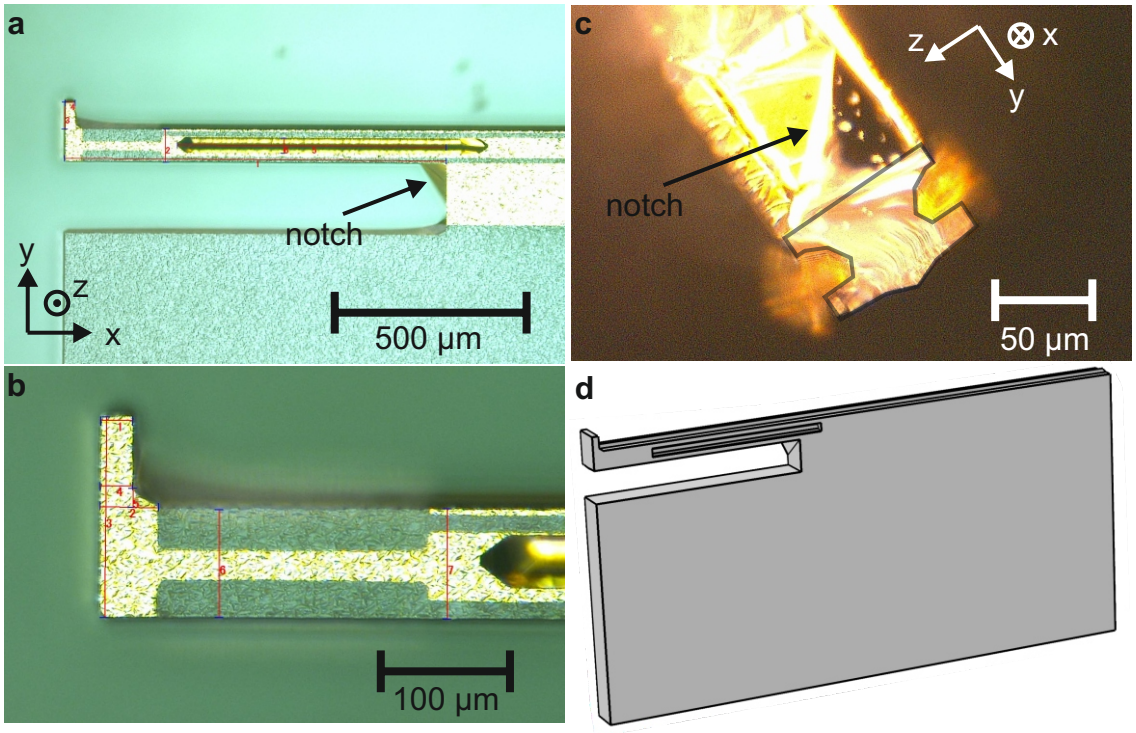

Figure A.2.: a,b, optical microscope images of the custom sensor of type 4. **c**, cross section of the beam, the contour is indicated. **d**, 3D model, boundary conditions are equal to the ones from Fig. A.1d.

(A.2). Additionally, $k_{m'}$ is determined via Eq. (A.2) where the mass of the appendix at the end of the beam is also taken into account. The dimensions used for the two custom qPlus sensors are determined from optical microscope images (Figs. A.1 and A.2). The mass of a rectangular beam with dimensions of sensor type 2 (4) is $m^{\text{type2}} = 1190\,\mu\text{m}\cdot 116\,\mu\text{m}\cdot 145\,\mu\text{m}\cdot 2650\,\text{kg/m}^3 = 5.30\cdot 10^{-8}\,\text{kg}$ ($m^{\text{type4}} = 3.24\cdot 10^{-8}\,\text{kg}$). The mass m' of the appendix at the end is the same for both types and is determined as $m' = [(69\,\mu\text{m}\cdot 29\,\mu\text{m}) + (0.5\cdot 20\,\mu\text{m}\cdot 15\,\mu\text{m})]\cdot 145\,\mu\text{m}\cdot 2650\,\text{kg/m}^3 = 8.27\cdot 10^{-10}\,\text{kg}$. The resulting stiffness values are summarized in Tab. A.1. The $k_{m'}$ values where the mass at the end is taken into account are expected to be the more accurate. On the other hand, the grooves were still not taken into account and additionally there is a notch at the lower clamping point of each beam which reduces the effective beam length. For proper modeling of the actual sensor geometry with a FEA program (COMSOL Multiphysics) a realistic 3D model was generated with a 3D-CAD program.[2] The 3D models of sensor type 2 and 4 are shown in Figs. A.1d and A.2d.

For the determination of the stiffness and eigenfrequencies the structural mechanics module from COMSOL was used. The stiffness was obtained from static bending of the

[2]Autodesk Inventor Professional 12.0, Autodesk Inc., San Rafael, California, USA.

	f_0 (Hz)	f_{lat} (Hz)	k_{FEA} (N/m)
type 2	67302	53045	2408
type 4	73382	79617	1870

Table A.2.: Resonance frequency of normal (f_0) and lateral (f_{lat}) oscillation mode and stiffness k_{FEA} along the direction of the normal mode.

quartz prong and the load force was applied to the end of the prong (Fig. A.1d). The material properties of quartz used for the simulation and also for the calculations above were Young's modulus $E = 78.6\,\mathrm{GPa}$, mass density $\rho = 2650\,\mathrm{kg/m^3}$, and Poisson's ratio $\nu = 0.136$ [89]. Before modeling the actual sensors, a rectangular beam with the dimensions of sensor type 2 was modeled. The obtained values for stiffness and first and second eigenmode (normal and lateral oscillation) were in excellent agreement (deviation of less than 1 %) with the analytic solutions.

The values for the eigenfrequencies and the stiffness from the simulations are summarized in Tab. A.2. The stiffness of sensor type 2 from the simulation is $k_{\mathrm{FEA}} = 2408\,\mathrm{N/m}$ and the corresponding resonance frequency is $f_0 = 67.302\,\mathrm{kHz}$. This is very close to the experimentally observed eigenfrequency of $f_0^{\mathrm{exp}} = 67.134\,\mathrm{kHz}$. The stiffness value k_{FEA} is almost exactly similar to $k_{\mathrm{m}'}$ from above. On the other hand, this nice agreement is somewhat by chance, because if one would take the mass of the grooves into account the effective mass of the beam changes and respectively, $k_{\mathrm{m}'}$ as well. In terms of resonance frequencies, the agreement for sensor type 4 is of similar quality, and also the stiffness $k_{\mathrm{FEA}} = 1870\,\mathrm{N/m}$ is quite close to $k_{\mathrm{m}'} = 1830\,\mathrm{N/m}$. Note, there is basically no variation of the values for k_{FEA} and f_0 depending on the boundary conditions (Fig. A.1d), e.g. if only the bottom face of the sensor is fixed the stiffness is reduced by only 0.5 %. An interesting finding from the simulations is the position of the frequency of the lateral bending mode. For sensor type 2 $f_{\mathrm{lat}} \approx 53\,\mathrm{kHz}$ which is about 14 kHz below the normal bending mode. In contrast, for sensor type 4 the lateral oscillation has a frequency of $f_{\mathrm{lat}} \approx 80\,\mathrm{kHz}$ which is about 7 kHz higher in frequency than the normal bending mode. Figures A.3 and A.4 show the normal and lateral bending mode for both sensors and the corresponding von Mises stress profiles.

At this position, the examined version of this thesis contained technical drawings of the MicroCrystal qPlus sensors of type 2 and 4. These were removed in the published version in accordance with the supervisor Prof. Dr. Franz J. Giessibl.

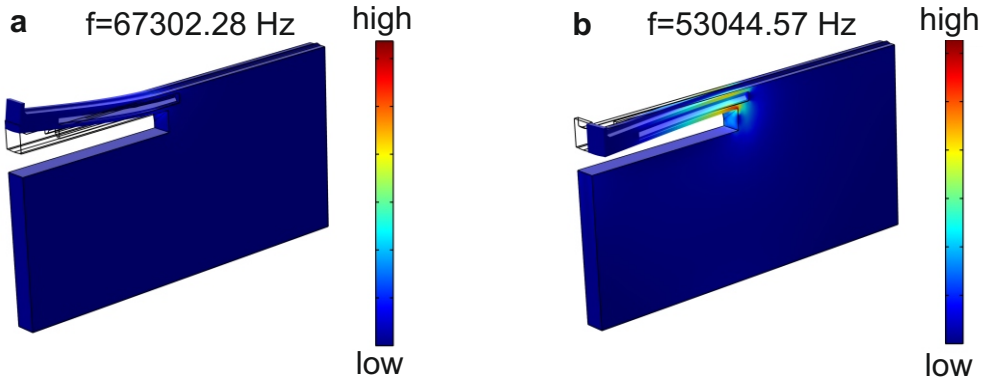

Figure A.3.: **a**,**b**, normal and lateral bending mode of sensor type 2. The color scale indicates the von Mises stress [245].

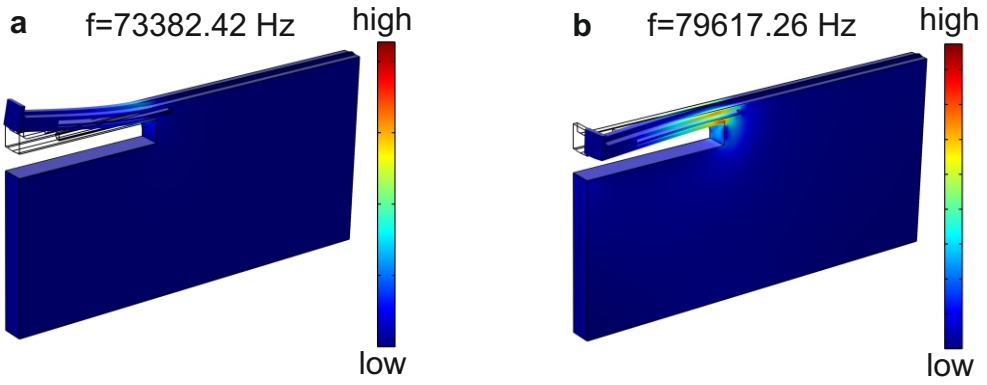

Figure A.4.: **a**,**b**, normal and lateral bending mode of sensor type 4. The color scale indicates the von Mises stress.

A.1.2. Thermal Peaks of Non-Standard qPlus Sensors

In Fig. 3.9 the calculated spectral noise density at the PLL output was compared between various kinds of quartz resonators. The required sensor parameters k, f_0, Q, and n_q are summarized in Tab. 3.5. These values were obtained from thermal excitation spectra similar as described in section 3.2 for standard qPlus and needle sensors. The corresponding thermal excitation spectra for these non-standard sensors are presented in Fig. A.5.

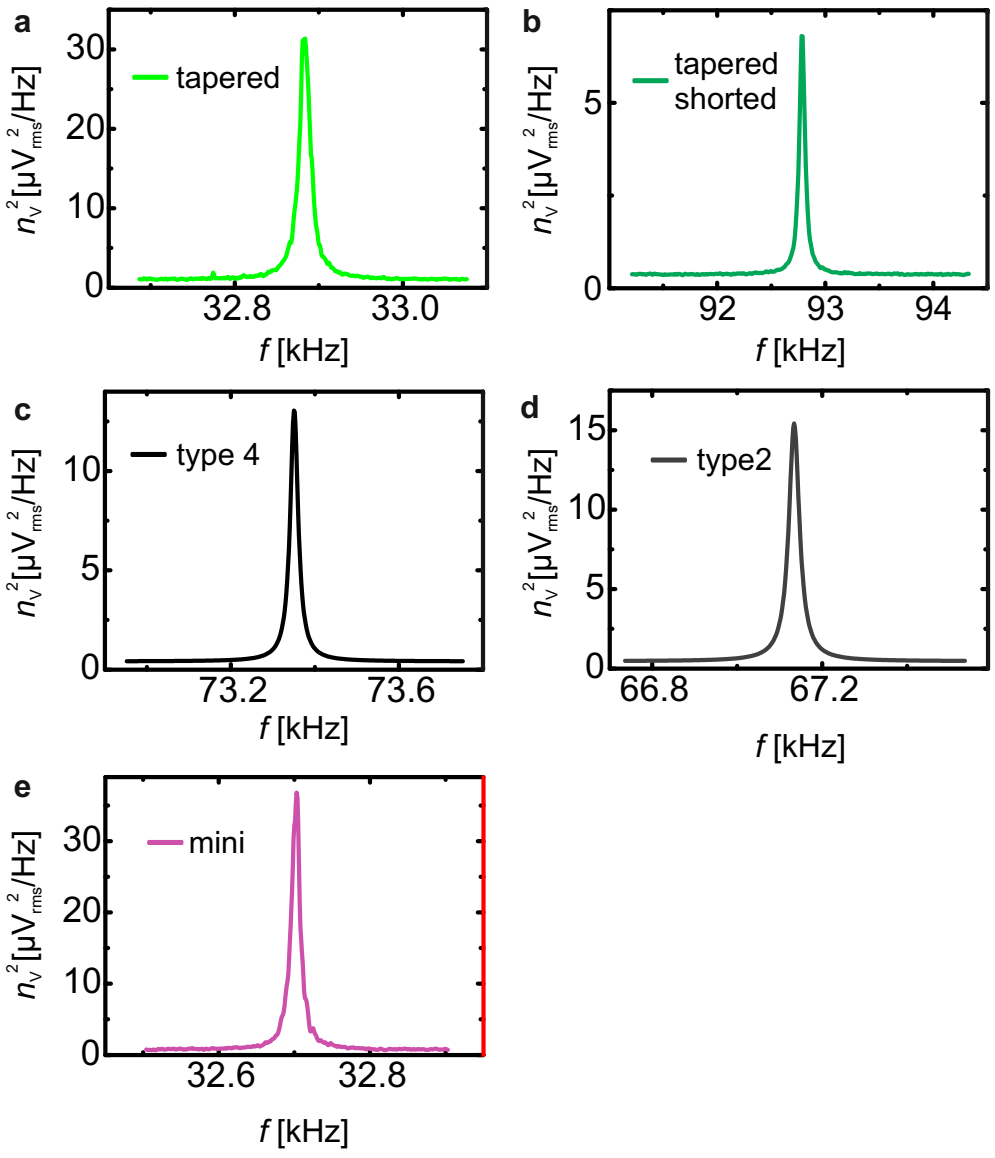

Figure A.5.: Thermal excitation spectra acquired at room temperature and ambient pressure. The commercial charge amplifier was used to measure the spectra. **a**, tapered tuning fork. **b**, shortened version of tapered tuning fork. **c**,**d**, custom qPlus sensors type 4 and 2. **e**, miniature tuning fork from Statek.

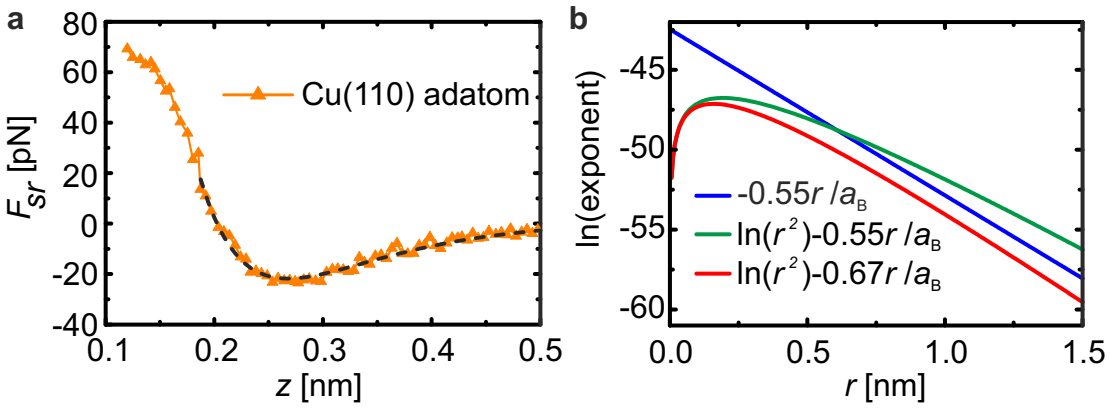

Figure A.6.: **a**, $F_{sr}(z)$ curve for the adatom on Cu(110) from Fig. 5.10. The dashed line indicates a fit with a Morse function. At closer distances ($z < 190\,\mathrm{pm}$) the data points deviate from an exponential behavior. **b**, comparison of exponents for simple exponentially decay (blue) and Slater type orbital (red). Note, the values for the blue curve are offset by -42.5 for clarity.

A.2. Charge Density Model: Determination of the Screening Constant

For the charge density model in section 5.3.3 a value of $\chi = 2/3$ is used. In the following, this value will be motivated. The screening constant or shielding constant χ determines the radial decay of the STOs. For isolated atoms, Slater derived rules on how to determine χ [167]. Following these rules one obtains a value of $\chi = 2.5$ for the $3d$ orbitals of Cu. For the Cu $4s$ orbital there is one more electron taken into account resulting in a value of $\chi = 0.9$ as determined by the Slater rules. These are the values for an isolated Cu atom, due to the additional screening of conduction and valence electrons these values are very likely too large for an adatom. Therefore we decided to estimate a screening constant or decay constant from the experimental $F_{sr}(z)$ data for the adatom on Cu(110) (Fig. A.6a).

By fitting a Morse function (dashed curve) similar to Eq. (2.9) to the data in Fig. A.6a one obtains a decay constant of $\kappa_F = 1.04 \cdot 10^{10}\,\mathrm{m}^{-1}$. The value of κ_F corresponds to an exponentially decaying function ($\propto \exp(-\kappa_F z)$) and in units of the Bohr radius $\kappa_F = \alpha/a_\mathrm{B} = 0.55/a_\mathrm{B}$. To relate $\alpha = 0.55$ to the screening constant χ of the STOs one should consider that the STOs are not simple exponentially decaying functions. Figure A.6b shows a comparison of the natural logarithms of the exponential function ($\propto \exp(-\kappa_F z)$) and the radial part of the STO ($\propto r^2 \exp(-\chi r/a_\mathrm{B})$) from Eq. (5.3). The r^2 term in the STO leads to a different slope of the radial decay at larger distances compared to the simple exponential decay (blue curve) for $\chi = \alpha = 0.55$ (green curve).

If a value of $\chi = 2/3$ (red curve) is used the slope of the radial decay of the STO is closer to the experimental value (blue curve). Therefore, $\chi = 2/3$ is used as screening constant for the STOs in section 5.3.3.

A.3. $TlBiSe_2$: Determination of the Surface Coverage

In section 7.2 atomically resolved Δf data of the $TlBiSe_2$ (111) surface was presented in Fig. 7.5c. Figure A.7a shows the corresponding raw data. In Fig. A.7b an image processing program[3] was used to find the local minima in the low-pass and Laplace filtered image. Each atomic position is indicated by a cross, the number of crosses is 420. Together with the total number of possible lattice sites in the image of 826, this gives a ratio of 0.51 as discussed in the main text.

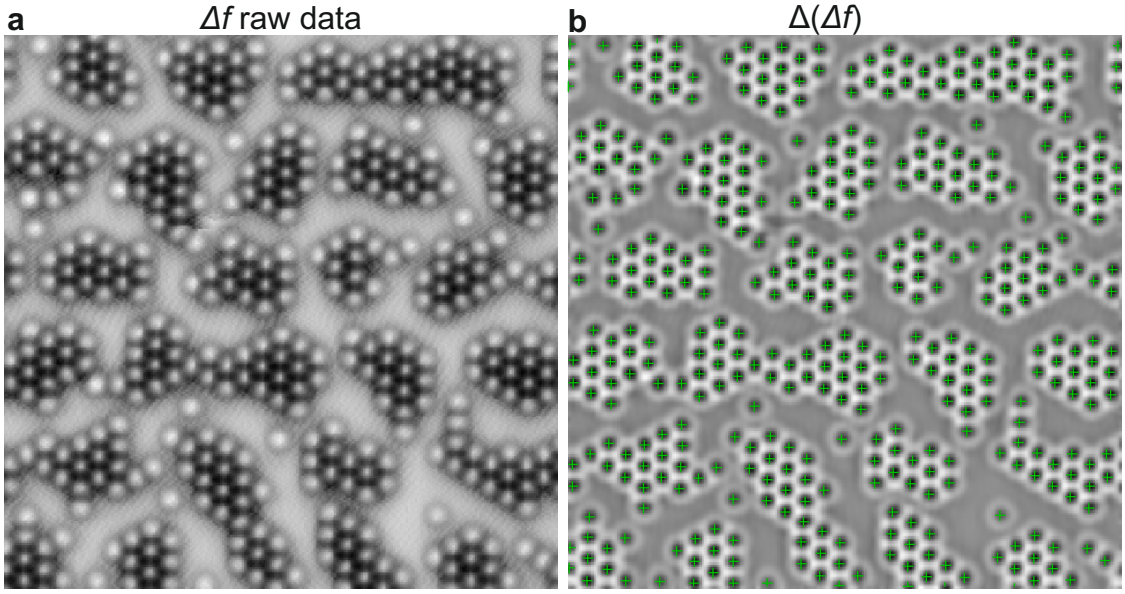

Figure A.7.: **a**, Δf raw data of the image presented in Fig. 7.5c. **b**, Laplace and low-pass filtered version from **a**. The atomic positions are marked with a cross. In total 420 crosses are counted.

[3]WSxM 5.0 Develop 5.1, Nanotec Electronica S.L., Madrid, Spain, [162].

Bibliography

[1] M. N. Baibich, J. M. Broto, A. Fert, F. N. Van Dau, F. Petroff, P. Etienne, G. Creuzet, A. Friederich, and J. Chazelas, *Giant Magnetoresistance of (001)Fe/(001)Cr Magnetic Superlattices*. Physical Review Letters, **61**, 2472, (1988), DOI: 10.1103/PhysRevLett.61.2472.

[2] G. Binasch, P. Grünberg, F. Saurenbach, and W. Zinn, *Enhanced magnetoresistance in layered magnetic structures with antiferromagnetic interlayer exchange*. Physical Review B, **39**, 4828, (1989), DOI: 10.1103/PhysRevB.39.4828.

[3] G. A. Prinz, *Magnetoelectronics*. Science, **282**, 1660, (1998), DOI: 10.1126/science.282.5394.1660.

[4] S. A. Wolf, D. D. Awschalom, R. A. Buhrman, J. M. Daughton, S. von Molnár, M. L. Roukes, A. Y. Chtchelkanova, and D. M. Treger, *Spintronics: a spin-based electronics vision for the future*. Science, **294**, 1488, (2001), DOI: 10.1126/science.1065389.

[5] B. Yan and S.-C. Zhang, *Topological materials*. Reports on progress in physics. Physical Society (Great Britain), **75**, 096501, (2012), DOI: 10.1088/0034-4885/75/9/096501.

[6] B. Krzanich, *Intel Developer Forum IDF13*. Intel Corporation Webcast, (2013), URL: http://intelstudios.edgesuite.net/idf/2013/sf/keynote/130910_bk/index.html.

[7] G. Binnig, H. Rohrer, C. Gerber, and E. Weibel, *Surface Studies by Scanning Tunneling Microscopy*. Physical Review Letters, **49**, 57, (1982), DOI: 10.1103/PhysRevLett.49.57.

[8] G. Binnig, C. F. Quate, and C. Gerber, *Atomic Force Microscope*. Physical Review Letters, **56**, 930, (1986), DOI: 10.1103/PhysRevLett.56.930.

[9] G. Binnig, H. Rohrer, C. Gerber, and E. Weibel, *7×7 Reconstruction on Si(111) Resolved in Real Space*. Physical Review Letters, **50**, 120, (1983), DOI: 10.1103/PhysRevLett.50.120.

[10] G. Meyer and N. M. Amer, *Optical-beam-deflection atomic force microscopy: The NaCl (001) surface*. Applied Physics Letters, **56**, 2100, (1990), DOI: 10.1063/1.102985.

[11] R. Wiesendanger, D. Bürgler, G. Tarrach, A. Wadas, D. Brodbeck, H.-J. Güntherodt, G. Güntherodt, R. J. Gambino, and R. Ruf, *Vacuum tunneling of spin-polarized electrons detected by scanning tunneling microscopy*. Journal of Vacuum Science & Technology B: Microelectronics and Nanometer Structures, **9**, 519, (1991), DOI: 10.1116/1.585560.

[12] Y. Martin and H. K. Wickramasinghe, *Magnetic imaging by "force microscopy" with 1000 Å resolution*. Applied Physics Letters, **50**, 1455, (1987), DOI: 10.1063/1.97800.

[13] S. Heinze, M. Bode, A. Kubetza, O. Pietzsch, X. Nie, S. Blügel, and R. Wiesendanger, *Real-Space Imaging of Two-Dimensional Antiferromagnetism on the Atomic Scale*. Science, **288**, 1805, (2000), DOI: 10.1126/science.288.5472.1805.

[14] U. Kaiser, A. Schwarz, and R. Wiesendanger, *Magnetic exchange force microscopy with atomic resolution*. Nature, **446**, 522, (2007), DOI: 10.1038/nature05617.

[15] F. J. Giessibl, *High-speed force sensor for force microscopy and profilometry utilizing a quartz tuning fork*. Applied Physics Letters, **73**, 3956, (1998), DOI: 10.1063/1.122948.

[16] F. J. Giessibl, *Advances in atomic force microscopy*. Reviews of Modern Physics, **75**, 949, (2003), DOI: 10.1103/RevModPhys.75.949.

[17] F. J. Giessibl, H. Bielefeldt, S. Hembacher, and J. Mannhart, *Calculation of the optimal imaging parameters for frequency modulation atomic force microscopy*. Applied Surface Science, **140**, 352, (1999), DOI: 10.1016/S0169-4332(98)00553-4.

[18] F. J. Giessibl, *Atomic resolution on Si(111)-(7×7) by noncontact atomic force microscopy with a force sensor based on a quartz tuning fork*. Applied Physics Letters, **76**, 1470, (2000), DOI: 10.1063/1.126067.

[19] S. Hembacher, F. J. Giessibl, and J. Mannhart, *Force microscopy with light-atom probes*. Science, **305**, 380, (2004), DOI: 10.1126/science.1099730.

[20] J. Welker and F. J. Giessibl, *Revealing the angular symmetry of chemical bonds by atomic force microscopy*. Science, **336**, 444, (2012), DOI: 10.1126/science.1219850.

[21] L. Gross, F. Mohn, N. Moll, P. Liljeroth, and G. Meyer, *The chemical structure of a molecule resolved by atomic force microscopy*. Science, **325**, 1110, (2009), DOI: 10.1126/science.1176210.

[22] L. Gross, F. Mohn, P. Liljeroth, J. Repp, F. J. Giessibl, and G. Meyer, *Measuring the charge state of an adatom with noncontact atomic force microscopy*. Science, **324**, 1428, (2009), DOI: 10.1126/science.1172273.

[23] M. Schmid, J. Mannhart, and F. J. Giessibl, *Searching atomic spin contrast on nickel oxide (001) by force microscopy*. Physical Review B, **77**, 045402, (2008), DOI: 10.1103/PhysRevB.77.045402.

[24] H. Momida and T. Oguchi, *First-principles study on exchange force image of NiO (0 0 1) surface using a ferromagnetic Fe probe*. Surface Science, **590**, 42, (2005), DOI: 10.1016/j.susc.2005.06.006.

[25] M. Granovskij, A. Schrön, and F. Bechstedt, *Magnetic exchange forces and d-state filling: Antiferromagnetic MnO(001) and NiO(001) surfaces*. Physical Review B, **88**, 184416, (2013), DOI: 10.1103/PhysRevB.88.184416.

[26] M. Z. Hasan and C. L. Kane, *Colloquium: Topological insulators*. Reviews of Modern Physics, **82**, 3045, (2010), DOI: 10.1103/RevModPhys.82.3045.

[27] M. Z. Hasan and J. E. Moore, *Three-Dimensional Topological Insulators*. Annual Review of Condensed Matter Physics, **2**, 55, (2011), DOI: 10.1146/annurev-conmatphys-062910-140432.

[28] K. Kuroda, M. Ye, A. Kimura, S. V. Eremeev, E. E. Krasovskii, E. V. Chulkov, Y. Ueda, K. Miyamoto, T. Okuda, K. Shimada, H. Namatame, and M. Taniguchi, *Experimental Realization of a Three-Dimensional Topological Insulator Phase in Ternary Chalcogenide $TlBiSe_2$*. Physical Review Letters, **105**, 146801, (2010), DOI: 10.1103/PhysRevLett.105.146801.

[29] T. R. Albrecht, P. Grütter, D Horne, and D Rugar, *Frequency modulation detection using high-Q cantilevers for enhanced force microscope sensitivity*. Journal of Applied Physics, **69**, 668, (1991), DOI: 10.1063/1.347347.

[30] T. Hofmann, F. Pielmeier, and F. J. Giessibl, *Chemical and Crystallographic Characterization of the Tip Apex in Scanning Probe Microscopy*. Physical Review Letters, **112**, 066101, (2014), DOI: 10.1103/PhysRevLett.112.066101.

[31] G. Binnig, K. Frank, H. Fuchs, N. Garcia, B. Reihl, H. Rohrer, F. Salvan, and A. Williams, *Tunneling Spectroscopy and Inverse Photoemission: Image and Field States*. Physical Review Letters, **55**, 991, (1985), DOI: 10.1103/PhysRevLett.55.991.

[32] G. Binnig, *Tunneling through a controllable vacuum gap*. Applied Physics Letters, **40**, 178, (1982), DOI: 10.1063/1.92999.

[33] C. J. Chen, *Introduction to Scanning Tunneling Microscopy*. (Oxford University Press, New York, 1993).

[34] M. Ternes, C. P. Lutz, and A. J. Heinrich, *Atomic Manipulation on Metal Surfaces* in *Noncontact Atomic Force Microscopy 2*, ed. by S. Morita, F. J. Giessibl, and R. Wiesendanger, (Springer Berlin Heidelberg, 2009).

[35] H. B. Michaelson, *The work function of the elements and its periodicity*. Journal of Applied Physics, **48**, 4729, (1977), DOI: 10.1063/1.323539.

[36] M. Ternes, C. González, C. P. Lutz, P. Hapala, F. J. Giessibl, P. Jelínek, and A. J. Heinrich, *Interplay of Conductance, Force, and Structural Change in Metallic Point Contacts*. Physical Review Letters, **106**, 016802, (2011), DOI: 10.1103/PhysRevLett.106.016802.

[37] J. Bardeen, *Tunnelling from a Many-Particle Point of View*. Physical Review Letters, **6**, 57, (1961), DOI: 10.1103/PhysRevLett.6.57.

[38] J. Tersoff and D. R. Hamann, *Theory of the scanning tunneling microscope*. Physical Review B, **31**, 805, (1985), DOI: 10.1103/PhysRevB.31.805.

[39] R. Wiesendanger, *Spin mapping at the nanoscale and atomic scale*. Reviews of Modern Physics, **81**, 1495, (2009), DOI: 10.1103/RevModPhys.81.1495.

[40] Y. Martin, C. C. Williams, and H. K. Wickramasinghe, *Atomic force microscope - force mapping and profiling on a sub 100 - Å scale*. Journal of Applied Physics, **61**, 4723, (1987), DOI: 10.1063/1.338807.

[41] M. Lee and W. Jhe, *General Theory of Amplitude-Modulation Atomic Force Microscopy*. Physical Review Letters, **97**, 036104, (2006), DOI: 10.1103/PhysRevLett.97.036104.

[42] F. London, *Zur Theorie und Systematik der Molekularkräfte*. Zeitschrift für Physik, **63**, 245, (1930), DOI: 10.1007/BF01421741.

[43] J. N. Israelachvili, *Intermolecular and Surface Forces*. (Elsevier, Academic Press, 2011).

[44] B. R. Holstein, *The van der Waals interaction*. American Journal of Physics, **69**, 441, (2001), DOI: 10.1119/1.1341251.

[45] F. Giessibl, *Forces and frequency shifts in atomic-resolution dynamic-force microscopy*. Physical Review B, **56**, 16010, (1997), DOI: 10.1103/PhysRevB.56.16010.

[46] G. Teobaldi, K. Lämmle, T. Trevethan, M. Watkins, A. Schwarz, R. Wiesendanger, and A. L. Shluger, *Chemical Resolution at Ionic Crystal Surfaces Using Dynamic Atomic Force Microscopy with Metallic Tips*. Physical Review Letters, **106**, 216102, (2011), DOI: 10.1103/PhysRevLett.106.216102.

[47] T. Göddenhenrich, U. Hartmann, M. Anders, and C. Heiden, *Investigation of Bloch wall fine structures by magnetic force microscopy*. Journal of Microscopy, **152**, 527, (1988), DOI: 10.1111/j.1365-2818.1988.tb01417.x.

[48] M. R. Koblischka and U Hartmann, *Recent advances in magnetic force microscopy*. Ultramicroscopy, **97**, 103, (2003), DOI: 10.1016/S0304-3991(03)00034-2.

[49] I. Schmid, M. A. Marioni, P. Kappenberger, S. Romer, M. Parlinska-Wojtan, H. J. Hug, O. Hellwig, M. J. Carey, and E. E. Fullerton, *Exchange Bias and Domain Evolution at 10 nm Scales*. Physical Review Letters, **105**, 197201, (2010), DOI: 10.1103/PhysRevLett.105.197201.

[50] H. Hölscher, W. Allers, U. D. Schwarz, A. Schwarz, and R. Wiesendanger, *Simulation of NC-AFM images of xenon(111)*. Applied Physics A: Materials Science & Processing, **72**, S35, (2001), DOI: 10.1007/s003390100724.

[51] W. Pauli, *Über den Zusammenhang des Abschlusses der Elektronengruppen im Atom mit der Komplexstruktur der Spektren*. Zeitschrift für Physik, **31**, 765, (1925), DOI: 10.1007/BF02980631.

[52] J. E. Jones, *On the Determination of Molecular Fields. - II. From the Equation of State of a Gas*. Proceedings of the Royal Society A: Mathematical, Physical and Engineering Sciences, **106**, 463, (1924), DOI: 10.1098/rspa.1924.0082.

[53] N. W. Ashcroft and N. D. Mermin, *Solid State Physics*. (Saunders College, 1976).

[54] K.-H. Hellwege, *Einführung in die Festkörperphysik*. (Springer, Berlin, 1988).

[55] F. Giessibl, *Theory for an electrostatic imaging mechanism allowing atomic resolution of ionic crystals by atomic force microscopy*. Physical Review B, **45**, 13815, (1992), DOI: 10.1103/PhysRevB.45.13815.

[56] J. E. Lennard-Jones and B. M. Dent, *Cohesion at a crystal surface*. Transactions of the Faraday Society, **24**, 92, (1928), DOI: 10.1039/tf9282400092.

[57] F. Giessibl and G. Binnig, *Investigation of the (001) cleavage plane of potassium bromide with an atomic force microscope at 4.2 K in ultra-high vacuum*. Ultramicroscopy, **42**, 281, (1992), DOI: 10.1016/0304-3991(92)90280-W.

[58] P. Morse, *Diatomic Molecules According to the Wave Mechanics. II. Vibrational Levels*. Physical Review, **34**, 57, (1929), DOI: 10.1103/PhysRev.34.57.

[59] W. Heisenberg, *Zur Theorie des Ferromagnetismus*. Zeitschrift für Physik, **49**, 619, (1928), DOI: 10.1007/BF01328601.

[60] S. Blundell, *Magnetism In Condensed Matter*. (Oxford University Press, USA, 2000).

[61] W. Heisenberg, *Mehrkörperproblem und Resonanz in der Quantenmechanik*. Zeitschrift für Physik, **38**, 411, (1926), DOI: 10.1007/BF01397160.

[62] F. J. Giessibl, *A direct method to calculate tip-sample forces from frequency shifts in frequency-modulation atomic force microscopy*. Applied Physics Letters, **78**, 123, (2001), DOI: 10.1063/1.1335546.

[63] B. Gotsmann, B. Anczykowski, C. Seidel, and H. Fuchs, *Determination of tip-sample interaction forces from measured dynamic force spectroscopy curves*. Applied Surface Science, **140**, 314, (1999), DOI: 10.1016/S0169-4332(98)00547-9.

[64] H. Hölscher, W. Allers, U. Schwarz, A. Schwarz, and R. Wiesendanger, *Determination of Tip-Sample Interaction Potentials by Dynamic Force Spectroscopy*. Physical Review Letters, **83**, 4780, (1999), DOI: 10.1103/PhysRevLett.83.4780.

[65] U Dürig, *Interaction sensing in dynamic force microscopy*. New Journal of Physics, **2**, 5, (2000), DOI: 10.1088/1367-2630/2/1/005.

[66] U. Dürig, *Extracting interaction forces and complementary observables in dynamic probe microscopy*. Applied Physics Letters, **76**, 1203, (2000), DOI: 10.1063/1.125983.

[67] J. E. Sader and S. P. Jarvis, *Accurate formulas for interaction force and energy in frequency modulation force spectroscopy*. Applied Physics Letters, **84**, 1801, (2004), DOI: 10.1063/1.1667267.

[68] J. Welker, E. Illek, and F. J. Giessibl, *Analysis of force-deconvolution methods in frequency-modulation atomic force microscopy*. Beilstein Journal of Nanotechnology, **3**, 238, (2012), DOI: 10.3762/bjnano.3.27.

[69] F. J. Giessibl, S. Hembacher, M. Herz, C. Schiller, and J. Mannhart, *Stability considerations and implementation of cantilevers allowing dynamic force microscopy with optimal resolution: the qPlus sensor*. Nanotechnology, **15**, S79, (2004), DOI: 10.1088/0957-4484/15/2/017.

[70] F. J. Giessibl, F. Pielmeier, T. Eguchi, T. An, and Y. Hasegawa, *Comparison of force sensors for atomic force microscopy based on quartz tuning forks and length-extensional resonators*. Physical Review B, **84**, 125409, (2011), DOI: 10.1103/PhysRevB.84.125409.

[71] F. J. Giessibl, *Device for contactless scanning of surface*. Patent DE-19633546 A1,(German Patent and Trademark Office, 1996).

[72] F. J. Giessibl, *High-speed force sensor for force microscopy and profilometry utilizing a quartz tuning fork*. Applied Physics Letters, **73**, 3956, (1998), DOI: 10.1063/1.122948.

[73] F. J. Giessibl, *Atomic resolution of the silicon (111)-(7x7) surface by atomic force microscopy*. Science, **267**, 68, (1995), DOI: 10.1126/science.267.5194.68.

[74] A. Labuda, Y. Miyahara, L. Cockins, and P. H. Grütter, *Decoupling conservative and dissipative forces in frequency modulation atomic force microscopy*. Physical Review B, **84**, 125433, (2011), DOI: 10.1103/PhysRevB.84.125433.

[75] M. Nonnenmacher, M. P. O'Boyle, and H. K. Wickramasinghe, *Kelvin probe force microscopy*. Applied Physics Letters, **58**, 2921, (1991), DOI: 10.1063/1.105227.

[76] F. Pielmeier, D. Meuer, D. Schmid, C. Strunk, and F. J. Giessibl, *Impact of thermal frequency drift on highest precision force microscopy using quartz-based force sensors at low temperatures*. Beilstein Journal of Nanotechnology, **5**, 407, (2014), DOI: 10.3762/bjnano.5.48.

[77] M. A. Lantz, H. J. Hug, R Hoffmann, P. J. van Schendel, P Kappenberger, S Martin, A Baratoff, and H. J. Güntherodt, *Quantitative measurement of short-range chemical bonding forces*. Science, **291**, 2580, (2001), DOI: 10.1126/science.1057824.

[78] Y. Sugimoto, P. Pou, M. Abe, P. Jelinek, R. Pérez, S. Morita, and O. Custance, *Chemical identification of individual surface atoms by atomic force microscopy*. Nature, **446**, 64, (2007), DOI: 10.1038/nature05530.

[79] P. Günther, U. C. Fischer, and K. Dransfeld, *Scanning near-field acoustic microscopy*. Applied Physics B Photophysics and Laser Chemistry, **48**, 89, (1989), DOI: 10.1007/BF00694423.

[80] J. Rychen, *Combined Low-Temperature Scanning Probe Microscopy and Magneto-Transport Experiments for the Local Investigation of Mesoscopic Systems*. PhD thesis, Swiss Federal Institute of Technology Zürich, (2001).

[81] K. Dransfeld, U. Fischer, P. Güthner, and K. Heitmann, *Acoustic screen scan microscope for the examination of an object in the short-range field of a resonant acoustic oscillator*. US Patent 5,212,987,(US Patent and Trademark Office, 1993).

[82] K. Bartzke, T. Antrack, K. Besocke, and E. Dammann, *Arrangement for determining the topography of a surface*. Patent DE-19513529 A1,(German Patent and Trademark Office, 1995).

[83] T. An, T. Eguchi, K. Akiyama, and Y. Hasegawa, *Atomically-resolved imaging by frequency-modulation atomic force microscopy using a quartz length-extension resonator*. Applied Physics Letters, **87**, 133114, (2005), DOI: 10.1063/1.2061850.

[84] T. An, T. Nishio, T. Eguchi, M. Ono, A. Nomura, K. Akiyama, and Y. Hasegawa, *Atomically resolved imaging by low-temperature frequency-modulation atomic force microscopy using a quartz length-extension resonator*. Review of Scientific Instruments, **79**, 033703, (2008), DOI: 10.1063/1.2830937.

[85] J. Brice, *Crystals for quartz resonators*. Reviews of Modern Physics, **57**, 105, (1985), DOI: 10.1103/RevModPhys.57.105.

[86] *Standards on Piezoelectric Crystals*, Proceedings of the IRE, **37**, 1378, (1949), DOI: 10.1109/JRPROC.1949.229975.

[87] E. Momosaki and S. Kogure, *The application of piezoelectricity to watches*. Ferroelectrics, **40**, 203, (1982), DOI: 10.1080/00150198208218170.

[88] R. W. Ward, *The Constants of Alpha Quartz* in *Piezoelectricity*, ed. by C. Z. Rosen, B. V. Hiremath, and R. Newnham, (American Institute of Physics, New York, 1992).

[89] P. Heyliger, H. Ledbetter, and S. Kim, *Elastic constants of natural quartz*. The Journal of the Acoustical Society of America, **114**, 644, (2003), DOI: 10.1121/1.1593063.

[90] J. Welker, F. de Faria Elsner, and F. J. Giessibl, *Application of the equipartition theorem to the thermal excitation of quartz tuning forks*. Applied Physics Letters, **99**, 084102, (2011), DOI: 10.1063/1.3627184.

[91] J. Welker, *Höchstauflösende Kraftmikroskopie mit subatomar definierten Bindungszuständen*. Ph.D. Thesis, University of Regensburg, (2012).

[92] I. Morawski, J. Blicharski, and B. Voigtländer, *Voltage preamplifier for extensional quartz sensors used in scanning force microscopy*. Review of Scientific Instruments, **82**, 063701, (2011), DOI: 10.1063/1.3594103.

[93] K. Kobayashi, H. Yamada, and K. Matsushige, *Frequency noise in frequency modulation atomic force microscopy*. Review of Scientific Instruments, **80**, 043708, (2009), DOI: 10.1063/1.3120913.

[94] W. Robins, *Phase Noise in Signal Sources*. (The Institution of Engineering and Technology, London, UK, 1984).

[95] Y. Hasegawa, T. Eguchi, T. An, M. Ono, K. Akiyama, and T. Sakurai, *Calculation of Noise Intensity in the Frequency Demodulation for Atomic Force Microscopy*. Japanese Journal of Applied Physics, **43**, L303, (2004), DOI: 10.1143/JJAP.43.L303.

[96] S. Hembacher, F. J. Giessibl, and J. Mannhart, *Evaluation of a force sensor based on a quartz tuning fork for operation at low temperatures and ultrahigh vacuum*. Applied Surface Science, **188**, 445, (2002), DOI: 10.1016/S0169-4332(01)00976-X.

[97] J. Welker, A. J. Weymouth, and F. J. Giessibl, *The influence of chemical bonding configuration on atomic identification by force spectroscopy*. ACS Nano, **7**, 7377, (2013), DOI: 10.1021/nn403106v.

[98] J. R. Vig, *Quartz crystal resonators and oscillators*. (IEEE Ultrasonics, Ferroelectrics and Frequency Control Society, 2007).

[99] U. Gysin, S. Rast, P. Ruff, E. Meyer, D. Lee, P. Vettiger, and C. Gerber, *Temperature dependence of the force sensitivity of silicon cantilevers*. Physical Review B, **69**, 045403, (2004), DOI: 10.1103/PhysRevB.69.045403.

[100] F. J. Giessibl, *Principle of NC-AFM* in *Noncontact Atomic Force Microscopy*, ed. by S. Morita, R. Wiesendanger, and E. Meyer, (Springer Berlin Heidelberg, 2002).

[101] J. W. Cooley and J. W. Tukey, *An algorithm for the machine calculation of complex Fourier series*. Mathematics of Computation, **19**, 297, (1965), DOI: 10.1090/S0025-5718-1965-0178586-1.

[102] D. Wastl, *Dynamische Rasterkraftmikroskopie mit Quartzsensoren unter Umgebungsbedingungen und in Flüssigkeiten*. Diploma Thesis, University of Regensburg, (2011).

[103] A.-K. B. Greitner, *Simulation of Tuning Forks with a FEA-Program for qPlus Sensor Applications*. Bachelor Thesis, University of Regensburg, (2012).

[104] D. S. Wastl, A. J. Weymouth, and F. J. Giessibl, *Optimizing atomic resolution of force microscopy in ambient conditions*. Physical Review B, **87**, 245415, (2013), DOI: 10.1103/PhysRevB.87.245415.

[105] F. Pielmeier and F. J. Giessibl, *Spin Resolution and Evidence for Superexchange on NiO(001) Observed by Force Microscopy*. Physical Review Letters, **110**, 266101, (2013), DOI: 10.1103/PhysRevLett.110.266101.

[106] T. Ando, *High-speed atomic force microscopy coming of age*. Nanotechnology, **23**, 062001, (2012), DOI: 10.1088/0957-4484/23/6/062001.

[107] R. Worley, M. Zemansky, and H. Boorse, *The Vapor-Pressure Curve of Helium between 4.2°K and 4.8°K*. Physical Review, **93**, 45, (1954), DOI: 10.1103/PhysRev.93.45.

[108] Wikipedia, *Luftdruck*. Wikipedia, Die freie Enzyklopädie, (2014), URL: http://de.wikipedia.org/w/index.php?title=Luftdruck&oldid=129112237#Tagesgang.

[109] J Rychen, T Ihn, P Studerus, A Herrmann, K Ensslin, H. J. Hug, P. J. A. van Schendel, and H. J. Güntherodt, *Operation characteristics of piezoelectric quartz tuning forks in high magnetic fields at liquid helium temperatures*. Review of Scientific Instruments, **71**, 1695, (2000), DOI: 10.1063/1.1150521.

[110] G. A. Lager, J. D. Jorgensen, and F. J. Rotella, *Crystal structure and thermal expansion of α-quartz SiO_2 at low temperatures*. Journal of Applied Physics, **53**, 6751, (1982), DOI: 10.1063/1.330062.

[111] G. K. White, *Thermal expansion of silica at low temperatures*. Cryogenics, **4**, 2, (1964), DOI: 10.1016/0011-2275(64)90029-3.

[112] T. H. K. Barron, J. G. Collins, and G. K. White, *Thermal expansion of solids at low temperatures*. Advances in Physics, **29**, 609, (1980), DOI: 10.1080/00018738000101426.

[113] J. S. Blinick and H. J. Maris, *Velocities of First and Zero Sound in Quartz*. Physical Review B, **2**, 2139, (1970), DOI: 10.1103/PhysRevB.2.2139.

[114] A. Vanelstraete and C. Laermans, *Ultrasonic-phase-velocity measurements in electron-irradiated quartz*. Physical Review B, **39**, 3905, (1989), DOI: 10.1103/PhysRevB.39.3905.

[115] A. Vanelstraete and C. Laermans, *Precision ultrasonic velocity measurements for the study of the low temperature acoustic properties in defective materials*. Materials Science and Engineering: A, **122**, 77, (1989), DOI: 10.1016/0921-5093(89)90775-2.

[116] M. A. Parshin and C. Laermans, *Ultrasound velocity in neutron-irradiated quartz crystals above 5 K*. physica status solidi (c), **1**, 2892, (2004), DOI: 10.1002/pssc.200405296.

[117] T. Hofmann, *Hochauflösende Rasterkraftmikroskopie auf Graphen und Kohlenmonoxid*. Ph.D. Thesis, University of Regensburg, (2014).

[118] E. W. Müller, *Das Feldionenmikroskop*. Zeitschrift für Physik, **131**, 136, (1951), DOI: 10.1007/BF01329651.

[119] G. H. Simon, M. Heyde, and H.-P. Rust, *Recipes for cantilever parameter determination in dynamic force spectroscopy: spring constant and amplitude*. Nanotechnology, **18**, 255503, (2007), DOI: 10.1088/0957-4484/18/25/255503.

[120] M. R. Koblischka, U. Hartmann, and T. Sulzbach, *Resolving magnetic nanostructures in the 10-nm range using MFM at ambient conditions*. Materials Science and Engineering: C, **23**, 747, (2003), DOI: 10.1016/j.msec.2003.09.146.

[121] M. Schneiderbauer, D. Wastl, and F. J. Giessibl, *qPlus magnetic force microscopy in frequency-modulation mode with millihertz resolution*. Beilstein Journal of Nanotechnology, **3**, 174, (2012), DOI: 10.3762/bjnano.3.18.

[122] S. Loth, K. von Bergmann, M. Ternes, A. F. Otte, C. P. Lutz, and A. J. Heinrich, *Controlling the state of quantum spins with electric currents*. Nature Physics, **6**, 340, (2010), DOI: 10.1038/nphys1616.

[123] S. Loth, S. Baumann, C. P. Lutz, D. M. Eigler, and A. J. Heinrich, *Bistability in Atomic-Scale Antiferromagnets*. Science, **335**, 196, (2012), DOI: 10.1126/science.1214131.

[124] T. Wutscher and F. J. Giessibl, *Note:* In situ cleavage of crystallographic oriented tips for scanning probe microscopy. Review of Scientific Instruments, **82**, 026106, (2011), DOI: 10.1063/1.3549628.

[125] A. J. Melmed, *The art and science and other aspects of making sharp tips*. Journal of Vacuum Science & Technology B: Microelectronics and Nanometer Structures, **9**, 601, (1991), DOI: 10.1116/1.585467.

[126] J. P. Ibe, P. P. Bey Jr., S. L. Brandow, R. A. Brizzolara, N. A. Burnham, D. P. DiLella, K. P. Lee, C. R. K. Marrian, and R. J. Colton, *On the electrochemical etching of tips for scanning tunneling microscopy*. Journal of Vacuum Science & Technology A: Vacuum, Surfaces, and Films, **8**, 3570, (1990), DOI: 10.1116/1.576509.

[127] G. Brauer, *Handbuch der präparativen anorganischen Chemie 3*. (Enke Ferdinand, Stuttgart, 1981).

[128] T. T. Tsong, *Atom-Probe Field Ion Microscopy*. (Cambridge University Press, Cambridge, New York, a.o., 1990).

[129] I. Ekvall, E. Wahlström, D. Claesson, H. Olin, and E. Olsson, *Preparation and characterization of electrochemically etched W tips for STM*. Measurement Science and Technology, **10**, 11, (1999), DOI: 10.1088/0957-0233/10/1/006.

[130] P. B. Sewell, C. D. Stockbridge, and M. Cohen, *An Electron Diffraction Study of Electropolished Iron*. Canadian Journal of Chemistry, **37**, 1813, (1959), DOI: 10.1139/v59-266.

[131] A. Härtl, *Herstellung und Charakterisierung magnetischer Rastersondenspitzen*. Bachelor Thesis, University of Regensburg, (2012).

[132] E. W. Müller, S. Nakamura, O. Nishikawa, and S. B. McLane, *Gas-Surface Interactions and Field-Ion Microscopy of Nonrefractory Metals*. Journal of Applied Physics, **36**, 2496, (1965), DOI: 10.1063/1.1714519.

[133] D. Weller, A. Moser, L. Folks, M. E. Best, W. Y. Lee, M. F. Toney, M. Schwickert, J.-U. Thiele, and M. F. Doerner, *High K_u materials approach to 100 Gbits/in^2*. IEEE Transactions on Magnetics, **36**, 10, (2000), DOI: 10.1109/20.824418.

[134] M. Herz, F. J. Giessibl, and J. Mannhart, *Probing the shape of atoms in real space*. Physical Review B, **68**, 045301, (2003), DOI: 10.1103/PhysRevB.68.045301.

[135] L. Bartels, G. Meyer, and K.-H. Rieder, *Controlled vertical manipulation of single CO molecules with the scanning tunneling microscope: A route to chemical contrast*. Applied Physics Letters, **71**, 213, (1997), DOI: 10.1063/1.119503.

[136] F. J. Giessibl, *Subatomic Features on the Silicon (111)-(7x7) Surface Observed by Atomic Force Microscopy*. Science, **289**, 422, (2000), DOI: 10.1126/science.289.5478.422.

[137] W. Demtröder, *Experimentalphysik 3, Atome, Moleküle und Festkörper*. (Springer Berlin Heidelberg, 2005).

[138] F. J. Giessibl and C. F. Quate, *Exploring the Nanoworld with Atomic Force Microscopy*. Physics Today, **59**, 44, (2006), DOI: 10.1063/1.2435681.

[139] M. Posternak, H. Krakauer, A. J. Freeman, and D. Koelling, *Self-consistent electronic structure of surfaces: Surface states and surface resonances on W(001)*. Physical Review B, **21**, 5601, (1980), DOI: 10.1103/PhysRevB.21.5601.

[140] L. F. Mattheiss and D. R. Hamann, *Electronic structure of the tungsten (001) surface*. Physical Review B, **29**, 5372, (1984), DOI: 10.1103/PhysRevB.29.5372.

[141] C. A. Wright and S. D. Solares, *On Mapping Subangstrom Electron Clouds with Force Microscopy*. Nano Letters, **11**, 5026, (2011), DOI: 10.1021/nl2030773.

[142] G. Blyholder, *Molecular Orbital View of Chemisorbed Carbon Monoxide*. The Journal of Physical Chemistry, **68**, 2772, (1964), DOI: 10.1021/j100792a006.

[143] Z. Zuo, W. Huang, P. Han, and Z. Li, *Adsorption of CO on Cu (110) and (100) surfaces using COSMO-based DFT*. Journal of Molecular Modeling, **15**, 1079, (2009), DOI: 10.1007/s00894-009-0471-8.

[144] M. Feng, P. Cabrera-Sanfelix, C. Lin, A. Arnau, D. Sánchez-Portal, J. Zhao, P. M. Echenique, and H. Petek, *Orthogonal interactions of CO molecules on a one-dimensional substrate*. ACS Nano, **5**, 8877, (2011), DOI: 10.1021/nn203041c.

[145] C. Y. Fong, J. P. Walter, and M. L. Cohen, *Comparison of band structures and charge distributions of copper and silver*. Physical Review B, **11**, 2759, (1975), DOI: 10.1103/PhysRevB.11.2759.

[146] J. G. Gay, J. R. Smith, and F. J. Arlinghaus, *Self-Consistent Calculation of Work Function, Charge Densities, and Local Densities of States for Cu(100)*. Physical Review Letters, **38**, 561, (1977), DOI: 10.1103/PhysRevLett.38.561.

[147] A. Euceda, D. M. Bylander, and L. Kleinman, *Self-consistent electronic structure of 6- and 18-layer Cu(111) films*. Physical Review B, **28**, 528, (1983), DOI: 10.1103/PhysRevB.28.528.

[148] R. Smoluchowski, *Anisotropy of the Electronic Work Function of Metals*. Physical Review, **60**, 661, (1941), DOI: 10.1103/PhysRev.60.661.

[149] A. Euceda, D. Bylander, L. Kleinman, and K. Mednick, *Self-consistent electronic structure of 7- and 19-layer Cu(001) films*. Physical Review B, **27**, 659, (1983), DOI: 10.1103/PhysRevB.27.659.

[150] J. A. Rodriguez and M. Kuhn, *Electronic and Chemical Properties of Ag/Pt(111) and Cu/Pt(111) Surfaces: Importance of Changes in the d Electron Populations*. The Journal of Physical Chemistry, **98**, 11251, (1994), DOI: 10.1021/j100095a004.

[151] L. Limot, J. Kröger, R. Berndt, A. Garcia-Lekue, and W. A. Hofer, *Atom Transfer and Single-Adatom Contacts*. Physical Review Letters, **94**, 126102, (2005), DOI: 10.1103/PhysRevLett.94.126102.

[152] C.-K. Yang, Y.-C. Cheng, K. Dy, and S.-Y. Wu, *Self-consistent method for the calculation of surface electronic structure and its application to Cu(110)*. Physical Review B, **52**, 10803, (1995), DOI: 10.1103/PhysRevB.52.10803.

[153] C. E. Schäffer and C. Klixbüll Jørgensen, *The angular overlap model, an attempt to revive the ligand field approaches*. Molecular Physics, **9**, 401, (1965), DOI: 10.1080/00268976500100551.

[154] M. F. Crommie, C. P. Lutz, and D. M. Eigler, *Imaging standing waves in a two-dimensional electron gas*. Nature, **363**, 524, (1993), DOI: 10.1038/363524a0.

[155] J. Licha, *Implementierung einer Driftkorrektur für subatomar aufgelöste 3D-Rastersondenspektroskopie*. Bachelor Thesis, University of Regensburg, (2013).

[156] H. J. Lee and W. Ho, *Single-Bond Formation and Characterization with a Scanning Tunneling Microscope*. Science, **286**, 1719, (1999), DOI: 10.1126/science.286.5445.1719.

[157] L. Gross, N. Moll, F. Mohn, A. Curioni, G. Meyer, F. Hanke, and M. Persson, *High-Resolution Molecular Orbital Imaging Using a p-Wave STM Tip*. Physical Review Letters, **107**, 086101, (2011), DOI: 10.1103/PhysRevLett.107.086101.

[158] N. Moll, L. Gross, F. Mohn, A. Curioni, and G. Meyer, *The mechanisms underlying the enhanced resolution of atomic force microscopy with functionalized tips*. New Journal of Physics, **12**, 125020, (2010), DOI: 10.1088/1367-2630/12/12/125020.

[159] L. Gross, F. Mohn, N. Moll, B. Schuler, A. Criado, E. Guitián, D. Peña, A. Gourdon, and G. Meyer, *Bond-order discrimination by atomic force microscopy*. Science, **337**, 1326, (2012), DOI: 10.1126/science.1225621.

[160] Z. Sun, M. P. Boneschanscher, I. Swart, D. Vanmaekelbergh, and P. Liljeroth, *Quantitative Atomic Force Microscopy with Carbon Monoxide Terminated Tips*. Physical Review Letters, **106**, 046104, (2011), DOI: 10.1103/PhysRevLett.106.046104.

[161] A. J. Weymouth, T. Hofmann, and F. J. Giessibl, *Quantifying molecular stiffness and interaction with lateral force microscopy*. Science, **343**, 1120, (2014), DOI: 10.1126/science.1249502.

[162] I. Horcas, R. Fernández, J. M. Gómez-Rodríguez, J. Colchero, J. Gómez-Herrero, and A. M. Baro, *WSXM: a software for scanning probe microscopy and a tool for nanotechnology*. Review of Scientific Instruments, **78**, 013705, (2007), DOI: 10.1063/1.2432410.

[163] B. Schuler, W. Liu, A. Tkatchenko, N. Moll, G. Meyer, A. Mistry, D. Fox, and L. Gross, *Adsorption Geometry Determination of Single Molecules by Atomic Force Microscopy*. Physical Review Letters, **111**, 106103, (2013), DOI: 10.1103/PhysRevLett.111.106103.

[164] R. McWeeny and C. A. Coulson, *Coulson's Valence*. (Oxford University Press, 1980).

[165] J. Tersoff and L. Falicov, *Electronic structure and local atomic configurations of flat and stepped (111) surfaces of Ni and Cu*. Physical Review B, **24**, 754, (1981), DOI: 10.1103/PhysRevB.24.754.

[166] C.-K. Yang, Y.-C. Cheng, and S. Wu, *Electronic structure calculation for a stepped Cu(110) surface by using a real space approach*. Physics Letters A, **188**, 68, (1994), DOI: 10.1016/0375-9601(94)90119-8.

[167] J. Slater, *Atomic Shielding Constants*. Physical Review, **36**, 57, (1930), DOI: 10.1103/PhysRev.36.57.

[168] D. Belkić and H. S. Taylor, *A unified formula for the Fourier transform of Slater-type orbitals*. Physica Scripta, **39**, 226, (1989), DOI: 10.1088/0031-8949/39/2/004.

[169] C. D. Chisholm, *Group theoretical techniques in quantum chemistry*. (Academic Press, London a.o., 1976).

[170] M. Emmrich, *N/A*. Ph.D. Thesis - in preparation, University of Regensburg, (2014).

[171] D. Z. Gao, J. Grenz, M. B. Watkins, F. Federici Canova, A. Schwarz, R. Wiesendanger, and A. L. Shluger, *Using metallic noncontact atomic force microscope tips for imaging insulators and polar molecules: tip characterization and imaging mechanisms.*. ACS nano, **8**, 5339, (2014), DOI: 10.1021/nn501785q.

[172] L Gerhard, T. K. Yamada, T Balashov, A. F. Takács, R. J. H. Wesselink, M Däne, M Fechner, S Ostanin, A Ernst, I Mertig, and W Wulfhekel, *Magnetoelectric coupling at metal surfaces.*. Nature nanotechnology, **5**, 792, (2010), DOI: 10.1038/nnano.2010.214.

[173] K. Mukasa, H. Hasegawa, Y. Tazuke, K. Sueoka, M. Sasaki, and K. Hayakawa, *Exchange Interaction between Magnetic Moments of Ferromagnetic Sample and Tip: Possibility of Atomic-Resolution Images of Exchange Interactions using Exchange Force Microscopy*. Japanese Journal of Applied Physics, **33**, 2692, (1994), DOI: 10.1143/JJAP.33.2692.

[174] H. Ness and F. Gautier, *Theoretical study of the interaction between a magnetic nanotip and a magnetic surface*. Physical Review B, **52**, 7352, (1995), DOI: 10.1103/PhysRevB.52.7352.

[175] K. Nakamura, H. Hasegawa, T. Oguchi, K. Sueoka, K. Hayakawa, and K. Mukasa, *First-principles calculation of the exchange interaction and the exchange force between magnetic Fe films*. Physical Review B, **56**, 3218, (1997), DOI: 10.1103/PhysRevB.56.3218.

[176] A. S. Foster and A. L. Shluger, *Spin-contrast in non-contact SFM on oxide surfaces: theoretical modelling of NiO (001) surface*. Surface Science, **490**, 211, (2001), DOI: 10.1016/S0039-6028(01)01334-6.

[177] H. Hosoi, K. Seuoka, K. Hayakawa, and K. Mukasa, *Atomic resolved imaging of cleaved NiO(100) surfaces by NC-AFM*. Applied Surface Science, **157**, 218, (2000), DOI: 10.1016/S0169-4332(99)00529-2.

[178] W. Allers, S. Langkat, and R. Wiesendanger, *Dynamic low-temperature scanning force microscopy on nickel oxide (001)*. Applied Physics A: Materials Science & Processing, **72**, S27, (2001), DOI: 10.1007/s003390100731.

[179] H. Hosoi, K. Sueoka, and K. Mukasa, *Investigations on the topographical asymmetry of non-contact atomic force microscopy images of NiO(001) surface observed with a ferromagnetic tip*. Nanotechnology, **15**, 505, (2004), DOI: 10.1088/0957-4484/15/5/018.

[180] U. Kaiser, A. Schwarz, and R. Wiesendanger, *Evaluating local properties of magnetic tips utilizing an antiferromagnetic surface*. Physical Review B, **78**, 104418, (2008), DOI: 10.1103/PhysRevB.78.104418.

[181] A. Schwarz, U. Kaiser, and R. Wiesendanger, *Towards an understanding of the atomic scale magnetic contrast formation in NC-AFM: a tip material dependent MExFM study on NiO (001)*. Nanotechnology, **20**, 264017, (2009), DOI: 10.1088/0957-4484/20/26/264017.

[182] R. Schmidt, C. Lazo, H. Hölscher, U. H. Pi, V. Caciuc, A. Schwarz, R. Wiesendanger, and S. Heinze, *Probing the magnetic exchange forces of iron on the atomic scale*. Nano Letters, **9**, 200, (2009), DOI: 10.1021/nl802770x.

[183] R. Schmidt, C. Lazo, U. Kaiser, A. Schwarz, S. Heinze, and R. Wiesendanger, *Quantitative Measurement of the Magnetic Exchange Interaction across a Vacuum Gap*. Physical Review Letters, **106**, 257202, (2011), DOI: 10.1103/PhysRevLett.106.257202.

[184] R. Schmidt, A. Schwarz, and R. Wiesendanger, *Magnetization switching utilizing the magnetic exchange interaction*. Physical Review B, **86**, 174402, (2012), DOI: 10.1103/PhysRevB.86.174402.

[185] E. Y. Vedmedenko, Q. Zhu, U. Kaiser, A. Schwarz, and R. Wiesendanger, *Atomic-scale magnetic dissipation from spin-dependent adhesion hysteresis*. Physical Review B, **85**, 174410, (2012), DOI: 10.1103/PhysRevB.85.174410.

[186] R. W. G. Wyckoff, *The Structure of Crystals*. (Reinhold Publishing Corporation, New York, 1935).

[187] J. R. Tomlinson, L. Domash, R. G. Hay, and C. W. Montgomery, *The High Temperature Heat Content of Nickel Oxide*. Journal of the American Chemical Society, **77**, 909, (1955), DOI: 10.1021/ja01609a032.

[188] G. A. Slack, *Crystallography and Domain Walls in Antiferromagnetic NiO Crystals*. Journal of Applied Physics, **31**, 1571, (1960), DOI: 10.1063/1.1735895.

[189] F. B. Lewis and N. H. Saunders, *The thermal conductivity of NiO and CoO at the Neel temperature*. Journal of Physics C: Solid State Physics, **6**, 2525, (1973), DOI: 10.1088/0022-3719/6/15/012.

[190] G. A. Sawatzky and J. W. Allen, *Magnitude and Origin of the Band Gap in NiO*. Physical Review Letters, **53**, 2339, (1984), DOI: 10.1103/PhysRevLett.53.2339.

[191] M. R. Castell, P. L. Wincott, N. G. Condon, C. Muggelberg, G. Thornton, S. L. Dudarev, A. P. Sutton, and G. A. D. Briggs, *Atomic-resolution STM of a system with strongly correlated electrons:NiO(001) surface structure and defect sites*. Physical Review B, **55**, 7859, (1997), DOI: 10.1103/PhysRevB.55.7859.

[192] D. Ködderitzsch, W. Hergert, W. M. Temmerman, Z. Szotek, A. Ernst, and H. Winter, *Exchange interactions in NiO and at the NiO(100) surface*. Physical Review B, **66**, 064434, (2002), DOI: 10.1103/PhysRevB.66.064434.

[193] P. W. Anderson, *Antiferromagnetism. Theory of Superexchange Interaction*. Physical Review, **79**, 350, (1950), DOI: 10.1103/PhysRev.79.350.

[194] M. T. Hutchings and E. J. Samuelsen, *Measurement of Spin-Wave Dispersion in NiO by Inelastic Neutron Scattering and Its Relation to Magnetic Properties*. Physical Review B, **6**, 3447, (1972), DOI: 10.1103/PhysRevB.6.3447.

[195] F. U. Hillebrecht, H. Ohldag, N. B. Weber, C. Bethke, U. Mick, M. Weiss, and J. Bahrdt, *Magnetic Moments at the Surface of Antiferromagnetic NiO(100)*. Physical Review Letters, **86**, 3419, (2001), DOI: 10.1103/PhysRevLett.86.3419.

[196] T. Okazawa, Y. Yagi, and Y. Kido, *Rumpled surface structure and lattice dynamics of NiO(001)*. Physical Review B, **67**, 195406, (2003), DOI: 10.1103/PhysRevB.67.195406.

[197] I. Sänger, V. V. Pavlov, M. Bayer, and M. Fiebig, *Distribution of antiferromagnetic spin and twin domains in NiO*. Physical Review B, **74**, 144401, (2006), DOI: 10.1103/PhysRevB.74.144401.

[198] S. L. Dudarev, A. I. Liechtenstein, M. R. Castell, G. A. D. Briggs, and A. P. Sutton, *Surface states on NiO (100) and the origin of the contrast reversal in atomically resolved scanning tunneling microscope images*. Physical Review B, **56**, 4900, (1997), DOI: 10.1103/PhysRevB.56.4900.

[199] M. R. Castell, S. L. Dudarev, G. A. D. Briggs, and A. P. Sutton, *Unexpected differences in the surface electronic structure of NiO and CoO observed by STM and explained by first-principles theory*. Physical Review B, **59**, 7342, (1999), DOI: 10.1103/PhysRevB.59.7342.

[200] B. Cullity and C. Graham, *Introduction to Magnetic Materials*. (Wiley-IEEE Press, 2008).

[201] T. Burkert, L. Nordström, O. Eriksson, and O. Heinonen, *Giant Magnetic Anisotropy in Tetragonal FeCo Alloys*. Physical Review Letters, **93**, 027203, (2004), DOI: 10.1103/PhysRevLett.93.027203.

[202] U. Kaiser, *Magnetische Austauschkraftmikroskopie*. PhD thesis, University of Hamburg, (2007).

[203] M. Ondráček, C. González, and P. Jelínek, *Reversal of atomic contrast in scanning probe microscopy on (111) metal surfaces*. Journal of physics. Condensed matter : an Institute of Physics journal, **24**, 084003, (2012), DOI: 10.1088/0953-8984/24/8/084003.

[204] Y. Sugimoto, A. Yurtsever, M. Abe, S. Morita, M. Ondráček, P. Pou, R. Pérez, and P. Jelínek, *Role of tip chemical reactivity on atom manipulation process in dynamic force microscopy*. ACS Nano, **7**, 7370, (2013), DOI: 10.1021/nn403097p.

[205] B. C. Stipe, H. J. Mamin, T. D. Stowe, T. W. Kenny, and D. Rugar, *Magnetic Dissipation and Fluctuations in Individual Nanomagnets Measured by Ultrasensitive Cantilever Magnetometry*. Physical Review Letters, **86**, 2874, (2001), DOI: 10.1103/PhysRevLett.86.2874.

[206] X.-L. Qi and S.-C. Zhang, *The quantum spin Hall effect and topological insulators*. Physics Today, **63**, 33, (2010), DOI: 10.1063/1.3293411.

[207] J. Maciejko, T. L. Hughes, and S.-C. Zhang, *The Quantum Spin Hall Effect*. Annual Review of Condensed Matter Physics, **2**, 31, (2011), DOI: 10.1146/annurev-conmatphys-062910-140538.

[208] S. Groves and W. Paul, *Band Structure of Gray Tin*. Physical Review Letters, **11**, 194, (1963), DOI: 10.1103/PhysRevLett.11.194.

[209] T. C. Harman, W. H. Kleiner, A. J. Strauss, G. B. Wright, J. G. Mavroides, J. M. Honig, and D. H. Dickey, *Band structure of HgTe and HgTe-CdTe alloys*. Solid State Communications, **2**, 305, (1964), DOI: 10.1016/0038-1098(64)90531-9.

[210] C.-Y. Moon and S.-H. Wei, *Band gap of Hg chalcogenides: Symmetry-reduction-induced band-gap opening of materials with inverted band structures*. Physical Review B, **74**, 045205, (2006), DOI: 10.1103/PhysRevB.74.045205.

[211] B. A. Bernevig, T. L. Hughes, and S.-C. Zhang, *Quantum Spin Hall Effect and Topological Phase Transition in HgTe Quantum Wells*. Science, **314**, 1757, (2006), DOI: 10.1126/science.1133734.

[212] C. L. Kane and E. J. Mele, *Quantum Spin Hall Effect in Graphene*. Physical Review Letters, **95**, 226801, (2005), DOI: 10.1103/PhysRevLett.95.226801.

[213] B. A. Bernevig and S.-C. Zhang, *Quantum Spin Hall Effect*. Physical Review Letters, **96**, 106802, (2006), DOI: 10.1103/PhysRevLett.96.106802.

[214] L. Fu, C. L. Kane, and E. J. Mele, *Topological Insulators in Three Dimensions*. Physical Review Letters, **98**, 106803, (2007), DOI: 10.1103/PhysRevLett.98.106803.

[215] K. von Klitzing, G. Dorda, and M. Pepper, *New Method for High-Accuracy Determination of the Fine-Structure Constant Based on Quantized Hall Resistance*. Physical Review Letters, **45**, 494, (1980), DOI: 10.1103/PhysRevLett.45.494.

[216] Y. K. Kato, R. C. Myers, A. C. Gossard, and D. D. Awschalom, *Observation of the spin Hall effect in semiconductors*. Science, **306**, 1910, (2004), DOI: 10.1126/science.1105514.

[217] M. König, S. Wiedmann, C. Brüne, A. Roth, H. Buhmann, L. W. Molenkamp, X.-L. Qi, and S.-C. Zhang, *Quantum spin hall insulator state in HgTe quantum wells*. Science, **318**, 766, (2007), DOI: 10.1126/science.1148047.

[218] C. Liu, T. L. Hughes, X.-L. Qi, K. Wang, and S.-C. Zhang, *Quantum Spin Hall Effect in Inverted Type-II Semiconductors*. Physical Review Letters, **100**, 236601, (2008), DOI: 10.1103/PhysRevLett.100.236601.

[219] W. Shockley, *On the Surface States Associated with a Periodic Potential*. Physical Review, **56**, 317, (1939), DOI: 10.1103/PhysRev.56.317.

[220] P. O. Gartland and B. J. Slagsvold, *Transitions conserving parallel momentum in photoemission from the (111) face of copper*. Physical Review B, **12**, 4047, (1975), DOI: 10.1103/PhysRevB.12.4047.

[221] S. LaShell, B. McDougall, and E. Jensen, *Spin Splitting of an Au(111) Surface State Band Observed with Angle Resolved Photoelectron Spectroscopy*. Physical Review Letters, **77**, 3419, (1996), DOI: 10.1103/PhysRevLett.77.3419.

[222] K. Oura, V. Lifshits, A. Saranin, A. Zotov, and M. Katayama, *Surface Science*. (Springer, Berlin, 2003).

[223] J. H. Dil, *Spin and angle resolved photoemission on non-magnetic low-dimensional systems*. Journal of physics: Condensed matter, **21**, 403001, (2009), DOI: 10.1088/0953-8984/21/40/403001.

[224] L. Fu and C. L. Kane, *Topological insulators with inversion symmetry*. Physical Review B, **76**, 045302, (2007), DOI: 10.1103/PhysRevB.76.045302.

[225] D. Hsieh, D. Qian, L. Wray, Y. Xia, Y. S. Hor, R. J. Cava, and M. Z. Hasan, *A topological Dirac insulator in a quantum spin Hall phase*. Nature, **452**, 970, (2008), DOI: 10.1038/nature06843.

[226] D. Hsieh, Y. Xia, L. Wray, D. Qian, A. Pal, J. H. Dil, J. Osterwalder, F. Meier, G. Bihlmayer, C. L. Kane, Y. S. Hor, R. J. Cava, and M. Z. Hasan, *Observation of Unconventional Quantum Spin Textures in Topological Insulators*. Science, **323**, 919, (2009), DOI: 10.1126/science.1167733.

[227] D. Hsieh, Y. Xia, D. Qian, L. Wray, F. Meier, J. H. Dil, J. Osterwalder, L. Patthey, A. V. Fedorov, H. Lin, A. Bansil, D. Grauer, Y. S. Hor, R. J. Cava, and M. Z. Hasan, *Observation of Time-Reversal-Protected Single-Dirac-Cone Topological-Insulator States in Bi_2Te_3 and Sb_2Te_3*. Physical Review Letters, **103**, 146401, (2009), DOI: 10.1103/PhysRevLett.103.146401.

[228] Y. L. Chen, J. G. Analytis, J.-H. Chu, Z. K. Liu, S.-K. Mo, X. L. Qi, H. J. Zhang, D. H. Lu, X. Dai, Z. Fang, S. C. Zhang, I. R. Fisher, Z. Hussain, and Z.-X. Shen, *Experimental Realization of a Three-Dimensional Topological Insulator, Bi_2Te_3*. Science, **325**, 178, (2009), DOI: 10.1126/science.1173034.

[229] Y. Xia, D. Qian, D. Hsieh, L. Wray, A. Pal, H. Lin, A. Bansil, D. Grauer, Y. S. Hor, R. J. Cava, and M. Z. Hasan, *Observation of a large-gap topological-insulator class with a single Dirac cone on the surface*. Nature Physics, **5**, 398, (2009), DOI: 10.1038/nphys1274.

[230] H. Lin, R. S. Markiewicz, L. A. Wray, L. Fu, M. Z. Hasan, and A. Bansil, *Single-Dirac-Cone Topological Surface States in the $TlBiSe_2$ Class of Topological Semiconductors*. Physical Review Letters, **105**, 036404, (2010), DOI: 10.1103/PhysRevLett.105.036404.

[231] B. Yan, C.-X. Liu, H.-J. Zhang, C.-Y. Yam, X.-L. Qi, T. Frauenheim, and S.-C. Zhang, *Theoretical prediction of topological insulators in thallium-based III-V-VI_2 ternary chalcogenides*. EPL (Europhysics Letters), **90**, 37002, (2010), DOI: 10.1209/0295-5075/90/37002.

[232] S. V. Eremeev, Y. M. Koroteev, and E. V. Chulkov, *Ternary thallium-based semimetal chalcogenides Tl-V-VI2 as a new class of three-dimensional topological insulators*. JETP Letters, **91**, 594, (2010), DOI: 10.1134/S0021364010110111.

[233] S. V. Eremeev, G. Bihlmayer, M. Vergniory, Y. M. Koroteev, T. V. Menshchikova, J. Henk, A. Ernst, and E. V. Chulkov, *Ab initio electronic structure of thallium-based topological insulators*. Physical Review B, **83**, 205129, (2011), DOI: 10.1103/PhysRevB.83.205129.

[234] Y. L. Chen, Z. K. Liu, J. G. Analytis, J.-H. Chu, H. J. Zhang, B. H. Yan, S.-K. Mo, R. G. Moore, D. H. Lu, I. R. Fisher, S. C. Zhang, Z. Hussain, and Z.-X. Shen, *Single Dirac Cone Topological Surface State and Unusual Thermoelectric Property of Compounds from a New Topological Insulator Family*. Physical Review Letters, **105**, 266401, (2010), DOI: 10.1103/PhysRevLett.105.266401.

[235] T. Sato, K. Segawa, H. Guo, K. Sugawara, S. Souma, T. Takahashi, and Y. Ando, *Direct Evidence for the Dirac-Cone Topological Surface States in the Ternary Chalcogenide $TlBiSe_2$*. Physical Review Letters, **105**, 136802, (2010), DOI: 10.1103/PhysRevLett.105.136802.

[236] S.-Y. Xu, Y. Xia, L. A. Wray, S. Jia, F. Meier, J. H. Dil, J. Osterwalder, B. Slomski, A. Bansil, H. Lin, R. J. Cava, and M. Z. Hasan, *Topological phase transition and texture inversion in a tunable topological insulator*. Science, **332**, 560, (2011), DOI: 10.1126/science.1201607.

[237] T. Sato, K. Segawa, K. Kosaka, S. Souma, K. Nakayama, K. Eto, T. Minami, Y. Ando, and T. Takahashi, *Unexpected mass acquisition of Dirac fermions at the quantum phase transition of a topological insulator*. Nature Physics, **7**, 840, (2011), DOI: 10.1038/nphys2058.

[238] L. Despont, F. Clerc, M. G. Garnier, H. Berger, L. Forró, and P. Aebi, *Multiple scattering investigation of the 1T-TaS_2 surface termination*. The European Physical Journal B, **52**, 421, (2006), DOI: 10.1140/epjb/e2006-00307-6.

[239] K. Kuroda, M. Ye, E. F. Schwier, M. Nurmamat, K. Shirai, M. Nakatake, S. Ueda, K. Miyamoto, T. Okuda, H. Namatame, M. Taniguchi, Y. Ueda, and A. Kimura, *Experimental verification of the surface termination in the topological insulator $TlBiSe_2$ using core-level photoelectron spectroscopy and scanning tunneling microscopy*. Physical Review B, **88**, 245308, (2013), DOI: 10.1103/PhysRevB.88.245308.

[240] S. N. Toubektsis and E. K. Polychroniadis, *Growth and structural considerations on single $TlBiSe_2$ crystals*. Journal of Crystal Growth, **84**, 316, (1987), DOI: 10.1016/0022-0248(87)90147-3.

[241] O. Madelung, *Semiconductors: Data Handbook*. (Springer, Berlin, 2004).

[242] J. Berwanger, *Oberflächencharakterisierung Topologischer Isolatoren mittels Rastersondenmikroskopie im Ultrahochvakuum*. Bachelor Thesis, University of Regensburg, (2013).

[243] A. J. Weymouth, T. Wutscher, J. Welker, T. Hofmann, and F. J. Giessibl, *Phantom Force Induced by Tunneling Current: A Characterization on Si(111)*. Physical Review Letters, **106**, 226801, (2011), DOI: 10.1103/PhysRevLett.106.226801.

[244] B. Anczykowski, B. Gotsmann, H. Fuchs, J. P. Cleveland, and V. B. Elings, *How to measure energy dissipation in dynamic mode atomic force microscopy*. Applied Surface Science, **140**, 376, (1999), DOI: 10.1016/S0169-4332(98)00558-3.

[245] R. von Mises,*Mechanik der festen Körper im plastisch- deformablen Zustand*, Nachrichten von der Gesellschaft der Wissenschaften zu Göttingen, Mathematisch-Physikalische Klasse, **1913**, 582, (1913), URL: http://eudml.org/doc/58894.

Acknowledgment

First, I want to thank my supervisor Prof. Dr. Franz Gießibl for giving me the opportunity to start a PhD thesis in his group. Moreover, many thanks for the possibility to carry out several interesting experiments besides the main project about spin-resolved measurements on NiO.
In this context I also want to address thanks to Prof. Dr. Jan H. Dil for supplying the $TlBiSe_2$ samples and for his work on the manuscript. Support by all other co-authors is also greatly appreciated.

Thanks to Prof. Dr. Christian Back for the second expertise of this thesis.

Special gratitude goes to Dr. Andreas Heinrich for enabling a research stay of several weeks in his laboratory at the IBM Research Center in Almaden (USA) and of course Prof. Gießibl for sending me there. Many thanks also to Chris P. Lutz, I gained a lot of knowledge from his tremendous experience in the field of low temperature scanning probe microscopy and electronics. Finally, also many thanks to Susanne Baumann who spent a lot of time in the lab with me and introduced me to the STM/AFM system.

For the low temperature characterization measurements of thermal frequency drift I want to thank Prof. Dr. Christoph Strunk for providing the He^4 stick and Daniel Schmid for technical support. Furthermore, Daniel Meuer for performing several of the long-term measurements in the beginning of this project.

Many thanks also to Florian Oberhuber, who sacrificed several hours for the FIB etching of the tips.

Special thanks are due to Joachim Welker and Thomas Hofmann for sharing their knowledge about the Omicron LT STM/AFM and the COFI measurements. Furthermore, I want to thank Matthias Emmrich and Maximilian Schneiderbauer together with the abovementioned for the enjoyable scientific and non-scientific discussions during coffee breaks and their great cooperativeness.

Any support by Dr. Jay Weymouth, in particular with MatLab and COMSOL, is greatly appreciated and also many thanks for proof reading this thesis.

I also want to thank all colleagues from the Gießibl group and visiting scientists for the pleasant atmosphere and working environment.

Particularly, I want to thank my parents for their support and sponsorship during my education. And finally, my wife Renate for her great support and encouragement and my son for distracting me from work ;)